Tire Modeling and Friction Estimation

Svendenius, Jacob

2007

Document Version:
Publisher's PDF, also known as Version of record

Tire Modeling and Friction Estimation

Jacob Svendenius

Department of Automatic Control
Lund University
Lund, April 2007

Department of Automatic Control
Lund University
Box 118
SE-221 00 LUND
Sweden

ISSN 0280–5316
ISRN LUTFD2/TFRT--1077--SE

Abstract

New system technologies are continuously improving the performance of vehicles regarding comfort, stability, environmental stresses, and safety. Novel sensors are developed and used together with advanced control algorithms and faster and more accurate actuators to help the driver to maneuver the vehicle in a safer way. The physical traction limit set by the friction between the tires and the road can, however, not be overridden. The behavior of tires is, therefore, an important issue since it determine the possibilities to control the vehicle. One essential task for the vehicle control system is to be able to fully utilize these limits. Another is to assist the driver choose an adequate driving style, adapted to the actual conditions.

A method to derive the tire forces for simultaneous braking, cornering and camber, by combining empirical models for the pure behavior of each of respective action is presented in the thesis. The method is based on the physical foundation brought by the simple, but well-suited brush model theory. The pure-slip tire models can be given as empirical models or as raw tabular data. The implementation is verified to be well-working and computationally sound and good results are obtained in validation with the available empirical data.

A new type of on board brush-model based friction-estimator using the local measurements on the vehicle is also proposed. A major invention is the way of collecting the measurements into bins, such that the available data used for optimization is evenly weighted along the force and slip axis. Experimental data has been collected and evaluated to ensure the validity of the brush model during certain conditions. The estimator has been implemented and validated on a personal car.

The wheel speed signal is an essential signal in many system applications. Based on problems observed during performed measurements, a few ways to reduce the noise on the signal, without adding any phase shift or time delay, are discussed in the thesis.

Acknowledgments

First of all I would like to express my gratitude to the persons that made the decisions, a huge amount of years ago, necessary to establish my situation as industrial PhD student, the former technical manager, Kent Jörgensen and the former personal manager, Lena-Maria Lundberg at Haldex Brake Products AB. I will also thank my supervisor, Björn Wittenmark, at the Department of Automatic Control for the administrative work he made to establish this collaboration. His advice, encouraging support and guiding corrections has all the time lead the projects and the thesis writing in a rewarding direction. Thanks to my assistant supervisor Per Hagander for proof reading and valuable comments on the thesis. I would also like thank my supervisor at Haldex, Per-Axel Roth, for good listening and finding nice parallels from his earlier experiences.

I'm very grateful to my group manager at Haldex, Anders Lindqvist, for giving great support in all kind of matters and being the only one at Haldex to always participate on the reference group meetings. It is a pleasure to be a part of a great working group, having Anders Nilsson, Ola Nockhammar, Lisette Pedersen, Sabine Marksell and Ola Ahlström as colleagues. Many thanks to Peter Nilsson for his wise opinions and skilled advices. I am particularly thankful Sverker Stomrud for his great commitments in all technical and patent related issues and strong belief in new ideas.

The work in the Road Friction Estimation project has been very interesting and rewarding and I will gratefully acknowledge Johan Hultén at Volvo Cars for good project leadership and Fredrik Bruzelius for fruitful and inspiring cooperation and nice fellowship and proof reading of the thesis. Both Johan and Fredrik are deeply involved the chapter concerning the road friction estimator. Special thanks to Magnus Gäfvert, now at Modelon AB, but former at both the Department of Automatic Control and at Haldex, for his enormous working spirit. I am glad for our rewarding discussions and nice collaboration. Magnus has contributed in both the

development of the semi-empirical tire model and of the friction estimator and most of my publications have been written together with him. He is to a large content involved in most sections of the thesis and I am glad for his careful proof reading and valuable comments on the dissertation.

An advantage when having two work places is that one get many colleagues and I am gifted with fantastic coworkers at two different workplaces. I am very pleased with the creative spirit and open atmosphere at the Department of Automatic Control in Lund, which has been a great source of inspiration.

It has everyday been a pleasure to enjoy the lunch at Sparta with "Spartagänget" that now has been reduced to Rolf Braun (I hope that you will not need to eat alone from now on). It is also a delight to quarrel with the always benevolent and helpful secretaries, Eva, Britt-Marie and Agneta. Thanks to Leif for all kind of help in report-writing issues and thanks to Brad for linguistic corrections on some of the important sections in the thesis.

I am really grateful for the encouragement and support from my mother, father and sister. It is good to know that they always care. Thanks to Inger and Christer for always stand by and being helpful. A lot of thanks go to all my friends, many of them have somehow helped me to come to this point.

Finally, I will thank my wife, Malin for her care and endless love and my son, Jonah that really makes life exciting and meaningful. I love you both very much!

Jacob

Contents

1

Introduction

1.1 Background and Motivation

This thesis is a result of cooperation between the R&D department at Haldex Brake Products in Landskrona and the Department of Automatic Control at Lund University. The work is closely related to the development of brake-by-wire systems using electrically actuated brakes for heavy trucks and buses performed at Haldex. One objective of the collaborative work has been to further investigate the new field for improvements of vehicle stabilizing and safety functions, opened by the enhanced controllability of an electrically actuated brake compared to the conventional pneumatic brake. For a well-working brake system, the physical properties of the brakes are not limiting, their capability to produce braking torque is very rarely used fully. Instead the conditions of the tire and the road surface set the functional limits for safe retardation of the vehicle. When the Anti-lock Braking System (ABS) was introduced in the luxury vehicles it greatly improved the surface friction utilization of the brake system in critical situations. Nowadays, it is standard equipment in most cars. The motivation for developing ABS relies on the observation that a locked wheel only produces a force in the sliding direction of the tire. Furthermore, a higher tire force can be obtained from a rolling wheel. Preventing the wheel from locking while still generating a high braking force is shown to reduce the braking distance. But, maybe more important is that it enables the possibility to the driver to control the vehicle direction by steering maneuvers.

There is an optimal wheel rotation velocity, depending on the tire properties, surface condition, and vehicle motion, for which the tire develops its maximal friction force. Finding and keeping this value under the current condition in critical maneuvers, while providing stable and safe motion

of the vehicle, is a great issue for improvement of today's systems. The new quicker brake actuators increase the possibilities for stable control of the wheel velocity in such situations. When increasing the bandwidth of the braking control loop the dynamic effects of the mechanical systems supporting the brake and participating in the transmission of the force to the road become crucial. Deflections in suspension, bushings, and the tire delay the generated tire force acting on the vehicle and may cause displacement of the wheel speed sensor. This disturbs the wheel speed measurements. The noise filters have to be faster to catch rapid signal variations, resulting in less attenuation of the disturbances. The inertia in the wheel rim might cause unwanted oscillations. Hence, utilization of the advantages in control of faster brakes requires the algorithms to further predict and estimate the dynamics of the surrounding system. Enhanced sensor quality and larger computational capacity increases the possibilities to achieve such estimations.

The new and improved technology emphasizes attempts to also detect the conditions surrounding the entire vehicle using existing sensors. The idea is attractive since the functionality of many other vehicle systems can be improved by such knowledge. Automatic cruise control (ACC), collision avoidance warning and, electronic stability program (ESP) are a few examples. Another important feature is to help the driver to adapt the driving style towards the current conditions. Within the EU-project *Intelligent Roads* [Vägverket, 2006a] research is performed about how the road surface limitations should be presented to the driver. It might be as estimated braking distance, or as a recommended maximal speed. For an on board road-condition estimator it seems quite impossible to determine the circumstances in front of the vehicle. It could however, be possible by using a preview sensor or having an infrastructure that receives and distributes frictional information about the roads. The distribution can be both to a common central or to share between the vehicles in a close neighborhood. Research regarding infrastructures that receives and distributes estimates of the surface friction along the road is performed within the national program *Safety Road Information Structure* [Vägverket, 2006c].

A major aim of this work is to explain and model the general behavior of tires and to find properties that are common for the majority of tire types. Simplicity in modeling is a keyword throughout the thesis. Often, the final solutions still tend to be sufficiently comprehensive. Starting with complex models might limit the usability in the end. Therefore, the basic form of the brush-model theory to describe the tire behavior has been fundamental in this work.

The developed theories are based on physical assumptions and most of them are validated from available data or by tests performed particularly for this purpose. Due to good experimental equipment at Haldex

and the close collaborative work with both Volvo Cars and VTI (Swedish National Road and transport Research Institute) a multitude of different test scenarios have been performed. There have been many possibilities to participate in the planning of the tests and most of them have been directly specified to serve the method development described in the thesis. There is a great benefit in participating during the testing, since it gives a better feeling for how the surrounding conditions and other unexpected factors might influence the result. All tests have be performed on real tires in real conditions. This has made it impossible to completely separate the measurement of, for example, the tire behavior from disturbances from the road and the wheel suspension, etc. On the other hand it gives the most realistic picture of the problems and difficulties that have to be dealt with. Although good equipment has been available, some of the issues addressed in the thesis, relating to very quick events, have not been validated completely. The reason is that the sensors and measurement systems that have been used have not been capable of such fast acquisition. Although there are weeks of testing behind the results in the thesis, further testing is still one of the most urgent issues for the future work.

Three different, but closely related topics, are treated in the thesis.

Semi-empirical tire-modeling

Simultaneous cornering affects the behavior of the tire during a braking phase. For some vehicle stability systems it is more important how the vehicle cornering performance is affected when applying a brake torque while turning. If a vehicle exhibits a large lateral acceleration such that a roll-over may be inevitable a concurrent controlled braking can reduce the lateral force stabilizing the vehicle, see for example [Schofield *et al.*, 2006]. Further, a system may not demand a higher brake force in a corner than that the vehicle can keep its course not running off the road.

The thesis includes a description of a newly developed semi-empirical tire-model that describes this interaction. A main focus in the model derivation is the possibility to extract as much information as possible from the pure slip data. This may simplify and reduce the number of calibration procedures needed to map the specific tire behavior. The longitudinal and lateral forces are described by scalings of the pure-slip forces. The used scale factors are calculated from physical relations between combined and pure slip.

Transient maneuvers in one direction have a dynamic effect on the tire behavior in both directions. The thesis derives the cross-coupling terms and studies the transient properties of a tire for low and high slip situations.

Improvement of wheel speed measurement

The wheel-speed signal is one of the most essential signals for the brake system control. Errors and disturbances on the measurements often require hard filtering that slows down the brake performance. The wheel speed is measured as the relative rotational speed between the rim and the axle. Transient force applications may disturb the sensor position and cause disturbances on the measurements. The effect became particularly evident during a test sequence where the ABS-function of the vehicle was triggered due to a response on the wheel speed from the quick brake torque application. The wheel was not even close to locking at that time. Also tolerances and unevenesses in sensor arrangement may cause extra jitter on the wheel speed signal. The thesis discusses methods to reduce such disturbances.

Road friction estimation

Friction is a prerequisite for the modern life of human beings. Technical solutions for transport and manufacturing would be completely different, if ever possible, if materials did not bond to achieve frictional forces. In many normal duties the anticipation of the friction has become automatic and is nothing that we really reflect over. Everything from small incidents to fatal accidents may occur if the friction differs from the expectations or changes suddenly. A pedestrian that slips on a slippery spot or a roller skater whose wheel bearing abruptly cuts are two examples.

A motivation for trying to estimate the friction is that the number of accidents related to slippery road conditions might be reduced if the driver is correctly informed about the limitations of the vehicle in the current condition. Safety can also be increased, since the performance of many applications in the vehicle can be enhanced by knowing the current frictional condition. The brake control can be made more efficient by knowing the available friction, for example the gain-scheduled slip controller proposed in [Solyom *et al.*, 2004] bases it switching on whether the actual slip is lower or higher than a the slip corresponding to the friction peak. This slip value is an important parameter for obtaining the optimal tire force and can be derived from an assumption on the estimated actual friction and the tire characteristics.

The last part of the thesis is results from the work within a cooperative project between Haldex, the Department of Automatic Control, and Volvo Cars within the *Intelligent Vehicle Safety Systems* (IVSS) programme. This part deals with on board model-based friction estimation based on the local measurements on the vehicle.

The proposed algorithm includes a memory-efficient way to store filtered values of the sampled data into storage bins, distributed over the

force and slip axis. This will maximize the persistence of excitation of the data feeding the estimator and it is a compact form to store and use old data, important for characterizing the tire behavior. The tire friction and tire stiffness parameters are derived by minimizing the error between the adopted tire model and the stored data. The model has a practical focus intended for implementation in production cars.

1.2 Main Results

The thesis mainly contributes in a few related areas. The first is the derivation of a new physically based semi-empirical tire model that predicts the tire behavior for simultaneous braking, cornering, and cambering given the tire characteristics for pure braking, cornering, and cambering. The method incorporates the following features:

- The tire forces at combined slip are derived using any longitudinal, lateral, and camber pure-slip model or data set.
- The scale factors for the combined tire forces are computed in a unique way from the relation between the combined tire force and the pure tire force. Any theoretical model describing the tire behavior at combined slip can therefore be used to form the scale factors.
- The model is, in its presented form, based on the most basic brush-model theory. The structure makes it straight forward to incorporate effects from more variables and more sophisticated modeling.
- Velocity dependence is included in the model, even though this is not explicitly present in the pure-slip models.
- The model has the possibility to convert between driving and braking data.
- All included parameters can automatically be computed from the shape of the pure-slip models.

The wheel speed is an important signal for the applications covered by the thesis. A few ways to improve the quality of the wheel speed measurements are discussed. Particularly, the contribution here is:

- The construction of a feedforward filter on the brake torque that predicts the the disturbances on the wheel speed due to the application of the brakes.

A method for friction estimation is another contribution of this thesis. Its major characteristics are:

- A filter that stores representatives of the sampled data in a compact form to maximize the possibilities to extract information from the force-slip relation.
- Estimations of the braking stiffness of the tire and the road-tire friction using non-linear optimization techniques.
- The model-based estimation relies on brush-model mechanics
- Promising results are shown in validation tests at different driving conditions.

1.3 Outline

The topics covered by the thesis are related to the wheel-tire-road interaction. Chapter2 explains the fundamental properties and definitions related to the characteristics of tires. In Chapter 3 there is a brief review of existing tire models. A basic concept for tire modeling is the brush model developed in the early age of the tire-modeling era. The theory behind the brush model and some extensions are described in Chapter 4. This model is fundamental, both in the derivation of the semi-empirical tire-model described in Chapter 5 and for the friction estimator developed in Chapter 7. Chapter 6 contains material describing a few ways to improve the quality of the wheel speed signal, which may enhance the performance of vehicle systems relying on this signal, e.g. the proposed friction estimator. Proposals for further work and some concluding remarks are mentioned in the final chapter of the thesis.

1.4 Related Publications

The thesis is based on research documented in several publications where the author of the thesis is a coauthor or the sole author.

The following publications and reports contain theory, implementation, and validating results of the semi-empirical tire model:

Gäfvert, M. and J. Svendenius (2003): "Construction of semi-empirical tire models for combined slip." Technical Report ISRN LUTFD2/TFRT--7606--SE. Department of Automatic Control, Lund University, Sweden.

Gäfvert, M. and J. Svendenius (2004): "A semi-empirical tire-model including the effects of camber." Technical Report ISRN LUTFD2/TFRT—7611–SE. Department of Automatic Control, Lund University, Sweden.

Gäfvert, M. and J. Svendenius (2005): "A novel semi-empirical tire model for combined slip." *Vehicle System Dynamics*, **43:5**.

Gäfvert, M., J. Svendenius, and J. Andreasson (2006): "Implementation and application of a semi-empirical tire-model in multi-body simulation of vehicle handling." In *Proceedings of the 8th International Symposium on Advanced Vehicle Control*. Taipei, Taiwan.

Svendenius, J. (2003): "Tire models for use in braking applications." Licentiate thesis ISRN LUTFD2/TFRT--3232--SE. Department of Automatic Control, Lund University, Sweden.

Svendenius, J. (2006): "Examples of scale factors for a semi-empirical tire-model." Technical Report ISRN LUTFD2/TFRT--7614--SE. Department of Automatic Control, Lund University, Sweden.

Svendenius, J. and M. Gäfvert (2004a): "A brush-model based semi-empirical tire-model for combined slips." SAE Technical Paper 2004-01-1064.

Svendenius, J. and M. Gäfvert (2004b): "A semi-empirical tire-model for transient combined-slip forces." In *AVEC '04*.

Svendenius, J. and M. Gäfvert (2005): "A semi-empirical tire model for combined slips including the effects of cambering." In Lugner and M.Plöchl, Eds., *Tyre Models For Vehicle Dynamics Analysis*, vol. 43, pp. 317–328. Taylor & Francis Group, Glasgow. Supplement to Vehicle System Dynamics Volume 43.

Svendenius, J. and M. Gäfvert (2006): "A semi-empirical dynamic tire model for combined-slip forces." *Vehicle System Dynamics*, **44:2**, pp. 189 – 208. Special Issue: AVEC '04: 7th International Symposium on Advanced VEhicle Control, 23-27 August 2004 HAN University, Arnhem, The Netherlands.

The conference paper [Svendenius and Gäfvert, 2004b] was chosen together with another six submissions from all contributions published at the AVEC-04 conference to be included in the special issue of the Journal of Vehicle System Dynamics, reflecting the highlights of the conference, see [Svendenius and Gäfvert, 2006].

The following publications and reports are related to friction estimation project:

Svendenius, J. (2007a): "Validation of the brush model towards VTI-measurement data recorded at Hällered 2005." Technical Report ISRN LUTFD2/TFRT—7616–SE. Department of Automatic Control, Lund University, Sweden. RFE-project.

Svendenius, J. (2007b): “Validation of the brush model towards VTI-measurement data recorded in Arjeplog 2006.” Technical Report ISRN LUTFD2/TFRT—7617–SE. Department of Automatic Control, Lund University, Sweden. RFE-project.

To be able to realize the described method for friction estimation into a future commercial product is has been necessary to try to protect the ideas on an early stage. The work on the friction estimator has therefore resulted in the following patent applications:

Svendenius, J. and M. Gäfvert (2005): “System and method for tire/road friction estimation.” Patent application. Assignee: Haldex.

Svendenius, J., M. Gäfvert, J. Hultén, and F. Bruzelius (2007): “Systems and methods for determining a parameter relating to a tire-to-road contact and/or a relation between a wheel and a vehicle motion.” Patent application. Assignee: Haldex & Ford.

2

Tire Fundamentals

2.1 History

The history of the tire started in 1839 when Charles Goodyear discovered the rubber vulcanization process [Continental, 2003], where sulphur is added to the natural rubber during heating. Varying the amount of sulphur the properties of the material was shown to better resist wear, ageing and water, and decrease the sensitivity to temperature changes. Solid rings of vulcanized rubber later was used around the wheel rims to reduce the vibration problem and to improve the traction properties for the early vehicles. A couple of years later, 1845, Robert W. Thomson patented the idea of using air-filled rubber tubes as tires. Due to the lower durability the invention fell into disuse [Thomson, 2003] and in 1888 John Boyd Dunlope reinvented the pneumatic tire claiming of no knowledge about the prior patent. The new patent was mainly directed for bicycles, but the advantages of using pneumatic tires also for cars were successfully examined by, among others, the brothers André and Édouard Michelin. They competed with a car equipped with pneumatic tires in the 1895 Paris-Bordeaux road race. Although they did not win, they gained a lot of interest due to the new type of tires. A few years later air filled tires became an obligation for driving on the highways. Today, Michelin, which besides Goodyear and Bridgestone, is the largest tire manufacture in the world with approximately 20% of the market. In 2004 the company had 126 000 employees and reported net sales of 15.700 million EUR [Michelin, 2004].

2.2 Design and Construction

The pneumatic tire is a flexible structure that together with the rim holds the pressure of the inflated air. The most important functions of the tire are to reduce vibrations from unevennesses in the road and to achieve a high friction coefficient in the interaction with the road surface. Its main structural component is the carcass, which consists of layers of stiff cords to hold the shape of the tire and the tension from the compressed air. High tensile steel wires, called beads, keep the carcass to the rim and when a load is applied on the wheel, the rim primarily hangs on the sidewall cords and the beads. The entire structure is covered with a wear resistant rubber compound, often styrene-butadiene, to protect the carcass and to build up the friction to the road. There are mainly two ways to design the carcass, radial-ply and bias-ply. Radial-ply implies that the sidewall cords are oriented radially and the wear surface cords are laid in layers tangentially with small angles between the cords in each layer. The bias-ply tires have the cord layers diagonally positioned over the entire tire surface. For a rolling bias-ply tire the deformation of the cords gives rise to a wiping motion of the rubber tread, which causes higher wear and power dissipation. Therefore, radial tires are nowadays mostly used for cars and trucks, even though their manufacturing process is more complex and the expense is about 50% higher than for a bias-ply tire [Thomson, 2003].

2.3 Standards

Many issues related to the tire are controlled by regulations and standards. One of those that might be interesting for the consumer is the standard for the tire marking. In Europe the ECE (Economic Commission for Europe) Regulation and EEC (European Economic Community) Directives set standards for the tire marking, which differ from the American way of marking the tires. However, the size of the tire is always printed on the sidewall as a combination of four designations, for instance P 205/75R15. The first letter (sometimes left out) signifies the vehicle for which the tire is intended. The following number denotes the tire width in millimeter. A slash separate the width from the height of the tire side, which is expressed as the fraction in percent of the width. After the letter R, the rim radius is given in inches. The size marking is often followed by markings denoting load and speed classes.

There are also standards for the nomenclature regarding the kinematics and the mechanics of the tire. The movements and forces developed by the tire are important signals for the control or simulation of the dynamics of the vehicle. Many errors can therefore be avoided by standardizing

the coupling between the tire model and the multi-body vehicle system. However, the multitude of different standards in this area can be confusing. In 1974 SAE published a vehicle dynamics standard specifying the choice of coordinate system and notations [SAE Recommended Practice J670e, 1976]. Fifteen years later the European version ISO 8855 was released [ISO 8855, 1991]. One of the greatest pioneers in tire modelling, H. B. Pacejka used an adapted version of the SAE standard [Pacejka, 1988] in his works. In 2002, TNO together with TU Delft promoted a version of the ISO 8855 in a standard specialized for acquisition of measurement data for calibration of tire model parameters called TYDEX (Tyre Data Exchange Format) [TYDEX-Working group, 1997]. In close connection to TYDEX is the Standard Tire Interface (STI) that prescribes the interface for the interaction between the tire model and the Multi Body Simulation-system. All of these four standards deviate regarding sign conventions of slips and forces, which makes it important to state which standard that is followed or, alternatively, clearly define the signification of the used notations.

The choice of reference system in this work follows the SAE standard [SAE Recommended Practice J670e, 1976], with the longitudinal x-axis aligned with the wheel heading, the lateral y-axis perpendicular to the wheel, and the vertical z-axis pointing downwards. The ISO-standard, instead prescribes the direction of the z-axis to be upwards. Hence, the direction of both the y- and z-axis differ between the two standards, since their reference systems are orthogonal. In Sections 2.4–2.5 the used notations and sign conventions are explained, as from [Gäfvert, 2003]. The table in Appendix A lists the nomenclature and its deviation from ISO 8855:1991.

2.4 Kinematics

This section describes the relevant tire kinematics and introduces definitions which are used in the thesis. The entities are illustrated in Figure 2.1. Vectors have two components and are denoted by a bar as in $\bar{v}$. The corresponding components and magnitude are denoted by v_x, v_y, and $v = \sqrt{v_x^2 + v_y^2}$. The x-axis is often refereed to as the longitudinal direction and the y-axis as the lateral direction. The *wheel-travel velocity* $\bar{v} = (v_x, v_y)$ deviates from the wheel orientation by the slip angle α

$$\tan(\alpha) = \frac{v_y}{v_x} \tag{2.1}$$

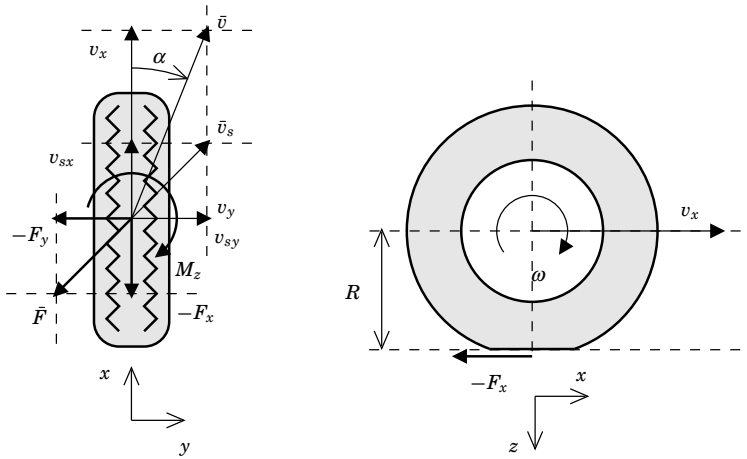

Figure 2.1 Kinematics of an isotropic tire during braking and cornering. Force vectors are also included. (Left: top view; Right: side view)

The circumferential velocity of the wheel is

$$v_c = \omega R_e \tag{2.2}$$

where ω is the wheel angular velocity, and R_e the effective rolling-radius of the tire, defined as the ratio v_x/ω_0, where ω_0 is the wheel speed for a free rolling wheel. The *slip velocity*, or the relative motion of the tire in the contact patch to ground, that arises when a horizontal force is transmitted, is

$$\bar{v}_s = (\, v_x - v_c, v_y \,) \tag{2.3}$$

The direction of the slip velocity is denoted by β where

$$\tan(\beta) = \frac{v_{sy}}{v_{sx}} \tag{2.4}$$

The *tire slip* is defined by normalizing the slip-velocity with a reference velocity. Three slip definitions are commonly used

$$\bar{\sigma} = (\sigma_x, \sigma_y) = \frac{\bar{v}_s}{v_c}; \qquad \bar{\kappa} = (\kappa_x, \kappa_y) = \frac{\bar{v}_s}{v_x}; \qquad \bar{s} = (s_x, s_y) = \frac{\bar{v}_s}{v} \tag{2.5}$$

Note that the slips are collinear with the slip velocity $\bar{v}_s$. It is the custom to describe tire-forces as functions of the slip rather than the slip velocity.

This convention is followed also in this work. Implicitly, this assumes that the forces do not depend on the magnitude of the slip velocity, v_s. In general, at least the sliding friction is velocity dependent. The ISO and SAE standards [ISO 8855, 1991; SAE Recommended Practice J670e, 1976] use $-100\kappa_x$ [%] to represent longitudinal slip, and α [deg] for lateral slip. Here, the slips are defined such that signs are consistent for the different slip definitions, and such that a generated tire force has opposite sign to the slip. This means that braking or left cornering will result in positive slip and negative force. For convenience the *slip ratio*, λ, will be used to denote longitudinal slip as: $\lambda = \kappa_x$. It is straightforward to translate between the different slip representations

$$\bar{\sigma} = \frac{(\, \lambda, \tan(\alpha) \,)}{(1-\lambda)} = \frac{\bar{\kappa}}{1-\kappa_x} = \frac{\bar{s}}{\sqrt{1-s_y^2}-s_x} \tag{2.6a}$$

$$\bar{\kappa} = (\, \lambda, \tan(\alpha) \,) = \frac{\bar{\sigma}}{1+\sigma_x} = \frac{\bar{s}}{\sqrt{1-s_y^2}} \tag{2.6b}$$

$$\bar{s} = (\, \lambda\cos(\alpha), \sin(\alpha) \,) = \frac{\bar{\sigma}}{\sqrt{(1+\sigma_x)^2+\sigma_y^2}} = \frac{\bar{\kappa}}{\sqrt{1+\kappa_y^2}} \tag{2.6c}$$

2.5 Tire Mechanics

Forces

Forces and torques working on a tire are shown in Figure 2.2, according to the SAE-definition.

The forces of interest for vehicle handling and control purposes are the planar lateral and longitudinal forces, F_x and F_y, and the self-aligning torque, M_z. The longitudinal tire force F_x is generated when braking or driving. In the following, when the word "braking" is used in the context of longitudinal tire force generation, this will actually mean "braking or driving" unless stated otherwise. The lateral force and the torque are generated when cornering. The self-aligning torque results from the fact that the planar forces have a point of action which is not positioned exactly under the wheel center. The rolling-resistance is related to the energy dissipation for a rolling tire and the overturning torque is the torque necessary to camber the wheel.

Tire slip

Pure slip There is a relation between the horizontal tire force and

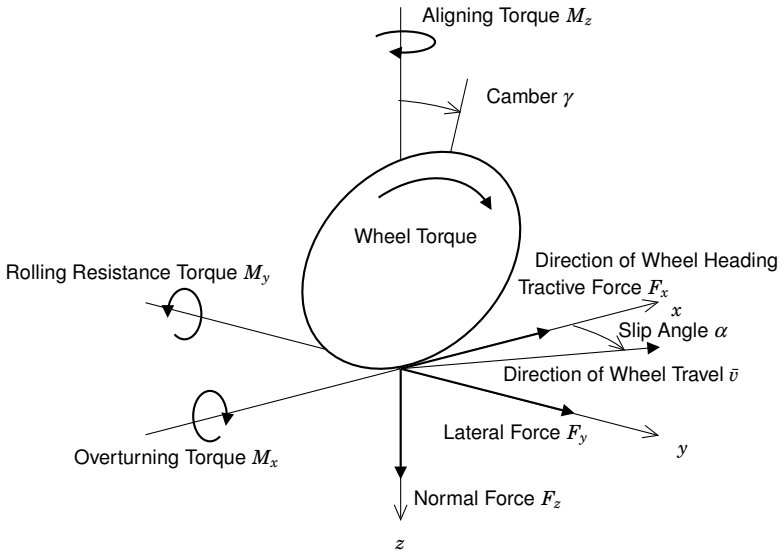

Figure 2.2 Forces and moments acting on a tire [SAE Recommended Practice J670e, 1976].

the slip of the tire. The velocity difference between the carcass and the road is a result from continuous deformation of the rubber treads and sliding between the tire and the road surfaces. At low slip the relation is approximately linear and the forces can be described as $F_x = -C_x\sigma_x$, longitudinally and $F_y = -C_y\sigma_y$, laterally. The *braking stiffness*, C_x and the *cornering stiffness*, C_y are correspondingly defined as the linearization of the force-slip relation at $\sigma_x = 0$ and $\sigma_y = 0$ [Wong, 2001]

$$\begin{aligned} C_x &= -\left.\frac{dF_x}{d\sigma_x}\right|_{\sigma_x=0,\sigma_y=0} \\ C_y &= -\left.\frac{dF_y}{d\sigma_y}\right|_{\sigma_x=0,\sigma_y=0} \end{aligned} \tag{2.7}$$

At higher slip the relation is strongly nonlinear and a more complex function is necessary to express the relation, see Sections 3.1 and 4.1. The normal behavior for a tire on asphalt is that the force increases with slip

up to a certain slip value (σ_x^*) and then diminishes slightly when σ_x goes to infinity or λ reaches unity, see the measurements in Figure 5.1.

Combined slip Combined slip signifies simultaneous longitudinal and lateral slip, i.e. braking and cornering actions performed at the same time. A steering maneuver during braking, generally, decreases the braking stiffness, the longitudinal peak force, and its corresponding slip value. A model for the interaction between the slip in both directions is therefore inevitable for more advanced vehicle simulations. In Section 3.2 and in Chapter 5 this topic will be discussed in detail.

Camber

The camber angle, γ, denotes the tilting angle of the tire about the x-direction, see Figure 2.3. Normally, the sign convention is related to the inclination relative the vehicle body [ISO 8855, 1991]. The effects from cambering are particularly important when deriving models for motorcycles that produces a large part of the cornering force by tilting. For cars and, in particular, trucks the achieved camber angles are much smaller and in many applications their effect can be neglected. However, many suspension designs make the wheels to camber when the axle load varies. Elasticity in bushings, beams, bolts and axles also allow cambering during cornering. Cambering of a tire creates a lateral force, even though there is no lateral slip.

Rolling resistance

The deformation of the tire due to the vertical load is often clearly visible. The wheel rotation for a moving vehicle continuously changes this deformation and power dissipates from the system due to the visco-elastic properties of the carcass, see Section 2.6. The effect is called rolling resistance and is, in general, assumed to depend linearly on the tire load [Wong, 2001] and radius, as

$$M_y = q_0 R|F_z| \tag{2.8}$$

For more accurate results the dependency on the velocity has to be included in the tire specific factor, q_0. In [Pacejka, 2002] an addition to the resistance torque due to the extra energy loss when a longitudinal force is developed, is proposed, as $M_{y,add} = (R_e - R)F_x$. The energy loss comes from the difference between the effective rolling radius and the tire radius that works as a lever for the torque on the rim to the transmitted tire force to the ground.

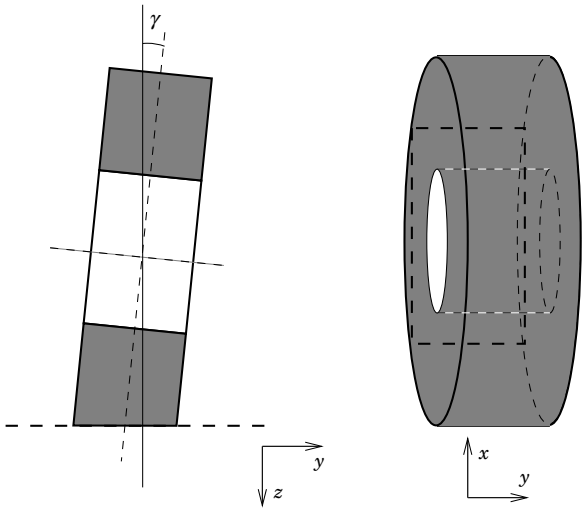

Figure 2.3 Cambered wheel. Left: Rear view; Right: Top view with contact patch (dashed rectangle). Note that the contact patch is greatly exaggerated in size.

2.6 Tire Deformation

One of the main tasks for the tire is to reduce the vibrations caused by the unevennesses in the road. The elastic and damping properties are therefore of great importance and large vertical shape deformations are required for efficient damping. The price is slower handling and reaction on maneuvers from the driver, since a softer tire, generally, allows larger horizontal deformation. The deformation can schematically be divided between the carcass and the tread. The carcass flexibility is the major source for the dynamic behavior and the rolling resistance of the tire. In the longitudinal direction the minor deflection of the rubber treads determines the force-slip characteristics, while both the tread and carcass deflections affects it in the lateral direction. A good way to illustrate the carcass behavior is to use the stretched string carcass model that originates from the work of von Schlippe in 1941, described in [Pacejka, 2002], which is still used for tire modeling, see for instance [Thorvald, 1998]. The carcass is then, as the name intends, approximated as a stretched string attached to the rim by visco-elastic springs, see Figure 2.4. Finite element methods, allowing more sophisticated models, are usually used to derive more accurate results for the tire deformation, since the shape is complex and the deflections are large [Pauwelussen *et al.*, 1999; Gipser, 2005]. The

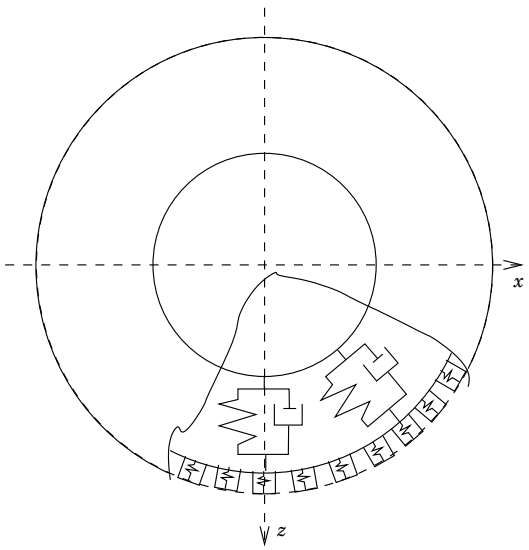

Figure 2.4 Illustration of the schematic tire structure used in this thesis. The carcass is visualized as a stiff string attached to the rim by visco-elastic springs. The springs are only showed in the radial direction but work also tangentially and laterally (out of the wheel plane). The same holds for the elastic tread springs.

stretched string method gives, however, a good visualization of the physics behind the tire behavior and in many cases the resulting equations can be solved analytically. Restrictions can be introduced to obtain results in fairly simple and sufficiently accurate expressions that easily can be used for estimation and control issues.

3

Review of Existing Tire-Models

An extensive amount of work has been done in the field of tire modeling. The research covers everything from derivation of simplistic expressions describing the tire behavior to advanced finite-element methods that predicts the important states at any point of the tire. The tire modeling was initiated by the vehicle and air craft industry back in the 1940's. The first descriptions of the tire characteristics were derived from physical modeling. Later on the interest for finding empirical equation structures, that easily could be adjusted to fit the measurements from the tire tests increased due to the complex nature of the tire. The early tire models only covered the static force-slip relation, but the development of fast control systems has now increased the focus on the dynamical aspects of the tire behavior. The larger amount of computer power has enabled the possibility to solve the physical differential equations related to the tire deformation. Therefore, physical modeling of both dynamical and frictional aspects has become popular again. This chapter gives a short review of the tire models that are relevant for the continuation of the thesis.

3.1 Steady-State Tire Models

The aim of a tire model is often to obtain a structure that can fit measurement data well by optimal choice of included parameters. A detailed description of the early tire models can be found in [Nguyen and Case, 1975], from where also the following examples in this section are gathered, if not otherwise is stated.

The first tire models did only concern the steady-state relation between the slip and the developed force. They were physically derived from variants of the brush model. The most common form of the brush model is

extensively presented in Section 4.1 and therefore left out here, but the different assumptions on the brush model often results in a polynomial including at least two parameters. One example is the proposal for the lateral force by Smiley and Horne in 1958

$$F_{0y} = \begin{cases} C_\alpha \alpha \left(1 - \dfrac{\alpha^2}{3(\alpha^\circ)^2}\right) & \alpha \leq \alpha^\circ = \dfrac{3\mu F_z}{2C_\alpha} \\ \mu F_z & \text{otherwise} \end{cases} \tag{3.1}$$

where C_α is the cornering stiffness and μ the friction coefficient. The definition of the slip angle α is given by (2.1). The friction is assumed to be constant in the model, which disables its ability to also characterize the longitudinal force accurately for longitudinal slips, since there, generally, is a pronounced peak of the force in this direction. Interpolation between the data points was then mostly used to model the longitudinal tire force. By use of velocity dependent friction, a relation for combined slip that better expressed the behavior of the brake force for large slip was derived in [Dugoff *et al.*, 1969], given on the form

$$F_x = \frac{C_x \lambda}{1-\lambda} f(\theta) \tag{3.2}$$

$$F_y = \frac{C_y \tan(\alpha)}{1-\lambda} f(\theta) \tag{3.3}$$

$$f(\theta) = \begin{cases} \theta(2-\theta) & \theta \leq 1 \\ 1 & \theta > 1 \end{cases} \tag{3.4}$$

where

$$\theta = \frac{\mu_0 F_z ((1 - \epsilon v \sqrt{\lambda^2 + \tan^2(\alpha)})(1-\lambda))}{\sqrt{2C_x^2\lambda^2 + C_y^2 \tan^2(\alpha)}} \tag{3.5}$$

and μ_0 is the nominal friction coefficient and ϵ is the velocity dependency factor. This model is one of the three models usually referred to as the HSRI-models developed at the Highway Safety Research Institute. The other two models are described in [Fancher *et al.*, 1972] and [Tielking and Mital, 1974] and are based on different assumptions on the brush model regarding the vertical pressure distribution and sliding properties of the rubber.

An empirical way to describe the lateral force and account for combined braking and cornering by using the friction circle criterion, has been proposed by Chiesa (1965) as

$$F_y = \sqrt{1 - \left(\frac{F_x}{2\mu N}\right)^n} F_z \left((a_1 + a_2 F_z)\alpha + (a_3 + a_4 F_z)\alpha^2 + \ldots\right) \tag{3.6}$$

The method requires that the longitudinal force is known instead of the longitudinal slip, compared to the previous methods. To further increase the flexibility in the modeling Holmes (1969) proposed an empirical structure, quite different to the others, to use for curve fitting

$$F_{0y} = a_0 + a_1 v_x + a_2 v_x^2 + a_3 \alpha + a_4 \alpha^2 + a_5 \alpha^3 + a_6 R + a_7 P \tag{3.7}$$

where P is a tire-pattern constant and R is a tire-tread constant. The coefficients $a_{1\ldots7}$ have no physical interpretation. The idea to treat the dependence of the vehicle velocity as an additional contribution was not really accepted by the other researchers in the field. Further references regarding these early tire models can also be found in [Bernard *et al.*, 1975].

In [Kiencke and Nielsen, 2000] another empirical model, developed by Burckhardt is used, which models the real tire behavior more accurately. The input s_{Res} denotes the resultant slip $(s_L^2 + s_S^2)^{1/2}$ and an additional slip definition (compare to Equation (2.5)) is used in $s_L = (v_c \cos(\alpha) - v_x)/v_x$, which is the slip in the travel direction of the wheel, $\bar{v}$, and perpendicular to this, $s_S = v_c \sin(\alpha)/v_x$. The model can then be used for combined slip situations and the direction of the resulting force is collinear to the slip vector $\bar{s}_{\text{Res}}$. Nonlinear effects of the wheel load can be accounted for in this model which is expressed as

$$F = \left(a_1 \left(1 - e^{-a_2 s_{\text{Res}}}\right) - a_3 s_{\text{Res}}\right) e^{-c_4 s_{\text{Res}} v} (1 - c_5 F_z^2) \tag{3.8}$$

A disadvantage in the approach is that the tire characteristic is assumed to be equal in both directions. Due to the influence of the carcass flexibility, which is further discussed in Section 4.3, this is generally not the case.

A way to use similarities between longitudinal and lateral tire behavior is used in [Lugner and Mittermayr, 1991], where a slip curve for a particular tire is separated in four regions depending on the slip. Each region has its function structure for the approximation. For low slips the relation is linear. At slightly higher slips up to the peak a polynomial function describes the behavior. The negative slope of the tire model is described by another polynomial and for very high slips the tire force is assumed to be constant. The combined-slip forces are then derived as

$$f_x(\sigma_x, F_z) = \bar{y}\left(\frac{\sigma_x}{f_{st2} s_{xm}(F_z)}\right) f_{st1} \mu_{x,max}(F_z) \tag{3.9}$$

$$f_y(\sigma_y, F_z) = \bar{y}\left(\frac{\sigma_y}{f_{st2} s_{ym}(F_z)}\right) f_{st1} \mu_{x,max}(F_z) \tag{3.10}$$

where $\bar{y}(\cdot)$ is the region-separated function-approximation. The adjusted combined slips σ_x, σ_y are shaped from combinations of the pure slips λ, α and γ and do not correspond to the physical slips from (2.5), see the original paper for a detailed description. The frictional values at the peak, $\mu_{x,max}$ and $\mu_{y,max}$ and corresponding slips $s_{xm}(F_z)$ and $s_{ym}(F_z)$ are then used to set the difference in the corresponding direction. The factors f_{st1} and f_{st2} are used to adjust between different surfaces. Similar ideas are proposed for deriving the self-aligning torque at combined slip. The method is claimed to have a short on-line calculation time, and to represent the tire behavior in areas without measurements in a reasonable way.

The paper [Bakker *et al.*, 1987] presents the "Magic Formula", which quickly became the most predominating model. The model expresses the lateral and longitudinal tire forces, as well as aligning torque, on the form

$$y(x) = D \sin\left[C \arctan\left[(1 - E)x + (E/B)\arctan(Bx)\right]\right] \tag{3.11}$$

where (x, y) is (λ, F_{0x}), (α, F_{0y}), or (α, M_{0z}). The four coefficients have interpretations as stiffness factor (B), shape factor (C), peak factor (D), and curvature factor (E), and are unique for each of F_x, F_y, and M_z. Approximation of the normal load dependence may be introduced as

$$C = a_0 \tag{3.12}$$

$$D = a_1 F_z^2 + a_2 F_z \tag{3.13}$$

$$B = (a_3 F_z^2 + a_4 F_z)/(C D e^{a_5 F_z}) \tag{3.14}$$

$$E = a_6 F_z^2 + a_7 F_z + a_8 \tag{3.15}$$

After its first presentation the Magic Formula has been extended to empirically express most of the interesting properties of the tire and also the interaction of many simultaneous actions, such as combined slip. The model has, during cooperation between TNO and TU-Delft, become a commercial product under the name *MF-tyre*. The entire model is presented in [Pacejka, 2002] and the commercial interest is mainly in delivering parameter sets for certain types a tire. The complete model includes approximately 85 parameters that has to be calibrated from measurement data. Another direction in the progress of the Magic Formula is proposed in [Sharp and Bettella, 2003], where one of the aims is to reduce the need of parameters in the model. The idea of using one reference model and having two parameters prescribing the peak force as in [Lugner and Mittermayr, 1991] is used, but the reference curve is described by the "Magic Formula"-structure using "normalized" parameters. The method shows an appreciable reduction of parameters, without losing much information.

3.2 Combined-Slip Semi-Empirical Tire-Models

The term *semi-empirical* is used for models that relies on physical modeling to transform empirical data collected at a certain condition to be valid for another situation at different conditions. There is always a trade-off since the semi-empirical model is more or less accurate. The measurement data on the other hand includes errors and disturbances. The testing circumstances also mostly differ from the driving or simulation circumstances. In some cases collection of data can be difficult, unreliable, or very expensive and a theoretical model is inevitable.

Semi-empirical methods are often used to derive the tire forces at combined slip situations, when the pure-condition tire-forces often are available from test-bench experiments.

The most simplistic model of combined forces is based on the friction ellipse concept, see for instance [Wong, 2001; Ellis, 1994; Nielsen and Eriksson, 1999]. While the friction ellipse is the envelope of the maximum achievable forces, the ellipse is here used also for modeling intermediate forces. It is used to compute a combined lateral force $F_y(\alpha,\lambda)$ at a given longitudinal force F_x, and is based on the assumption

$$\left(\frac{F_x}{F_{0x}^*}\right)^2 + \left(\frac{F_y(\alpha,\lambda)}{F_{0y}(\alpha)}\right)^2 = 1 \tag{3.16}$$

where F_{0x}^* is the maximum achievable longitudinal force, and $F_{0y}(\alpha)$ describe the lateral force at pure slip. The combined lateral force becomes

$$F_y(\alpha,\lambda) = F_{0y}(\alpha)\sqrt{1-\left(\frac{F_x}{F_{0x}^*}\right)^2} \tag{3.17}$$

An objection to this model is the assumption (3.16), which is not true, since adhesion limits are not necessarily fully reached for combined forces in the interior of the friction ellipse.

Another simple model is the Kamm Circle [Kiencke and Nielsen, 2000], where the resultant force magnitude is described as a function of the total slip magnitude. The force and slip vectors are then assumed to be collinear, possibly with a corrective factor k_s:

$$F_x = F(s)\frac{s_x}{s} \qquad \text{and} \qquad F_y = k_s F(s)\frac{s_y}{s} \tag{3.18}$$

A drawback with this model is that longitudinal and lateral characteristics are assumed to be the same, modulo the corrective factor.

Some early efforts to model tire forces under combined-slip conditions are described and compared in [Nguyen and Case, 1975]. One of the most well-known is presented in [Nicholas and Comstock, 1972]:

$$\begin{aligned} F_x(\lambda,\alpha) &= \frac{F_x(\lambda)F_y(\alpha)\lambda}{\sqrt{\lambda^2F_y^2(\alpha)+\tan^2(\alpha)F_x^2(\lambda)}} \\ F_y(\lambda,\alpha) &= \frac{F_x(\lambda)F_y(\alpha)\tan(\alpha)}{\sqrt{\lambda^2F_y^2(\alpha)+\tan^2(\alpha)F_x^2(\lambda)}} \end{aligned} \tag{3.19}$$

In [Brach and Brach, 2000] this model is shown to give incorrect result for small slips and a modified version is presented.

In [Bakker *et al.*, 1987], a procedure for computing combined forces for the Magic Formula is presented. It is essentially a refinement of the Kamm Circle for non-isotropic tire characteristics and a normalization of the slips to guarantee simultaneous sliding. The normalized slip

$$\sigma_N = \sqrt{\left(\frac{\sigma_x}{\sigma_x^*}\right)^2 + \left(\frac{\sigma_y}{\sigma_y^*}\right)^2} \tag{3.20}$$

is an entity that is less than one for non-sliding conditions. It is based on an elliptic assumption where σ_x^* and σ_y^* are the longitudinal and lateral slips that corresponds to full sliding for pure slips, normally taken as the slips at the peak values F_{0x}^*, and F_{0y}^*. Now the combined forces are computed as

$$F_x = -\cos(\beta^\circ)F_{0x}(\sigma_x^*\sigma_N) \qquad \text{and} \qquad F_y = -\epsilon_d(\sigma_N)\sin(\beta^\circ)F_{0y}(\sigma_y^*\sigma_N) \tag{3.21}$$

with $\tan(\beta^\circ) \triangleq (\sigma_y/\sigma_y^*)/(\sigma_x/\sigma_x^*)$. For large slip conditions the factor $\epsilon_d(\sigma_N)$ must be included to give correct direction of the resulting forces. The reason is the fact that for small slips real tire-forces are essentially produced by elastic deformation, and for large slips by sliding friction. Therefore slip vectors of the same orientation but different magnitudes may result in forces with different orientation. It is not clear how to determine $\epsilon_d(\sigma_N)$, and in [Bakker *et al.*, 1989] a modified procedure was presented:

$$F_x = \cos\left((1-\vartheta)\beta^\circ + \vartheta\beta\right)F_{0x}' \quad \text{and} \quad F_y = \sin\left((1-\vartheta)\beta^\circ + \vartheta\beta\right)F_{0y}' \tag{3.22}$$

with $\vartheta \triangleq \frac{2}{\pi}\arctan(q_1\sigma_N^2)$ and

$$\begin{aligned} F_{0x}' &\triangleq F_{0x}(\sigma_N) - \text{sat}(\sigma_N)\left(F_{0x}(\sigma_N) - F_{0y}(\sigma_N)\right)\sin^2(\beta^\circ) \\ F_{0y}' &\triangleq F_{0y}(\sigma_N) + \text{sat}(\sigma_N)\left(F_{0x}(\sigma_N) - F_{0y}(\sigma_N)\right)\cos^2(\beta^\circ) \end{aligned} \tag{3.23}$$

The variables ϑ, F'_{0x}, and F'_{0y} describe the gradual change of orientation of the resulting force from adhesion to sliding. At large slip-magnitudes the force is collinear with the slip vector.

In [Bayle *et al.*, 1993] a model for combined braking and cornering is presented, which is based on functional representation. The model is much inspired by the Magic Formula and uses functions based on arc tangents to describe forces under combined-slip conditions. These ideas were used in the development of the MF-tyre model, see Section 3.1, and is one of the differences between the descriptions in [Bakker *et al.*, 1989] and [Pacejka, 2002].

A method that shares ideas proposed in [Lugner and Mittermayr, 1991], where a common function describes the tire behavior in each direction is described in [Radt, 1995]. The method also uses so called non-dimensionalising of the pure-slip tire behavior. The non-dimensionalised entities are here marked by bars. The normalised combined slip is defined as

$$k = \sqrt{\bar{\lambda}^2 + \bar{\alpha}^2}; \quad \bar{\lambda} = \frac{\lambda C_x}{\mu_x F_z} \quad \bar{\alpha} = \frac{\alpha C_y}{\mu_y F_z} \tag{3.24}$$

and a normalised "resultant" force as

$$R(k) = \sqrt{\bar{F}_x^2 + \bar{F}_y^2}; \quad \bar{F}_x = \frac{F_x}{\mu_x F_z} \quad \bar{F}_y = \frac{F_y}{\mu_y F_z} \tag{3.25}$$

The tire-force function $R(k)$ is chosen to give most accurate fit for both the longitudinal and lateral directions. The combined slip tire forces are then proposed to be computed as

$$\bar{F}_y = \frac{\eta(k) R(k) \tan(\alpha)}{\sqrt{\lambda^2 + \eta^2(k) \tan^2(\alpha)}}; \quad \bar{F}_x = \frac{R(k)\lambda}{\sqrt{\lambda^2 + \eta^2(k) \tan^2(\alpha)}}; \tag{3.26}$$

where

$$\eta(k) = \begin{cases} 0.5(1+\eta_0) - 0.5(1-\eta_0)\cos(0.5k) & |k| \le 2\pi \\ 1 & |k| > 2\pi \end{cases} \tag{3.27}$$

This method has also been used and further developed in [Sharp, 2004].

The COMBINATOR model [Schuring *et al.*, 1996; Pottinger *et al.*, 1998] is another variation on the Kamm Circle. Here the tire force magnitude is described by

$$F = F_{0x}(s)\cos^2(\beta) + F_{0y}(s)\sin^2(\beta) \tag{3.28a}$$

and the combined forces as

$$F_x = F\cos(\beta) \qquad \text{and} \qquad F_y = F\sin(\beta) \tag{3.28b}$$

The model assumes collinearity between resulting force and the slip vector.

Further references regarding Semi-empirical tire-modeling may, for example be found in [Böhm and Willumeit, 1996].

3.3 Transient Tire-Models

The dynamic behavior of the tire has lately gained a large interest. In applications such as state-of-the-art active safety systems that intervene in limited conditions by controlled braking actions the transient properties of the tire affects the vehicle dynamics. Tire forces, in general, do not develop instantaneously at maneuvering actions, but require a certain rolling distance of the tire to build up, due to the flexible structure. This is of practical significance in, for example, systems for control of longitudinal tire slip. The motion sensors are, here, attached to the wheel rim, but it is the tire motion relative road contact that is of interest for the force generation. A simple way to model this difference, was described and validated in [Clark *et al.*, 1971], but proposed already by von Schlippe around thirty years earlier. The method lets a first-order transfer function describe the relation between the measured slip, λ', and the slip that generates the tire forces, λ, such that

$$\frac{\sigma_{ax}}{v_x}\frac{d\lambda}{dt} = \lambda - \lambda' \tag{3.29}$$

The time constant of the system σ_{ax}/v_x is then speed dependent and equal to the time for the wheel to roll a specific distance, called relaxation length, see Section 4.3 and Equations (4.80)–(4.82). Same approach can be applied in the lateral direction.

A different concept is employed in the LuGre model. The LuGre friction model is known for describing special cases of friction situations and was developed as a joint cooperation between the Department of Automatic Control at Lund University (Sweden) and Laboratoire d'Automatique de Grenoble (France) [Olsson, 1996]. The model describes a dynamic force phenomenon that arises when frictional surfaces are sliding on each other. In the formulation for tires the LuGre model assumes the frictional surface to consist of bristles, with movements described by differential equations. An assumption of the vertical pressure distribution between the tire and road is necessary to state an expression for the steady-state force-slip relation. This is used to calibrate the included parameters to fit measurement data. The deflections of bristles are then lumped together in one variable and in [Velenis *et al.*, 2002] the LuGre model is written, for two dimensions, on the following form

$$\dot{\bar{z}}_i = v_{ri} - \frac{\sigma_{0i}\lambda(v_r)}{\mu_{ki}^2}\bar{z}_i - \kappa_i(t)|\omega r|\bar{z} \tag{3.30}$$

$$F_i = -F_n(\sigma_{0i}z_i(t) + \sigma_{1i}\dot{z}_i(t) + \sigma_{2i}v_{ri})),\ i = x, y \tag{3.31}$$

where

$$\lambda(v_s) = \frac{||M_k^2 v_s||}{g(v_s)} \tag{3.32}$$

and the friction function is redefined as

$$g(v_s) = \frac{||M_k^2 v_s||}{||M_k v_s||} + \left(\frac{|M_k^2 v_s|}{|M_k v_s|} - \frac{|M_k^2 v_s|}{|M_k v_s|}\right)\exp\left(-\frac{|v_s|^\gamma}{v_{st}}\right) \tag{3.33}$$

$$M_k = \begin{bmatrix} \mu_{kx} & 0 \\ 0 & \mu_{ky} \end{bmatrix} \quad M_s = \begin{bmatrix} \mu_{sx} & 0 \\ 0 & \mu_{sy} \end{bmatrix} \tag{3.34}$$

and the parameters from the distributed steady-state description can then be used in the lumped formulation. The derivation of κ, from (3.30) has to be done to cover for the difference between the distributed and the lumped formulation. More details on the model are given in [Velenis *et al.*, 2002]. A drawback with the method is that the description of the bristle dynamics is complicated, resulting in comprehensive equations, while other phenomenon are roughly simplified. The major source of the tire dynamics still comes from the carcass behavior.

The Short Wavelength Intermediate Frequency Tyre (SWIFT) model described, for instance, in [Pacejka, 2002] developed at TU-Delft and TNO-Helmond is a collection of methods employed to extend the MF-tire concept with dynamic properties and ability to handle uneven roads. The model can handle frequencies up to 60 Hz and wavelengths larger than 0.2 m and acts on longitudinal and lateral slip, camber, and turn slip. The tire belt is modelled as a rigid ring with inertia. The ring has a flexible attachment to the rim, with stiffnesses in all directions, compare to the stretched string model in Section 2.6. To improve the transient properties further, the stiffness in the contact patch rubber is modelled as a first order differential equation with a time constant corresponding to the size of the adhesion area in the patch (see Section 4.1 for explanation of adhesive area). The pneumatic trail, used for the self-aligning torque is modelled as a second order differential function from the lateral slip, which means that self-aligning torque builds up slower than the lateral force. The turn-slip torque-contribution to M_z on the rigid ring is modelled as a fourth order polynomial function relative the turn slip in the contact patch. To calculate the position for the contact patch when running on an uneven

road, the patch is described by cams, see Figure 3.1. The contact between the road and the cam decides the vertical position of the contact patch. To be able to manage inclination of the surface, two cams (tandem) are necessary. Four cams (two rows of tandem cams) are needed to derive camber angles due to road inclination in the lateral direction.

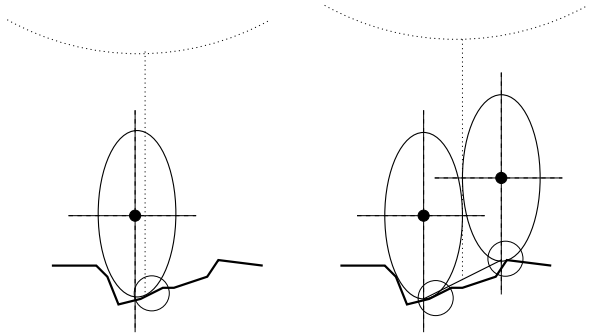

Figure 3.1 Illustration of the method of the SWIFT-model to derive the vertical position for the contact point between the tire and the road. To the left single cam and to the right tandem cams allowing determination of patch inclination.

3.4 Finite Element Models

The increase of available computation power has provided a new platform for use of finite element methods to solve the complex partial differential equations describing the behavior of the tire. Briefly, this means that the tire structure is divided into small elements. Each element has a set of differential equations describing its physical behavior. The elements are connected to each other through boundary surfaces. All elements contains points or nodes, with constraints on the externally applied force, or deflection. The constitutive conditions and laws of equilibrium of forces, torques, and energy flow are used to derive matrix equations from which the states in each node are solved. The finer meshing (small elements) the larger matrices and memory consumption. The *F-tire* model [Gipser, 2005] uses between 80 and 200 sector elements to describe the carcass deformation. Each element has five degrees of freedom denoting, longitudinal, lateral and vertical displacement, rotation, and bending. Above that, between 5 and 10 tread elements on each carcass element are used to model the rubber treads. Each tread element contains information about wear, temperature, and deflection. Since the tread elements outside the

contact area are unloaded they will not be included in the calculations of the deflections. For a normal PC (2005) the calculations takes about 2 to 10 times real time. The model properties are determined by sets of parameters, which can be calibrated from measurement data. F-tire is the middle-complexity part in a family of three models. The simpler *R-tire* is restricted by having a rigid carcass which is similar to the SWIFT-model in Section 3.3. The most advanced model *FE-tire* is a coarse mesh finite element tire model allowing multiple elements in the lateral direction.

The *Rmod-K* [Oertel and Fandre, 1999] is another tire model that similarly to the FE-tire is based on coarse-mesh finite-elements.

3.5 Conclusions

Much research is devoted to tire-modeling related issues and the brief survey above does by no means cover the area. The aim is more to show on the variety and width of the expressions and approaches that have been proposed in the literature than to try to give a complete view of the results presented in this area.

When choosing among the tire models it is important to consider the purpose of the particular application. If the time constraints are sufficiently long such that steady-state model can be used or which fidelity requirement should be set on the description of the dynamics. For vibrational and deformation analysis at high frequencies the choice of a finite element method is often inevitable, while some vehicle handling analysis situations may be well described without any dynamic effects. Using a too comprehensive model is inefficient use of time and computation resources. If only general behavior of a tire is needed in a certain application, a very simple physical model might be used. For a requiring algorithm calibration a more accurate model may be needed and an empirical method might be good choice. It is then necessary to be convinced that the actual parameter sets are derived from representable test conditions and that changed conditions have a large effect on the tire characteristics.

4

Tire Modeling According to the Brush Model Theory

The objective of this chapter is to explain the underlying physics for the derivation of the semi-empirical tire-model presented in Chapter 5. The main prerequisite for the generation of the forces in the contact patch is the presumption of the brush-model theory assuming a stiff carcass, which is described in the first section. The next section explains the effect of camber on the forces, and torque. Finally, modeling of some consequences due to the elasticity of the tire carcass, that can enhance the performance of the model, are discussed. In particular, the dynamic properties of the development of the tire forces are examined. The main part of the contents in this chapter is gathered from previous publications by other authors and rewritten with a slightly new touch.

4.1 Basics of the Brush Model

The brush model is a well-known approach to model tire forces, see e.g. [Dugoff *et al.*, 1969], [Pacejka, 1988], or [Wong, 2001]. The model was very popular in the 1960's and 1970's before the empirical approaches became dominating and describes the physics behind the tire behavior in an educational way. In this section the brush-model concept is applied to combined slips, much like the approach of [Gim and Nikravesh, 1991]. The brush model describes the generation of tire forces based on partitioning of the contact patch into an adhesion and a sliding region. Forces in the adhesive region are assumed to be caused by elastic deformations in the rubber volume that is between the tire carcass and the ground. The carcass is assumed to be stiff, which means that effects of carcass deformation are neglected. In the sliding region, forces are caused by sliding friction.

The model is obtained by dividing the rubber volume in the contact

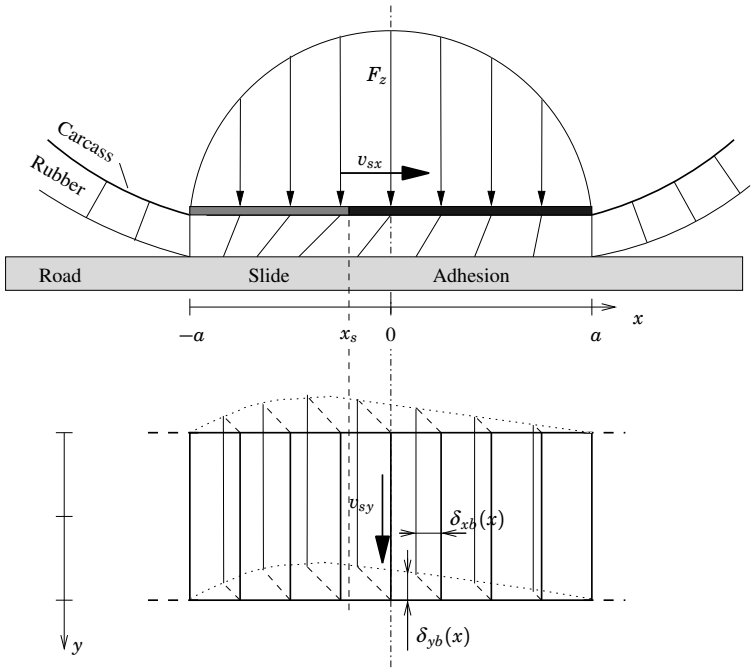

Figure 4.1 The deformation of the rubber layer between the tire carcass and the road according to the brush model. The carcass moves with the velocity (v_{sx}, v_{sy}) relative the road. The contact zone moves with the vehicle velocity $(v_x, v_y = v_{sy})$. The break-away point, x_s, is the coordinate that separates the sliding and adhesive areas. (Top: side view; Bottom: top view)

region into small brush elements. Each element stretches laterally (y-direction) over the entire contact region, but their length is infinitesimal in the longitudinal, x, direction. The elements are regarded as elastic rectangular blades, or bristles, see Figure 4.1. Even though rubber, in general, is not linearly elastic, this assumption is made in the brush model. Positions in the contact region are expressed in a reference system attached to the carcass, with the origin located in the center of the contact region. The length of the contact region is $2a$. Each bristle is assumed to deform independently in the longitudinal and lateral directions. In the adhesive region the bristles adhere to the road surface and the deformation force is carried by static friction. In the sliding region the bristles slide on the road surface under influence of sliding friction. Hence, in the sliding region the resulting force is independent of the bristle deformations.

Adhesive bristle forces Regard the specific infinitesimal bristle which is attached to the carcass at position x relative the origin in the center of the contact patch. Assume that this bristle belongs to the adhesive region. The bristle is in contact with the road surface at position $x_r(x)$, $y_r(x)$, see Figure 4.2. Since there is no sliding in the adhesive region the contact-point position may be described by

$$\begin{aligned} x_r(x) &= a - \int_0^{t_c(x)} v_x \, dt \\ y_r(x) &= -\int_0^{t_c(x)} v_y \, dt \end{aligned} \tag{4.1}$$

where $t_c(x)$ is the time elapsed since the bristle entered the contact region. The velocities v_c, v_x and v_y are assumed to be constant as a bristle travels through the adhesive region of the contact patch, i.e. during the integration interval $[0, t_c(x)]$. Hence, the bristle position is $x = a - v_c t_c(x)$, and $t_c(x) = (a - x)/v_c$. The deformation becomes

$$\begin{aligned} \delta_{xs}(x) &= x_r(x) - x \\ \delta_{ys}(x) &= y_r(x) \end{aligned} \tag{4.2}$$

Insertion of (4.1) and the expression for $t_c(x)$ yields

$$\begin{aligned} \delta_{xs}(x) &= -\frac{v_x - v_c}{v_c}(a - x) = -\sigma_x (a - x) \\ \delta_{ys}(x) &= -\frac{v_y}{v_c}(a - x) = -\sigma_y (a - x) \end{aligned} \tag{4.3}$$

where the slip definition from (2.5) is used in the last equality. As the carcass is assumed to be stiff the the bristle deformations are accordingly, $\delta_{xb} = \delta_{xs}$ and $\delta_{yb} = \delta_{ys}$. With the assumption of linear elasticity, the deformation force working on the bristles becomes

$$\begin{aligned} dF_{ax}(x) &= c_{px} \, dx \, \delta_{xb}(x) \\ dF_{ay}(x) &= c_{py} \, dx \, \delta_{yb}(x) \end{aligned} \tag{4.4}$$

where c_{px} and c_{py} are the longitudinal and lateral bristle stiffnesses per unit length. The assumption of constant v_c, v_x, v_y in the interval $[0, t_c(x)]$ is relaxed to the assumption of slow variations in σ_x and σ_y with respect to the duration $2a/v_c$, which is the maximum time for a bristle to travel through the adhesion region. The total adhesive tire force is computed by

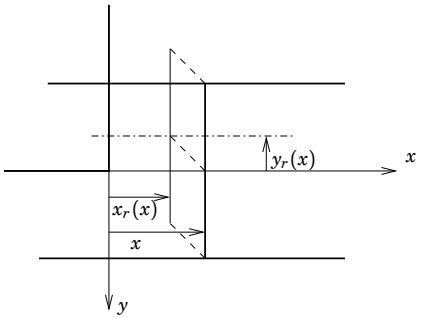

Figure 4.2 The deformation of a bristle element in the contact patch. Compare with Figure 4.1.

integration of (4.4) over the adhesive region. With (4.3) this gives

$$\begin{aligned} F_{ax} &= \int_{x_s}^{a} dF_{ax}(x) = -c_{px}\sigma_x \int_{x_s}^{a} (a-x)\,dx \\ F_{ay} &= \int_{x_s}^{a} dF_{ay}(x) = -c_{py}\sigma_y \int_{x_s}^{a} (a-x)\,dx \end{aligned} \tag{4.5}$$

where x_s is the position in the contact patch which divides the adhesive and sliding regions. To compute the total adhesive force it is necessary to know x_s.

The size of the adhesion region The size of the adhesive region is determined by the available static friction. The deformation will be limited by the largest force that can be carried by the static friction between the tire and the road. The static friction is assumed to be anisotropic (i.e. depending on the sliding direction) with the friction coefficients μ_{sx} and μ_{sy}, respectively. With a normal force $dF_z(x)$ acting on the infinitesimal bristle at position x, the available static friction force is described by the elliptic constraint

$$\left(\frac{dF_{ax}(x)}{dF_z(x)\mu_{sx}}\right)^2 + \left(\frac{dF_{ay}(x)}{dF_z(x)\mu_{sy}}\right)^2 \leq 1 \tag{4.6}$$

As a result, the magnitude of the available static friction force is dependent of the direction of the deformation force $d\bar{F}_a(x)$, defined by (4.4). The static friction constraint is illustrated in Figure 4.3. When $d\bar{F}_a(x)$ exceeds the static friction constraint the bristle will leave the adhesive

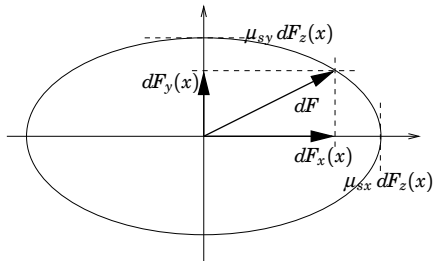

Figure 4.3 Illustration of the elliptic static friction constraint at anisotropic friction and rubber characteristics. Note that the direction of $d\bar{F}(x)$ and $\bar{\sigma}$ is equal only if $c_{px}/c_{py} = \mu_{sx}/\mu_{sy}$.

region and start to slide. Introduce the pressure distribution $q_z(x)$, with $dF_z(x) = q_z(x)\,dx$. By combining (4.3) and (4.4) with (4.6) the static friction constraint may be written as

$$\sqrt{\left(\frac{c_{px}\sigma_x}{\mu_{sx}}\right)^2 + \left(\frac{c_{py}\sigma_y}{\mu_{sy}}\right)^2}\,(a-x) \leq q_z(x) \tag{4.7}$$

The position x_s in the contact area is the break-away point where the static friction limit is reached and the bristles starts to slide. If the pressure distribution $q_z(x)$ is known then x_s can be calculated by setting equality in (4.7) with $x = x_s$.

A common assumption is to describe the pressure distribution in the contact patch as a symmetric parabolic function:

$$q_z(x) = \frac{3F_z}{4a}\left(1 - \left(\frac{x}{a}\right)^2\right) \tag{4.8}$$

This is proposed, for example, in [Tielking and Mital, 1974] and has shown to give a good agreement with experimental longitudinal force-slip curves for real tires. In [Svendenius, 2003] the influence of the pressure distribution is further examined. A more realistic pressure distribution is obtained by moving the pressure-peak slightly forward in the contact patch. The gain in accuracy is, however, small compared to increase in complexity of the resulting formulas and it can be concluded that the proposed parabolic assumption is sufficient for the applications related to the brush model in this work. Inserting (4.8) in (4.7) with equality gives

$$\sqrt{\left(\frac{c_{px}\sigma_x}{\mu_{sx}}\right)^2 + \left(\frac{c_{py}\sigma_y}{\mu_{sy}}\right)^2}\,(a-x_s) = \frac{3F_z}{4a^3}\,(a-x_s)\,(a+x_s) \tag{4.9}$$

The solution for the break-away point x_s is then

$$x_s(\sigma_x,\sigma_y) = \frac{4a^3}{3F_z}\sqrt{\left(\frac{c_{px}\sigma_x}{\mu_{sx}}\right)^2 + \left(\frac{c_{py}\sigma_y}{\mu_{sy}}\right)^2} - a \tag{4.10}$$

Since x_s is a point in the contact patch it must belong to the interval $[-a, a]$. If $x_s = a$ the entire contact patch is sliding. In the case of pure slip, i.e. either σ_x or σ_y is zero, this will occur at the limit slips $\sigma_x = \sigma_x^\circ$ or $\sigma_y = \sigma_y^\circ$ with σ_x° and σ_y° given by the following

$$\sigma_x^\circ \triangleq \frac{3F_z\mu_{sx}}{2a^2c_{px}}; \quad \sigma_y^\circ \triangleq \frac{3F_z\mu_{sy}}{2a^2c_{py}} \tag{4.11}$$

Introduction of normalized slips with respect to the limit slips will simplify the notation in the following. The normalized slip is defined as

$$\psi(\sigma_x,\sigma_y) \triangleq \sqrt{\left(\frac{\sigma_x}{\sigma_x^\circ}\right)^2 + \left(\frac{\sigma_y}{\sigma_y^\circ}\right)^2} \tag{4.12}$$

Equation (4.10) may now be rewritten as

$$x_s(\sigma_x,\sigma_y) = (2\psi(\sigma_x,\sigma_y) - 1)a \tag{4.13}$$

It is clear that partial sliding occurs when $\psi(\sigma_x,\sigma_y) < 1$. At full sliding then $\psi(\sigma_x,\sigma_y) \geq 1$ and $F_{ax}(\sigma_x,\sigma_y) = F_{ay}(\sigma_x,\sigma_y) = 0$. In the following the construction of adhesive and sliding forces at partial sliding will be determined.

Adhesion force Knowing the size of the adhesive region, $x_s(\sigma_x,\sigma_y)$, given by (4.13), the adhesive forces are obtained by solving the integrals (4.5) yielding

$$\begin{aligned} F_{ax}(\sigma_x,\sigma_y) &= -2a^2c_{px}\sigma_x\left(1-\psi(\sigma_x,\sigma_y)\right)^2 \\ F_{ay}(\sigma_x,\sigma_y) &= -2a^2c_{py}\sigma_y\left(1-\psi(\sigma_x,\sigma_y)\right)^2 \end{aligned} \tag{4.14}$$

for $\psi(\sigma_x,\sigma_y) < 1$. At full sliding, $\psi(\sigma_x,\sigma_y) \geq 1$, the adhesion forces becomes $F_{ax}(\sigma_x,\sigma_y) = F_{ay}(\sigma_x,\sigma_y) = 0$. Special notations for the forces at pure slip are introduced as

$$\begin{aligned} F_{0ax}(\sigma_x) &\triangleq F_{ax}(\sigma_x,0) \\ F_{0ay}(\sigma_y) &\triangleq F_{ay}(0,\sigma_y) \end{aligned} \tag{4.15}$$

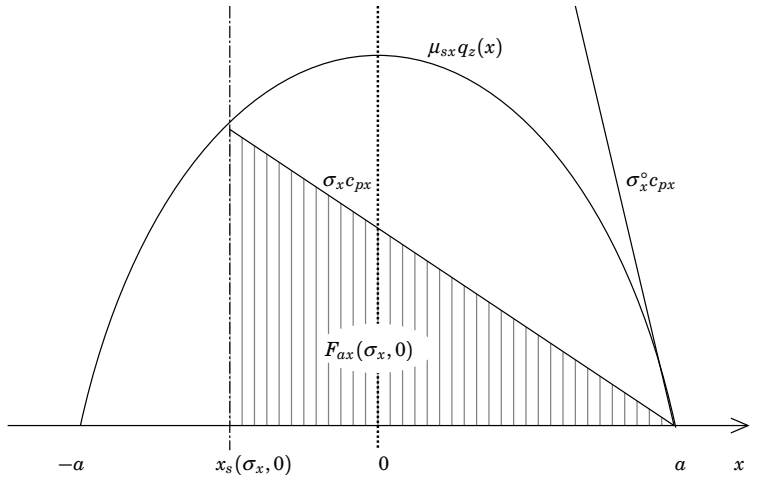

Figure 4.4 Illustration of the adhesive tire-force for pure longitudinal slip. The elastic deformation force for an element at x in the adhesive region depends linearly on x as $c_{px}\sigma_x(x-a)$, where the slope is proportional to the slip σ_x. The transition from adhesion to slide occurs at the intersection of the lines at the break-away point x_s. For slips $\sigma_x > \sigma_x^\circ$ full sliding occur in the contact area since there is then no intersection.

Note that it follows from (4.4) and (4.3) that the produced adhesive force per unit length in the adhesion region is not affected by combined slips:

$$\begin{aligned} \frac{dF_{ax}(\sigma_x,x)}{dx} &= -c_{px}\sigma_x\,(a-x) \\ \frac{dF_{ay}(\sigma_y,x)}{dx} &= -c_{py}\sigma_y\,(a-x) \end{aligned} \tag{4.16}$$

The adhesive forces thus grow linearly with slopes $c_{px}\sigma_x$ and $c_{py}\sigma_y$ as the contact element moves into the adhesion region. To illustrate the generation of the adhesive force the case of pure longitudinal slip is regarded, i.e. $\sigma_y = 0$. From (4.7) the size of the contact region is determined by the point where $c_{px}\sigma_x\,(a-x) = \mu_{sx}q_z(x)$. That is, where the straight line describing the produced force per unit length intersects $\mu_{sx}q_z(x)$, as is shown in Figure 4.4. The striped area under the line corresponds to the total adhesion force. The slope corresponding to full sliding, i.e. $\sigma_x = \sigma_x^\circ$, is also shown. The case of pure lateral slip is analogous.

Combined-slip slide forces The normal force acting on the sliding region at partial sliding may be computed from (4.8) and (4.13) as

$$F_{sz}(\sigma_x,\sigma_y)=\int_{-a}^{x_s(\sigma_x,\sigma_y)} q_z(x)\,dx = F_z\psi^2(\sigma_x,\sigma_y)\,(3-2\psi(\sigma_x,\sigma_y)) \tag{4.17}$$

In case of isotropic sliding friction with the friction coefficient μ_k, the friction force is collinear with the slip velocity with the magnitude $F_{sz}(\sigma_x,\sigma_y)\mu_k$. Its components are given by

$$\begin{aligned} F_{sx}(\sigma_x,\sigma_y) &= -\cos(\beta)\mu_k F_{sz}(\sigma_x,\sigma_y)\\ F_{sy}(\sigma_x,\sigma_y) &= -\sin(\beta)\mu_k F_{sz}(\sigma_x,\sigma_y) \end{aligned} \tag{4.18}$$

where β is defined by (2.4). Assumptions on isotropic sliding friction are common in tire modeling, see for instance [Schuring *et al.*, 1996].

If the sliding-friction is anisotropic with the different friction coefficients μ_{kx} and μ_{ky}, there are several ways to calculate the magnitude and the direction of the resulting force. Three different methods are presented in the following and which one to choose depends on the assumptions made on the friction behavior for the actual case.

Collinear slide forces This method should be used if the friction between two surfaces is supposed to be isotropic, but the values of μ_{kx} and μ_{ky} are unequal. A reason for that could, for instance, be errors in the measurements of the pure-slip forces. The friction forces are given by

$$\begin{aligned} F_{sx}^{\mathrm{Col}}(\sigma_x,\sigma_y) &= -\cos(\beta')\mu_{kx}F_{sx}(\sigma_x,\sigma_y)\\ F_{sy}^{\mathrm{Col}}(\sigma_x,\sigma_y) &= -\sin(\beta')\mu_{ky}F_{sy}(\sigma_x,\sigma_y) \end{aligned} \tag{4.19}$$

where β' is defined as

$$\tan(\beta') \triangleq \left(\frac{\mu_{ky}}{\mu_{kx}}\right)^{-1}\frac{v_{sy}}{v_{sx}} \tag{4.20}$$

The choice of β' ensures that $\bar{F}_s$ acts in the opposite direction to the sliding motion, with a friction coefficient that is somewhere in the interval $[\mu_{kx},\mu_{ky}]$ depending on the sliding angle β.

Maximum dissipation rate The correct way to treat anisotropic friction according to the literature is to apply the Maximum Dissipation Rate (MDR) principle. The theory which is further presented in [Goyal, 1989] claims that the resulting sliding-friction force $\bar{F}_s^{\mathrm{MDR}}$ is generated in such

a way that the mechanical work $W=-\bar{v}_s\cdot\bar{F}_s^{\mathrm{MDR}}$ is maximized under the constraint

$$\left(\frac{F_{sx}^{\mathrm{MDR}}}{F_{sz}\mu_{kx}}\right)^2+\left(\frac{F_{sy}^{\mathrm{MDR}}}{F_{sz}\mu_{ky}}\right)^2\le 1 \tag{4.21}$$

This results in the sliding forces

$$\begin{aligned} F_{sx}^{\mathrm{MDR}}(\sigma_x,\sigma_y) &= -\frac{\mu_{kx}^2 v_{sx}}{\sqrt{(\mu_{kx}v_{sx})^2+(\mu_{ky}v_{sy})^2}}F_{sz}(\sigma_x,\sigma_y) = -\mu_{kx}\cos(\beta^{\mathrm{SPM}})F_{sz}\\ F_{sy}^{\mathrm{MDR}}(\sigma_x,\sigma_y) &= -\frac{\mu_{ky}^2 v_{sy}}{\sqrt{(\mu_{kx}v_{sx})^2+(\mu_{ky}v_{sy})^2}}F_{sz}(\sigma_x,\sigma_y) = -\mu_{ky}\sin(\beta^{\mathrm{SPM}})F_{sz} \end{aligned} \tag{4.22}$$

where β^{SPM} is defined as

$$\tan(\beta^{\mathrm{SPM}}) \triangleq \frac{\mu_{ky}}{\mu_{kx}}\frac{v_{sy}}{v_{sx}} \tag{4.23}$$

The angle of the resulting force $\bar{F}_s^{\mathrm{MDR}}$ is denoted by β^{MDR} and is given by

$$\tan(\beta^{\mathrm{MDR}}) = \left(\frac{\mu_{ky}}{\mu_{kx}}\right)^2\frac{v_{sy}}{v_{sx}} \tag{4.24}$$

Slip-projection method An intermediate approach to model anisotropic sliding friction is to simply replace μ_k in (4.18) with μ_{kx} and μ_{ky} in the corresponding directions:

$$\begin{aligned} F_{sx}^{\mathrm{SPM}}(\sigma_x,\sigma_y) &= -\cos(\beta)\mu_{kx}F_{sz}(\sigma_x,\sigma_y)\\ F_{sy}^{\mathrm{SPM}}(\sigma_x,\sigma_y) &= -\sin(\beta)\mu_{ky}F_{sz}(\sigma_x,\sigma_y) \end{aligned} \tag{4.25}$$

This means a projection of the pure-slip sliding-forces on the slip vector. The angle of the resulting force is then equal to β^{SPM}. From the definitions of β (2.4), β^{SPM} (4.23), and β^{MDR} (4.24), it is clear that the direction of $\bar{F}_s^{\mathrm{SPM}}$ is between the directions of $\bar{F}_s^{\mathrm{Col}}$ and $\bar{F}_s^{\mathrm{MDR}}$, see Figure 4.5.

To summarize: The sliding forces are described by

$$\begin{aligned} F_{sx}(\sigma_x,\sigma_y) &= -\cos(\beta_f)\mu_{kx}F_{sz}(\sigma_x,\sigma_y)\\ F_{sy}(\sigma_x,\sigma_y) &= -\sin(\beta_f)\mu_{ky}F_{sz}(\sigma_x,\sigma_y) \end{aligned} \tag{4.26}$$

with

$$F_{sz}(\sigma_x,\sigma_y) = F_z\psi^2(\sigma_x,\sigma_y)\,(3-2\psi(\sigma_x,\sigma_y)) \tag{4.27}$$

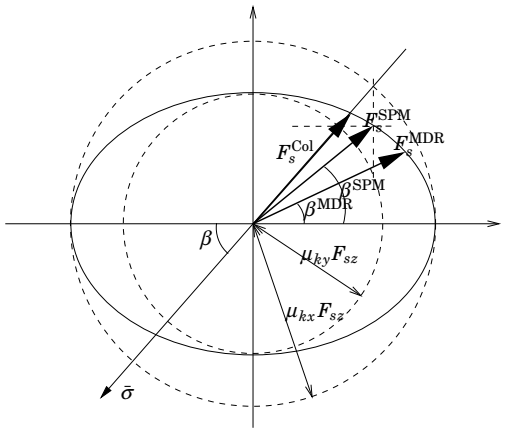

Figure 4.5 Illustration of methods to describe kinetic friction in case of different longitudinal and lateral friction coefficients.

and β_f is any of β' (collinear), β (slip-projection) or β^{SPM} (MDR) depending on choice of friction model:

$$\tan(\beta') \triangleq \left(\frac{\mu_{ky}}{\mu_{kx}}\right)^{-1} \frac{v_{sy}}{v_{sx}}; \quad \tan(\beta) \triangleq \frac{v_{sy}}{v_{sx}}; \quad \tan(\beta^{\mathrm{SPM}}) \triangleq \frac{\mu_{ky}}{\mu_{kx}} \frac{v_{sy}}{v_{sx}} \tag{4.28}$$

In the special case of pure-slip the sliding-forces are

$$\begin{aligned} F_{0sx}(\sigma_x) &= -\mu_{kx} F_{sz}(\sigma_x, 0)\, \mathrm{sgn}(\sigma_x) \\ F_{0sy}(\sigma_y) &= -\mu_{ky} F_{sz}(0, \sigma_y)\, \mathrm{sgn}(\sigma_y) \end{aligned} \tag{4.29}$$

In Figure 4.6 the case of pure longitudinal slip is again regarded, now with also the sliding force introduced. Since $q_z(x)$ is the normal force per unit length, the sliding force per unit length is simply $\mu_{kx} q_z(x)$, as marked in the figure. The horizontally striped area corresponds to the total sliding force.

Effects of combined slips The total tire force is given by adding the adhesive forces of (4.14) and the sliding forces of (4.26):

$$\begin{aligned} F_x(\sigma_x, \sigma_y) &= F_{ax}(\sigma_x, \sigma_y) + F_{sx}(\sigma_x, \sigma_y) \\ F_y(\sigma_x, \sigma_y) &= F_{ay}(\sigma_x, \sigma_y) + F_{sy}(\sigma_x, \sigma_y) \end{aligned} \tag{4.30}$$

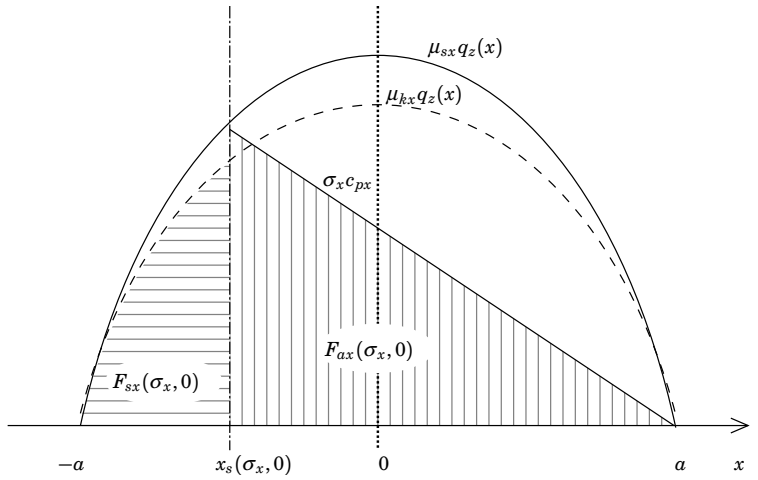

Figure 4.6 Illustration of partition of the contact area into a sliding and an adhesive region for the case of pure longitudinal slip. The slide force for an element at x is determined by the pressure distribution $\mu_{kx} q_z(x)\, dx$. The horizontally striped area is the total slide force.

To illustrate the effect of combined slips Figure 4.7 shows the production of longitudinal force in the case of combined longitudinal and lateral slip (σ_x, σ_y) with $\sigma_x \neq 0$, $\sigma_y \neq 0$. Equation (4.13) shows that the adhering region shrinks compared to the case with pure slip $(\sigma_x, 0)$. The sliding region grows accordingly. From (4.16) it is clear that the adhesive force per unit length is the same for the combined slip (σ_x, σ_y) as for the pure-slip $(\sigma_x, 0)$. Hence, the slope is the same, but the area corresponding to the force is smaller since the adhering region is smaller. The corresponding adhesive-force slope derived from (4.16) is $c_{px} \sigma_x^{\circ} \psi(\sigma_x, \sigma_y)$. The corresponding expression applies for the lateral force. It is therefore clear that sliding will occur simultaneously in both directions as $\psi(\sigma_x, \sigma_y)$ approaches unity. It is important to note that the indicated area under the pressure distribution no longer corresponds to the resulting sliding force. Instead it describes $\mu_{kx} F_{sz}(\sigma_x, \sigma_y)$, which is the force that would result for pure longitudinal sliding with the sliding region $x_s(\sigma_x, \sigma_y)$. This force must be limited by a friction constraint according to Section 4.1.

The braking and cornering stiffnesses are the linearizations of the pure-slip friction curves at small slips and may be computed by derivation

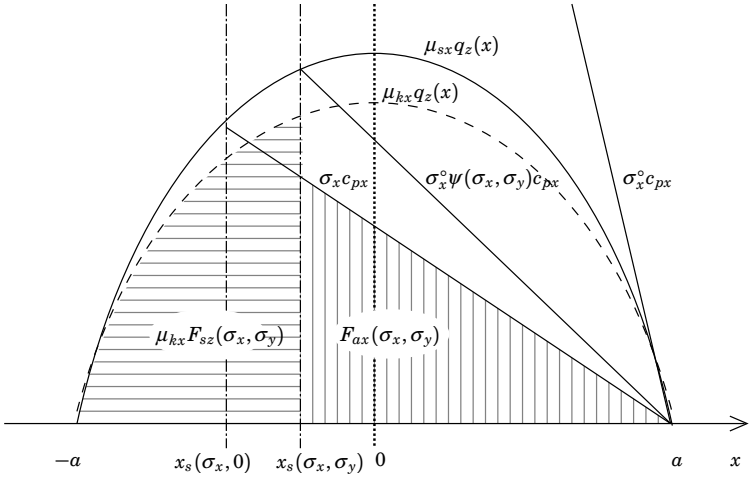

Figure 4.7 Illustration of the effect of combined slip. The combined-slip has the effect of decreasing the size of the adhesive region, compare with Figure 4.6.

of (4.30):

$$\begin{aligned} C_x &= -\left.\frac{\partial F_x(\sigma_x,0)}{\partial \sigma_x}\right|_{\sigma_x=0} = 2c_{px}a^2 \\ C_y &= -\left.\frac{\partial F_y(0,\sigma_y)}{\partial \sigma_y}\right|_{\sigma_y=0} = 2c_{py}a^2 \end{aligned} \tag{4.31}$$

Self-aligning torque The self-aligning torque consists of two parts. The main part is M_z', which is the torque developed by the non symmetric distribution of the lateral force F_y. The additional part M_z'' is due to the deformation of the tire.

The torque dM_z' developed at position x in the contact region is

$$dM_z'(x) = dF_y(x)\,x \tag{4.32}$$

In the adhesive part of the contact region the expression for $dF_y(x)$ is given by (4.4) together with (4.3). In the sliding zone it is given by differentiating (4.26) using $dF_z(x) = q_z(x)\,dx$ from (4.8). Integration over the

adhesive and sliding area separately gives

$$\begin{aligned} M_{az}'(\sigma_x,\sigma_y) &= -c_{py}\sigma_y \int_{x_s(\sigma_x,\sigma_y)}^{a} x\,(a-x)\,dx \\ &= -c_{py}a^3\sigma_y \frac{2}{3}(1-\psi(\sigma_x,\sigma_y))^2(4\psi(\sigma_x,\sigma_y)-1) \end{aligned} \tag{4.33}$$

$$\begin{aligned} M_{sz}'(\sigma_x,\sigma_y) &= -\mu_{ky}\sin(\beta)\int_{-a}^{x_s(\sigma_x,\sigma_y)} x\,q_z(x)\,dx \\ &= -3\mu_{kx}\sin(\beta)aF_z\psi^2(\sigma_x,\sigma_y)(1-\psi(\sigma_x,\sigma_y))^2 \end{aligned} \tag{4.34}$$

$$M_z'(\sigma_x,\sigma_y) = M_{az}'(\sigma_x,\sigma_y) + M_{sz}'(\sigma_x,\sigma_y) \tag{4.35}$$

When there is a lateral slip the tire deflects laterally and the point of action for the longitudinal force will have an offset from the central plane of the wheel. This produces an additional deformation torque in the z-direction. A longitudinal deflection together with a lateral force has the same effect. Since it is assumed that the carcass is stiff the deformation is here described by bristle deflections, see also Section 4.3. The deformation torque developed at position x in the contact region is described by

$$dM_z''(x) = dF_y(x)\delta_{xb}(x) - dF_x(x)\delta_{yb}(x) \tag{4.36}$$

In the same way as above, integration over the adhesive and the sliding regions is performed separately. The deformation $\delta_{xb}(x)$ is computed from (4.3) in the adhesive region and from (4.4) using the infinitesimal sliding force in the sliding region. Hence

$$\begin{aligned} M_{az}''(\sigma_x,\sigma_y) &= \int_{x_s(\sigma_x,\sigma_y)}^{a} c_{py}\sigma_y(a-x)\sigma_x(a-x)\,dx \\ &\quad - \int_{x_s(\sigma_x,\sigma_y)}^{a} c_{px}\sigma_x(a-x)\sigma_y(a-x)\,dx \\ &= \frac{4}{3}(C_y-C_x)a\sigma_x\sigma_y(1-\psi(\sigma_x,\sigma_y))^3 \\ &= \frac{4}{3}\left(\frac{1}{C_x}-\frac{1}{C_y}\right)\frac{a}{(1-\psi(\sigma_x,\sigma_y))}F_{ax}(\sigma_x,\sigma_y)F_{ay}(\sigma_x,\sigma_y) \end{aligned} \tag{4.37}$$

$$
\begin{aligned}
M''_{sz}(\sigma_x,\sigma_y) &= \int_{-a}^{x_s(\sigma_x,\sigma_y)} \mu_{ky}\sin(\beta_f) q_z(x)\mu_{kx}^2\cos(\beta_f)\frac{1}{c_{px}}q_z(x)\,dx \\
&\quad - \int_{-a}^{x_s(\sigma_x,\sigma_y)} \mu_{kx}\cos(\beta_f) q_z(x)\mu_{ky}\sin(\beta_f)\frac{1}{c_{py}}q_z(x)\,dx \\
&= \frac{6}{5}\left(\frac{1}{C_x}-\frac{1}{C_y}\right)\mu_{kx}\mu_{ky}a\sin(\beta_f)\cos(\beta_f)F_z^2 \\
&\quad \cdot \psi^3(\sigma_x,\sigma_y)(10-15\psi(\sigma_x,\sigma_y)+6\psi^2(\sigma_x,\sigma_y)) \\
&= \frac{6}{5}\left(\frac{1}{C_x}-\frac{1}{C_y}\right)\frac{a(10-15\psi(\sigma_x,\sigma_y)+6\psi^2(\sigma_x,\sigma_y))}{\psi(\sigma_x,\sigma_y)(3-2\psi(\sigma_x,\sigma_y))^2} \\
&\quad \cdot F_{sx}(\sigma_x,\sigma_y)F_{sy}(\sigma_x,\sigma_y)
\end{aligned}
\tag{4.38}
$$

where (4.14) and (4.26) have been used in the last step. The total additional torque is

$$
M''_z(\sigma_x,\sigma_y) = M''_{az}(\sigma_x,\sigma_y) + M''_{sz}(\sigma_x,\sigma_y) \tag{4.39}
$$

and finally the total self-aligning torque is

$$
M_z(\sigma_x,\sigma_y) = M'_z(\sigma_x,\sigma_y) + M''_z(\sigma_x,\sigma_y) \tag{4.40}
$$

A commonly used parameter is the pneumatic trail, which denotes the distance between the center of the tire and point of action for the lateral force. It is defined as $t(\sigma_x,\sigma_y) = M_z(\sigma_x,\sigma_y)/F_y(\sigma_x,\sigma_y)$. The coordinate for the point of action for the adhesive force is denoted by $t_a(\sigma_x,\sigma_y)$ and for the sliding force by $t_s(\sigma_x,\sigma_y)$. By using (4.33) and (4.14) respectively (4.34) and (4.26) the contributions from $M'_z(\sigma_x,\sigma_y)$ to the pneumatic trail, $t'_a(\sigma_x,\sigma_y)$ and $t'_s(\sigma_x,\sigma_y)$, are given by

$$
\begin{aligned}
t'_a(\sigma_x,\sigma_y) &= \frac{M'_{az}(\sigma_x,\sigma_y)}{F_{ay}(\sigma_x,\sigma_y)} = \frac{a}{3}(4\psi(\sigma_x,\sigma_y)-1) \\
t'_s(\sigma_x,\sigma_y) &= \frac{M'_{sz}(\sigma_x,\sigma_y)}{F_{sy}(\sigma_x,\sigma_y)} = -3a\frac{(1-\psi(\sigma_x,\sigma_y))^2}{(3-2\psi(\sigma_x,\sigma_y))}
\end{aligned}
\tag{4.41}
$$

The contributions from $M''_z(\sigma_x,\sigma_y)$ can be read directly from (4.37) and (4.38).

In the same way as for the braking and cornering stiffness, the aligning stiffness is defined as

$$
C_z = \left.\frac{\partial M_z}{\partial \sigma_y}\right|_{\sigma_x,\sigma_y=0} = c_{py}a^3\frac{2}{3} = C_y\frac{a}{3} \tag{4.42}
$$

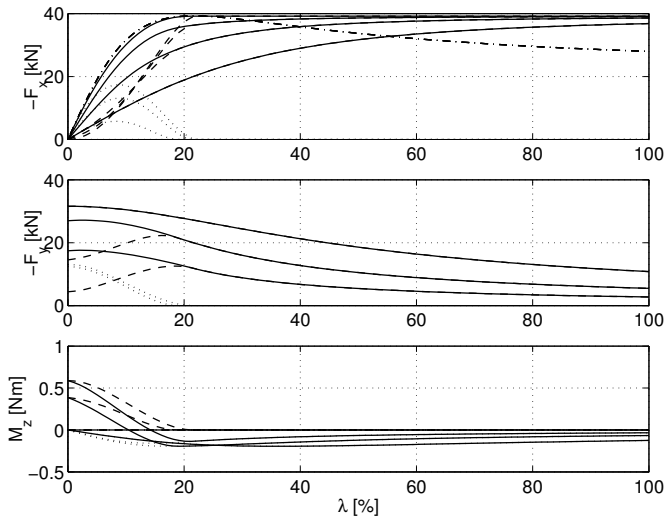

Figure 4.8 Tire forces as function of λ with $\alpha = [0, 5, 10, 20]$ deg. The dotted line shows the force from the adhesive region, the dashed line shows it from the sliding region. The solid line is the total force and the dashed-dotted line is the reference curve generated from a Magic Formula approximation of real tire data [Gäfvert and Svendenius, 2003]. For the self aligning torque the dotted line denotes the deformation torque M''_z and the dashed line M'. The slip definition λ is used since it is most common when data is visualized. Refer to Equation (2.6) for transformation between λ and σ_x.

Properties of the brush-model

Figures 4.8 and 4.9 show the behavior of the brush model at pure and combined slip. The pure slip curves are compared to a Magic-Formula parametrisation of a classified truck tire. The brush-model parameters are chosen so that the pure-slip curves have the same braking and cornering stiffnesses and the same peak force as of the Magic-Formula reference-curve. The length of the contact-patch is chosen such that the aligning-stiffness agrees with the self-aligning torque reference-curve. For small pure longitudinal slip the coherence between the brush model and the reference curve is good. For slips larger than the value corresponding to the peak force, the curves do not agree since no velocity-dependency is modelled for the friction. This have the effect that the modelled tire force is constant for higher slip, while here and most commonly the tire force decreases in the region. Different ways to introduce velocity dependence in the friction is, for example, discussed in [Svendenius, 2003]. At partial sliding ($\psi < 1$) this approximation normally has small effects.

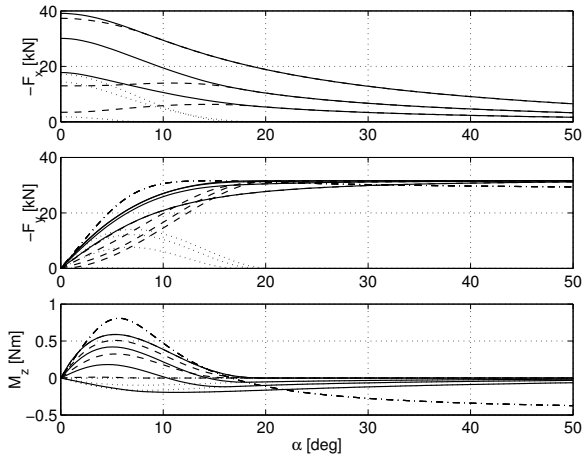

Figure 4.9 Tire forces as function of α with $\lambda = [0, 5, 10, 20]$ deg. The dotted line shows the force from the adhesive region, the dashed line shows it from the sliding region. The solid line is the total force and the dashed dotted line is the Magic-Formula reference curve. For the self aligning torque the dotted line denotes the deformation torque M_z'' and the dashed line M'. The slip definition α is used since it is most common when data is visualized. Refer to Equation (2.6) for transformation between α and σ_y.

For pure lateral slip there are disparities in the lateral force and in the self-aligning torque compared to the Magic-Formula reference, even at lower slips. Probably, the main reason for this is the assumption of a stiff carcass, which is reasonably accurate in the longitudinal direction. Laterally, where the carcass is weaker, the effects of this simplification is noticeable.

There are several ways to include carcass flexibility based on assumptions on stretched string or beam behavior in the brush model. Some of them are further discussed in Section 4.3. Also the self-aligning torque depends on the flexibility of the carcass which might explain some of its disagreement to the reference. A factor that can explain the deviation of the self-aligning torque, particularly at high lateral slip is the deviation of the actual pressure distribution from the parabolic assumption in (4.8). If the position of the center of the vertical load differs from the hub center, the pneumatic trail will not become zero at higher slips. Hence, the lateral force then gives a torque contribution. This have not been further examined in this thesis, but the effects on the longitudinal tire force, due to non-uniform pressure distribution is penetrated in [Svendenius and Wittenmark, 2003].

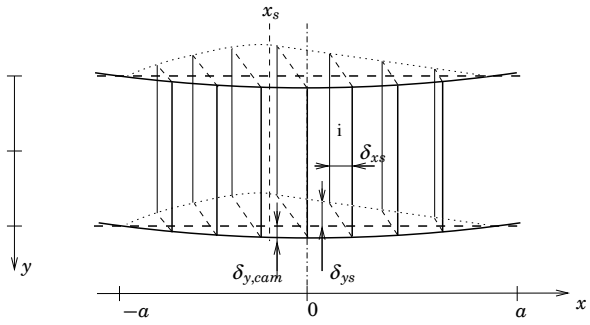

Figure 4.10 Schematic illustration of the contact patch showing the bristle deformation due to longitudinal and lateral slip and cambering.

Due to lack of data there were no possibilities to verify the deformation torque, M_z'', which probably is underestimated since only the rubber deformations are considered here. Torque addition due to carcass deflection is discussed in Section 4.3.

4.2 The Effect of Camber

Bristle deflection

The developed tire force due to tilting of the tire, can with some approximations, be explained by the brush model. In Figure 2.3 a cambered tire is shown together with the orbit, an ellipse, that describes the projection on the road surface of a point on the carcass during rolling motion. The deviation from the straight contact patch from a non-cambered tire is

$$y = -\sin(\gamma)\left(\sqrt{R^2 - x^2} - \sqrt{R^2 - a^2}\right) \tag{4.43}$$

where R is the average wheel radius and a is half the contact length. Figure 4.10 also shows the deformation of bristle element due to cambering and lateral slip according to the brush model. Relation (4.43) will result in difficult expressions when the standard parabolic pressure distribution is employed. In, for example, [Gim and Nikravesh, 1991] and [Pacejka, 2002] the deviation due to cambering is approximated as a parabolic function similar to the assumed pressure distribution as

$$\delta_{y,cam}(x) = -\gamma k\left(a^2 - x^2\right) \tag{4.44}$$

where k is chosen such that the average camber deflection is correct in the contact patch

$$\int_{-a}^{a} \delta_{y,cam} dx = \int_{-a}^{a} y dx \Rightarrow k \approx \frac{3}{4} \frac{R - \sqrt{R^2 - a^2}}{a^2} \tag{4.45}$$

The approximation simplifies the calculations considerably. The deformation of a bristle that adheres to the road in the contact patch is then $-\delta_{y,cam}$ and the total bristle deformation including the effects caused by slip, under the assumption of a stiff carcass, can be written as

$$\delta_{xb}(x) = -\sigma_x (a - x) \tag{4.46}$$

$$\delta_{yb}(x) = -\sigma_y (a - x) + \gamma k (a^2 - x^2) \tag{4.47}$$

Size of adhesive region

The calculations in Section 4.1 can be used to determine the size of the adhesion region. By using (4.5) in (4.6) with the addition from camber on δ_{yb} from (4.44), the expression for deriving the break-away point is given as

$$\sqrt{\left(\frac{c_{px}\sigma_x}{\mu_{sx}}\right)^2 + \left(\frac{c_{py}\left(\sigma_y + \gamma k (a + x_s)\right)}{\mu_{sy}}\right)^2} (a - x_s) \leq q_z(x_s) \tag{4.48}$$

with the assumption of the pressure distribution from (4.8) and the definition of the normalized slip, ψ, compared to (4.12), is extended to

$$\psi(\sigma_x, \sigma_y, \gamma) \triangleq \frac{\gamma^{\circ 2}}{\gamma^{\circ 2} - \gamma^2} \left(\frac{\sigma_y \gamma}{\sigma_y^\circ \gamma^\circ} + \sqrt{\left(\frac{\sigma_x}{\sigma_x^\circ}\right)^2 + \left(\frac{\sigma_y}{\sigma_y^\circ}\right)^2 - \left(\frac{\sigma_x \gamma}{\sigma_x^\circ \gamma^\circ}\right)^2} \right) \tag{4.49}$$

where the limit slips, σ_x°, σ_y° are defined in (4.11), and the camber limit angle γ° are defined as

$$\gamma^\circ \triangleq \frac{3 F_z \mu_{sy}}{2 C_y k a} \tag{4.50}$$

The break-away point can be written as in (4.13)

$$x_s(\sigma_x, \sigma_y, \gamma) = (2\psi(\sigma_x, \sigma_y, \gamma) - 1)\, a \tag{4.51}$$

The partitioning of the contact patch and the significance of ψ and x_s is visualized in Figure 4.11. It is clear that values of ψ larger than unity lack physical interpretation. Since the bristle deformation due to cambering

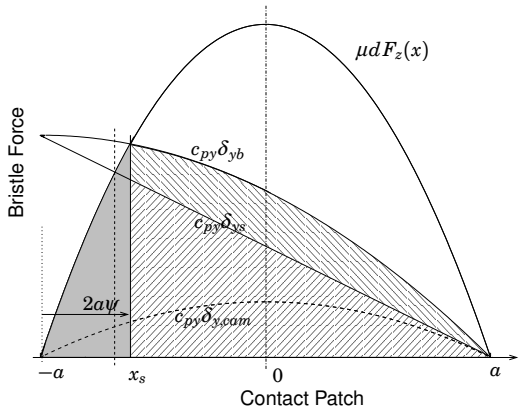

Figure 4.11 Force generation in the contact patch due to slip and camber. The shaded area is the force generated in the sliding region. The lower area with diagonal lines denotes the adhesion force generated by slip and the upper the contribution due to camber. The dashed straight line indicates the sliding region in case of zero camber.

has the same shape as the pressure distribution along the contact patch, ψ will be zero as long as $\sigma_x = \sigma_y = 0$. At the camber angle γ° the whole contact patch starts to slide against the road and ψ can not be computed since the denominator reaches zero. In this case the model is not valid and if accurate results are to be obtained a different tire model should be used. Such large camber angles are, however, not relevant for studies on trucks and cars.

Forces and torque

The forces generated in the contact patch are in Section 4.1 derived separately for the adhesive and sliding regions. As mentioned, camber affects the natural path of the carcass in the contact region, which affects the force contribution from the adhesive region. In the sliding area the deformation, δ_x, δ_y, changes, since the vertical force on the bristle varies according to the parabolic pressure distribution. The rate of change of the deformation is small and the effect on the sliding velocity is neglected. The curvature of the bristle path resulting from cambering is small for small camber angles and the effect on the sliding friction forces is neglected. In other words, the only effect cambering has on the sliding force is that it changes the size of the sliding region, which already is included by use of ψ from (4.49)

Adhesion The forces from the adhesive region derived in (4.14) with use of ψ from (4.49) are still valid. In the lateral direction the force addition due to the camber is the sum of the force contribution from each bristle given by (4.44) with (4.4) as

$$\begin{aligned} F_{ay,cam}(\sigma_x,\sigma_y,\gamma) &= \int_{x_s(\sigma_x,\sigma_y,\gamma)}^{a} c_{py}\gamma k(a^2-x^2)dx \\ &= \frac{2}{3}\gamma k a C_y \left(2\psi^3(\sigma_x,\sigma_y,\gamma) - 3\psi^2(\sigma_x,\sigma_y,\gamma) + 1\right) \end{aligned} \quad (4.52)$$

The camber stiffness, C_γ is defined as

$$C_\gamma = \left.\frac{\partial F_y(0,0,\gamma)}{\partial\gamma}\right|_{\gamma=0} = \frac{2kaC_y}{3} = \frac{F_z\mu_{sy}}{\gamma^\circ} \quad (4.53)$$

In case of pure cambering for $\gamma < \gamma^\circ$ the lateral force is

$$F_{0,cam}(\gamma) = C_\gamma\gamma \quad (4.54)$$

The total adhesive lateral force is

$$F_{ay}(\sigma_x,\sigma_y,\gamma) = -C_y\sigma_y\left(1-\psi(\sigma_x,\sigma_y,\gamma)\right)^2 + F_{ay,cam}(\sigma_x,\sigma_y,\gamma) \quad (4.55)$$

Self-aligning torque

According to the conditions assumed here, pure cambering will not give rise to any self-aligning torque. As long as there is no sliding region in the contact patch the bristle deformation is symmetric. A simultaneous slip causes a sliding region and the addition to the torque due to camber in the adhesive region can be written as

$$M_{z,cam} = \int_{x_s(\sigma_x,\sigma_y,\gamma)}^{a} c_{py}x\delta_{y,cam}dx = 2\gamma k a^2 C_y\psi^2(\sigma_x,\sigma_y,\gamma)\left(1-\psi(\sigma_x,\sigma_y,\gamma)\right)^2 \quad (4.56)$$

The total self-aligning torque can be expressed as

$$\begin{aligned} M_z(\sigma_x,\sigma_y,\gamma) = M_{az}(\sigma_x,\sigma_y,\gamma) + M_{sz}(\sigma_x,\sigma_y,\gamma) \\ + M_{z,cam}(\sigma_x,\sigma_y,\gamma) + M_{z,add}(\sigma_x,\sigma_y,\gamma) \end{aligned} \quad (4.57)$$

In Section 5.4 results on how the combined slip forces and torque are affected by camber are shown.

4.3 Effects of a Flexible Carcass

Lateral deformation of the carcass

As mentioned previously the brush model described in Section 4.1 is based on the assumption of a stiff carcass. In reality the carcass is flexible, as mentioned in Section 2.6 and exhibits significant deformation. Figure 4.12 illustrates how the carcass deformation affects the brush model laterally. Mainly, the break-away point will move backwards and the deflection of the bristles increases differently in the contact patch. The bristles and the carcass can be seen as two spring elements connected serially, with the distinction that each bristle deflects individually, when the carcass is a coherent unit. The total carcass deflection is denoted by δ_{yctot}, and δ_{yc} is the relative deflection, compared to the deflection in the leading point of the contact patch, $(x = a)$, as $\delta_{yc}(x) = \delta_{yctot}(x) - \delta_{yctot}(a)$. The total deformation relative the carcass deformation in same point is the sum of the bristle and carcass deflections $\delta_{yb}(x)$ and $\delta_{yc}(x)$

$$\delta_{ys}(x) = \delta_{yb}(x) + \delta_{yc}(x) \quad (4.58)$$

and

$$dF_{yb}(x) = dF_{yc}(x) = dF_y(x) \quad (4.59)$$

Let $F'_y(\sigma_y)$ denote the lateral tire-force for a tire with flexible carcass. Regard again how the deformation at position x in the adhesive region, $\delta_y(x)$, is described by (4.3). This is a purely kinematic relation which holds also in the case of flexible carcass. The force acting on the bristle element at x will then be

$$dF'_y(x) = c_{py}\delta_{yb}(x)\,dx = -c_{py}(\sigma_x(a-x) + \delta_{yc}(x)) \quad (4.60)$$

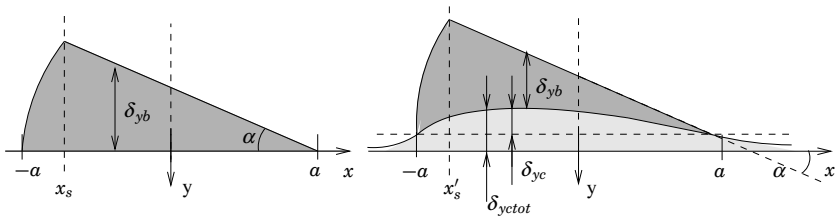

Figure 4.12 Lateral tire deformation in the contact patch according to the brush-model. Left: Stiff carcass. Right: Flexible carcass.

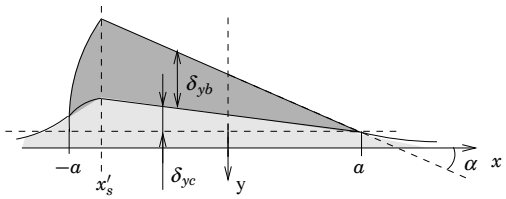

Figure 4.13 Lateral tire deformation in the contact patch with carcass deformation according to the assumption in Section 4.3.

when the bristle starts to slide the force is

$$dF_y'(x) = \mu dF_z(x) \tag{4.61}$$

The relation between the carcass deflection and the lateral force distribution has to be established and the literature propose several ways. Common proposals are to treat the carcass as a string or as a beam. For the string model the force-deflection relation has the following differential form

$$S\frac{d^2\delta_{yc}(x)}{dx^2} = q_{yc}(x) \tag{4.62}$$

where S is the tension in the thread and $q_{yc} = q_y$ is the lateral force per length unit equal to dF_y/dx. A system of equations consisting of an expression for the break-away point given by the equality of (4.60) and (4.61) and one differential expression for lateral force per unit for $x_s \leq x \leq a$ from (4.62) and (4.60) and for $-a \leq x \leq x_s$ given by (4.61), can be established. The approach requires extensive calculations and will not be further treated here. It has, however, been solved and a few results is presented in [Pacejka, 1988]. A simpler approach is to assume a certain shape of the carcass deformation with an amplitude depending on the total lateral force. Here the simplest one is used, where it is assumed that the carcass is straight in the adhesion area, but have a deviation towards the rolling direction. The incline is proportional to the lateral force, see Figure 4.13. The deflection is given by

$$\delta_{yc}(x) = -\frac{F_y'(\sigma_y)}{C_c}(a-x) \tag{4.63}$$

where C_c relates to the lateral the carcass stiffness and F_y' the lateral tire force under the assumption of a flexible carcass. The proposal is in analogy with an assumption by von Schlippe discussed in [Pacejka, 2002]. From (4.58), (4.63) and (4.3) it holds that

$$dF_y'(x) = c_{py}\delta_{yb}(x)\,dx = -c_{py}\left(\sigma_y - \frac{F_y'(\sigma_y)}{C_c}\right)(a-x)\,dx \tag{4.64}$$

Using (4.6) at pure lateral slip together with a parabolic pressure distribution (4.8) the position for the break-away point can be solved from

$$c_{py}\left(\sigma_y - \frac{F_y'(\sigma_y)}{C_c}\right) = \frac{3\mu_{ay}F_z}{4a^3}(a+x_s) \tag{4.65}$$

The total lateral force can be derived from the following equation

$$F_y'(\sigma_y) = \int_{x_s(F_y'(\sigma_y))}^{a} c_{py}\left(\sigma_y - \frac{F_y'(\sigma_y)}{C_c}\right)(a-x)dx + \int_{-a}^{x_s(F_y'(\sigma_y))} \mu q_z dx \tag{4.66}$$

It is realized that the analytical solution to this strongly simplified approach will not become a smooth expression. Numerical solution can easily be found and a comparison between this compensation and the ordinary brush model can be seen in Figure 4.14. Important information can, however, be derived from this model considering the effect of the flexible carcass on σ_y° , see Equation (4.11). Regard the case when the entire contact patch slides, i.e $x_s = a$, $\sigma_y = \sigma_y^{\circ\prime}$, and $F_y'(\sigma_y^{\circ\prime}) = \mu_{ky}F_z$. Solving (4.65) for $\sigma_y^{\circ\prime}$ under these conditions gives

$$\sigma_y^{\circ\prime} = \frac{3F_z\mu_{sy}}{2a^2c_{py}} + \frac{\mu_{ky}F_z}{C_c} = F_z\left(\frac{3\mu_{sy}}{2a^2c_{py}} + \frac{\mu_{ky}}{C_c}\right) \tag{4.67}$$

The next step is to derive an expression for the relation between C_c and the cornering stiffness C_y'. The apostrophe marks that the cornering stiffness is derived under the assumption of a flexible carcass. At very small slips $\sigma_y \approx 0$ there is no sliding in the contact patch and the tire force only consists of adhesive force. Therefore,

$$\begin{aligned} C_y' &= \left.\frac{dF_y'(\sigma_y)}{d\sigma_y}\right|_{\sigma_y=0} = -\left.\frac{d}{d\sigma_y}\left(\int_{-a}^{a} c_{py}\delta_{yb}(x)\,dx\right)\right|_{\sigma_y=0} \\ &= 2a^2c_{py}\left(1 - \frac{1}{C_c}\left.\frac{dF_y'(\sigma_y)}{d\sigma_y}\right|_{\sigma_y=0}\right) = 2a^2c_{py}\left(1 - \frac{C_y'}{C_c}\right) \end{aligned} \tag{4.68}$$

Hence, the cornering stiffness including the flexible carcass is given by

$$C_y' = \frac{C_c 2a^2c_{py}}{C_c + 2a^2c_{py}} \tag{4.69}$$

Further, the rubber will be assumed to behave isotropically, $c_{py} = c_{px}$, which is a realistic assumption. In Section 4.1 the carcass deformation was included in the lateral rubber stiffness and in that case $c_{py} \neq c_{px}$.

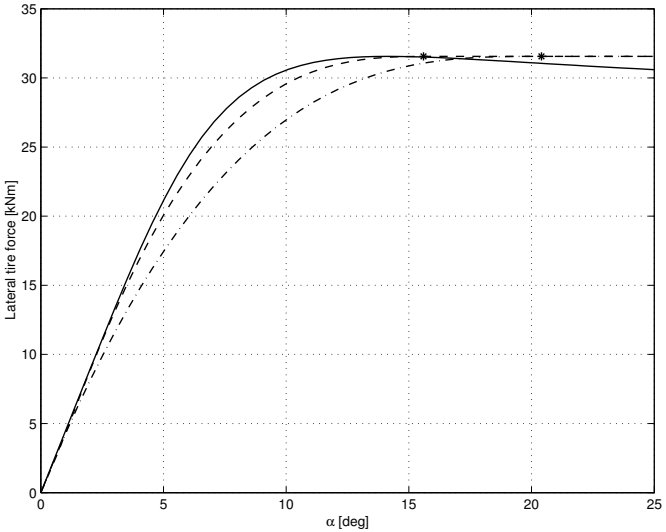

Figure 4.14 Comparison of the brush-model with (dashed) and without (dashed dotted) compensation for a flexible carcass. Asterisks denotes points for total sliding $\alpha^{\circ\prime}$ and α°. Solid line is a Magic-Formula parametrisation of empirical data further presented in [Gäfvert and Svendenius, 2003].

The divergence between the longitudinal and lateral stiffnesses may now be explained by the carcass stiffness, which can be calculated from (4.69) as

$$C_c = \frac{C_x C_y'}{C_x - C_y'} \tag{4.70}$$

where $2a^2 c_{px} = C_x$ according to (4.31). Using (4.70) then the limit-slip adjusted for carcass deformation of (4.67), $\sigma_y^{\circ\prime}$, can be written as

$$\sigma_y^{\circ\prime} = F_z \mu_y \left(\frac{2}{C_x} + \frac{1}{C_y'} \right) \tag{4.71}$$

Discussion Introducing flexibility in the carcass as described above improves the accuracy of the brush model in the lateral direction significantly, as can be seen in Figure 4.14. The approach can be used even for combined slip. The reliability of the brush model is still better in the longitudinal direction, but assuming more realistic lateral deflections will complicate the expressions considerably. The major aim of this section is

the derivation of an enhanced prediction of the slip corresponding to the lateral peak-force value in (4.71).

Effects on the self-aligning torque

In Section 4.1 a second-order effect of combined slip on the self-aligning torque, due to the bristle deformation, was derived in (4.36). Probably this effect is small compared to the torque generated by the displacement of the points of action for the tire forces due to the carcass deformation. This torque can be described as

$$M_{cz}''(\sigma_x, \sigma_y, \gamma) = F_x(\sigma_x, \sigma_y, \gamma) F_y(\sigma_x, \sigma_y, \gamma) \left(\frac{1}{C_{cx}} - \frac{1}{C_{cy}} \right) \tag{4.72}$$

where C_{cx} and C_{cy} are the carcass-stiffness coefficients, which may be calculated from (4.82). The self-aligning torque contribution M_{cz}'' should be added to the result in Equation (4.40).

Tire dynamics

In a tire with rigid carcass the motion in tire-road interface may be directly described by the motion of the wheel rim. With a flexible carcass there is a dynamic relation between these motions. When deriving the relation a few entities have to be redefined, compare to Figure 2.1 and Section 2.4. The slip speed in the contact patch of a tire with rigid carcass is given by

$$v_{sx}' = v_x - \omega R_e; \qquad v_{sy}' = v_y \tag{4.73}$$

where the motion of the rim is described by the velocities v_x' and v_y', the wheel rotational velocity Ω, and the effective rolling radius R_e. To be able to distinguish between motions related to the carcass and the motions related to the rim, the latter entities are marked by an apostrophe. The corresponding slip velocities with a flexible carcass are

$$v_{sx} = v_{sx}' + \dot{\delta}_x; \qquad v_{sy} = v_{sy}' + \dot{\delta}_y \tag{4.74}$$

where δ_x and δ_y are the deformations of the carcass as illustrated in Figure 4.15. The slip velocities may be normalized to form the tire slips. In practical models they are best normalized with the longitudinal velocity v_x. The slips corresponding to tires with rigid (primed variables) and flexible carcasses can be written as

$$\begin{aligned} \lambda' &= \frac{v_{sx}'}{v_x}; & \lambda &= \lambda' + \frac{\dot{\delta}_x}{v_x} \\ \tan(\alpha') &= \frac{v_{sy}'}{v_x}; & \tan(\alpha) &= \tan(\alpha') + \frac{\dot{\delta}_y}{v_x} \end{aligned} \tag{4.75}$$

The tire forces that are generated in the contact patch, $F_x(\lambda,\alpha,\gamma)$ and $F_y(\lambda,\alpha,\gamma)$, are transmitted to the wheel rim by the flexible carcass. The contact patch forces depend on the motion in the friction interface, which may be described by the tire slips, and the camber angle γ. In this section (λ,α) are chosen to represent the slip instead of (σ_x,σ_y) as used previously. The reason is that (λ,α) is most commonly used when visualizing data and results and the conversion between the slips are often straight forward by using (2.6). Here, those slips are used to show the extra step that is necessary for the differentiation of $\tan(\alpha)$, see (4.79). Use of (σ_x,σ_y) simplifies the calculations in that λ, $\tan(\alpha)$ and v_x are replaced by σ_x, σ_y and v_c in (4.75).

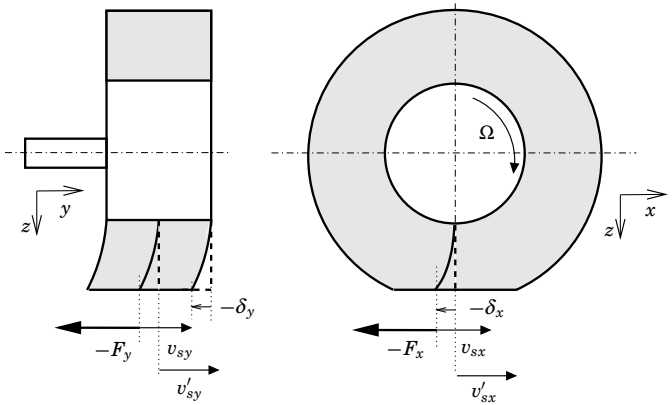

Figure 4.15 Carcass deformation of a tire. To the left: Lateral deformation. To the right: Longitudinal deformation for a braked wheel.

The tire carcass is assumed to behave like a linear spring and damper such that

$$F_x = C_{cx}\delta_x + D_x\dot{\delta}_x; \qquad F_y = C_{cy}\delta_y + D_y\dot{\delta}_y \tag{4.76}$$

where C_{cx} and C_{cy} are the carcass stiffnesses in respective directions. Using (4.75) together with the time derivative of (4.76) gives

$$\begin{aligned} \lambda - \lambda' &= \frac{\dot{F}_x}{C_{cx}v_x} - \frac{D_x\ddot{\delta}_x}{C_{cx}v_x} \\ \tan(\alpha) - \tan(\alpha') &= \frac{\dot{F}_y}{C_{cy}v_x} - \frac{D_y\ddot{\delta}_y}{C_{cy}v_x} \end{aligned} \tag{4.77}$$

Then, by expansion of the time derivative of the forces as

$$\begin{aligned} \dot{F}_x &= \frac{\partial F_x}{\partial\lambda}\dot{\lambda} + \frac{\partial F_x}{\partial\alpha}\dot{\alpha} + \frac{\partial F_x}{\partial\gamma}\dot{\gamma} \\ \dot{F}_y &= \frac{\partial F_y}{\partial\lambda}\dot{\lambda} + \frac{\partial F_y}{\partial\alpha}\dot{\alpha} + \frac{\partial F_y}{\partial\gamma}\dot{\gamma} \end{aligned} \tag{4.78}$$

and by differentiation of the right column of (4.75) under the assumption that the vehicle velocity varies slowly, the carcass dynamics are formulated as

$$\lambda - \lambda' = \frac{D_x}{C_{cx}}\dot{\lambda}' + \frac{1}{C_{cx}v_x}\left[\left(\frac{\partial F_x}{\partial\lambda} - D_x v_x\right)\dot{\lambda} + \frac{\partial F_x}{\partial\alpha}\dot{\alpha} + \frac{\partial F_x}{\partial\gamma}\dot{\gamma}\right] \tag{4.79a}$$

$$\begin{aligned} \tan(\alpha) - \tan(\alpha') = \frac{D_y}{C_{cy}}(1+\tan^2(\alpha'))\dot{\alpha}' + \frac{1}{C_{cy}v_x} \\ \cdot\left[\frac{\partial F_y}{\partial\lambda}\dot{\lambda} + \left(\frac{\partial F_y}{\partial\alpha} - D_y v_x(1+\tan^2(\alpha))\right)\dot{\alpha} + \frac{\partial F_y}{\partial\gamma}\dot{\gamma}\right] \end{aligned} \tag{4.79b}$$

which relates the contact patch slips to the wheel-rim slips. Note that the dynamics include cross-couplings.

Without damping the system becomes unstable in slip regions where the slip-force characteristics have positive slope. To avoid this, the damping coefficients should be chosen so that $D_x v_{x,\min} > \sup(\partial F_x/\partial\lambda)$ and $D_y v_{x,\min} > \sup(\partial F_y/\partial\alpha)$ for an arbitrary choice of slowest $v_{x,\min} > 0$. The system is then well posed for all $v_x \geq v_{x,\min}$. In [Pacejka, 2002] it is suggested to solve this problem by preventing the diagonal terms, $\partial F_x/\partial\lambda$, $\partial F_y/\partial\alpha$ from being positive by limitation. The introduction of damping may be a more physically motivated modification.

The carcass stiffnesses are properties that might not be available for the specific tire, but quite often the relaxation length, σ_a of a tire is measured. The relaxation length is usually defined for small slips [Pacejka, 2002] and relate the dynamics between the rim and the carcass as

$$\frac{\sigma_{ax}}{v_x}\dot{\lambda} + \lambda = \lambda'; \quad \frac{\sigma_{ay}}{v_x}\dot{\alpha} + \alpha = \alpha' \tag{4.80}$$

Note that v_x is time varying, and that (4.80) therefore is not a linear time-invariant system. Instead, the differential equations are linear space-invariant, since the independent time variable t can be exchanged for the space variable s (rolling distance) as $\dot{\lambda} = d\lambda/ds \cdot ds/dt$ and $ds/dt = v_x$,

and correspondingly for the lateral slip. In the case of small pure slip, zero camber, and neglecting the damping effects (4.79) might be simplified to

$$\lambda - \lambda' = \frac{1}{C_{cx} v_x} \frac{\partial F_x}{\partial \lambda} \dot{\lambda}; \quad \alpha - \alpha' = \frac{1}{C_{cy} v_x} \frac{\partial F_y}{\partial \alpha} \dot{\alpha} \tag{4.81}$$

It is then clear that the relaxation lengths are related to the stiffnesses as

$$\sigma_{ax} = \frac{C_x}{C_{cx}}; \qquad \sigma_{ay} = \frac{C_y}{C_{cy}} \tag{4.82}$$

4.4 Summary

In this chapter the well-known brush model has been presented in detail. The brush model in its ordinary form renders simplistic expressions for the tire-force and slip relations. There are, however, many shortcomings, which can be overcome by more extensive modeling. The trade-off problem between simplicity and accuracy is obvious and it is important to be aware about the demands of the application when adopting a model for a particular purpose. Each extra feature increases the complexity considerably. An example shown here is the introduction of camber, which still is possible with reasonable complexity.

In the presented form, the brush model gives a good description of the longitudinal tire characteristic at low slip up to the peak force. If good accuracy for higher slip is necessary the velocity dependence has to be included in friction coefficient, which is discussed in Section 5.2 and more generally in e. g. [Svendenius and Wittenmark, 2003; Pacejka, 1988]. An extensive evaluation of the accuracy of the longitudinal properties of the brush model can be found in Section 7.2. In the lateral direction also the behavior of the carcass effects the tire characteristics. An accurate modeling of the carcass require more sophisticated software, such as Finite-Element tools, see Section 3.4.

The most simple corrections available in the literature have been discussed here. A new touch is given by the practical way of calculating the lateral slip corresponding to the peak force in Equation (4.71). Most of the contents in this section are gathered from earlier presented material by other authors.

5

A Dynamic Semi-Empirical Tire-Model for Combined Slips and Camber

This chapter presents a method to derive the tire forces during combined slip and camber, given the empirical tire-force models at pure slip. The method has previously been presented in a number of journal articles [Gäfvert and Svendenius, 2005; Svendenius and Gäfvert, 2005; Svendenius and Gäfvert, 2006] and conference proceedings [Svendenius and Gäfvert, 2004a; Svendenius and Gäfvert, 2004b; Gäfvert *et al.*, 2006]. A detailed presentation of the theory behind the model can be found in [Gäfvert and Svendenius, 2003], while the first publication was in [Gäfvert, 2003].

The steady-state part of the model, described in Sections 5.1–5.3, is based on the observation that the pure-slip characteristics contains all necessary information to reproduce combined-slip behavior with reasonable accuracy. The separation of the empirical pure-slip forces into components of adhesion and sliding and the different treatment of respective contribution are fundamental parts of the method. The model is "semi-empirical", since the pure-slip models may be entirely empirical, while the method to construct the combined-slip characteristics strictly follows from theory on brush-model mechanics, explained in Section 4.1. This distinguishes the presented model from similar previous methods that are purely empirical, for example [Bakker *et al.*, 1989; Schuring *et al.*, 1996; Lugner and Mittermayr, 1991; Sharp, 2004]. Due to the physical assumptions adopted, it is possible to include velocity dependency in the model, even if this is not explicitly present in the pure-slip models.

A validation and a presentation of the results of the model are given in Section 5.4 using measurement data from a Jeep Cherokee. The Magic Formula is used to approximate the pure-slip data. An implementation

and a simulation of the dynamic model derived in Section 4.3 are described, here. The dynamics behavior is explained by the deflection of the tire carcass, that causes differences between the forces and movements of the rim and the forces and movements in the contact patch. This is of practical significance in, for example, systems for control of the longitudinal tire slip where motion sensors are, in general, attached to the wheel rim and the force are generated by the motions in the contact patch.

5.1 Introduction

Semi-empirical methods are often used to derive the tire force at combined slip situations, since pure-condition tire-forces may be described well by rather compact and simple empirical models. Pure-slip tire data from test-bench experiments are also often available for calibration. The situation for mixed conditions is somewhat different. The transition from one to two dimensions makes it more difficult to apply functional approximations.

Empirical models tend to be either rough approximations or quite complex, difficult to understand, and rely on parameters that need to be calibrated with mixed-condition experimental data. This is a drawback since such data are expensive and time consuming to collect and therefore rarely available for a specific tire. Semi-empirical models for combined-slip uses the information from the pure-slip models to generate the tire forces when the vehicle brakes and turns simultaneously. Based on the mechanics of the tire and the available empirical data, a number of criteria for combined models may be stated (in the spirit of [Brach and Brach, 2000]):

1. The combined force $\bar{F}(\lambda, \alpha)$ should preferably be constructed from pure slip models $F_{0x}(\lambda)$ and $F_{0y}(\alpha)$, with few additional parameters.
2. The computations involved in the model must be numerically feasible and efficient.
3. The formulas should preferably be physically motivated.
4. The combined force $\bar{F}(\lambda, \alpha)$ should reduce to $F_{0x}(\lambda)$ and $F_{0y}(\alpha)$ at pure braking or cornering:

$$\bar{F}(\lambda, 0) = [\, F_{0x}(\lambda), 0\,]$$
$$\bar{F}(0, \alpha) = [\, 0, F_{0y}(\alpha)\,]$$

5. Sliding must occur simultaneously in longitudinal and lateral directions.

6. The resulting force magnitudes should stay within the friction constraints.
7. The combined force should be $\bar{F} = -F_z \mu \bar{v}_s / v_s$ at full sliding for tires with isotropic friction characteristics, i.e. equal friction properties in all directions.

These criteria are used when developing the semi-empirical tire-model for combined slip presented in the following.

Main approach

The general idea of this method to derive the forces at a combined slip $(\sigma_x, \sigma_y, \gamma)$ is to scale the forces given by the empirical pure-slip model at certain pure slips $\sigma_{0x}(\sigma_x, \sigma_y, \gamma)$ and $\sigma_{0y}(\sigma_x, \sigma_y, \gamma)$. The pure slips can be chosen in various ways, but their relations to σ_x, σ_y and γ have to be well motivated and different proposals are discussed below. For convenience, the arguments $(\sigma_x, \sigma_y, \gamma)$ for σ_{0x} and σ_{0y} are left out in the following. The scale factors depend on the combined longitudinal and lateral slip, the camber angle, and the relation between the used pure slip and the cambered combined-slip. The arguments $(\sigma_x, \sigma_y, \gamma)$ are also left out for the scale factors, G_{ij}, in the following. Since the generation of forces from the adhesive and the sliding regions are built on different physical phenomena they are treated separately. The following equation shows the form

$$\hat{F}_x(\sigma_x, \sigma_y, \gamma) = G_{ax} \hat{F}_{0x}(\sigma_{0xa}) + G_{sx} \hat{F}_{0x}(\sigma_{0xs}) \tag{5.1}$$
$$\hat{F}_y(\sigma_x, \sigma_y, \gamma) = G_{ay} \hat{F}_{0y}(\sigma_{0ya}) + G_{sy} \hat{F}_{0y}(\sigma_{0ys}) + G_{\mathrm{cam}y} \hat{F}_{0\mathrm{cam}}(\gamma) \tag{5.2}$$

where $\hat{F}_{0x}$ and $\hat{F}_{0y}$ are the empirical pure slip models and $\hat{F}_{0\mathrm{cam}}$ is the empirical pure cambering model. The pure-slip tire behavior can be given in any form, either as an empirical model or as tabular data, as long as the vertical and horizontal shift are zero, i.e. that the curves cross the origin. If not known the pure camber model may be as simple as the cambering stiffness, $\hat{C}_\gamma$, times the camber angle as assumed in (4.54). If no information about the camber properties is available, then C_γ can be calculated from the cornering stiffness using (4.53). The half patch-length a is either assumed or derived from (4.42) using the aligning stiffness. The tire radius R and the contact patch length is used to calculate k by Equation (4.45).

Analogously, the combined self-aligning torque can be derived as

$$\hat{M}_z(\sigma_x, \sigma_y, \gamma) = G_{fz} \hat{F}_{0y}(\sigma_{0z}) + G_{mz} \hat{M}_{0z}(\sigma_{0z}) + G_{\mathrm{cam}z} \hat{F}_{0\mathrm{cam}}(\gamma) \tag{5.3}$$

The scale factors, G_{ij}, are derived from the analytical expressions of the

brush model, as

$$F_{ax}(\sigma_x,\sigma_y,\gamma)=\frac{F_{ax}(\sigma_x,\sigma_y,\gamma)}{F_{0x}(\sigma_{0xa})}F_{0x}(\sigma_{0xa})=G_{ax}F_{0x}(\sigma_{0xa})\approx G_{ax}\hat{F}_{0x}(\sigma_{0xa}) \tag{5.4}$$

$$\begin{aligned}F_{ay}(\sigma_x,\sigma_y,\gamma)&=\frac{F_{ay}(\sigma_x,\sigma_y,\gamma)}{F_{0y}(\sigma_{0ya})}F_{0y}(\sigma_{0ya})+\frac{F_{ay,cam}(\sigma_x,\sigma_y,\gamma)}{F_{0\mathrm{cam}}(\gamma)}F_{0\mathrm{cam}}(\gamma)\\&=G_{ay}F_{0y}(\sigma_{0ya})+G_{\mathrm{cam}y}F_{0\mathrm{cam}}(\gamma)\approx G_{ay}\hat{F}_{0y}(\sigma_{0ya})+G_{\mathrm{cam}y}\hat{F}_{0\mathrm{cam}}(\gamma)\end{aligned} \tag{5.5}$$

$$F_{sx}(\sigma_x,\sigma_y,\gamma)=\frac{F_{sx}(\sigma_x,\sigma_y,\gamma)}{F_{0x}(\sigma_{0xs})}F_{0x}(\sigma_{0xs})=G_{sx}F_{0x}(\sigma_{0xs})\approx G_{sx}\hat{F}_{0x}(\sigma_{0xs}) \tag{5.6}$$

and

$$F_{sy}(\sigma_x,\sigma_y,\gamma)=\frac{F_{sy}(\sigma_x,\sigma_y,\gamma)}{F_{0y}(\sigma_{0ys}}F_{0y}(\sigma_{0ys})=G_{sy}F_{0y}(\sigma_{0ys})\approx G_{sy}\hat{F}_{0y}(\sigma_{0ys}) \tag{5.7}$$

For the self-aligning torque the structure is slightly different, and the reader is referred to the computations in Appendix B.

5.2 Scale Factors

The structure for deriving the scale factors require the assumption of a model that describes the relation between the combined-slip and the pure-slip forces. It also gives a freedom in the choice of the relation between the pure slips $(\sigma_{0x},\sigma_{0y})$ and the combined slip situation $(\sigma_x,\sigma_y,\gamma)$. This section proposes the choices for the pure slip relations and derives the scale factor using the basic brush-model assumptions proposed in Section 4.1.

Adhesive region

The bristle deformations are the source of the adhesion forces. Therefore, for adhesion forces it makes sense to regard pure slips that result in the same deformation as the combined slip. The deformation state depends on the slip, $\bar{\sigma}$. The pure slip is therefore constructed to maintain $\bar{\sigma}$ constant. Hence

$$\sigma_{0xa}=\sigma_x;\quad \sigma_{0ya}=\sigma_y \tag{5.8}$$

The scale factors G_{ax} and G_{ay} can now be calculated as

$$G_{ax}=\frac{3\left(1-\psi(\sigma_x,\sigma_y,\gamma)\right)^2}{\Upsilon(\sigma_x,0,0)};\quad G_{ay}=\frac{3\left(1-\psi(\sigma_x,\sigma_y,\gamma)\right)^2}{\Upsilon(0,\sigma_y,0)} \tag{5.9}$$

when $\psi<1$, otherwise $G_{ax}=G_{ay}=0$, with

$$\Upsilon(x,y,z)\triangleq\psi^2(x,y,z)-3\psi(x,y,z)+3 \tag{5.10}$$

Here Equations (5.4) and (5.5) are used together with (4.14), (4.29), and (4.30). Details on the computation of the scale factors can be found in Appendix B. The scale factor of the camber force can be calculated from (5.5), (4.52), and (4.54), as

$$G_{\mathrm{cam}y}=2\psi^3(\sigma_x,\sigma_y,\gamma)-3\psi^2(\sigma_x,\sigma_y,\gamma)+1 \tag{5.11}$$

when $\psi<1$, otherwise $G_{\mathrm{cam}y}=0$.

Sliding region

In the literature, slip-velocity is mentioned as a significant factor that influences the friction coefficient for a specific tire on a certain road foundation [Wong, 2001]. Therefore, it is reasonable to define the pure slip used for the sliding forces such that the slip velocity is invariant. The sliding-velocity invariant pure-slips are defined as

$$\begin{aligned}\sigma_{0x}^{\mathrm{vel}}&=\frac{v\sqrt{\sigma_x^2+\sigma_y^2}\,\mathrm{sgn}(\sigma_x)}{v_0\sqrt{(1+\sigma_x)^2+\sigma_y^2}-v\sqrt{\sigma_x^2+\sigma_y^2}\,\mathrm{sgn}\,(\sigma_x)}\\\sigma_{0y}^{\mathrm{vel}}&=\frac{v\sqrt{\sigma_x^2+\sigma_y^2}\,\mathrm{sgn}(\sigma_y)}{\sqrt{v_0^2\left((1+\sigma_x)^2+\sigma_y^2\right)-v^2(\sigma_x^2+\sigma_y^2)}}\end{aligned} \tag{5.12}$$

Hence $(\sigma_{0x}^{\mathrm{vel}},0,0)$ and $(0,\sigma_{0y}^{\mathrm{vel}},0)$ at the wheel-travel velocity v_0 result in the same slip velocity, v_s, as the combined slip $(\sigma_x,\sigma_y,\gamma)$ at the wheel-travel velocity v. Note that v is the actual wheel travel velocity and v_0 the velocity at which the pure slip model is valid. For details on the computation the reader is referred to Appendix B. The sliding pure-slip are chosen as, $\sigma_{0xs}=\sigma_{0x}^{\mathrm{vel}}$, and, $\sigma_{0ys}=\sigma_{0y}^{\mathrm{vel}}$, and the scaling factors G_{sx} and G_{sy} can be computed from (4.14), (4.15), (4.29) and (4.26), using $\beta_{\mathrm{f}}=\beta'$ as

$$G_{sx}=|\cos(\beta')|\cdot\Gamma_x;\qquad G_{sy}=|\sin(\beta')|\cdot\Gamma_y \tag{5.13}$$

with

$$\Gamma_x\triangleq\begin{cases}\left|\left(v_0\sqrt{(1+\sigma_x)^2+\sigma_y^2}-v\sqrt{\sigma_x^2+\sigma_y^2}\,\mathrm{sgn}\,(\sigma_x)\right)\Lambda\sigma_x^\circ\right| & \\ \quad\cdot\dfrac{\psi(\sigma_x,\sigma_y,\gamma)(3-2\psi(\sigma_x,\sigma_y,\gamma))}{v\Upsilon(\sigma_{0x}^{\mathrm{vel}},0,0)} & \text{if } \psi(\sigma_{0x}^{\mathrm{vel}},0,0)<1\\ \psi^2(\sigma_x,\sigma_y,\gamma)(3-2\psi(\sigma_x,\sigma_y,\gamma)) & \text{if } \psi(\sigma_{0x}^{\mathrm{vel}},0,0)\geq 1\end{cases} \tag{5.14a}$$

and

$$\Gamma_y \triangleq \begin{cases} \left| \left(v_0^2\left((1+\sigma_x)^2+\sigma_y^2\right) - v^2(\sigma_x^2+\sigma_y^2)\right)^{\frac{1}{2}} \Lambda\sigma_y^\circ \right| \\ \quad \cdot \dfrac{\psi(\sigma_x,\sigma_y,\gamma)(3-2\psi(\sigma_x,\sigma_y,\gamma))}{v\Upsilon(0,\sigma_{0y}^{\mathrm{vel}},0)} & \text{if } \psi(0,\sigma_{0y}^{\mathrm{vel}},0) < 1 \\ \psi^2(\sigma_x,\sigma_y,\gamma)(3-2\psi(\sigma_x,\sigma_y,\gamma)) & \text{if } \psi(0,\sigma_{0y}^{\mathrm{vel}},0) \geq 1 \end{cases} \tag{5.14b}$$

and

$$\Lambda \triangleq \frac{\gamma^{\circ 2}}{\gamma^{\circ 2}-\gamma^2}\left(\frac{\sin(\beta)}{\sigma_y^\circ}\frac{\gamma}{\gamma^\circ} + \sqrt{\left(\frac{\cos(\beta)}{\sigma_x^\circ}\right)^2\left(1-\left(\frac{\gamma}{\gamma^\circ}\right)^2\right)+\left(\frac{\sin(\beta)}{\sigma_y^\circ}\right)^2}\right) \tag{5.15}$$

if $\psi(\sigma_x,\sigma_y,\gamma) < 1$, otherwise

$$\Gamma_x \triangleq \begin{cases} \psi^{-1}(\sigma_{0x}^{\mathrm{vel}},0,0)\Upsilon^{-1}(\sigma_{0x}^{\mathrm{vel}},0,0) & \text{if } \psi(\sigma_{0x}^{\mathrm{vel}},0,0) < 1 \\ 1 & \text{if } \psi(\sigma_{0x}^{\mathrm{vel}},0,0) \geq 1 \end{cases} \tag{5.16a}$$

and

$$\Gamma_y \triangleq \begin{cases} \psi^{-1}(0,\sigma_{0y}^{\mathrm{vel}},0)\Upsilon^{-1}(0,\sigma_{0y}^{\mathrm{vel}},0) & \text{if } \psi(0,\sigma_{0y}^{\mathrm{vel}},0) < 1 \\ 1 & \text{if } \psi(0,\sigma_{0y}^{\mathrm{vel}},0) \geq 1 \end{cases} \tag{5.16b}$$

The friction-constraint angle β' can be derived from

$$\tan(\beta') = \frac{\sigma_y\Gamma_x\hat{F}_{0x}(\sigma_{0x}^{\mathrm{vel}})}{\sigma_x\Gamma_y\hat{F}_{0y}(\sigma_{0y}^{\mathrm{vel}})} \tag{5.17}$$

see (4.20).

Self-aligning torque

For simplicity, another pure-slip definition is used for the self-aligning torque. The pure slips $(\sigma_{0x}^{\mathrm{reg}},0,0)$ and $(0,\sigma_{0y}^{\mathrm{reg}},0)$, with

$$\sigma_{0x}^{\mathrm{reg}} = \sigma_x^\circ\psi(\sigma_x,\sigma_y,\gamma)\,\mathrm{sgn}(\sigma_x)\,; \qquad \sigma_{0y}^{\mathrm{reg}} = \sigma_y^\circ\psi(\sigma_x,\sigma_y,\gamma)\,\mathrm{sgn}(\sigma_y) \tag{5.18}$$

result in adhesion and sliding regions of the same size as the combined slip $(\sigma_x,\sigma_y,\gamma)$. It is therefore obvious to choose $\sigma_{0z} = \sigma_{0y}^{\mathrm{reg}}$ and the self-aligning torque is derived as

$$M_z(\sigma_x,\sigma_y,\gamma) = G_{fz}F_{0y}(\sigma_y^{\mathrm{reg}}) + G_{mz}M_{0z}(\sigma_y^{\mathrm{reg}}) + G_{\mathrm{cam}z}F_{0\mathrm{cam}}(\gamma) \tag{5.19}$$

where

$$G_{mz} = |\sin(\beta')| \tag{5.20}$$

$$G_{fz} = a\frac{(4\psi-1)(1-\psi)^2}{\Upsilon}\left(\frac{|\sin(\beta)|}{\sigma_y^\circ\Lambda_z} - |\sin(\beta')|\right) \tag{5.21}$$

and

$$G_{\mathrm{cam}z} = 3a\psi^2(\sigma_x,\sigma_y,\gamma)\left(1-\psi(\sigma_x,\sigma_y,\gamma)\right)^2 \tag{5.22}$$

with

$$\Lambda_z \triangleq \frac{\gamma^{\circ 2}}{\gamma^{\circ 2}-\gamma^2} \cdot \left(\frac{\sin(\beta)}{\sigma_y^\circ}\frac{\gamma}{\gamma^\circ} + \sqrt{\left(\frac{\cos(\beta)}{\sigma_x^\circ}\right)^2+\left(\frac{\sin(\beta)}{\sigma_y^\circ}\right)^2-\left(\frac{\cos(\beta)\gamma}{\sigma_x^\circ\gamma^\circ}\right)^2}\,\mathrm{sgn}(\beta\sigma_y)\right) \tag{5.23}$$

Note that the brush model states that the contact patch length can be derived by the relation between the cornering stiffness and the self-aligning stiffness, see (4.42), as $a = 3C_z/C_y$. When using the region-invariant slips the friction angle is computed from

$$\tan(\beta') = \frac{\sigma_y}{\sigma_x}\frac{\hat{F}_{0x}(\sigma_x^{\mathrm{reg}})}{\hat{F}_{0y}(\sigma_y^{\mathrm{reg}})} \tag{5.24}$$

5.3 Parameters

Four parameters are needed in the steady-state part of the model and two if the transient properties are to be included. The parameters

- σ_x°, longitudinal limit slip
- σ_y°, lateral limit slip
- γ°, adhesive camber limit
- v_0, velocity for the pure-slip model
- C_{cx}, longitudinal carcass stiffness
- C_{cy}, lateral carcass stiffness

all have clear physical interpretations. The parameters σ_x° and σ_y°, describe the pure slips where transition from partial to full sliding occur. They are needed to compute the normalized slip, $\psi(\sigma_x, \sigma_y, \gamma)$. A common assumption is that these transitions occur when the tire forces obtain their maximum. Some road foundations, such as gravel and snow might not provide a clear maximum point. In any case, the parameters may simply be set to the slip values corresponding to the maximum of the tire forces, F_{0x}^* and F_{0y}^*. From the brush model it can be shown that

$$\sigma_x^\circ \approx \frac{3\hat{F}_{0x}^*}{\hat{C}_x}; \qquad \sigma_y^\circ \approx \frac{2\hat{F}_{0y}^*}{\hat{C}_x} + \frac{\hat{F}_{0y}^*}{\hat{C}_y} \tag{5.25}$$

which is a result from (4.11) and (4.71).

The parameter v_0 denotes the wheel-travel velocity at which the empirical pure-slip model is valid. The actual wheel-travel velocity v is assumed to be a model input. If v_0 is not known then $v/v_0 = 1$ may be used, which will neglect any velocity dependence. This is the common assumption in most other models.

The camber parameter, γ°, is outside the cambering range that is normally measured on truck and car wheels. Therefore, it is not possible to obtain it directly from measurement data. Instead it can be used that (4.53) is well approximated by

$$\gamma^\circ \approx \hat{F}_{0y}^*/\hat{C}_\gamma \tag{5.26}$$

The camber stiffness can either be given from the empirical camber model or be computed from tire parameters according to (4.53) using (4.45) and (4.42).

The carcass stiffnesses can be derived from (4.82) as

$$C_{cx} = \frac{\hat{C}_x}{\sigma_{ax}}; \qquad C_{cy} = \frac{\hat{C}_y}{\sigma_{ay}} \tag{5.27}$$

if the relaxation lengths are known. This is further discussed in the last part of Subsection 5.4

5.4 Validation and Results of the Semi-Empirical Model

Empirical data, provided by NHTSA, US, for P225/75R15 Goodyear Wrangler RT/S, OWL, all terrain steel belted radials [Salaani *et al.*, 1999], are used for validation. The reference speed used was 48 km/h and inflation pressure 2.4 bar. The data consist of pure-slip forces and aligning moments in the slip ranges $\lambda = [-50, 50]\%$ and $\alpha = [-15, 15]$ deg. Forces

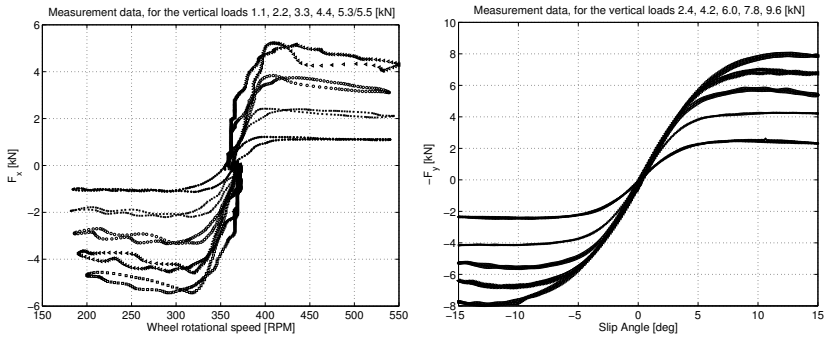

Figure 5.1 Available measurement data. Left: Longitudinal force for different wheel rotational speeds; Right: Lateral force for sweeps of α.

at combined slip at $\alpha = [\pm 2, \pm 4]$ deg for sweeps of λ and forces at some camber angles were also included. The different vertical loads for the measurements of the pure longitudinal behavior are 1.1, 2.2, 3.3, 4.4, 5.3 or 5.5 kN. It is unclear from the data whether the highest load for sweeps of λ and the only load for the combined slip is 5.3 kN or 5.5 kN. For the pure lateral and cambering behavior 2.4, 4.2, 6.0, 7.8, 9.6 kN. The available steady-state measurement data are shown in Figures 5.1, 5.2 and 5.3. Measurements of the transient properties of the tire are available as sinusoidal excitations of the slip angle at nine different frequencies. The data are shown in Figure 5.17 and further discussed in Section 5.4.

Validation of tire-forces at combined slip

The measurements of the pure lateral properties were performed at different conditions than the longitudinal and combined properties. The vertical loads do not correspond between the different setups. The longitudinal pure slip model and the combined validation data are taken at highest available load and the lateral pure slip model at 6.0 kN. A linear correction is applied to adjust for the different loads. The pure slip models are Magic Formula parametrisation of the raw data, but for the torque model interpolation of the tabular data was used. The empirical pure slip models are shown in Figure 5.4. In Figure 5.5 the forces and torque from the model are compared with the measured values for sweeps of λ. In Figure 5.6 the pure slip measurement for sweep of α is shown together with the pure slip Magic Formula parametrisation and the computed characteristics for combined slip. Note that (λ, α) is used to signify the slip instead of (σ_x, σ_y), since it is the most common slip definition when dealing with

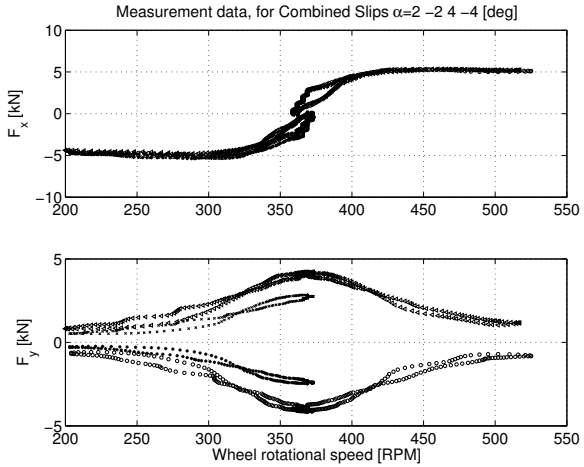

Figure 5.2 Available measurement data for combined slip. Longitudinal and lateral force at F_z=5.3 or 5.5 kN, see comment in text.

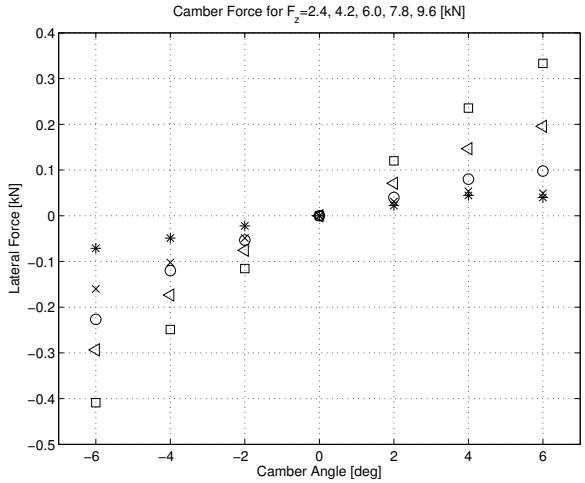

Figure 5.3 Available camber data. Lateral force as a function of the camber angle (γ) for different vertical loads.

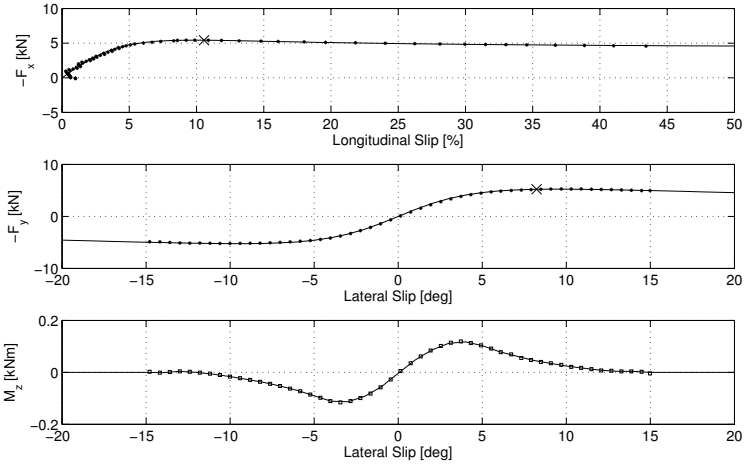

Figure 5.4 Pure-slip measurement data (dots) with Magic Formula parametrisation (solid lines) for the forces and interpolation of raw data for the aligning moment. The limit slips calculated from (5.25) are marked by crosses in the two upper plots.

measurement data and may look more familiar to the reader. Conversions between the two slips can be found in Appendix B. The overall behavior of the model is very similar to the real measurements. Particularly good agreement is shown at small and large slips. The largest deviations can be found at slips around the force peak value. Since the tire behavior is sensitive to many factors it is very important that the pure slip empirical models are generated at the same conditions as the combined slip measurements. The change of test equipment and the different vertical loads between the collection of longitudinal and lateral data sets affects the reliability of the data and the validation.

Comparison with other models In Figure 5.7, comparisons are shown between the proposed model, the BPL model [Bakker *et al.*, 1989], and the COMBINATOR model [Schuring *et al.*, 1996]. It is clear that the proposed model performs better than the COMBINATOR model at small slip-angles. The COMBINATOR model may be written as

$$F_x = F\cos(\beta)\,; \qquad F_y = F\sin(\beta) \tag{5.28}$$

where

$$F = F_{0x}(s)\cos^2(\beta) + F_{0y}(s)\sin^2(\beta) \tag{5.29}$$

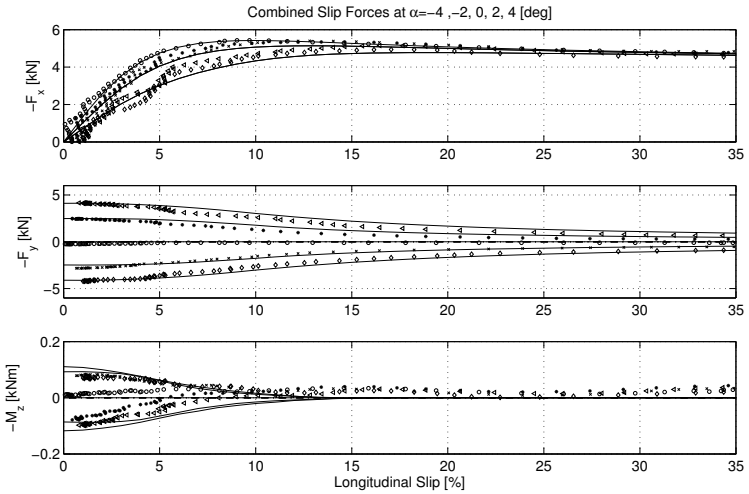

Figure 5.5 Combined measurement data compared to the presented model (solid line) for sweeps of λ at different slip angles.

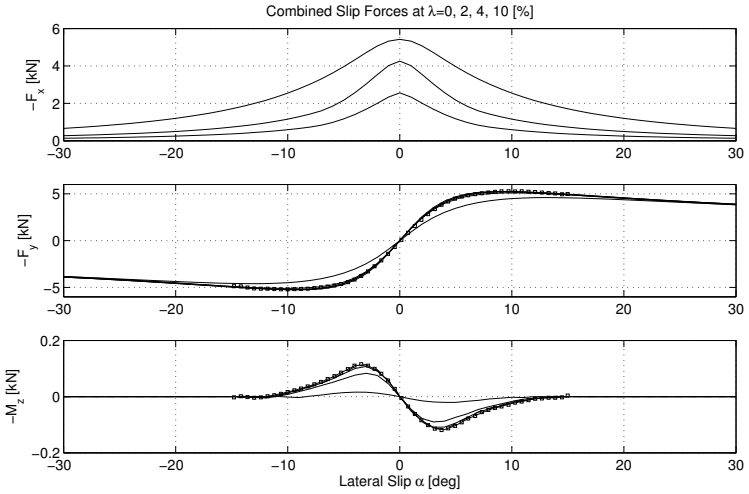

Figure 5.6 Lateral behavior for combined slip of the model. The measured data at pure slip is also showed.

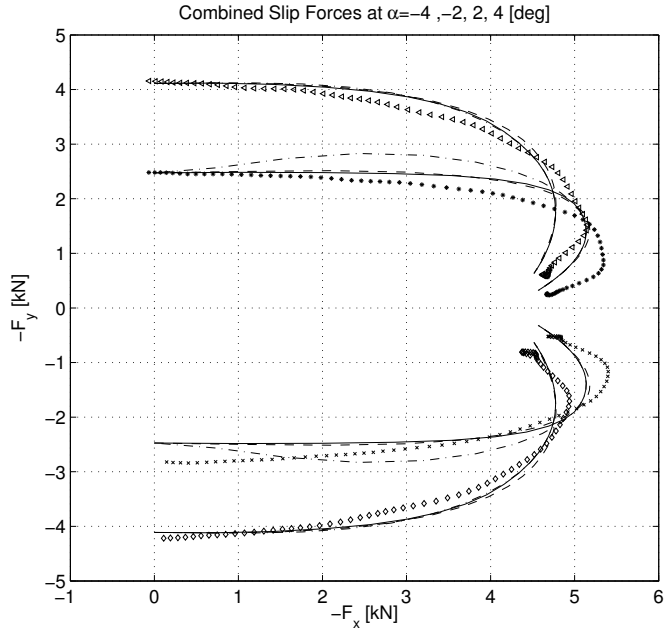

Figure 5.7 Combined-slip forces with the proposed model (solid line) compared to the COMBINATOR model (dashed-dotted line) and the BPL model (dashed-line), for fixed slip angles α and varying λ ranging from 0 to 35%. for comparison.

The resulting force is always collinear with the slip vector, which is an assumption with weak physical motivation. In the COMBINATOR model the lateral force initially increases, as a longitudinal slip is applied. This is a result of the assumption of a collinear combined-slip tire-force in the full slip range, in combination with the use of the combined-slip magnitude in the empirical pure-slip models.

The proposed method performs similar to the BPL model. In fact the essence of the two methods are much like each other, even though the structures may appear different. The BPL model, see (3.2), uses convex combination of angles corresponding to adhesion and sliding, to determine the orientation of the resulting force. In the proposed method the magnitude of respective force component also relies on convex combinations of adhesion and sliding force contributions. The pure-slip used for the adhesion force, most prominent at low slip, behaves differently than the region-invariant slips defined in (5.18) that are used in the BPL-method. However, the sliding-velocity invariant pure-slip $(\sigma_{0x}^{\text{vel}}, \sigma_{0y}^{\text{vel}})$ de-

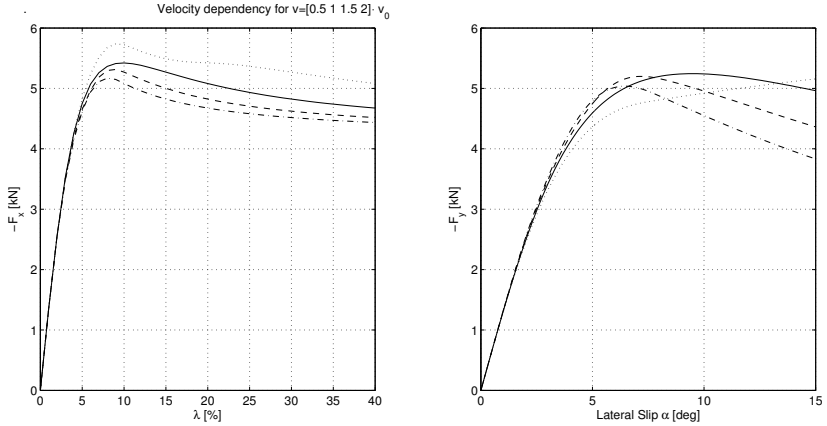

Figure 5.8 Velocity dependence at pure slips using the models shown in Figure 5.4. Velocities: $v = 0.5v_0$, (dotted) v_0 (solid), $1.5v_0$ (dashed), $2v_0$ (dash-dotted).

fined in (5.12) used for the sliding contribution behaves more similar to the region-invariant slips, when $v = v_0$. The resultant magnitude for the BPL model at full sliding is

$$F = F_{0x}\cos^2(\beta^\circ) + F_{0y}\sin^2(\beta^\circ) \tag{5.30}$$

Note that β° defined as $(\tan(\beta^\circ) = (\sigma_y\sigma_x^*)/(\sigma_x\sigma_y^*))$ depends on the tire stiffnesses and the static friction coefficient, which do not have any physical significance at full sliding. For the proposed model the corresponding magnitude is

$$F_{0x}F_{0y}/\sqrt{F_{0x}^2\sin^2(\beta) + F_{0y}^2\cos^2(\beta)} \tag{5.31}$$

Compare with (5.29) for the COMBINATOR model. The resulting force is collinear to the slip vector in all three methods at high slip.

Velocity dependence The dependence on wheel-travel velocity is illustrated in Figures 5.8 and 5.9, by varying v. The reference speed v_0 is approximately 48 km/h. The pure-slip Magic Formula model is calibrated with data from tire measurements at the wheel-travel velocity v_0. Tire forces are shown for velocities that are 0.5–2 times the wheel-travel velocity of the pure-slip model. The longitudinal direction behaves qualitatively well with what is reported in e.g. [Pacejka, 2002], while the behavior in the lateral direction is unexpected with an increase in tire force for higher velocities. The semi-empirical tire-model generates the

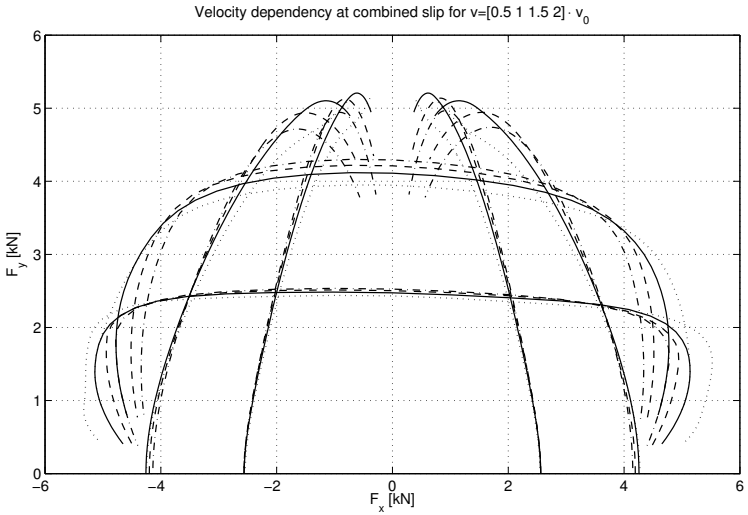

Figure 5.9 Velocity dependence at combined slips using the pure-slip models shown in Figure 5.4. Sweeps of λ for $\alpha = -2, -4$ [deg] and sweeps of α for $\lambda = \pm 2, \pm 4$ [%]. Velocities: $v = 0.5v_0$, (dotted) v_0 (solid), $1.5v_0$ (dashed), $2v_0$ (dash-dotted).

forces from the sliding area by extracting the friction coefficients in each direction for the actual slip velocity. The slip velocity at a combined slip λ, α, is $v_s = v\left((\lambda\cos(\alpha))^2 + \sin^2(\alpha)\right)^{1/2}$. The (α, λ)-definition is used here, since it is the common slip definition for calibration of Magic Formula, see Appendix B for conversion between slip definitions. Corresponding pure slips for the empirical pure-slip model are given by $v_s = \lambda_0^{\text{vel}}v_0$ and $v_s = \sin(\alpha_0^{\text{vel}})v_0$. Figure 5.10 shows the extracted friction coefficients, calculated from $\Gamma_{x,y}\hat{F}_{0x,y}(\sigma_{0x}^{\text{vel}})\ /F_{sz}(\sigma_x, \sigma_y, \gamma)$, see (5.13) and (4.27), as functions of the slip velocity, which explains the reason behind the strange result of the model. It clearly shows that the extracted lateral friction first increases with the speed up to a certain value and then decreases.

It is realistic to assume that the friction, ideally, should be identical in the both directions. In reality, test disturbances, uncertainties in measurements and modeling approximations shows something else. However, the choice of limit slip is very important for the friction extraction and the rule of thumb for the choice of α° seems not to be sufficiently good. A higher limit slip than proposed in (5.25) gives the lateral friction more similar appearance to the longitudinal direction. Note that this behavior may change from tire to tire and it is not possible to state general

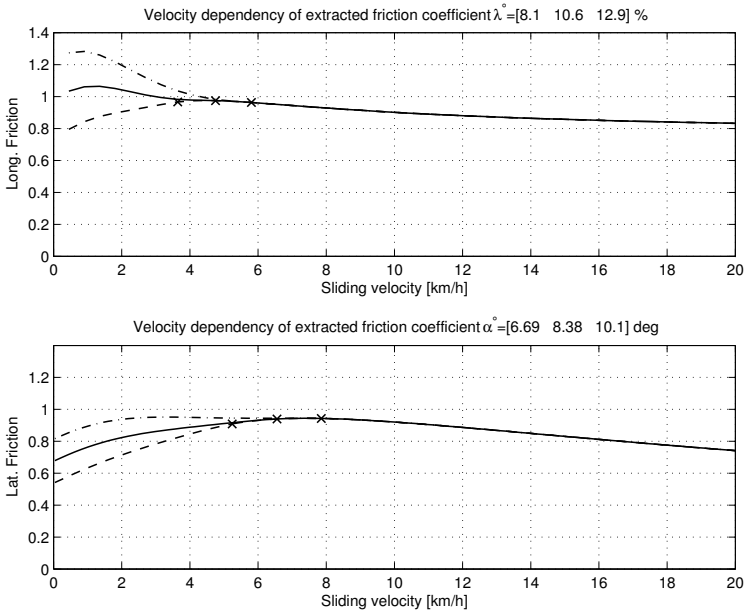

Figure 5.10 Calculated friction coefficient for different choices of limit slip. Respective limit slip, in increasing order, are denoted by dashed, solid and dash-dotted line.

recommendations for the choice of limit slip in this aspect.

If it is necessary to elaborate with the lateral limit slip to get proper velocity dependence it is also important to study the effect on the combined slip behavior. Figure 5.11 shows the parameter sensitivity of the force envelopes at combined slip for variation of α°. The figure shows that the resulting tire force gets larger for higher values on α°. A higher limit slip increases the proportion of the adhesion contribution for lower slip than this limit. The force limitation due to the friction constraints, therefore, starts to act later. This will give higher forces before the limit slip is reached.

The expressions for pure slips can be solved for $\lambda_0^{\text{vel}} < 100\%$ ($\sigma_{0x}^{\text{vel}} < 1$) and $\alpha_0^{\text{vel}} < 90$ deg ($\sigma_{0y}^{\text{vel}} < 1$), which is when $(v/v_0)^2 \left(\lambda^2 \cos^2(\alpha) + \sin^2(\alpha)\right) \leq 1$ is fulfilled, see (5.12) or (B.20). This restricts the interval of v, λ, and α. If λ_0^{vel} or α_0^{vel} are outside the valid range of the pure-slip model, then extrapolation is necessary. This is actually when the model tries to extract the friction properties from speeds not available in the empirical model. A straightforward method is to use the end points of the models. The Magic

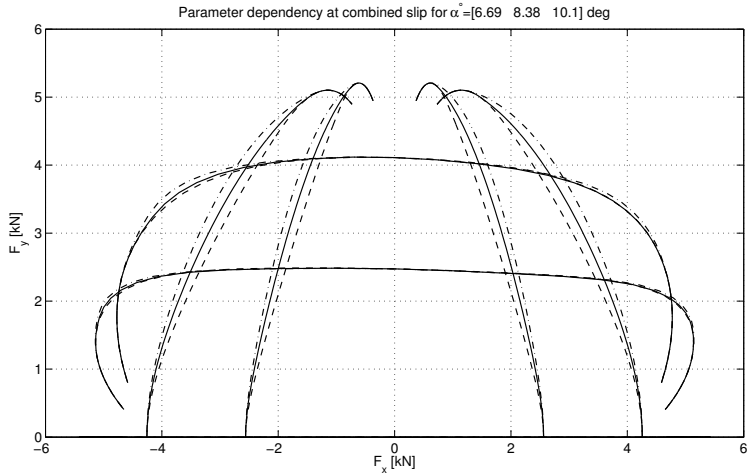

Figure 5.11 Illustration of the parameter sensitivity of the force envelopes at combined slip with sweeps of λ for α =-2, -4 [deg] and sweeps of α for $\lambda = \pm 2, \pm 4$. The different limit slip, in increasing order, are denoted by dashed, solid and dash-dotted lines, respectively.

Formula with default shape factors has decent extrapolation properties and may be used with slip ratios $\lambda_0^{\text{vel}} > 100\%$, but α_0^{vel} is limited to 90 deg. In general, extrapolation of empirical data must be carried out with great care.

At actual speeds, v, lower than v_0 the friction properties are extracted from lower slip at v_0 to the ensure that the sliding velocity is invariant (obvious from (5.12)). At low slip the sliding contributions are small and they have to be magnified to match the proportion of sliding friction at v. Normally neglectable uncertainties of the model are then also magnified which might cause strange and non-accurate results.

Utilizing braking data to generate driving data In the proposed model it is assumed that the given longitudinal pure-slip model, $\hat{F}_{0x}(\lambda)$, is valid both at braking ($\lambda > 0$) and driving ($\lambda < 0$). The Magic Formula is an odd function and therefore $\hat{F}_{0x}(\lambda) = -\hat{F}_{0x}(-\lambda)$. Generally, this is not in accordance with empirical observations. If the pure-slip model is assumed to be valid for braking, then the following procedure suggests how to modify the argument to the pure-slip model at driving, so that a more accurate force is obtained.

The brush model states that the adhesion force developed at braking with a slip $\sigma_x > 0$ will have the same size and the opposite sign, as the

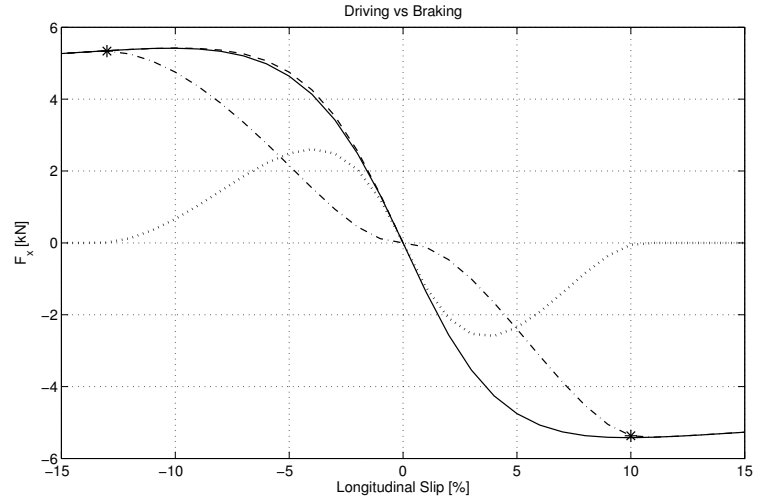

Figure 5.12 Illustration of the difference between driving and braking. Solid line is the proposed method to convert between braking and driving, with sliding contribution as the dashed dotted line and the adhesive part as the dotted line. Dashed line shows the Magic Formula tire-model, $F_{0x}(\lambda) = -F_{0x}(-\lambda)$.

force generated at driving with slip $-\sigma_x$:

$$F_{0ax}(\sigma_x) = -F_{0ax}(-\sigma_x) \tag{5.32}$$

With $\sigma_x = -\lambda_{\text{driving}}/(1-\lambda_{\text{driving}})$ and $\sigma_x = \lambda_{\text{braking}}/(1-\lambda_{\text{braking}})$ this means that

$$\lambda_{\text{braking}} = -\frac{\lambda_{\text{driving}}}{1-2\lambda_{\text{driving}}} \tag{5.33}$$

Hence, when computing adhesion forces using an empirical model for braking, the pure-slip forces

$$\begin{cases} -\hat{F}_{0x}\left(\frac{-\lambda}{1-2\lambda}\right) & \lambda < 0 \\ \hat{F}_{0x}(\lambda) & \lambda \geq 0 \end{cases} \tag{5.34}$$

are best used for driving and braking, respectively. For the sliding case it is more natural to let the force depend on the relative velocity $v_s = \lambda v_x$. Then, $-v_s$ will simply correspond to $-\lambda$.

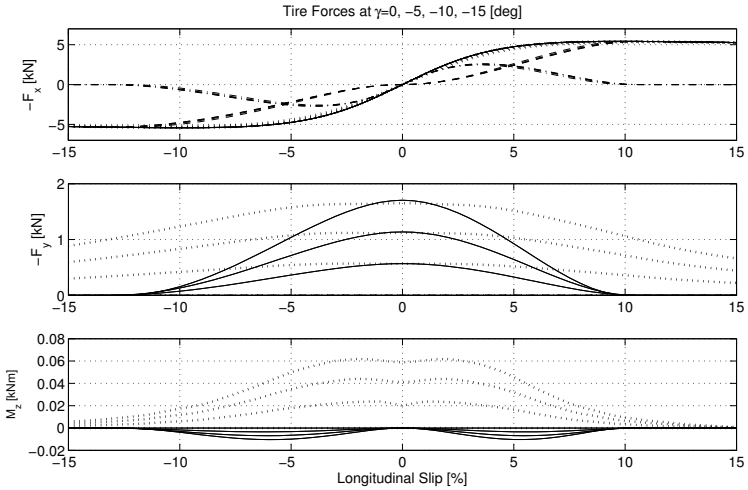

Figure 5.13 The effect of camber on the tire forces. The dashed dotted lines are the adhesion force and the dashed line the sliding forces. The camber effect when included as a shift on the lateral slip is shown by the dotted line for $\gamma = 0, -5, -10,$ and -15 deg.

Therefore, when computing sliding forces using an empirical model for braking, the pure-slip forces

$$\begin{cases} -\hat{F}_{0x}(-\lambda) & \lambda < 0 \\ \hat{F}_{0x}(\lambda) & \lambda \geq 0 \end{cases} \tag{5.35}$$

are best used for driving and braking respectively.

The effect of the described procedure is shown in Figure 5.12. It is clear that the influences are small and neglectable compared to the uncertainties in measurements. Interesting is, however, to see the difference between the proportion adhesion and sliding force for driving and braking respectively. The magnitude of the longitudinal limit-slip is, theoretically, equal if expressed as σ_x°. If using λ° it is important to notice that $|\lambda^\circ_{\text{driving}}| > |\lambda^\circ_{\text{braking}}|$ as a consequence of the definition, see Equation (B.16).

Results of cambering

The information about the camber properties for the tire in the available data was restricted to a few measurement points at different loads,

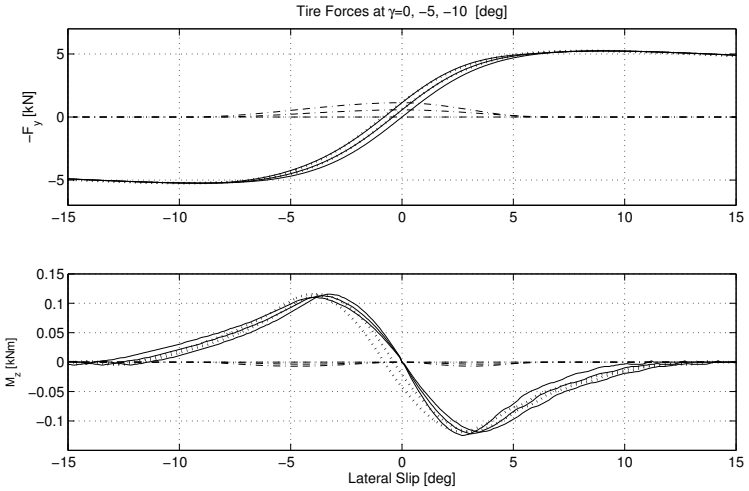

Figure 5.14 Illustration of the effects of camber on the tire forces. Solid lines are the total force and aligning torque. The dashed dotted lines are the camber forces. For the torque the dashed dotted lines denote the additional torque from the cambering forces. The camber effect when included as a shift on the lateral slip is shown by the dotted lines for $\gamma = 0, -5$, and -10 deg.

see Figure 5.3. A validation of the effect of camber on combined slip was therefore, not possible. Instead the properties and results are illustrated in the following. The parameters of interest for cambering are $C_y = 1.4$ kN/deg, $C_z = 54$ Nm/deg, and $C_\gamma = 26$ N/deg. It can be noticed that the influence of camber on the lateral tire force is very low for the tire, i.e. C_γ is small, and can be neglected for any practical case. Interestingly, the camber stiffness calculated from the aligning stiffness, as described in Section 4.2 by combining (4.53), (4.45) and (4.42), $\hat{C}'_\gamma = 2k\hat{C}_z$, is significantly larger, $\hat{C}'_\gamma = 120$ N/deg. To be able to visualize the effects of camber, the computed larger stiffness was chosen. In Figure 5.13 the effect of camber is shown for sweeps of λ and in Figure 5.14 for sweeps of α.

It can be seen from the result that camber hardly affects the longitudinal force. It affects the partitioning between sliding and adhesion, but the lower adhesion force is compensated by a higher sliding force. In other tire models, for example presented in [Hirschberg *et al.*, 2002] the camber effect is included as a shift on the lateral slip, i.e. the lateral slip gets an additional term of $C_\gamma\gamma/C_y$. This much simpler approach to handle the

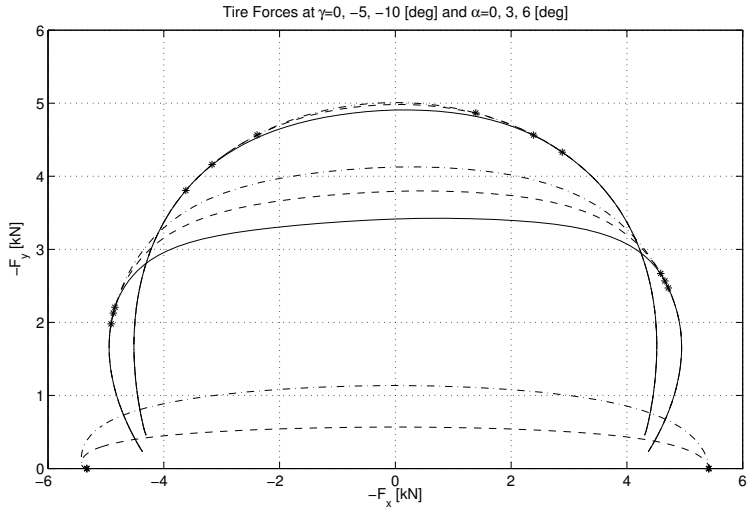

Figure 5.15 Illustration of the effects of camber on the lateral force as a function of the longitudinal tire force at combined slip. The solid lines shows zero camber, dashed lines $\gamma = -5$ deg and dashed-dotted lines $\gamma = -10$ deg. The transitions to full sliding are marked with asterisks.

camber is plotted in the figures and the results for pure slip cases are similar. For the combined-slip cases the results differ significantly, since the offset has an undesired influence on the sliding velocity and also on the sliding-force component. The self-aligning torque also differs between the two methods. Figure 5.15 shows the camber effect on the lateral force as a function of the longitudinal tire force at combined slip. Note that camber has a strong influence on the point of transition to full sliding at larger lateral slip.

Discussion The difference between the theoretical camber stiffness, $\hat{C}'_\gamma$ and the measured camber stiffness, $\hat{C}_\gamma$ for six different tires is shown in Table 5.1. It is noticed that the deviation between the calculated and the measured camber stiffness is smaller for tires for personal cars and motorcycles than for tires for heavier vehicles as trucks or the Jeep, used in the example above. A theory that is discussed in [Pacejka, 2002] is that the assumed bristle deformation due to the camber is most accurate for tires with a rounded shoulder. For wider and flatter tires the camber effect might be better explained by deformation in the tire walls and changes in the contact pressure distribution instead of bristle deflections and carcass

Table 5.1 Comparison between measured and computed camber stiffness for different tires and loads. Note that $\hat{a}$ is calculated as $3\hat{C}_y/\hat{C}_z$ for all tires except 185/60 R14, where it is measured. The calculation is an approximation which gives unrealistic values at higher vertical loads.

	P225/75R15					*7.60-15* [Pacejka, 1988]			
F_z [kN]	2.4	4.2	6.0	7.8	9.6	2.5	4.5	6.3	8.1
R [mm]	350	350	350	350	350	317	317	317	317
$\hat{C}_y$ [kN/deg]	0.75	1.2	1.4	1.4	1.4	0.7	0.8	0.9	1
$\hat{C}_z$ [Nm/deg]	16	33	54	75	94	20	30	50	70
$\hat{a}$ [mm]	64	83	116	161	201	86	112	167	210
$\hat{C}_\gamma$ [N/deg]	9.2	17	26	40	61	100	125	133	145
$\hat{C}'_\gamma$ [N/deg]	40	82	135	187	235	50	75	125	175

	195/65 R15 [Pacejka, 2002]	*185/60 R14* [Kageyama and Kuwahara, 2002]			*315/80 R22.5* [Pacejka, 2002]	*160/70ZR17* [Pacejka, 2002]
F_z	7	1.9	2.5	2.9	41	3
R	317	289	289	289	540	330
$\hat{C}_y$	1	1	1.2	1.4	4	0.5
$\hat{C}_z$	60	x	x	x	125	15
$\hat{a}$	180	75	87	96	94	90
$\hat{C}_\gamma$	100	30	45	50	<100	50
$\hat{C}'_\gamma$	150	62	87	112	312	37

deformations, see Figure 5.16. Through the difference between $\hat{C}_\gamma$ and $\hat{C}'_\gamma$ it may be possible to calculate the stiffness of the carcass during camber, since $\gamma_{tot} = \gamma + C_{c\gamma} M_x$, $C_{c\gamma}$ is the carcass stiffness in the actual direction and M_x the overturning torque. It would also hold that $\hat{C}'_\gamma \gamma = \hat{C}_\gamma \gamma_{tot}$ for small angles, which gives $C_{c\gamma} = \gamma(\hat{C}'_\gamma - \hat{C}_\gamma)/M_x$. A further validation has not been performed and the reasoning should be seen as a possible explanation to the distinction between the measured and calculated camber stiffnesses.

The dynamic properties of the tire model

The available measurements from NHTSA included data for evaluation of the lateral dynamic properties at one velocity. The transient data is shown in Figure 5.17 and generated by a sinusoidal excitation of the slip angle. The amplitude of the oscillations is small and the tire can be assumed

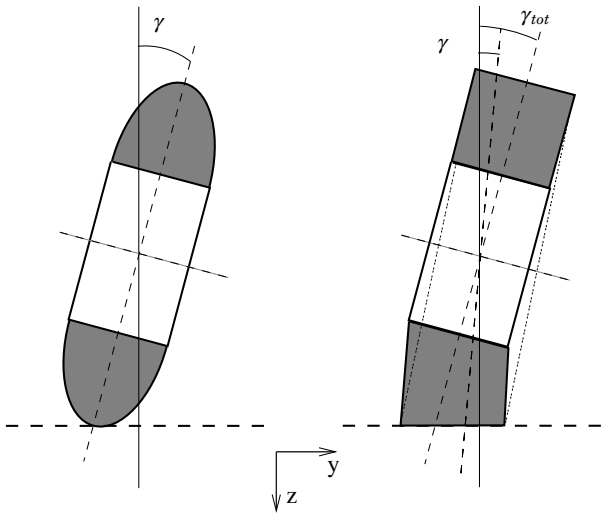

Figure 5.16 Schematic picture of a cambered wheel, illustrating the effect of flexibility in the carcass, which may explain the difference between the theoretic and the actual camber stiffness

to behave linearly. According to the the relaxation-length concept from (4.80) the relation between the wheel rim slip angle and the lateral force is given by the transfer function

$$F_y = \frac{C_y}{\frac{\sigma_{ay}}{v_x}s + 1}\alpha' \tag{5.36}$$

The parameters in (5.36) were identified from the measurement data as $C_y = 1.4$ kN/deg and $\sigma_{ay} = 0.57$ m. In Figure 5.18 the identified transfer function is compared with the data in a Bode-plot. The misfit of the phase was supposed to be the effect of a time delay between the collection of the slip-angle signal and the force signal. The fit is greatly improved with the addition of a delay of a half sampling period. The identified stiffness also corresponds well to the static measurements in Figure 5.4 where C_y =1.3 kN/deg and $C_x = 1.4$ kN/%. Since no measurements are available in the longitudinal direction $\sigma_{ax} = 0.5$ m is used. Relation (4.82) now gives the carcass stiffnesses as C_{cy} =2.3 kN/deg·m and C_{cx} =2.8 kN/%·m. Carcass damping coefficients were chosen to $D_x = 4$ s/%·m and $D_y = 7$ s/deg·m. The aligning stiffness was identified from Figure 5.4 to C_z =60 Nm/deg.

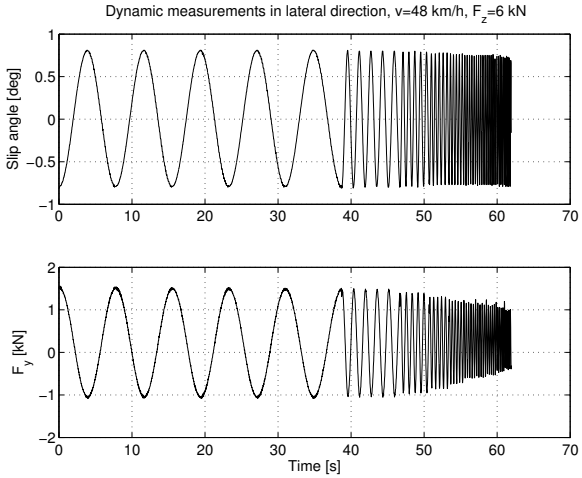

Figure 5.17 Measurement of the force response for sinusoidal slip-angle inputs at different frequencies. The sampling frequency is 50 Hz.

The test velocity was given as $v_0 = 48$ km/h. All results below is for $v = v_0$.

Result for transient input The dynamic system (4.79) was simulated on the form

$$\begin{bmatrix} \frac{\partial F_x}{\partial \lambda} - D_x v_x & \frac{\partial F_x}{\partial \alpha} \\ \frac{\partial F_y}{\partial \lambda}\cos^2(\alpha)\cos(\alpha') & \left(\frac{\partial F_y}{\partial \alpha}\cos^2(\alpha) - D_y v_x\right)\cos(\alpha') \end{bmatrix} \begin{bmatrix} \dot{\lambda} \\ \dot{\alpha} \end{bmatrix} = \begin{bmatrix} C_x \sigma_{ax}^{-1} v_x (\lambda - \lambda') \\ C_y \sigma_{ay}^{-1} v_x \cos(\alpha)\sin(\alpha - \alpha') \end{bmatrix} \quad (5.37)$$

where the contributions from $\dot{\lambda}'$ and $\dot{\alpha}'$ are neglected. Note the trigonometric re-writings to avoid numerical problems at slips angles of 90 deg. Partial derivatives of tire forces with respect to slips are required for simulation of the model. In general, these are not analytically available and in the following they are computed by finite differences in each simulation step.

Figure 5.19 shows the response of the contact slip, λ, and longitudinal force for rim-slip steps, λ', of different magnitude at pure longitudinal slip and constant lateral rim slip $\alpha' = 5$ deg. The results agree qualitatively well with reports in the literature [Pacejka, 2002]. Note the quicker

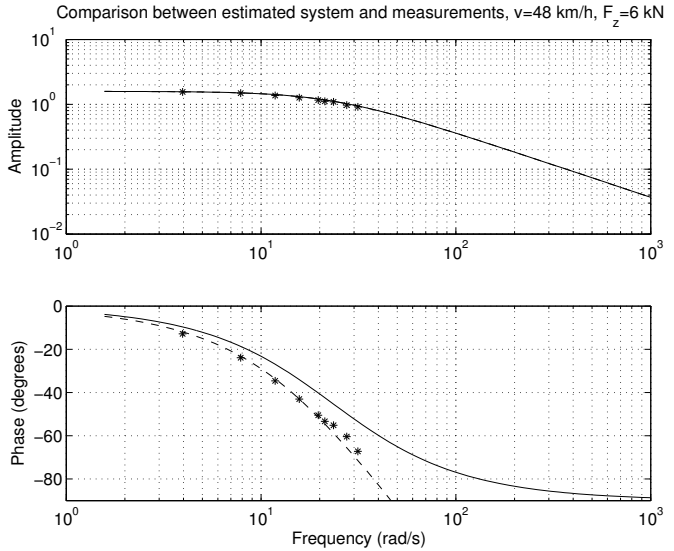

Figure 5.18 Bode plot showing the fit of a linear relaxation-length model (solid) with the measurement data (stars). Addition of a time delay (10 ms) results in better fit for the phase (dashed).

response for larger steps. The figure also illustrates the influence of combined slip on the dynamics. Figure 5.20 illustrates the dynamic cross-coupling between λ and α at step inputs in λ' and α'. The cross-coupling is larger and the dynamics are faster at larger slips.

To visualize the effect of the dynamics of the tire in a more realistic setup the following results consider the dynamic of a whole wheel. In automotive applications the control of λ' using the brake torque is a delicate problem. Regard the wheel in Figure 4.15. Torque equilibrium can be stated as

$$J\dot{\omega} = T - F_x(\lambda)R_e \quad (5.38)$$

where R_e is the wheel radius and T is the applied torque. Assuming constant vehicle velocity v_x the equilibrium can be rewritten as

$$J\dot{\lambda}' v_x = (F_x(\lambda)R_e - T)\,R_e \quad (5.39)$$

Note that the tire is not a rigid body and that the assumption of a fixed inertia J is an approximation. The inertia for the tested wheel was not known and was set to $J = 5$ kg·m^2. It is also pointed out that the effective rolling radius R_e might not be identical to the moment arm by which

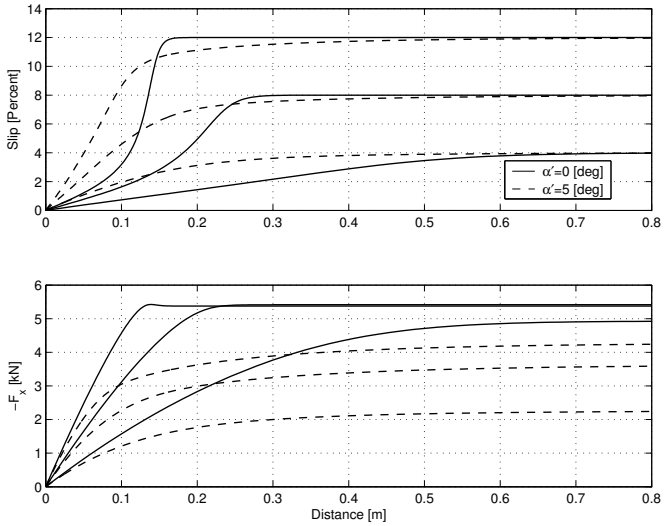

Figure 5.19 Illustration of the responses in λ and F_x for 10%, 20% and 30% steps in λ' at $\alpha' = 0$ deg and $\alpha' = 10$ deg.

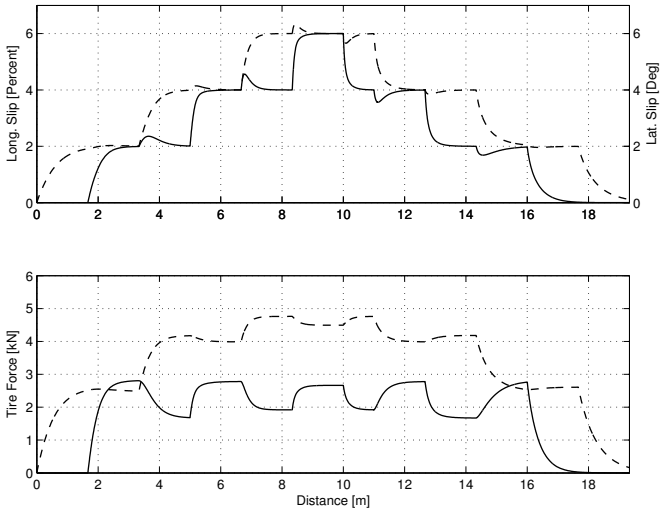

Figure 5.20 Illustration of the effect of dynamic cross-coupling on λ, α, F_x, F_y at step inputs in λ' and α' (solid: longitudinal; dashed: lateral).

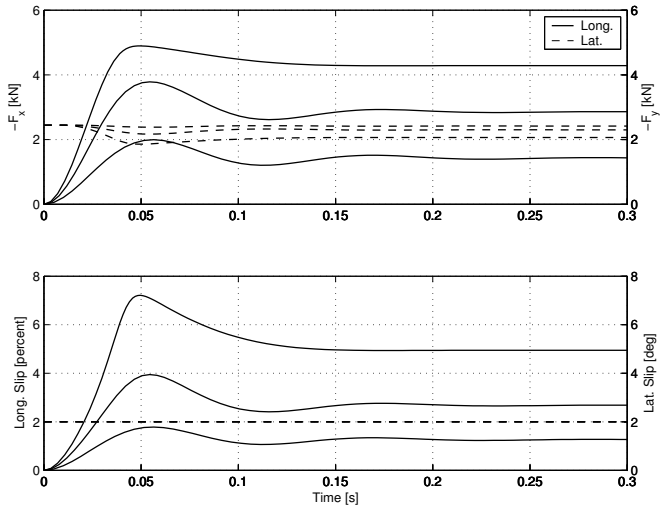

Figure 5.21 Simulation of step responses in the brake torque (500, 1000, 1500 Nm) while keeping the rim-slip angle constant at 2 deg. Upper plot: contact forces; Lower plot: contact slips.

the tire force applies a moment on the wheel. However, the difference is in practice small and they are assumed to be equal in the following. Figure 5.21 shows the response of the wheel dynamics (5.39) in combination with the tire model (5.37) for step inputs in the brake torque at a constant lateral rim-slip. Note that the effect of cross-coupling is greatly reduced when the wheel dynamics are introduced. In practice, the brake torque may appear like a spike in which case the cross-coupling effect would again have more influence. It is clear that the responses are less damped for smaller brake applications. This may be understood from a closer examination of the combined dynamics.

The characteristic polynomial of the linearized constant-speed wheel dynamics at a stationary operating point with constant brake torque is

$$s^2 + \frac{\varphi R_e^2 D_x - C_{cx} v_x J}{J(\varphi - D_x v_x)} s + \frac{\varphi R_e^2 C_{cx}}{J(\varphi - D_x v_x)} \tag{5.40}$$

where $\varphi = \partial F_x(\lambda)/\partial\lambda|_\circ$ is the gain from contact-patch slip to longitudinal contact-force at the operating slip. Note that $\varphi < 0$ in the small-slip region. Figure 5.22 shows the root locus of the characteristic equation with respect to φ. This corresponds to the slope of the force-slip curve that is transversed during a braking action. For large negative φ that corre-

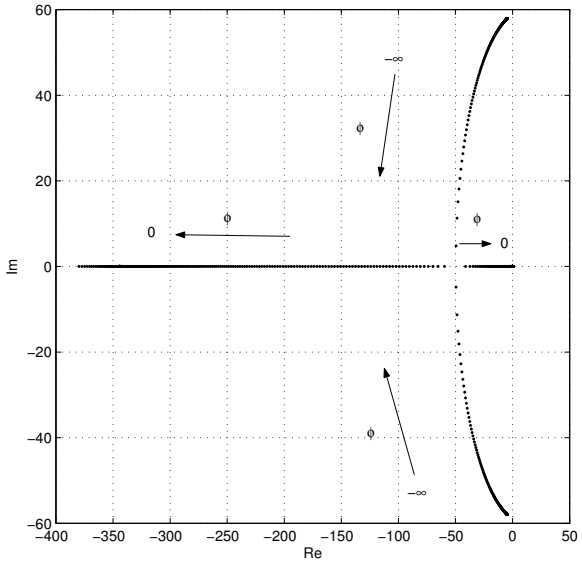

Figure 5.22 Root locus of the characteristic polynomial (5.40).

sponds to the braking stiffness at small slip the poles are complex and poorly damped. When φ increases the poles become real. This explains the increased damping at larger brake torques. As φ approaches zero one pole goes to a stable limit and the other approaches zero. The introduction of the damping D_x lets φ grow to the positive value specified by the conditions in Section 4.3 while maintaining stability for the carcass dynamics. The wheel dynamics, however, becomes unstable as the slope of the force-slip curve gets positive. The root locus clearly shows that wheel and tire dynamics can not be separated and that any control application that involves the wheel rotation benefits from taking the tire dynamics into account. It is well known that the vehicle velocity v_x greatly affects the wheel dynamics and that slip control is harder at low velocities. Inspection of the characteristic polynomial at limit conditions reveals the interesting fact that the dynamics change equally for variations in the slip operating point and the vehicle velocity. For $\varphi \to -\infty$ or $v_x \to 0$ the characteristic polynomial goes to

$$s^2 + \frac{R_e^2 D_x}{J} s + \frac{R_e^2 C_{cx}}{J} \tag{5.41}$$

and for $\varphi \to 0$ or $v_x \to \infty$ to

$$s\left(s + \frac{C_{cx}}{D_x}\right) \tag{5.42}$$

Future work will address quantitative validation with measured transient data. A problem in this context is the possibilities to separate the contribution of dynamic behavior from the wheel and tire from deflections, back-lash, and hysteresis of the wheel suspension in a real application. Section 6.2 treats these questions in a more practically way.

It is also of interest to reveal if the cross coupling between the longitudinal and lateral dynamics is relevant in practical applications.

5.5 Implementation and Application in Multi-Body Simulation of Vehicle Handling

There are many different software environments available for modeling and simulation of multi-body mechanics, both for general mechanics and applications specific for vehicle dynamics. The VehicleDynamics Library™-[Modelon, 2006] for Dymola™ [Dynasim, 2006] is chosen, due to the close connection to the developers, to extend the usability and the possibility of validation of the model, see [Gäfvert *et al.*, 2006]. Dymola is a modeling and simulation environment for general multi-domain modeling and simulation. It is based on the open high-level Modelica® language that is maintained by the Modelica Association [Mod, 2005]. The VehicleDynamics Library is an add-on to Dymola that offers complete and detailed multi-body vehicle models for vehicle dynamics analysis.

The multi-body model describes the vehicle as a set of rigid bodies connected by joints (constraints) or force elements. The description is based on orthonormal reference frames that are attached to the bodies. The reference frames follows the ISO 8855 standard with x pointing forward, y to the left, and z upwards.

The wheels are treated as bodies with force elements that describe the interactions between the chassis and the track surface. The rim of each wheel is rigidly connected to the suspension wheel carrier by the hub, and may be kinematically defined by the chassis and wheel-spin states. The tire is a vertically deformable body that is attached to the rim and interacts with the ground in a contact patch of varying size and location. In principle, the contact patch is represented by a contact point at which the forces and moments are assumed to apply, located where a line through the wheel center, aligned with the wheel plane, intersects the track surface. Moreover, the deformation of the tire is normally only

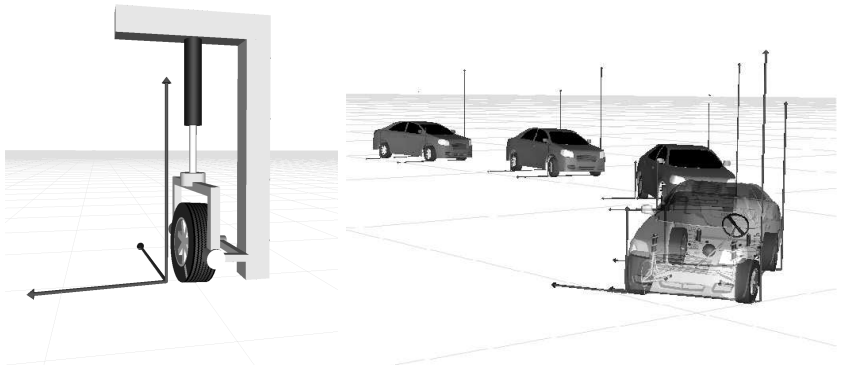

Figure 5.23 To the left: Simulated test rig for analyzing the transient and stationary behaviour of tyre models. The test rig can apply longitudinal and lateral slips as well as camber at desired loads and velocities. To the right: Visualization of simulated NHTSA-Fishhook handling maneuver.

explicitly described in the radial direction. In this way, many effects of the tire deformation are lumped into the description of contact forces in the contact point. This also makes it easy to use empirical data from experiments to characterize the tire. The orthonormal reference frames of the wheels are chosen to support this tire-modeling paradigm, and follow the TYDEX conventions [TYDEX-Working group, 1997].

Simulation Results

The combined-slip model is combined with the Magic Formula pure-slip models described in [Bakker *et al.*, 1987] with parameters from the same source. The combined-slip characteristics of the model were first determined by simulations in the virtual test rig shown to the left in Figure 5.23. The experiment is a sequences of sweeps in either λ or α, with the non-swept slip held constant. The result can be visualized as in Figure 5.24 and give a good view of the characteristics and limits of the tire. The first figure shows the resulting forces for zero inclination without velocity dependence. It is seen that small slips give negligible combined-slip influence, while at larger slips the force envelope describes the ellipse-formed limits of the tire. The second plot shows the shift effects of adding camber. The third and fourth plots show how lower speeds will increase and higher speeds decrease the force envelopes as the velocity dependence is turned on. The tire model was also used in simulation of handling

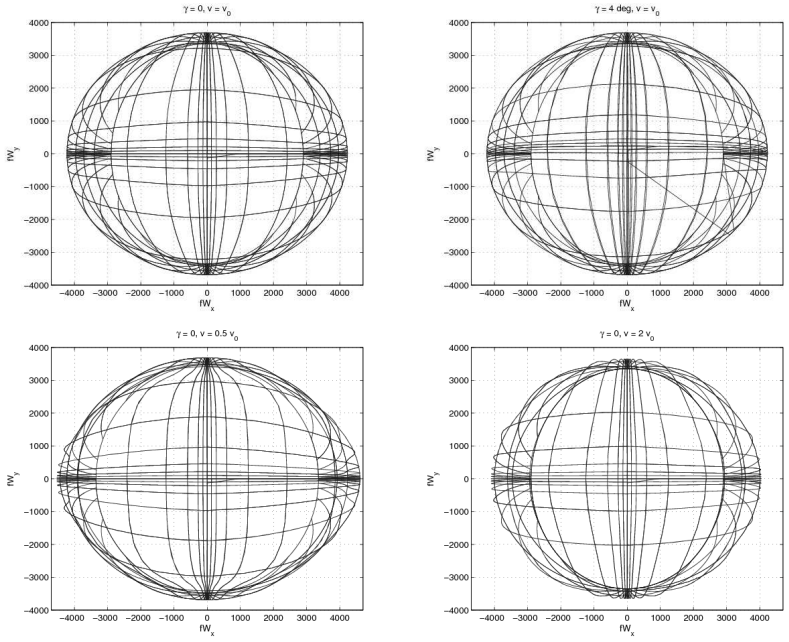

Figure 5.24 Combined-slip force characteristics at 4kN load as plots of lateral force as function of longitudinal force for experiment in tyre test rig with slip sweeps $\lambda \in [-1,1]$ and $\alpha \in [-89,89]$ deg at constant levels $\lambda \in \{0, \pm\text{logspace}(-3,0,10)\}$ and $\alpha \in \{0, \pm\text{logspace}(0.1,89,10)\}$. Upper right shows the effect of adding 4 deg camber, and the lower left and right plots show velocity dependence at $v = 0.5v_0$ and $v = 2v_0$, correspondingly. Note that the plots include some straight lines that are the result of re-adjusting the rig between the slip sweeps.

maneuvers with a 40-DOF chassis model with elasto-kinematic suspension models, see the right hand side of Figure 5.23. The presented tire model gave similar results as Magic Formula [Pacejka, 2002] and TMEasy [Hirschberg *et al.*, 2002] with similar simulation performance. Absence of calibrated parameters for the three compared models for one specific tire makes it difficult to draw detailed conclusions.

5.6 Conclusions

This chapter has presented a new method to derive the tire forces for simultaneous braking, cornering, and camber, by combining empirical models for pure braking, cornering, and cambering. The proposed model is

based on understanding of the physical sources of tire forces, as given by the theoretical rigid-carcass brush-model. Based on the brush model, the combined-slip forces may be described by a scaling of corresponding empirical pure-slip forces. There is a freedom in choosing the pure-slip forces, which may be used to emphasize different physical effects. This made it easy to include velocity dependence in the model, in a unique way. The generation of the camber force has been described in a simple, but physically motivated manner. Its influence on the partitioning of the sliding and adhesive regions in the tire contact patch, affects the scale factors for the tire-forces. For pure slips it is common to introduce camber by an offset on the lateral slip. However, for the self-aligning torque and the combined slip forces the proposed model gives significantly different result. It has also been discussed that the effects of camber, with varying accuracy, can be approximated from the lateral properties of the tire. The model is simple to use since it does not introduce any new parameters. All necessary information is given by the used pure-slip model.

Even though the model in its present state is useful for a number of applications, the addition of effects of turn-slip and flexible carcass would further enhance the applicability. The physical foundation of the model is expected to make this possible with reasonable effort.

Relations to similar, previously published combined-slip models are analyzed. Previous models are partly heuristically based, while the proposed model is entirely based on physical principles. An advantage with the presented model is that it combines the data-fitting accuracy of empirical pure slip models with the stringency of physical modeling. The calibration of physically-based models to measurements is often limited by the small set of parameters and the approximations and idealized or neglected effects in such models. Therefore, more flexible heuristic models such as the Magic Formula [Pacejka, 2002] are more commonly used nowadays both for pure and combined slip situations. Despite good fit at calibration with measurement data, deviations from real behaviour will still arise as the normal operating conditions for a tire usually differ significantly from those at calibration-measurement experiments. Empirical models are normally valid only within the input intervals where calibration measurements exists and extrapolation properties are often very unreliable. Moreover, the large amount of factors that affects the tire behavior makes it practically impossible to collect and manage data for all kind of influencing factors. These observations raise the question whether it is better to use physically based models with less perfect fit to measurement data, but with better extrapolation properties outside the measurements ranges.

Good results are obtained in validation with the available empirical data. Experimental validation indicates that the proposed model and the

BPL model [Bakker *et al.*, 1989] performs similarly. The COMBINATOR model [Schuring *et al.*, 1996] behaves slightly differently at small combined slips. None of these previous models include velocity dependence.

The tire model is successfully implemented in Matlab code and in the multi body simulation environment, Dymola. It works well and is computationally sound on both platforms.

The proposed dynamic extension of the proposed combined-slip model exhibits a qualitatively realistic tire relaxation behaviour. The model includes cross-couplings between longitudinal and lateral dynamics, that are not commonly found in other models of similar complexity. The issue of stability is handled by including a physically motivated damping. Examination of the combined dynamics of a wheel and the tire model gives insights that might be relevant for brake-control applications.

6

Measurement and Processing of the Wheel Speed Signal

6.1 Introduction

The rotational velocity of the wheels are some of the most essential signals for vehicle control and stabilization. The signals contain information about several factors, relating to the road foundation, the tires, and the motion of the vehicle. In some road detection systems the variance of the wheel speed signal is used to distinguish between smooth and uneven foundations. In vehicle simulations and in many friction estimators the normalized difference between the wheel and vehicle speed, *slip*, is very important in its relation to the tire force. The proportion between the wheel speeds on each tire can reveal information about tire pressure or tread wear. For the stability of the vehicle it is of major concern that the wheel do not loose the grip on to the road. Any tendency to wheel-lock must be detected early from the speed signal and then be safely prevented. The high degree of information makes the speed signals valuable, but on the other hand noisy and hard to utilize, if the different effects are not correctly separated from each other.

The common way to measure the wheel speed is to use a sensor that registers the magnetic field between the sensor and a tooth-wheel. The sensor is mounted at the end of the axle and the tooth wheel is attached to the wheel rim, see Figure 6.1. The general idea is to measure and count repeated variations in the magnetic field due to the rotation of the tooth wheel. The measurement methods are mostly based on induction, or

direct measurement of the magnitude of the magnetic field. An inductive sensor consists of a core and a coil, which generates a voltage due to the changes of the magnetic field, see [ProAuto Limited, 2006]. The output, when the wheel is rolling, is a wave formed signal, centered around zero. The frequency and amplitude depends on the number of passed teeth per time unit, which makes the velocity signal hard to distinguish from the noise at low speeds. This sets a lower limit of the working range for this type of sensor.

The magnitude of the magnetic field can be measured by a *Hall*-element. A Hall-element has to be used with a magnetic tooth wheel or with a magnetic material placed behind the sensor such that the tooth wheel can affect the magnetic field surrounding the sensor. Practically, the Hall-element produces a voltage depending on the distance to the closest teeth. A sensor with Hall-element is often refereed to as an active sensor, since a circuit for signal processing often is included in the sensor package. The processing unit is necessary to identify the passage of the tooth flanks, which is more difficult for a Hall-element since the output is not centered around zero and the bias, sensitive to the gap between the sensor and the tooth wheel, might vary with time and around the peripheral. Two Hall-elements are often used together to improve the repeatability, and to make the sensor possess the ability for status diagnosing and determination of the wheel-rotation direction. The processed output use to be, each time a tooth flank passes, a short pulse containing coded information from the sensor. More detailed information can be found in, for example, [Ana, 2001]. The speed of the wheel is derived from the inverse of the time between the pulses from the sensor. Modern microprocessors provide flexible timers, separated from the main core, that counts the elapsed time without affecting the execution of the real-time kernel. An interrupt at each pulse might be necessary for storage and data processing in more advanced routines. At high speed the pulses come often and the number of performed instructions at each pulse are limited by the controller capability.

It is important to get an accurate disturbance free wheel-speed signal, since the noise may be heavily amplified in certain computations. Particularly in applications depending on the slip or on the actual tire force. The slip is the difference between two almost equal signals and a noise level of up to one percent of the wheel speed is much compared to a slip signal in the range of 0 to 20 percent of the wheel speed. The derivative of the speed is used to calculate the magnitude of the wheel-inertia torque that opposes the brake torque when deriving the actual tire force. Differentiation of a noisy signal is a crucial operation requiring effective filters which often deteriorates the timing capability.

Normal noise filters that introduce extra phase lag has to be used

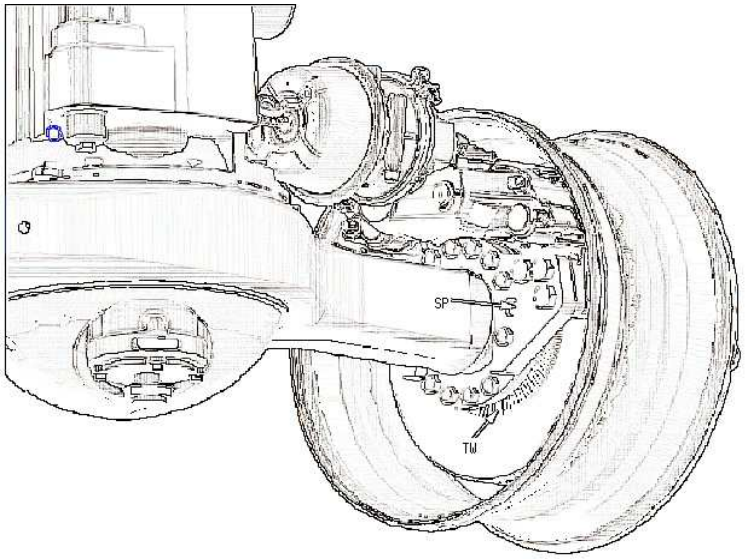

Figure 6.1 Picture of a rear truck-axle showing axle, rim, brake unit, tooth wheel (TW) and the placement of the speed sensor (SP) (Modified, by courtesy of Haldex Brake Products AB).

with great care, not to delay the detection of a beginning wheel-lock situation. In some conditions, particularly at low speed, the wheel might lock quickly and any delay on the signal might be hazardous for the stabilization system. However, the signal processing has to be efficient enough not to unnecessarily invoke e. g. the anti-lock system.

The sensors used nowadays often measure accurately, but it is important to regard that they measure the magnetic field due to the passage of a tooth in front of the sensor pick-up. This do not always coincide with the tire speed that is useful for the vehicle control system. There are three main noise sources, among others, that affect the measurement of the wheel speed:

- **Brake force transients** There is a dynamic response from the mechanical system around the wheel axle when a braking torque is applied onto the wheel. Two different physical effects are then present. First, the movement of the wheel-axle end, where the brake and wheel speed sensor is mounted, when the axle is subjected to a reaction torque from the brake affects the wheel speed measurement. Since the relative speed between the wheel and the sensor is

measured the sensor movement has to be accounted for in such a situation. The second effect is the dynamic system consisting of the wheel inertia and the tire stiffness. The tire deflects and affects the force transmission from the brake pads to the tire-road contact.

- **Rotational dependent noise** Irregularities of the tire shape and asymmetries of the tooth wheel causes disturbance patterns on the speed measurements. The disturbance patterns are repeated each wheel revolution.

- **Road irregularities** Bumps and unevenesses in the road might temporarily effect the rolling radius of the wheel. For this type of disturbances there might be a correlation between the front wheels and the rear wheel with a delay corresponding to the wheel base of the car. In some axle constructions, suspension movements affects the sensor position, which causes even further measurement errors.

A simple model of the axle behavior and a proposal on how the influence of the transient brake force on the measured wheel speed can be accounted for is described in the following section. The tire dynamics is previously treated in Section 2.6 and 4.3. Section 6.3 reviews and describes some methods to eliminate the rotation dependent noise from the speed signal. Processing the noise from road irregularities is a large area for further work. In, for example, [Gustafsson *et al.*, 2006a] the dependency between the front and the rear wheel speed covariances are used for determination of the absolute velocity of the car. This field in not further treated in this thesis. Additional noise sources are, e. g. mentioned and discussed in [Schwarz, 1999]

6.2 Effect of Tire Force Transients on the Wheel Speed Measurements

This section will mainly discuss the disturbance on the wheel speed measurements caused by movements of the sensor position. The effect is particularly obvious for front axles, since these, generally, are relatively weak and flexible mechanical constructions. The brake that creates and carries the reacting braking torque is mounted on the axle end, which deflects when supporting the load. Forces acting on the tire due to, for example, the engine torque are also subjected to a dynamic behavior, but do not, in the same way, affect the wheel speed measurement. Rear axles are often of more robust design and deflects less, while the dynamic behavior of the tire still is present.

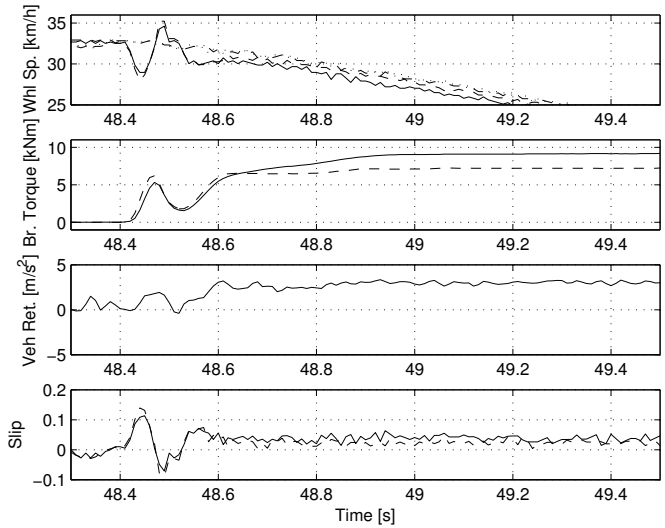

Figure 6.2 Plot showing the effect of a front-axle brake-force transient on the wheel-speed measurement. A step command on the brake pedal causes an apparent decrease of the wheel speed. The ABS reacts and lowers the brake force. After an overshoot the wheel speed returns to a stable level and the brake system can come back to normal mode. The rear axle is totally unbraked. The solid lines denotes the front left, dashed lines the front right, dashed dotted the rear left and dotted line describes the rear right wheel. The vehicle retardation (third plot) are derived from accelerometer measurements.

An example of the effect can be viewed in Figure 6.2, that shows measurements collected from a Scania test truck at Haldex. The transient of the brake torque, in the interval t=48.4–48.6 s, causes a dynamic behavior of the wheel speed signal, which is clearly seen from the top and bottom subplots. The overshoot in slip during the application phase largely exceeds the settled value at the end of the data series even though the brake torque is as largest at the end.

In [Schwarz *et al.*, 1997b] the effect is modelled as longitudinal suspension stiffness and accounted for in the slip determination. In [Sugai *et al.*, 2003] a method is presented to on-line estimate a coefficient denoting the entire influence of the longitudinal suspension motion and tire carcass stiffness. Here, the behavior will be modelled and discussed. Based on the available measurements, the requirements on a model that predicts the tire-wheel-axle dynamics are studied in an empirical way.

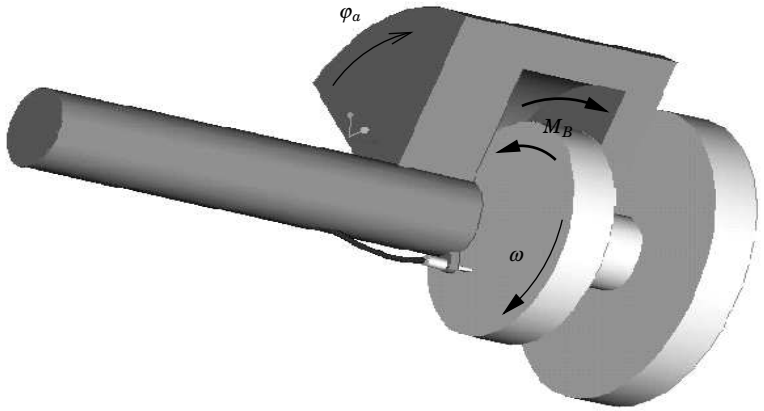

Figure 6.3 Schematic figure of the axle and wheel hub. The axle rotation are here supposed to carry the effects from all kind of deflections of the suspension and tire. The movement of the sensor causes the disturbances on the wheel rim speed measurements.

Dynamic model

The reaction of the wheel speed measurements, due to transients in the brake forces, is explained by many different effects. One part is the movement of the wheel hub and wheel speed sensor due to deflection of the axle and suspension. Another part is the dynamics of the tire, caused by the carcass flexibility and the inertia of the wheel, discussed in detail in Sections 4.3 and 5.4.

In the following it is assumed that the movement of the sensor relative the tooth wheel is caused by axle torsion, see Figure 6.3. In reality, the movements of the axle are much more complex, see e. g. [Matschinsky, 1997], and the sensor together with the wheel axle will additionally exhibit linear motions. The deflections are here lumped together in one equation, since the major part of the respective dynamics can be described as a mechanical system, characterized as

$$\varphi_a = \frac{1}{J_a s^2 + D_a s + K_a} M_B \tag{6.1}$$

It is therefore emphasised that, the inertia, J_a, the damping, D_a, and, the stiffness, K_a are generic parameters gathered from the entire system. They do not directly correspond to the physical, measurable quantities of

the axle, since many parallel systems are incorporated in this equation. The deflection angle, φ_a, denotes the movements of the wheel speed sensor and the brake torque is denoted by M_B. The actual speed of the rim ω can be calculated from

$$\omega = \hat{\omega} - \dot{\varphi}_a \tag{6.2}$$

where $\hat{\omega}$ is the measured wheel speed. For the wheel speed measurement there is a difference if the sensor makes a rotational movement or if the sensor and the wheel axle together gets a linear deflection. In the first case the speed measurement is actually wrong, since the sensor moves with the wheel. In the other case the speed is correct, but the wheel reference speed, ω actually deviates from the vehicle reference. It is assumed that lumping of these motions into one rotational motion is a good engineering approximation.

Inserting (6.1) in (6.2) gives

$$\omega = \hat{\omega} - \frac{s}{J_a s^2 + D_a s + K_a} M_B \tag{6.3}$$

Included in ω there is another dynamic response of the force transient due to the tire deformation. The response is velocity dependent and should be considered when the speed of the tire carcass in the contact with the road is to be derived, which normally is the case when modeling tire forces from the slip. The relation between the wheel rim speed and tire carcass speed is in detail discussed in Section 5.4. In Figure 6.4 the result from a simulation of the axle, wheel, and tire including these effects is shown. For the axle simulation Equation (6.1) is used and the tire and wheel is modelled according to (5.37) and (5.38). The brake torque sequence visible in Figure 6.2 is used as input signal to the system. It can be seen that major part of the dynamics is caught by the model. Proper parameters for the system is, however, difficult to find since the tire and axle parameters are not entirely known. The unknown parameters used in the simulation example are more or less manually chosen to give acceptable result and more effort can be done to further increase the accuracy. Tire characteristics given by the manufacturer is used, even though the reliability is low since the conditions at the testing facilities certainly, are different from those at the measurement occasion.

Identification of the dynamics

The System Identification toolbox in Matlab is employed to increase the agreement of the model. The aim is to find an accurate relation between the brake torque and the wheel speed during transients. Finding a simple transfer function with good accuracy is of more interest than finding the optimal parameters to the physical model from the prior section. The

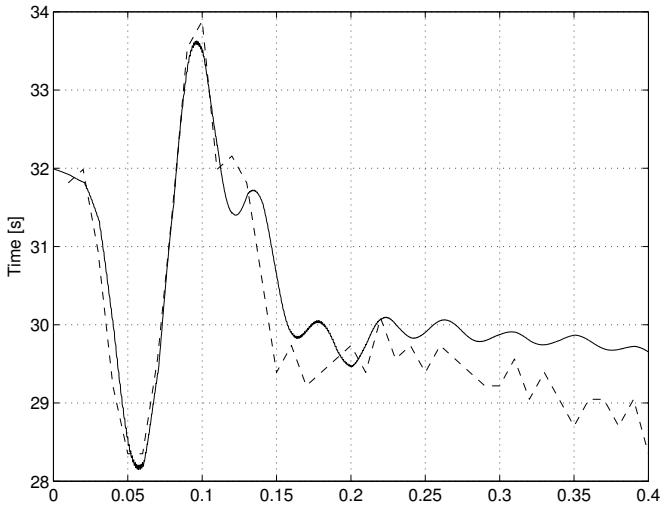

Figure 6.4 Simulated wheel speed response (solid line) compared to measurements (dashed line) for the scenario shown in Figure 6.2.

identified model dynamics is assumed to behave as any first or second-order transfer function, $G(s)$. The signals necessary for the identification are derived from Equation (6.3), rewritten as

$$\omega - \hat{\omega} = G(s) M_B \tag{6.4}$$

The real wheel velocity ω can not be measured. Here, it is approximated from wheel speed measurements of the unaffected rear axle, but compensated for the slip (due to the applied brake force), such that there is no stationary gain in the identified system. The slip is caused by the tire behavior and should not be incorporated in the axle behavior. In that way the transient effects of the torque application becomes clear, see Figure 6.5.

The velocity dependency of the dynamics caused by the tire carcass is then completely neglected, since it is incorporated in the velocity independent system for identification. In practise it is difficult to distinguish between the different effects. Tests at different speed are required for a further evaluation.

Using the Matlab command `arx`, the discrete equivalence $H(q)$ to $G(s)$ is identified on the form

$$H(q) = \frac{b_0 + b_1 q^{-1} + b_2 q^{-2}}{a_0 + a_1 q^{-1} + a_2 q^{-2}} \tag{6.5}$$

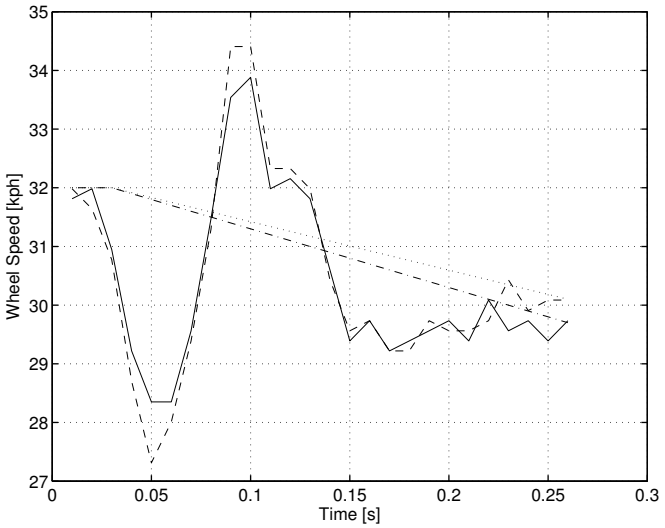

Figure 6.5 Illustration of measured wheel velocity, $R_e\hat{\omega}$ (full line, left wheel and dashed, right wheel) and the constructed accurate wheel velocities $R_e\omega$ (dashed-dotted line for the left wheel and dashed for the right wheel).

The measured data set contains two occasions where the effects of the torque transients are clearly visible. The first is shown in Figure 6.2 from where the time slot [48.4, 48.65] is used for identification. The second occasion is used only for validation. The identified parameter values are presented in Table 6.1 and the obtained dynamics are graphically shown in Figure 6.6. The result is almost similar for the first and second order system and no accuracy is gained by higher order than one. The right wheel shows better accuracy than the left-side from where there seems to be a timing error of approximately 0.01 s between the simulation result and the measurements. Reasons for this are discussed later on.

The result from the identification is used to reduce the disturbance of the brake force application on the wheel speed. The corrected rim speed is then calculated as

$$\omega(t) = \hat{\omega}(t) - H(q)M_B(t) \tag{6.6}$$

In Figures 6.7 and 6.8 the correction is validated towards the measurement data for the two available test occasions. It is clear that the disturbance on the wheel speed is greatly reduced. The best result is seen in the first transient on the right side, where the disturbance is almost

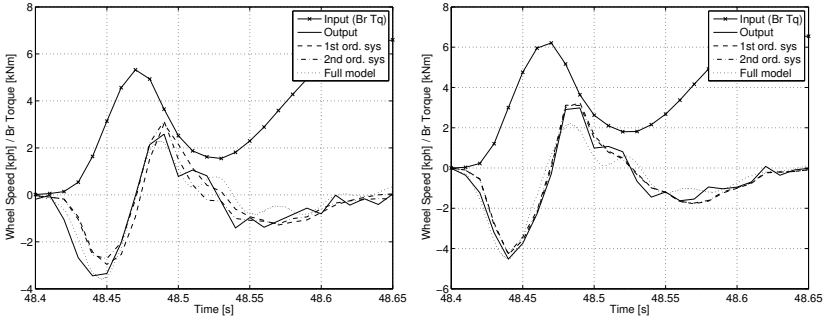

Figure 6.6 Comparison between the output from the identified system and the measurements $\omega - \hat{\omega}$ for left (left plot) and right (right plot) front wheels. The dotted line denotes the result from the full-model simulation described in Section 6.2

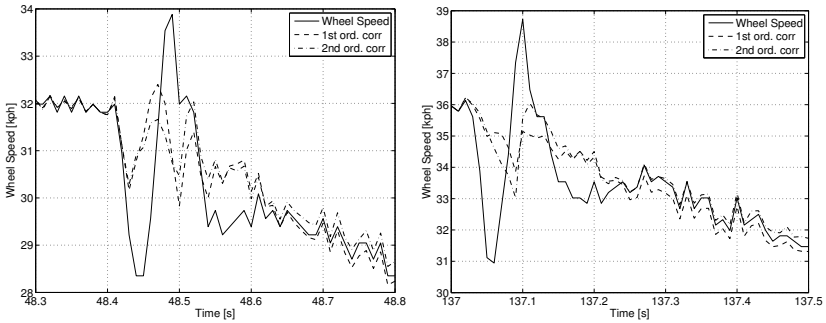

Figure 6.7 Comparison between the measured wheel velocity and the corrections applied with the two different filters according to (6.6). To the left: The first brake application where the disturbance is seen, which also is used for the identification. To right: The second brake application for validation. Data from the left-front wheel.

removed. In the other plots the disturbances still are present, but reduced by at least 50% and the first order system performs slightly better than the second order system.

Conclusion The aim of this section has been to find a way to compensate for disturbances on the wheel speed signal created by axle and suspension deflections during the brake application. From the validation it can be seen that the disturbance is not entirely eliminated, but its amplitude is greatly reduced by very simple means. The correction on the wheel speed signal can be seen as a feed-forward filter of the brake torque, predicting the disturbance. A first order filter is sufficient and higher or-

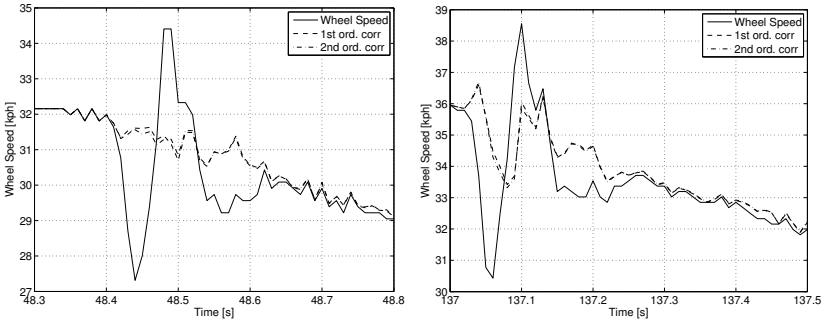

Figure 6.8 Data from the right front wheel, compare to Figure 6.7.

Table 6.1 Result of the parameter identification of (6.5).

Side	a_0	a_1	a_2	b_0	b_1	b_2
Left	1	0.283	0	-0.00249	0.00255	0
Right	1	0.411	0	-0.00301	0.00299	0
Left	1	-0.131	-0.217	-0.00293	0.00497	-0.00206
Right	1	-0.15	-0.348	-0.00319	0.00531	-0.00213

der filters do not improve the results. A remarkable result is that poles of the identified discrete system are on the negative real axis. For the second order system one pole stays on the negative and the other on the positive stable axis. This makes it impossible do a physical interpretation of the systems. Comparing the pole to the slightly unstable zero in the first order system shows that behavior due to the pole is overridden by the effect of the zero. The behavior can almost be seen as a pure differentiation, which also will be the result if the the denominator is set a constant while re-doing the identification.

The disturbances are reduced by at least 50% in the available validation data and this is probably sufficient to increase the performance of vehicle systems relying on the wheel-speed signal during the brake-force transients. A drawback, so far, is the limited amount of measurement data. More test occasions are necessary for a more comprehensive validation. Tests on different types of axles are another necessary requirement. A question mark is if the neglection of the tire characteristics still is acceptable in the identification of a stiffer axle or at a lower vehicle velocity. Since the relative contribution of the tire then is larger. Also, the stiffer

axles have less impact on the wheel speed and the dynamics then might be completely disregarded. In practise, it is difficult to distinguish the tire dynamics from the axle dynamics. A result from Section 5.4 is that the impact of the carcass deflections are less obvious at higher slip. Comparing the dynamics at high and low slip might be an accessible way to separate between wheel and axle dynamics. Performing experiment at different vehicle velocities is another. The method of approximating the suspension and tire stiffnesses in one coefficient and identify it on-line as described in [Sugai *et al.*, 2003] seems to be an realistic approach, since the major part of the dynamics shows to be described by this coefficient. A problem with on-line estimation in this case may be that quick and substantial excitations necessary for the estimation might occur rarely during normal run. When they suddenly occurs it might be in a limited condition and optimal performance of the system is a demand.

On the other hand there are many ways to further improve the parameter identification. The system is very fast and the sample time of 0.01 s, used in the collected measurements, is quite slow compared to the reaction of the wheel speed. It is therefore assumed that shorter sampling time would be advantageous for the estimation. For such fast system dynamics delays and jitter on the signals caused by the CAN-bus transmission and different sensor characteristics can be crucial. In Figure 6.6 there is a delay of 0.01 s between the measurements and the identified systems for the left side, while the right axle shows better agreement. The setup is identical, but with the hard timing constraints the error may be explained by varying latency on the signals.

6.3 Method for Elimination of Rotation Dependent Noise

There is, in general, noise on the wheel speed signal that is repeated every revolution, with a scheme that is depending on the rotation angle of the wheel. This type of noise might be hard to discern since its pattern is distorted after sampling and filtering. To clearly see this kind of disturbance, the signal has to be unfiltered and should be sampled at each passage of a tooth flank or faster. This is not commonly done even on test vehicles. The sources for the disturbances come, for example, from irregularities of the teeth, varying air-gap between sensor, and a distorted tooth wheel, and uneven worn or oval tires. To be able to eliminate such a noise source, the position of the rim has to be known during the wheel rotation. It is not necessary to determine the absolute angle, if there are sufficient time for calibration of the algorithm after each restart of the system. The important thing is to be able to compare a pulse signal at a certain position to the pulses from the same position at the prior revolutions. The

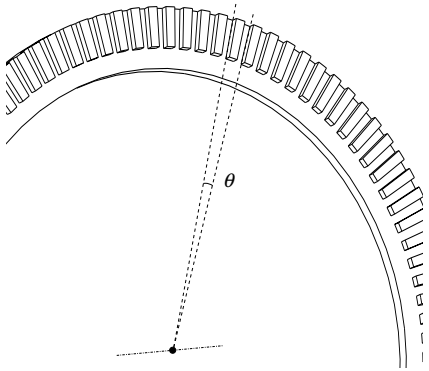

Figure 6.9 Illustration of a part of a tooth wheel, with angle θ between the teeth, ideally.

general idea for the noise elimination is to derive a vector containing one element per pulse generated by the sensor during one revolution of the tooth wheel. The vector values are used for correction of the actual wheel speed signal and calibrated in such a way that the signal irregularities are cancelled. Similar methods have been presented in [Schwarz *et al.*, 1997a] and [Persson, 2002].

The measurement system

Let N denote the number of pulses from the sensor during one revolution. Each pulse is indexed by k. Hence, t_k is the time at pulse k, which is generated by the tooth flank i_k (when i is used as index, k will be left out). The rotation angle of the rim between each pulse is ideally $\theta = 2\pi/N$, see Figure 6.9. Due to the circumstances mentioned above the pulses are not evenly distributed along the travelled distance for one revolution of the wheel. The angle corresponding to the rolled distance between two pulses at the tooth i, see Figure 6.10, is

$$\theta_i = \theta + \delta\theta_i \tag{6.7}$$

where $\delta\theta_i$ is a measure for the distortions in the tooth wheel and uneven rolling radius around the peripheral of the tire and belongs to the vector $\boldsymbol{\delta\theta}$,

$$\boldsymbol{\delta\theta} = [\,\delta\theta_1 \quad \delta\theta_2 \quad .. \quad \delta\theta_N\,], \qquad \sum_{i=1}^{N} \delta\theta_i = 0 \tag{6.8}$$

The measurement of the rotational velocity can be expressed as a time

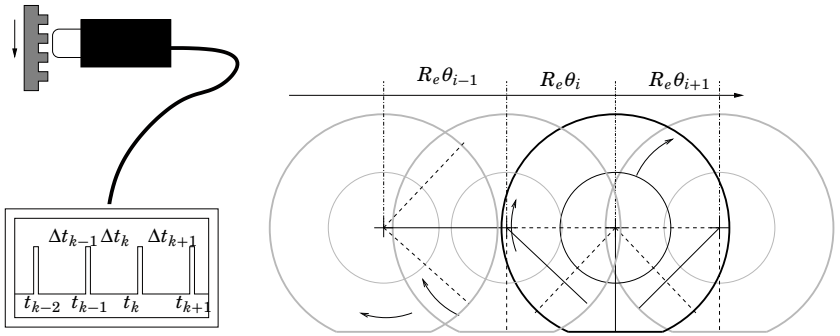

Figure 6.10 Illustration of the pulses from the wheel speed sensor relative the rotation of the wheel. The space between the pulses relates to the distance travelled by the wheel, when it is not subjected to a slip. Any irregularities in the tooth wheel and the dynamic tire radius are accounted for in $\delta\theta$. Therefore, R_e might be treated as constant.

varying system on state-space form as

$$\boldsymbol{x}(t_{k+1}) = \boldsymbol{\Phi}\boldsymbol{x}(t_k) + \boldsymbol{e_p} \tag{6.9}$$

$$y(t_k) = \boldsymbol{C}(i_k, t_k)\boldsymbol{x}(t_k) + e_m \tag{6.10}$$

where the state vector $\boldsymbol{x}$ is

$$\boldsymbol{x}(t_k) = \left[\, \frac{1}{\omega(t_k)} \quad \delta\theta_1 \quad \delta\theta_2 \quad .. \quad \delta\theta_N \,\right]^T \tag{6.11}$$

The system matrix, $\boldsymbol{\Phi}$ is the identity matrix with $N+1$ rows and columns. The mean velocity during the time between t_{k-1} and t_k is denoted by $\omega(t_k)$. The process error, $\boldsymbol{e_p}$ relates to the assumed variation of the inverted wheel speed and the irregularities of the teeth. The irregularities are assumed not to change, hence

$$\boldsymbol{e_p} = [\, e_\omega \quad 0 \quad 0 \quad .. \quad 0\,]^T \tag{6.12}$$

The observation $y(t_k) = [\Delta t_k] = t_k - t_{k-1}$ is the time elapsed between the two latest pulses. The observation vector becomes

$$\boldsymbol{C}(i_k, t_k) = \left[\, \theta \quad 0 \quad .. \quad 0 \quad \tfrac{1}{\omega(t_k)} \quad 0 \quad .. \quad 0 \,\right] \tag{6.13}$$

where the factor $1/\omega(t_k)$ is placed corresponding to the element $\delta\theta_i$, i. e. on instance i_k+1. The measurement error, e_m is assumed to be white noise

due to road irregularities and disturbances from the signal conversion in the sensor. Hence, the observation of the inverse velocity is

$$y(t_k) = \Delta t_k = \frac{\theta}{\omega(t_k)} + \frac{\delta\theta_i}{\omega(t_k)} + e(t_k) \tag{6.14}$$

From the observations of Δt the aim is to identify the correct velocity, or in this case, its inverse. By estimation of the irregularities of the teeth, their influence on the noise on the speed can be eliminated.

Wheel speed filtering by use of a minimal-variance technique

If the disturbances on the system are Gaussian and respective covariances are known sufficiently accurately, than a Kalman filter is an optimal way to estimate the state vector even for time-variant system [Åström, 1970]. The recursive Kalman filter and the state estimation scheme is formulated as

$$\hat{\boldsymbol{x}}(t_{k+1}) = \hat{\boldsymbol{x}}(t_k) + \boldsymbol{K}(y(k) - \boldsymbol{C}(i_k,t_k)\hat{\boldsymbol{x}}(t_k)) \tag{6.15}$$

$$\boldsymbol{K}(t_k) = \boldsymbol{P}(t_k)\boldsymbol{C}^T(i_k,t_k)(R_2 + \boldsymbol{C}(i_k,t_k)\boldsymbol{P}(t_k)\boldsymbol{C}^T(i_k,t_k))^{-1} \tag{6.16}$$

$$\begin{aligned}\boldsymbol{P}(t_{k+1}) &= \boldsymbol{P}(t_k) + \boldsymbol{R_1} \\ &-(\boldsymbol{P}(t_k)\boldsymbol{C}(i_k,t_k)^T)(R_2 + \boldsymbol{C}(i_k,t_k)\boldsymbol{P}(t_k)\boldsymbol{C}(i_k,t_k)^T)^{-1}(\boldsymbol{C}(i_k,t_k)\boldsymbol{P}(t_k))\end{aligned} \tag{6.17}$$

$$\boldsymbol{P}(0) = \boldsymbol{R_0} \tag{6.18}$$

The condition of having the sum of $\boldsymbol{\delta\theta}$ equal to zero is not yet included in the formulations. To fulfill this specification, the observer, y, is extended to also observe $\sum(\boldsymbol{\delta\theta})$. Hence,

$$\boldsymbol{y_E}(t_k) = \begin{bmatrix}\Delta t_k) \\ 0\end{bmatrix};\ \boldsymbol{C_E}(i,k) = \begin{bmatrix}\theta & 0 & .. & 0 & \dfrac{1}{\omega(t_k)} & 0 & .. & 0 \\ 0 & 1 & .. & 1 & 1 & 1 & .. & 1\end{bmatrix};\ \boldsymbol{e_m} = \begin{bmatrix}e_t \\ 0\end{bmatrix} \tag{6.19}$$

which means that an error-less observation that the sum is zero is performed at each instant and the estimated states will adapt to this condition. The covariance matrices can be chosen as

$$\boldsymbol{R_0} = \begin{bmatrix}r_\omega & 0 & \cdots & 0 \\ 0 & r_\theta & \cdots & 0 \\ \vdots & \vdots & \ddots & \vdots \\ 0 & 0 & 0 & r_\theta\end{bmatrix};\ \boldsymbol{R_1} = \begin{bmatrix}r_\omega & \boldsymbol{0}(1,N) \\ \boldsymbol{0}(N,1) & \boldsymbol{0}(N,N)\end{bmatrix};\ \boldsymbol{R_2} = \begin{bmatrix}r_t & 0 \\ 0 & 0\end{bmatrix} \tag{6.20}$$

where r_ω is the variance relating to the change rate of the wheel speed, or more correctly, the inverse of the wheel speed. The variance of non-repeating measurement errors due to, i.e road irregularities are incorporated in r_t. It should, however, be a balance between r_t and r_ω such that quick wheel speed changes not are misinterpreted as temporal disturbances. To be on the safe side, then r_t are set very low. The covariance of the irregularities, r_θ, might not be known at the beginning, but after a successful state estimation, it can be computed as cov($\boldsymbol{\delta\theta}$). The vector $\boldsymbol{\delta\theta}$ does not change during normal run. However, there are occasions where the counter can miss a tooth. Therefore, both at start up and when a missed tooth is suspected the filter has to be reinitialized. Earlier computations of cov($\boldsymbol{\delta\theta}$) can then be used for r_ω. An alternative is to set the diagonal elements in the process covariance matrix, $\boldsymbol{R_1}$ in the same way as those of $\boldsymbol{R_0}$ and in that way introduce a forgetting factor in the estimations. A drawback is that a trade off problem is encountered in choosing between a quick re-adaptation and minimum variance on the estimates. Different ways to supervise the algorithm, using different update modes, can be more effective and give and better output in this case.

As an illustration of the method, a tooth wheel and a sensor that outputs 10 pulses per revolution are simulated at constant speed. A vector of tooth asymmetries is created, but there are no other disturbances on the signals, so that the function of the state estimator can be easily illustrated. Signal disturbances would increase the convergence time. The difference of the measured output (time between the pulses, Δt_k) and the corrected output $(1/\omega(t_k))$ is shown in Figure 6.11 using the proposed method. It can clearly be seen that the variance of the corrected signal decreases while the values in $\boldsymbol{\delta\theta}$-vector adjust. The result of the $\boldsymbol{\delta\theta}$ estimation is shown in Figure 6.12. Note, that all values in the vector changes at each update such that the sum of the entire vector is zero.

The presented observer is regarded as an optimal observer, predicting the states with minimal variance relating the to available measurements. Setting r_t low, the major tuning parameter is r_ω. It is important to have a sufficiently high value on r_ω such that the velocity estimate reacts fast and is calculated with minimum delay. If the actual wheel velocity changes rapidly, for example, in a wheel-lock situation and the estimated velocity can not adapt quick enough, there will be a disturbance on the $\boldsymbol{\delta\theta}$-estimates. On the other hand, if the velocity reacts to fast the $\boldsymbol{\delta\theta}$-values will not be calculated correctly, since the tooth-irregularities can not be separated from velocity changes. In the method illustrated above the variances are set as $r_\theta = 0.04$, $r_\omega = 0.0005$, and $r_t = 0$. In a realistic approach the variances much be set more careful, concerning the temporal disturbances on the wheel speed signal and the desired ability of the algorithm to catch velocity changes of the wheel. A separate algorithm may

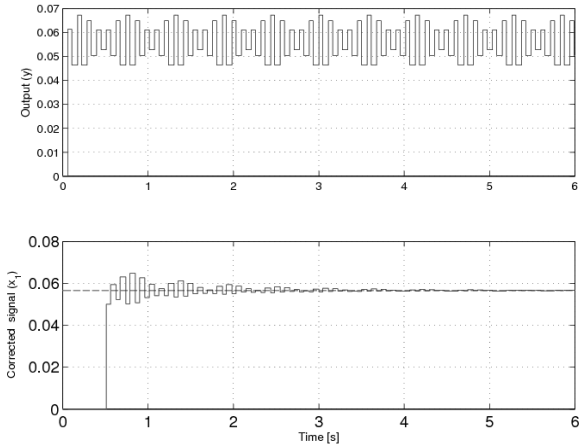

Figure 6.11 Results from minimum variance estimation of simulated tooth irregularities. The upper plot shows the "measured" pulse time and the lower plot shows the pulse time corrected for the estimated $\boldsymbol{\delta\theta}$. The algorithm starts at 0.5 s.

be employed to compute the corrected velocity, ω, directly using (6.14) backwards and the working areas of the algorithm may be limited to the cases when the wheel velocity is not rapidly changing.

In practise, the presented minimum-variance method is too computationally demanding and memory consuming to be implemented in a limited real-time system for this problem. Processors used in the automotive sector constantly increase in power, and a demanding solution today might be applicable in a few years.

Wheel speed filtering for suitable for on-line implementation

There are some ways to do the wheel speed filtering more computationally efficiently. One example can be found in [Schwarz *et al.*, 1997a] protected by the patent [Isermann *et al.*, 2000], where a vector, v, with calibration factors, one value per pulse, is created and updated on-line. The measured velocity is corrected as $\omega_{corr}(t_i) = 2\pi v_i / y(t_i)$, where v_i is iteratively calculated from

$$v_i(j+1) = v_i(j) + \gamma \left[\bar{\omega} - \frac{2\pi}{\Delta t} v_i(j) \right] \tag{6.21}$$

on the corresponding tooth. The revolution number is denoted by j. The update factor γ is updated according to the Recursive Least Squares

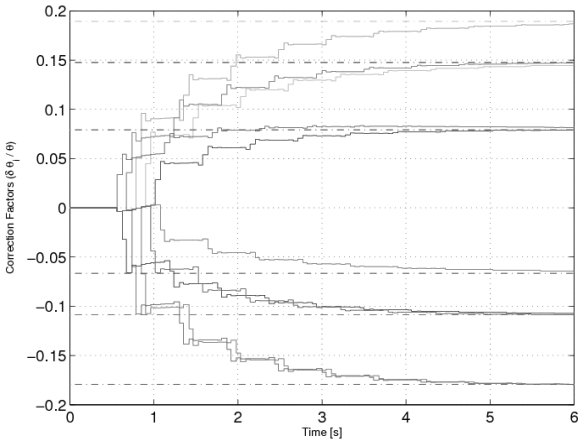

Figure 6.12 Estimated normalized angle errors compared to the true error (dashed-dotted lines)

method for effective elimination of disturbances on $\boldsymbol{v}$. A method to correct and detect a missed tooth by comparing the sequences of the latest v_i to the older values before update is also proposed. The actual speed $\omega(t_k)$ is reconstructed one lap afterwards according to a fuzzy fusion of the measured speed of the teeth around the updated tooth. The algorithm requires a good quantity of memory and computation power, but can be implemented in a 16-bit microprocessor. The implementation is not provided in detail, but as understood from its presentation the need of storage for $y(t_k)$ and $\boldsymbol{v}$, are 2N values. At each detected tooth a parameter update for a first order system, according to (6.21), is performed together with a second order least squares identification, to get the wheel velocity.

In [Persson and Gustafsson, 2001] a similar method is proposed with the alternative updated scheme of the calibration factors as

$$\delta\theta_i(j+1) = \delta\theta_i(j) + \gamma \left[\omega(t_k)\Delta t_k - \frac{2\pi}{N} - \delta\theta_i(j) \right] \tag{6.22}$$

The reference speed is calculated in a more simple way compared to the previous method as $\omega(t_k) = 2\pi/(t_k - t_{k-N})$. The calibration factor corresponds directly to the angle error of the teeth. In [Persson, 2002] the same author proposes another method to cope with the disturbances caused by the tooth irregularities. In an algorithm for detection of low tire pressure the resonance frequency of the tire is one of the major detection points

for indicating the tire pressure. Therefore the frequency spectra for the wheel speed signal is derived during the travel of the vehicle. It has been showed that the tooth irregularities creates disturbing frequency peaks in the spectrum plot at the frequencies $f_K(m) = m\omega_k/(2\pi)$ and the proposed method do only attempt to suppress the harmonics in the frequency window of interest. A Fourier series is employed to describe the disturbance pattern around the tooth wheel peripheral

$$\delta\theta_k = a_0 + \sum_{m=1}^{N/2} a_m \cos\left(m\frac{2\pi}{N}k\right) + \sum_{m=1}^{(N-1)/2} b_m \sin\left(m\frac{2\pi}{N}k\right) \tag{6.23}$$

and the included parameters a and b are estimated from the recursive scheme

$$\theta = [a_m \quad b_m]^T \tag{6.24}$$

$$\varphi_k = \frac{1}{\Delta t_k}\left[\cos\left(m\frac{2\pi}{N}k\right) \quad \sin\left(m\frac{2\pi}{N}k\right)\right] \tag{6.25}$$

$$\varepsilon_k = y_k - \varphi_k^T\theta_k \tag{6.26}$$

$$\theta_{k+1} = \theta_k + \mu_k\varphi_k\varepsilon_k \tag{6.27}$$

where $y_k = 2\pi(1/\Delta t_k - 1/(t_{k+N/2} - t_{k-N/2}))$. The harmonics to be attenuated is determined by the value on m. It is concluded that the complexity of this algorithm increases for each frequency reduction. The number of memorized variables are $2M$ (M denotes the number of suppressed harmonics), required additions $6M + 3$ and multiplications $12M + 4$. It is emphasised that the method is derived for suppressing a limited number of harmonics and it is not particularly efficient and usable for wheel speed filtering in the time domain.

Conclusive remarks

Measurements performed on cars have shown a rotational dependent noise level up to 1.5% percent of the wheel speed. The expectation is that the disturbances be heavily reduced leaving noise levels of maximum 0.5% on smooth asphalt roads during free rolling. In [Pavkovi *et al.*, 2006] even better results are shown. The variance of the remaining noise in a general case is difficult to determine since it depends on many factors, for example, the actual surface conditions and the sensitivity towards the force transients.

6.4 Conclusion

The functionality of many vehicle system relies on the wheel speed signals. In some important applications traditional noise filtering is difficult since the timing constraints on the signal are high. This section has discussed a few methods to improve the quality of the wheel speed signal, without causing any phase shift or time delay.

On, particularly, front axle wheels force transients caused by quick changes of the brake command can give large disturbances on the wheel speed signal. The disturbances arise due to wheel axle deflection and a corresponding movement of the speed sensor position, since the measured speed is the relative speed between the wheel and the sensor. The result shows that the effect of such a disturbance can by simple means be reduced by over 50% by appling a first-order feed forward filter from the brake torque signal.

Further, the wheel speed signal has a rotation-dependent noise, due to, tolerance errors on the tooth wheel that together with a sensor generate the pulses to the frequency counter that calculates the wheel speed. The noise pattern can be removed by creating a vector that adaptively keeps track on the error related to each tooth. The expectation is that noise of 1.5% on the speed signal could be reduced to around 0.5% for free rolling on smooth asphalt roads.

7

Road Friction Estimation

This chapter cover work done within the sub project, *Model-based road friction estimation* in the IVSS-programme, *Road Friction Estimation*, RFE.

IVSS, *Intelligent Vehicle Safety Systems*, is a unique joint venture by public-sector agencies, private-sector companies, and industry organizations, that was set up to stimulate research and development for the road safety of the future and aims at moving the emphasis from passive solutions to active systems. In other words, preventing problems from arising in the first place [Vägverket, 2006b].

7.1 Introduction

The Road Friction Estimation project

Road vehicles rely strongly on friction. Their large masses that often move at high speeds may cause fatal damage if they loose steerability. The controlling tire forces are generated by and dependent on a sometimes abruptly changing friction. A large safety margin in the traffic should be compulsory, but is often not sufficiently regarded by the drivers. Modern vehicle control systems can, to some extent, correct for incautious actions from the driver, but a correct appraisal of the driving circumstances is mandatory for safe driving.

Many investigations show a correlation between the road condition and the accident risk, see e.g. [Wallman and Åström, 2001]. The output from a road friction estimator might be used as a detecting device that warns the driver about a bad or suddenly changed road condition. Information about the friction can also be used to enhance the functionality of active and adaptive control systems within the vehicle or sent to a global infrastructure that receives and transmits information about the roads.

The aim of the RFE project is to estimate the friction between tire and road and to evaluate and optimize the reliability as well as the delay of the estimation. Three different concepts are analysed within the RFE-project.

Sensor equipment for accurate determination of tire forces Friction estimators often relies on estimated tire forces. Hence, errors on the derived forces might have an crucial effect on the reliability of the friction estimate. To enhance the signal quality SAAB investigates the possibilities to mount force sensors close to the wheel hub to enable direct measurements of the lateral and longitudinal force and the self-aligning torque.

Surface detection by preview techniques Volvo Technology and Luleå Technical University study different concepts to estimate the surface condition in front of the vehicle by optical means. A proposal under evaluation is a sensor called RoadEye [Optical Sensors, 2006] that transmits a couple of laser frequencies on to the road and measures the reflections. With this technique it is possible to detect whether there is a coating layer on the road surface, such as water, snow, or ice, see [Casselgren *et al.*, 2007].

Model-based road friction estimation The thesis presents work performed within this sub project. The main aim is to develop algorithms for friction estimation during longitudinal tire force excitations. The results are derived in close cooperation with Johan Hultén at Volvo Cars, Fredrik Bruzelius at Volvo Technology, and Magnus Gäfvert at Modelon AB. Besides IVSS Haldex Brake Products AB and Volvo Cars finance the work.

Model-based road friction estimation

A popular and in many circumstances successful approach to assess the friction is to estimate the braking stiffness, i.e. the incline of the tire force relative the slip at low slips and from this value distinguishing between different surface conditions. Note that the term “braking” in this context refers to longitudinal slips and forces and is also used to denote the force-slip inclination at low slips during driving. A linear tire model is hereby used with an assumption on the relation between the slope and the friction condition, see e.g. [Gustafsson, 1997]. The braking stiffness depends on many factors and a generic relation between the slope and the exact friction coefficient is therefore not possible to obtain. Even the surface detection is not always reliable due to the large variation of the braking stiffness caused by other reasons, see for instance [Pavkovi *et al.*, 2006].

This work aims at estimating the value of the friction coefficient by using a well-defined accurate model for the effect of the friction on the

tire behavior. The model adopted for this purpose is the physically based brush-model, that describes the effects of the rubber deformation and frictional limitations in the contact patch and specifies the curvature of the force-slip relation. The information of the friction is derived from the deviation from linearity in the force-slip slope, which is clearly detectable at larger slips. The estimation of the linearity at small slips is a similarity to the previous method, but its slope is not used as indicator of the friction. In the proposed method the detection of the incline at low slip is a necessity for deriving the curvature.

One advantage of the method is that the algorithm is based on a clear, verified relation between the measurements and the friction, which makes the estimation more reliable. The drawback is it that two tire-road related parameters have to be estimated and the method requires higher force and slip excitations compared to stiffness-based methods.

Another problem that arises when the curvature of a slope is to be determined is that the measurement data need to be sufficiently spread in the force and slip plane for an accurate estimate. If the data is clustered around one point the solution become ambiguous and any parameter couple that results in a curve that crosses this point may be a possible solution. The robustness of the estimation decreases and noise, model error, and other temporal disturbances will have a very large impact on the result. To overcome this, a particular data storage system is developed to, as good as possible, utilize the spread of the available measurements.

Outline

A main prerequisite for the choice of a model-based estimator for the road friction is a clear formulation of the model, which describes how the friction coefficient influences the behavior of the tire in the interaction with the road. Here, it is assumed that the friction affects the relation between the slip and the developed tire force and that these signals are available for measurement or estimation. The model also has to reflect the variation rate of the included parameters and should specify the expected model and measurement noise distributions.

The function of this kind of estimator can be divided into three sub problems:

- Choice of the tire model
- Determination of signals to the tire model. In this case the normalized tire force and the slip.
- Construction of the estimator algorithm

In this work the brush model, see Section 4.1 is used to describe the tire behavior. Section 7.2 contains an evaluation of its reliability for friction estimation by a validation towards measurement data. Section 7.3 presents the idea of storing sampled data in data bins, which is a way to lump measurements in separate regions distributed over the force and slip axles together. This is a way to remember and filter old data and to decrease the sensitivity to disturbances. The states in the data bin, representing the normalized longitudinal tire force and the tire slip are used in the cost function from which the optimal parameters denoting the braking stiffness and friction coefficient are calculated. The least squares method and the Gauss-Newton algorithm are proposed for this purpose.

Implementation details and the additional vehicle estimators necessary for deriving the tire force and slip signal are described in Section 7.4 followed by Section 7.5 presenting the results from tests in reality. The chapter concludes with a discussion about the estimator properties and the requirements on further work.

Friction estimation — Prior art

Much effort is world-widely spent on developing algorithms for friction estimation. A literature study in this area is quite difficult, since published articles often describe academic nice solutions, but these are often restricted to certain circumstances with few real implementations. The companies, having powerful test equipment, mostly do not publish articles due to the hard competition. Instead the ideas are protected by patents, that are difficult to penetrate and understand. One exception is work done by NIRA-dynamics, which is been presented in many articles, for example [Gustafsson, 1997] and also developed into a product. The product is an algorithm that uses information from the wheel speed signal, the vehicle velocity, and the engine torque to distinguish between the road foundations: gravel, ice, snow, and asphalt. The idea is to evaluate the braking stiffness and correlate its value to the surface friction. Using the braking stiffness as a friction indicator is not always reliable and the algorithm is limited to certain conditions. The variance in the wheel speed signal is used to separate between rough and smooth surfaces. Further developments and discussion about this method can be found in [Müller and Uchanski, 2001] and [Müller *et al.*, 2003]. Another approach has been published in [Ray, 1997] where the vehicle longitudinal and lateral accelerations, the vehicle yaw rate, and the speed of the wheels are measured. The corresponding tire forces are estimated by an extended Kalman-Busy filter and among several tire models the most probable is chosen through Bayesian learning. An expectation is that such an algorithm is depending on extensive calibration and that the choice of tire models has to take the behavior of the actual tire into account.

One method based on the brush model is published in [Pasterkamp and Pacejka, 1997], where the relation between the self-aligning torque

and the lateral tire force is used to estimate the friction while turning. The approximations in the brush model becomes apparent in the real application and neural networking is employed to learn the estimator to determine the friction. A simpler method for using the relation between the self-aligning torque and the lateral tire force can be found in [Yasui *et al.*, 2004].

Several different friction-estimation techniques are discussed in [Eichhorn and Roth, 1992]. One unique approach that is presented is to mount a microphone close to the tire-road contact and by the acoustics separate the different road surfaces. It is concluded that the recorded sound contains information about the friction, but distinguishing it from the other possible noise sources is difficult. The paper also includes an evaluation of a tread strain sensor, which shows promising result at least for detecting low friction. This kind of sensor is further described in [Pohl *et al.*, 1999]. Due to the varying pressure distribution in the contact patch there is often a region where the tread slides on the road. The friction is derived by evaluating the vertical and horizontal tread forces in that region.

In [Umeno *et al.*, 2002] the frequency contents of the wheel speed signal is analysed. From the frequency and magnitude of the resonance peak, the tire stiffness is estimated. The method can not predict the friction coefficient, but might work as a detector of a change of the road surface.

The number of patents dealing with this kind of problem is voluminous. Searching on friction estimation of tires give almost 500 hits at this date. In this project, a share of the found patents were selected for further examination, but a suitable approach for friction estimation was not found among those. Probably, related innovations are hidden from being found by forming the title without mentioning words as “friction” and “estimation”. One such example is [Levy and Fangeat, 2004] which describes a device that measures the secant $G(\lambda) = f_x(\lambda)/\lambda$ in the force-slip plane. From the presumed tire model, $G(\lambda) = a - b\lambda$, predicting the secant behavior, a and b are estimated. By knowing a and b, further conclusions about μ and λ°, substantiated by measurement data, can be drawn. Similar expectations can be derived from the brush model where $\sigma^\circ \approx b/a$, $\lambda^\circ = 1/(\sigma^\circ + 1)$ and $\mu \approx a^2/(3b)$ even if these differ slightly from the conclusions in the patent. The proposed method resembles this approach in that two parameters are estimated from the tire characteristics. The estimation routines are, however, completely different.

7.2 Experimental Validation of the Brush Model

This section presents an experimental validation of the brush-tire model used in the Road Friction Estimation project. The aim is to validate the

agreement of the tire model towards real conditions and to investigate the sensitivity of the included parameters toward various factors that may change during normal run of the vehicle. It is important to validate the model to measurement data collected at real driving. The environmental disturbances and the limited measurement conditions in a production car have to be regarded when evaluating the fit of the data to the brush model. Otherwise, the results may not be valid and the estimator will not work as expected in the real implementation. However, in the first verification of the usability of the brush model, it is desirable to minimize the uncertainties from the signal estimations, necessary for the limited sensor situation in a normal car. Therefore, the measurements are performed by a special tire test-truck from VTI, but the tires and road conditions are normal. Additional available tests results, not collected within the project will also be referenced in this section.

Test equipment The test vehicle, denoted *BV12*, is a Scania truck LB80, see Figure 7.1, owned and run by VTI and equipped with a fifth wheel for various measurements and slip and force excitations of tires for personal cars. The test wheel is pressed against the road by the pressure from a hydraulic cylinder, which can achieve different vertical loads in the range 1–6 kN. A varying brake torque can be applied on to the wheel through a disc brake controlled by a hydraulic brake system. The angle between the vehicle travel and the wheel rotational direction can also be changed during a test sequence. There are sensors on the wheel suspension for measurements of the vertical and horizontal forces and the vertical torque working on the wheel hub. There is also a sensor to measure the rotational velocity of the test wheel. The vehicle reference speed is obtained from the left-front wheel of the truck. Further information is available from [Nordström and Åström, 2001].

Test facilities To be able to collect information about a number of tires on several different road foundations with rich variation, tests were performed at two test grounds.

- **Hällered** is a proving ground close to Borås owned by Volvo Company. The facility has an area of 700 hectares and includes tracks for high-speed, endurance, off-road, and comfort testing tracks [Volvo AB, 2006]. For the testing in this project mainly the brake and handling area was used, where high and low-friction tracks are available with the possibility of water spraying. The high friction surface is normal asphalt, having the same properties as a well treated highway. The low friction area is built up by basalt bricks providing low friction when sprayed with water.

Figure 7.1 The test truck BV12 in Arjeplog.

- **Arjeplog** is a famous place in northern Sweden for winter testing of vehicles. Many companies provide test facilities for the automotive industry. The tests in the project were performed at the proving ground run by Colmis AB, see [Colmis AB, 2006], since both Haldex and GM have contracts with them. The available surfaces are ice, snow and asphalt. The asphalt patch is held free from snow by heat from elements in the ground, but when it is snowing the lanes quickly fills with water and melting snow. The frictional properties of both snow and ice are temperature sensitive and the temperature can change in a large interval from day to day.

Test procedure The longitudinal tire data was generated by applying a braking torque on the wheel as a ramp function from free rolling to complete lock-up of the wheel. When the wheel got locked the brake pressure was released and this sequence was repeated for a number of times depending on the available road length. Between 2–5 sequences where collected in one file. For each test setup 1–3 files were recorded. In Hällered the vehicle speed was 70 km/h during the braking phases and in the Arjeplog it was 50 km/h. The winter tire with 4 kN vertical load was chosen as reference setup and was subjected to all available test conditions. The load dependence was measured by varying the vertical load between 2, 4, and 6 kN. Dry asphalt was tested both for summer and winter tires. Result from wet basalt giving a low-friction firm surface were only obtained for the winter tires. Snow and ice was tested with all three tire types,

which were:

- Winter tire: Continental ContiWinterContact TS810 215/55R16
- Summer tire: Continental ContiSportContact 225/45R17 91W
- Studded tire: Gislaved Nordfrost 3 215/55R16

Data from lateral steering tests and braking with a few different slip angles were also collected and results can be found in [Svendenius, 2007a] and [Svendenius, 2007b].

Test results

The result from the measurements are shown in figures with the slip, λ, see definition in (2.5), on the x-axis and the normalized longitudinal brake force $-F_x/F_z$ on the y-axis. The different plot-styles of the data points denote which of the repeated sequences in the test file the measurements belong to. The solid line is the optimal-fitting brush-model adaptation to the data. The brush model is given by

$$F_x = \begin{cases} -C_x\sigma_x + \frac{1}{3}\frac{C_x^2\sigma_x|\sigma_x|}{\mu F_z} - \frac{1}{27}\frac{(C_x\sigma_x)^3}{(\mu F_z)^2} & \text{if} \quad |\sigma_x| < \sigma_x^\circ \\ -\mu F_z \text{sign}(\sigma_x) & \text{otherwise} \end{cases} \tag{7.1}$$

where $\sigma_x^\circ = 3\mu F_z/C_x$ and the optimal values on $C_{0x} = C_x/F_z$ and μ are derived by minimizing the squared error along the y-axis. The optimization algorithm is a Gauss-Newton method similar to the one that will be presented in Section 7.3. For the optimization all visible data points in the plots, with slip lower than approximately 20% are used and equally weighted in the cost function. The shown data points belongs to the first part of the test sequences where the braking torque is increasing.

The measured signals contain biases which effect the fit of the brush model. The bias on the longitudinal force sensor is mostly small and need no further correction. The bias on the longitudinal slip may be explained by error in the estimated free rolling wheel-radius, R_e, defined as the rolling radius of the wheel when no force is transmitted by the tire, see Section 2.4. Before start up of the tests R_e is identified. There are, however, many factors that affect R_e and changes in the radius may alter the slip bias. Therefore, R_e has to be identified and accounted for in each test sequence. The slip bias, often called horizontal shift, s_h, is related to changes in the wheel radius as

$$s_h \approx \frac{\Delta R_e}{R_e} \tag{7.2}$$

Only a few of the available measurements are shown here, but more resulting plots and results can be found in [Svendenius, 2007a] and [Svendenius, 2007b].

Winter tire Winter tires, generally, have relative soft rubber compound getting its optimal stiffness in a lower temperature region than the summer tire, which can be seen on lower values on C_{0x}. The rubber texture is rough to provide good grip in loose foundations such as snow.

Measurements together with the adaptations of the brush model to the winter tire on wet asphalt are shown in the force-slip-plane to the left in Figure 7.2. The right plot shows the test sequences generating the data. The force excitation is similar to the other tests, but the number of applications varies. The results from dry asphalt and from basalt are shown in Figure 7.3. On both wet and dry asphalt the agreement of the brush model is very good. The measurement deviations are symmetrical around the model realisation and can be explained by temporary disturbances. The cluster of points in the low-force region ($|f_x| < 0.3$) are explained by the vibrations in the measurement rig when the braking torque is released. See the force measurements in the upper plot to the right in Figure 7.2 between, for instance, 2.5 and 3 sec. For the low-friction foundation the temporal disturbances largely affects the measurements. The splices between the basalt bricks introduce extra road unevennesses and the disturbances are slightly larger than for asphalt, but their relatively impact become larger due to the lower excitation force needed to lock the wheel. It is difficult to verify the model from these measurements, but no consistent deviation from the model realisation seems to be present.

Results in winter conditions from Arjeplog are presented in Figure 7.4 for snow and ice. The snow measurements are noisier due to the unevennesses and traces in the randomly packed snow. In spite of this, it can be seen from the data that the performance on snow diverge from the brush model particularly at normalized forces above 0.2. The tire curve has more substantial curvature and no pronounced force peak. The tire force increases with the slip, at least up to $\lambda = 40\%$. This is probably an effect of the snow deformation.

Due to the large spread in the data it is difficult to draw any clear conclusions of the ice measurements.

Summer tire Summer tires are designed to achieve good grip in summer condition. Compared to the winter tire, the somewhat simpler task increases the possibilities to improve properties such as rolling resistance and wear resistance to provide a more cost-effective driving. Slick tires without texture is said to give best grip in good weather conditions on asphalt [Haney, 2003]. Grooves in the tire are, however, inevitable for

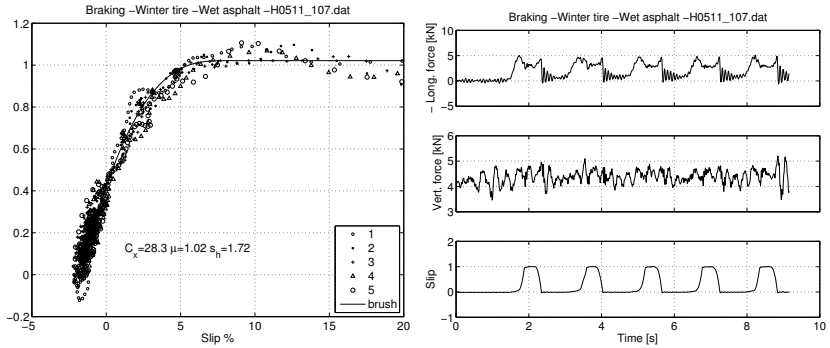

Figure 7.2 Measurement data from Hällered showing results from the winter tire on wet asphalt with a vertical load of 4 kN. To the left: Adaptation of the brush model. The normalized brake force is shown as a function of the slip, λ. To the right: Recorded signals showing the test sequences in the measurement file.

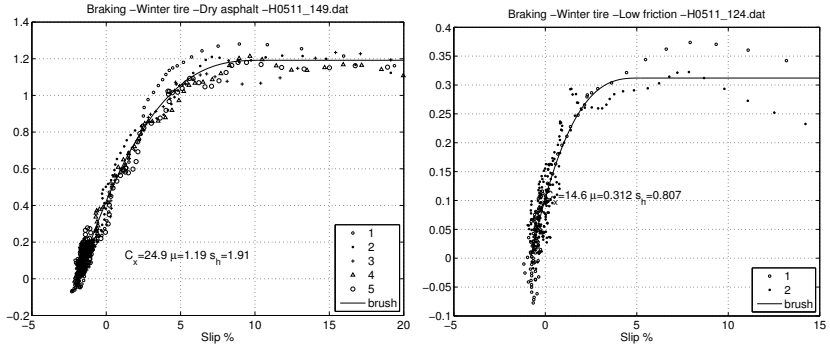

Figure 7.3 Measurements of the winter tire at Hällered together with a brush model adaptation at the vertical load 4 kN. To the left: On wet asphalt. To the right: On basalt. Note, that scaling on the axes differs between the figures.

evacuating water from the contact patch to prevent friction losses due to a water film when driving on a wet road. The texture on the tested summer tire seems to efficiently cope with the water, since the difference in performance between the dry and wet asphalt is small, which can be seen in Figure 7.5. A difference is that the tire force for the wet asphalt has a slightly less curvature up to the peak, which comes at an lower slip then predicted by the brush model. The force peak is more pronounced in the wet condition and the friction force reduces quicker for higher slip. The poor frictional properties of the summer tire on snow and ice, can be seen

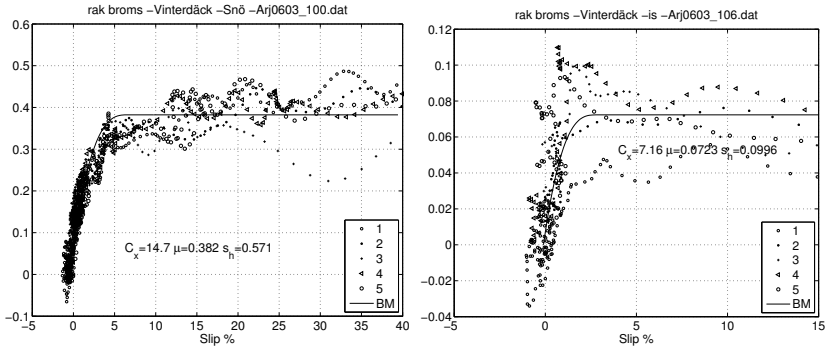

Figure 7.4 Adaptation of the brush model towards measurements data from Arjeplog with winter tire and with the vertical load 4 kN. To the left: On snow. To the right: On Ice. Note, that scaling on the axes differs between the figures.

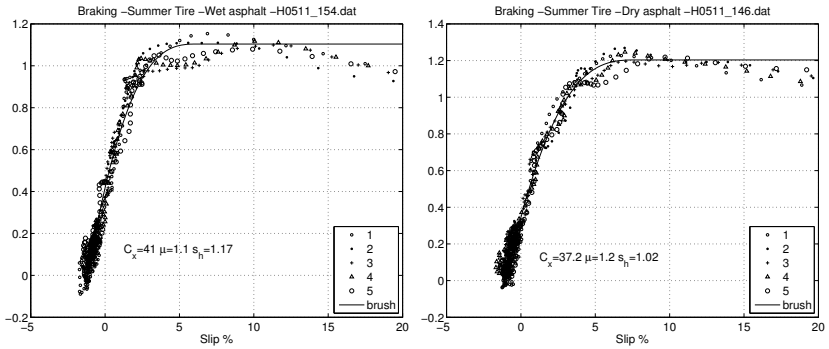

Figure 7.5 Adaptation of the brush model towards measurement data from Hällered with the summer tire and with a vertical load of 4 kN. To the left: On wet asphalt. To the right: On dry asphalt. Note that scaling on the axes differs between the figures.

in Figure 7.6. The tire do not get a good grip in the snow and the characteristics clearly differs from both the winter and studded tire, in that the friction is lower and do not increase for higher slip. The ice properties do not significantly diverge from the winter tire.

Studded tire Studded tires are gripping the road foundation with spikes. The tire force is build up with approximately 10% from the rubber friction and 90% from the spikes. A drawback with studded tires is that the abrade on the roads is extensive, and that micro particles are spread

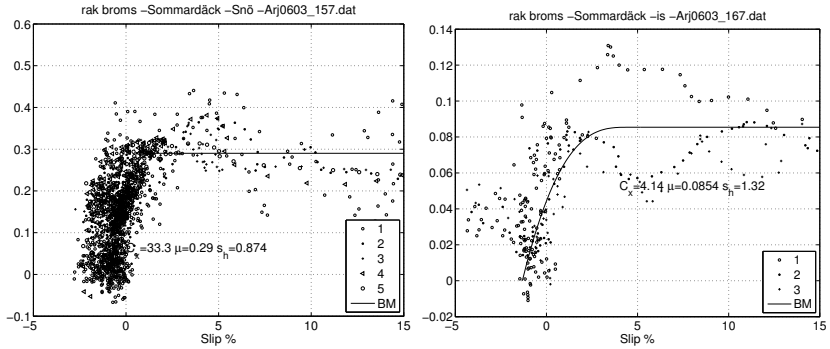

Figure 7.6 Adaptation of the brush model towards measurement data from Arjeplog with summer tire and with a vertical load of 4 kN. To the left: On snow. To the right: On Ice. Note that scaling on the axes differs between the figures.

in the environment to a larger extent than when using normal tires. The attention to this kind of pollution problem have gained a larger interest recently. Studded tires have a positive effect on the road friction in that they tear away the polished surface caused by normal tires. On the other hand, the traces from the tires in the road get deeper and collect more water, which require more extensive road maintenance [Gustafsson *et al.*, 2006b]. The studded tire is, however, outstanding in friction on ice, which can be seen from the results in Figure 7.7. Particularly on ice, the measurement signals contain more noise than the other tires. The grip of the spikes seems to be varying and unpredictable. The measured behavior on snow is very similar to the winter tire, but with a larger noise level. The latter is most probably a result of the snow packing when running back and forth on the test lane or of shifting of the snow properties by other reasons.

In Figure 7.8 the footprints from the studded tire on ice in a braking phase can be seen. The increasing length on grooves from the spikes is a consequence of the increasing tire slip caused by ramping up the braking torque. Since a bristle, according to the brush-model theory from Section 4.1 both enters and leaves the road undeformed, the sliding distance of a bristle onto the ground is $l_s \approx v_{sx} t_c(-a)$ where v_{sx} is the relative velocity between the tire carcass and the road and $t_c(-a)$ is the time that a bristle spends in the contact patch. The time for the road contact can also be expressed as $t_c(-a) = 2a/v_c$. The groove length can then be calculated as $l_s \approx v_{sx} 2a/v_c = \sigma_x 2a$. Hence, the slip could theoretically be derived from measurements of the groove length if the length of the contact patch, $2a$, is known.

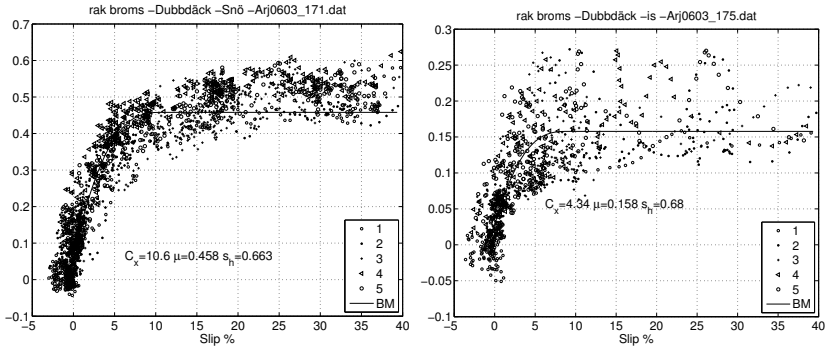

Figure 7.7 Adaptation of the brush model towards measurements data from Arjeplog with studded tire and with the vertical load 4 kN. To the left: On snow. To the right: On Ice. Note that scaling on the axes differs between the figures.

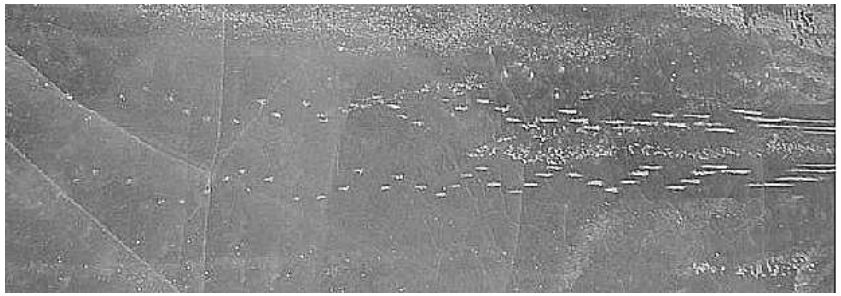

Figure 7.8 Footprints of the studded tire on ice during brake application. The brake torque is applied as a ramp and the increasing grooves are a result of the increasing tire force. the wheel is rolling from the left to the right.

Conclusions From the shown figures it can be seen that the brush model mostly fits the measurement data well. The optimized tire model is well within the spread of the data points. The spread is, however, relatively large on the low friction surfaces, which depends on that the force disturbances on the measurement rig becomes more apparent when the force excitation is low. The disturbances mainly come from low frequency vibrations in the mechanical structure invoked by unevenesses in the road and the force excitation on the wheel. The major question about the usability of the brush model for friction estimation for the tested tires on the available surfaces are treated further on.

The derived tire parameters for the different test setups are presented in Table 7.1 and visualized in Figure 7.9. From the results it is stated that

- The braking stiffness for the summer tire is larger than for the winter tire and the studded tire.
- The difference between the friction of the summer and the winter tire on asphalt is small.
- The normalized braking stiffness seems to increase for increasing vertical load for the winter tire on asphalt and snow, but not on ice. This topic is important for the friction estimator and further discussed later on.
- The studded tire has better friction on ice, that the other tires.
- The summer tire has poor grip on snow, when studded tire and the winter tire performs similar.
- There seems to be a relation between the tire stiffness and friction coefficient, see Figure 7.9.
- The braking stiffness is larger for wet asphalt than for dry. This is further discussed later on.

An interesting observation is that the winter tire and the studded tire behaves similar on snow. The force-slip curve has no obvious maximal point and the tire force seems to be an increasing function of the slip. The curve also bends off more than the brush model which might be an effect of that the tires grip into the snow which yields at a particular strain. The summer tire differs and behaves more as it would slide on the packed snow surface. There are models on how to deal with deformable foundations, e.g [Meschke *et al.*, 1996] and [Saino, 2001] and they tend to become very complex. One reason for not incorporating the snow behavior in the brush model is the reluctance in introducing more parameters in the model in this work.

The higher noise levels on the measurements on snow for both the summer tire and the studded tire compared the winter tire might be confusing. These are most probably results of the snow packing when running back and forth on the test lane or of shifting of the snow properties by other reasons. It is most unlikely that the different noise levels entirely depends on the tire properties.

Brush model verification

The most relevant issue when evaluating the measurement data is the ability to estimate the friction coefficient from the brush model realisation. It is obvious that the friction can be accurately estimated when data from the full slip curve $0 < \lambda < 1$ is available since the friction is completely given by the normalized tire force at high slip. At low slip the entire

Table 7.1 Results of the parameter optimization

Tire	Foundation	Load	C_{0x}	μ	s_h [%]
Winter	Wet asphalt	2 kN	23.8	0.98	1.2
Winter	Wet asphalt	4 kN	27.6	1.0	1.7
Winter	Wet asphalt	6 kN	28	1.1	1.9
Winter	Dry asphalt	4 kN	25	1.2	1.8
Winter	Basalt	4 kN	16	0.27	1.2
Winter	Snow	2 kN	9.04	0.40	0.69
Winter	Snow	4 kN	13.6	0.40	0.55
Winter	Snow	6 kN	14.4	0.41	0.20
Winter	Ice	2 kN	6.27	0.10	0.64
Winter	Ice	4 kN	6.25	0.078	0.077
Winter	Ice	6 kN	6.72	0.081	-0.25
Summer	Wet asphalt	4 kN	42.8	1.1	1.1
Summer	Dry asphalt	4 kN	37.3	1.2	1.0
Summer	Snow	4 kN	22.8	0.26	1.1
Summer	Ice	4 kN	3.6	0.077	1.35
Studded	Snow	4 kN	11.4	0.51	0.77
Studded	Ice	4 kN	5.6	0.16	-0.70

contact surface is adhesively bonded to the ground and according to the brush model the force-slip relation do not contain any information about the friction then. The eventual relation between the braking stiffness and the friction is a different issue discussed further on in this section. To be able to estimate the friction from the data using the brush model, the curvature on the measured force-slip relation must be detectable. An important issue is the accuracy of the estimation if only low-slip data is used. This section will investigate how the value of the highest available slip or force affects the accuracy of the friction estimation. It might be possible to detect a lowest slip value where the friction can be detected within a certain accuracy from the slip and force measurements. Figures 7.10–7.11 show the results from the winter tire on snow and asphalt, where the tire parameters are identified for data upto a certain slip. The obtained tire characteristics are shown for the slip limits, $0.5, 1, 1.5...15\%$. The slip limits are marked in the graph as vertical dashed-dotted lines. On re-

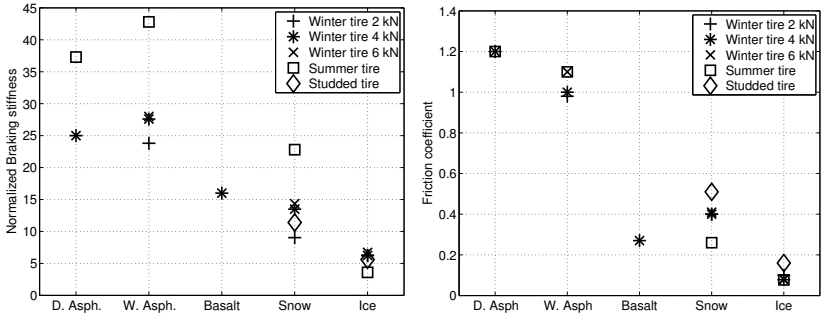

Figure 7.9 Visualization of the results from Table 7.1. The normalized tire stiffnesses and friction coefficients of the tested tires at different loads are plotted as functions of the surface.

spective line there is a asterisk denoting the friction estimate and a ring prescribing the braking stiffness. The parameters are derived by using only the data to the left on the actual slip-limit value. The tire characteristics belonging to the different parameter results are drawn with solid thin lines. A small asterisk in the intersection between the vertical slip limit line and the tire characteristic line shows to which parameter set the line belongs. In some cases the small asterisk is obscured by the larger friction estimate marking. An observation is that the friction is underestimated in both the shown examples. The more apparent deviation from the brush model for snow makes this particularly obvious. An advantage is that the estimation early says that the friction is low. The drawback is that it might too early state that the friction peak is reached. For asphalt it is clear that there is more available friction, for instance, at 2% slip the estimation is 0.6 and the normalized tire force is around 0.4. When the normalized tire force is around 0.9 the algorithm states that the friction limit is reached. This is within the tolerances.

In Table 7.2 the need of tire force excitation necessary to provide an friction estimation within the specified accuracy of ± 0.15 is presented. The tabular values prescribes the degree of utilization of available friction force. Generally more than 65% of the available friction force must be generated before an accurate estimate can be derived. Ice can not produce an estimate before the limit is reached. The available friction is, however, very low and the friction is estimated at a low slip value. The friction is given before the locking phase of the wheel, which might be good information for the ABS-system. The poor result for the summer tire on wet asphalt is explained by deviation between the tire behavior and the brush

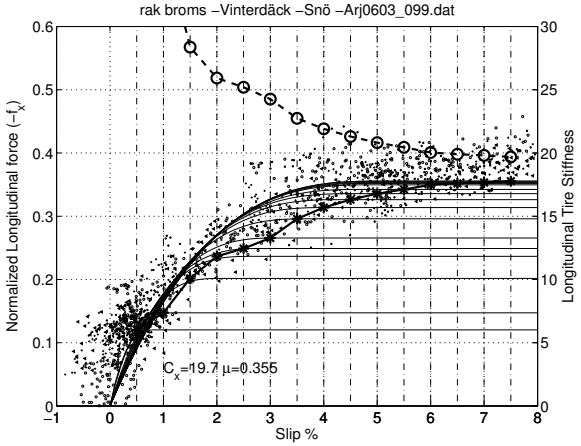

Figure 7.10 Parameter estimates as functions of the highest used slip value for the winter tire on snow. The estimated tire stiffness (dashed line with circles) and friction coefficient (full line with asterisks) by using only the data points to the left of the slip limits [0.5,1,1.5 .. 8] (dashed-dotted vertical lines) are plotted. Also the tire characteristics for the estimated parameters at each slip limit are plotted.

Table 7.2 Required utilization of friction (in percent) to achieve a friction estimate within an accuracy of ±0.15. Only tests at 4 kN is used.

Road foundation	Winter	Summer	Studded tire
Dry asphalt	75	69	-
Wet asphalt	74	95	-
Basalt	87	-	-
Snow	66	81	74
Ice	100	100	68

model around the force peak which is mentioned earlier.

The investigation shows on the possibilities and restrictions for an friction estimator relying on the brush model. The study has to be considered as very approximate, since some of the disturbances that are present will not affect the signals in a car. One example is the sensitivity towards road unevenesses. The hydraulic piston generating the pressure between the tire and the road has stiff and slow suspension. The vertical load on the tire therefore fluctuates more than what is expected in a passenger car. The sensors in a car do, on the other hand, not deliver that precise

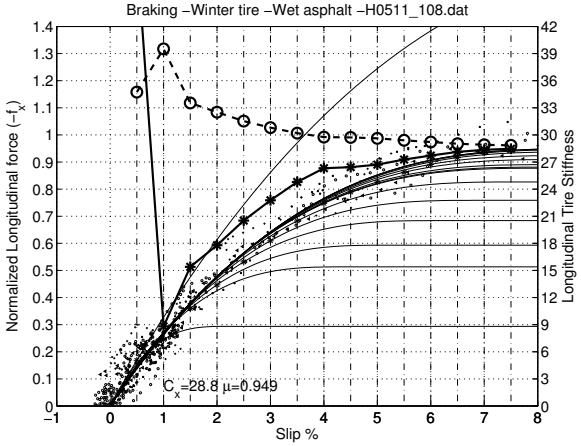

Figure 7.11 Parameter estimates as functions of the highest used slip value for the winter tire on asphalt.

measurements. The optimization algorithm used to derive the examples is not fully developed and further enhancements, such as filter and correct data weighting may improve the result significantly. Overall, from the experiences from the brush model verification, the conclusion is that an estimation algorithm based on the brush model will work, but high friction utilization is required for an accurate friction estimate.

Parameter sensitivity

This section will discuss the sensitivity of the tire behavior to a few conditional factors. It is also important to know in what ranges and circumstances a parameter might be expected to vary when designing an estimator. An aim with the investigation is to find out whether further signals, to cover for parameter changes, have to be regarded within the algorithm.

The friction coefficient depends on the tire-road interaction, while the braking stiffness is assumed to depend on more tire related properties as the tread stiffness and the size of the contact patch between the tire and road, see (4.31). As been noticed previously and in, for example, [Gustafsson, 1997] and [Müller and Uchanski, 2001] there is a co-variation between the friction coefficient and the braking stiffness. The relation is physically difficult to explain and does not always hold. Tests have confirmed that very rough asphalt can provide high friction, but a low stiffness, due to the smaller effective contact patch compared to a smooth surface. The braking stiffness is sensitive to many other factors and a change of the stiffness

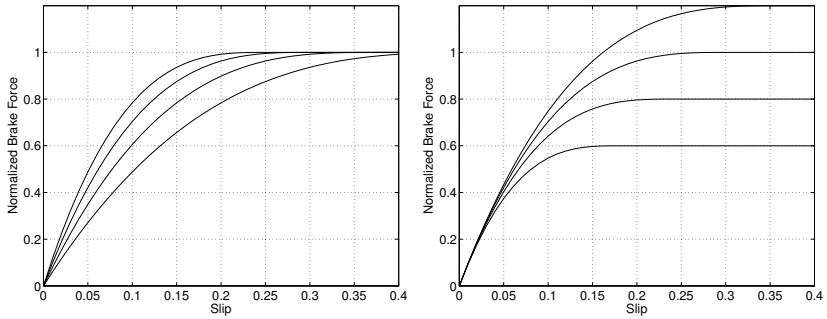

Figure 7.12 Plot of the force-slip relation of the original brush model. To the left: Varying tire stiffness $C_x = [6, 8, 10, 12]$. To the right: Varying road friction coefficient, $\mu = [0.6, 0.8, 1, 1.2]$.

might not guarantee a change in friction. The effects on the brush model characteristics when varying the parameters are shown in Figure 7.12. The rolling radius of the tire is another parameter that is important to estimate accurately. Small changes from its nominal value will give an offset on the slip calculation, see (7.2), which largely effects the estimation of C_x and μ.

Vertical load The vertical load on the tire affects the size of the contact patch. If the pressure distribution in the tire-road contact was uniform the area would be easily calculated as F_z/p_t. This is not, normally, the case, see [Svendenius, 2003] or [Pauwelussen *et al.*, 1999]. The pressure distribution varies within the patch and with the magnitude of the vertical load, [Kim and Savkoor, 1996]. At larger deformations of the tire, the pressure in the tire increases due to the shape change of the carcass. The braking stiffness is dependent of the contact patch size, but a simple physical model of the relation between the stiffness and the vertical load is difficult to obtain. The load on the tire is an important factor since it varies widely, due to the load transfer during braking and acceleration. In trucks and trailers the variation range of the tire load is particularly large, since the weight of the cargo is the major share of the total load. There are, however, good possibilities to estimate or measure the load on each tire.

Figure 7.13 shows the load sensitivity of the normalized tire stiffness $C_{0x} = C_x/F_z$ and the friction coefficients from the previously presented measurements. In Figure 7.14 the tire stiffnesses from the test on a Jeep Cherokee, with Goodyear Wrangler tire, see Section 5.4 and Figure 5.4 is shown. In [Nordström, 1983] measurements of a Firestone 10.00x20/F

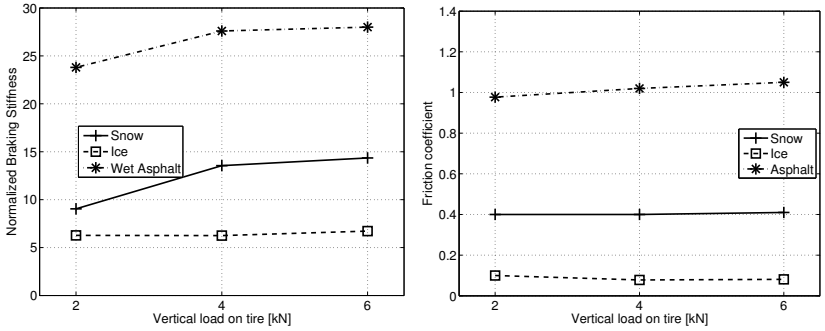

Figure 7.13 Diagrams showing the load dependence in the previously presented measurements, see Table 7.1. To the left: The normalized braking stiffness, C_{0x}. To the right: The friction coefficient, μ.

truck tire shows an slightly decreasing normalized stiffness, C_{0x}=[14.3, 9.8, 7.6] at the loads [10,25,40] kN. The available measurements regarding the load dependence of the braking stiffness clearly states that different tires behaves differently. The braking stiffness increases with increasing load, but not linearly since the normalized braking stiffness is not, generally, constant and behaves differently from tire to tire. Within the observed load range and the studied tires it seems reasonable and less wrong to assume the normalized braking stiffness as constant rather than the braking stiffness as constant.

Figure 7.15 shows the load dependence on the rolling wheel radius from the measurements in Table 7.1. The rolling radius changes up to 1 mm/kN or 0.3%/kN from the nominal values. In [Carlson and Gerdes, 2003], an article diligently cited in the following, the tire stiffness and rolling radius is estimated for the ContiWinterContact TS790 and the Goodyear Eagle F1 tires under various conditions. The reported load sensitivity of, R_e from that article is in good agreement to this results.

Impact of water film on road A layer of water on the road affects the size of the contact patch, since the layer can be assumed to carry a part of the vertical load without any frictional force contributions. This is verified in [Pauwelussen *et al.*, 1999] where it also is stated that the decrease of the dynamic contact size, i.e. for a rolling wheel, strongly depends on wheel velocity.

A conclusion is that the braking stiffness, characterized as $2c_{px}a^2$ in the brush model, see Equation (4.31), decreases since the utilization of the contact length, $2a$ decreases. Result presented in Table 7.1 shows the opposite, that the braking stiffness increases for the wet road. An

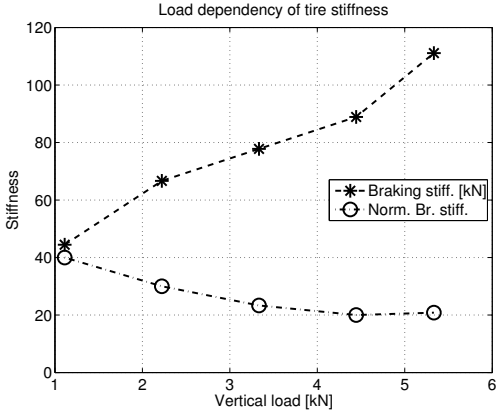

Figure 7.14 Comparison of the load dependence between the braking stiffness and the normalized braking stiffness. Longitudinal data from vehicle test, described in Section 5.4 and [Salaani *et al.*, 1999].

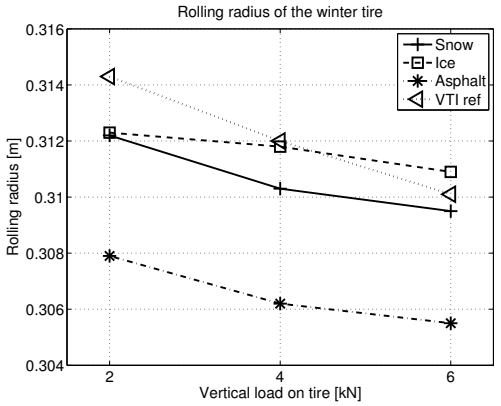

Figure 7.15 Diagram showing the load dependence of the rolling radius

explanation is that the water cools the tire and the lower temperature will raise the braking stiffness. An observation in [Carlson and Gerdes, 2003] where wet and dry asphalt surfaces have been compared is that the impact, on the braking stiffness, due to the used water layer, was smaller than any other influencing factor, such as temperature, tire pressure, and wear.

The friction force on a wet surface mainly decreases by two reasons.

Table 7.3 Braking stiffnesses for two different inflation pressures. Test results from measurements performed at Haldex.

Pressure		C_{0x}	
		Asphalt	Snow
	6 bar	24	18
	8 bar	16	14
ratio	0.75	0.67	0.78

First, the lower share of load on the frictional carrying contact surface and then the lubricating effect of the water in the effective area in the contact. In [Gothie *et al.*, 2001] the friction for different tires, asphalt surfaces, and water depths is further examined.

Inflation pressure The tire pressure is an important factor for the contact patch properties. The size of the patch depends on the relation between the pressure and the vertical load. The complex geometry of the tire makes the pressure distribution non-uniform and changing with tire deformation, hence it is difficult to derive this relation. Often a decrease of the inflation pressure has similar effect on the tire properties as an increase of the vertical load. In a test performed by Haldex at the test facility in Arjeplog with a Scania test truck, see [Svendenius, 2003], the impact of the inflation pressure on braking stiffness was measured. The result for the tested truck tires is shown in Table 7.2 which shows a nearly linear relation between the tire pressure and the braking stiffness. Large variation of the dependence on the inflation pressure of the tire stiffness for different tires has be noticed in [Schmeitz *et al.*, 2005]. Out of five tested tires three showed similar behavior as above, but two showed almost the opposite, where the tire stiffness increased for higher pressure.

In [Carlson and Gerdes, 2003] an increase of 30% on the braking stiffness for a pressure decrease of 20% from nominal tire pressure is reported. The rolling radius decreased 0.5–1 mm (nominal 309 mm) for the tested tires under the same conditions. The pressure dependence on the rolling radius is e.g. used in a tire pressure monitoring device, described in [Persson *et al.*, 2002], as one of the factors for detection of low tire pressure.

Effect of tire wear When the depth of the tread decreases the tire stiffness increases. The decreasing amount of rubber also makes the rolling radius smaller. These observations are verified in [Carlson and Gerdes,

2003] where shaved tires are tested. The friction properties are mainly effected on wet road or on loose foundation such as snow and gravel, where the tread pattern is important.

Velocity dependence The velocity mainly affects the friction in the meaning that the sliding velocity between the tire and the road is higher for a higher vehicle speed at a particular slip. The friction is often refereed to as sliding speed dependent, see e.g. [Guo *et al.*, 2006]. Different road foundations and different tires certainly exhibits different interactions. A water film on the road increases the velocity dependence and increasing velocity drastically increases the risk for aquaplaning. An example of the velocity dependence of the friction on a 3 mm thick water layer on the road can be found in [Do and Delanne, 2003], where the locked wheel friction drops from 0.7 at stand still to around 0.05 at 100 km/h.

In [Pirelli, 2005] the velocity dependence on the rolling radius was tested for a few type of tires. The result showed that the rolling radius increases for higher speed, but first above a (in Sweden) non-legally speed limit it became noticeable.

Temperature sensitivity Rubber is normally very sensitive to temperature changes. Therefore, also the tire parameters will change with the temperature. In [Carlson and Gerdes, 2003] a decrease of 20% on the braking stiffness between the first and the fifth braking in a number of braking sequences is reported which is explained by the temperature increase. For the same condition the increase in rolling radius was less 0.1% (0.3 mm). In [Mizuno *et al.*, 2005] the braking stiffness was modelled, based on measurement data, to decrease 5% within a temperature change from 40 to 60 [deg] C.

Summary The dependence of the parameters in the brush model and the rolling radius towards the examined factors are summed up in Table 7.4

Conclusions

This section has treated the issue, whether it is possible to describe any tire at any common road surface with the brush model containing only two parameters. The answer is of course, that it depends on the requirements on the accuracy of the model. In this context the accuracy of the model towards the data affects the possibilities to estimate the friction coefficient. A conclusion is that there are deviations between the data and the model, but friction estimation is possible, even though rather high utilization of the friction is required for an accurate estimate. The utilization of the friction for estimating the friction coefficient within $\pm 15\%$ is in the

Table 7.4 Summary of parameter dependence. A, '+', signifies that the factor increases if the factor increases and vice versa. – means the opposite. A small and normally neglectable relation is denoted by $\sim$. No sign means that no results are available.

Parameter	Pressure	load	Wear	Water	Temp.	Vel.
R_e	+	−	−		$\sim +$	$\sim +$
C_x	−	+	+		−	
μ			−	−		−

best case 66%, i.e if $\mu = 0.5$ a normalized tire force of $0.5 \cdot 0.66 = 0.33$ is required. In the worst case the utilization has to be 95%. The used parameter optimization is a pure minimization of the squared error between the data and the model. It is emphasized that a more advanced estimation algorithm might reduce the need of friction utilization. The measurements performed by VTI incorporate discrepancies not present in a personal car. High demands on the signal processing that provides the required signals, F_x, F_z, λ from the existing sensors, might further improve the estimation results. It is also concluded that the parameters included in the brush model varies with many factors. Particularly important for a friction estimator is the load dependence of the rolling radius and the braking stiffness. Since the application of an acceleration or retardation force causes a load transfer on the vehicle, the vertical force on the tires will change. Changes in the rolling radius will then affect the slip calculation and cause a distorted slip-force curve. The variation of the braking stiffness for varying loads differs between the tires. Generally, the normalized braking stiffness is less sensitive to load fluctuations than the braking stiffness. Another important factor is the temperature sensitivity of the braking stiffness. The braking stiffness can change around 20% within a couple of brake applications, due to warming, without any change in friction.

7.3 Tire Parameter Estimation

The literature contains many different methods to identify a relation that describes the behavior of an observed system, see for instance [Johansson, 2002]. In some cases the identification aims at finding the set of equations that best describes the relation between the input and output signal of an unknown, so called *black-box* system. In the actual case the system is partly known and better explained as a *grey-box* model, where the behav-

ior is described by a particular equation structure, which includes known and unknown parameters. The latter are to be estimated. Normally, the procedures for parameter estimation aim at finding the set of parameters that minimizes the error between the adopted model and the measured output for a known input signal. The calculation of the error differs between the methods. In *off-line* methods the accumulated error for a set of data is used for the minimization. In the parameter computation all values in the data set, which can be measurement during a certain time period or observations collected by other means, are regarded without any demands on causality. In real-time systems often *recursive* methods are used to on-line update the estimation at each sampling instant. Mostly, the estimates at each time instant are based on a weighted sum of the previous estimate and information that can be extracted from the present measurements, see [Åström and Wittenmark, 1994]. Previous input data are only remembered implicitly in the estimated parameters and are forgotten as time passes.

A major problem in the present application is the issue of persistence of excitation. For the further description, the excitation is separated into space and time domains. Having persistence of excitation in the space domain requires that measurements are available in a sufficiently large region in the force-slip plane, providing an accurate stiffness and friction estimation. The aim of the method is to, as good as possible, estimate the friction coefficient at a low force excitation. The lower friction utilization, the smaller amount of information about the friction is contained in the data. Hence, the sensitivity towards measurement errors and model deviations toward real conditions increases. Further, it is required that the data is spread over sufficiently large region to be able to get an accurate and robust estimate. If the data points are clustered the cost function will not have a distinct minimum and the quality of the results decrease.

Having persistence of excitation in the time domain requires that the inputs vary sufficiently irregularly and often. When the conditions have changed, the data information should be fresh, to provide an accurate estimation that reflects the actual surface and tire condition.

Traditional estimation techniques are time depending which makes it hard to formulate the space-distributional requirement on the data. A typical situation where those methods fail is a brake application starting with a tire-force ramp which provides evenly spread data in the space domain. If the final tire-force value is large enough, this excitation is sufficient for a proper parameter estimation. When the ramp has settled the tire force is kept constant for the major part of the event. A recursive algorithm calibrated to be fast enough to catch the parameters during the ramp phase will soon forget the information collected in the low slip region and adapt to the measurements around the reached stationary

point. The measurements around this point will not contain information sufficient to estimate two parameters and the parameter observability and accuracy decreases drastically. As long as the estimated curve intersects the stationary point the parameters will change in between according to the present noise conditions and lose the relation to the actual friction condition and braking stiffness. Proposals on how to supervise adaptive controllers in related problems at limited excitation situations are given in, e.g [Hägglund and Åström, 2000]. A different approach is proposed in this work.

In the first phase, invariant surface conditions are assumed, such that there is no need to distinguish between old and new data. Information from the force and slip measurements are stored in data bins distributed over the force and slip-axis. The optimal tire parameters are then calculated using the stored data. Techniques to treat detection of a new surface and adaptation to slow changes of the braking stiffness and friction can be implemented together with the data storage and will be discussed afterwards.

Formulation of the estimation problem

The tire characteristic according to the normalized brush model, compare to Equation (7.1) used for the estimation is given as

$$\Psi(\sigma_x, C_{0x}, \mu) = \begin{cases} -C_{0x}\sigma_x + \frac{1}{3}\frac{C_{0x}^2\sigma_x|\sigma_x|}{\mu} - \frac{1}{27}\frac{(C_{0x}\sigma_x)^3}{\mu^2} & \text{if} \quad |\sigma_x| < \sigma_x^\circ \\ -\mu \cdot \text{sign}(\sigma_x) & \text{otherwise} \end{cases} \tag{7.3}$$

where the slip, σ_x and the normalized tire force, $f_x = F_x/F_z = \Psi(\sigma_x, C_{0x}, \mu)$ are the measured signals. The included parameters $\boldsymbol{\theta} = [C_{0x}, \mu]$ are to be estimated.

Data filtering by use of storage-bins

The motivation for data-filtering based on storage-bins is the problem of estimating the parameters of a scalar nonlinear function.

$$y = g(x, \boldsymbol{\theta}) \tag{7.4}$$

The specific application at hand is the estimation of the normalized braking stiffness, C_{0x}, and the friction coefficient, μ, from measurements of tire slip, σ_x, and normalized tire force, f_x, using the brush tire-model (7.3). The problem is divided into the construction of a point-wise approximation of Ψ described by pairs (σ'_{xi}, f'_i) and $(\sigma''_{xi}, f''_{xi})$ constructed from the measurements, and the estimation of C_{0x} and μ is performed by minimizing

the cost:

$$\sum_i w'_i \left(f'_{xi} - \Psi(\sigma'_{xi}, \hat{C}_{0x}, \hat{\mu})\right)^2 + \sum_j w''_j \left(f''_{xj} - \Psi(\sigma''_{xj}, \hat{C}_{0x}, \hat{\mu})\right)^2 \tag{7.5}$$

using parameter optimization methods.

The storage-bin concept is introduced to offer input data of a suitable format for the optimization algorithm. It is a method to store, in a compact form, information from different operating points with persistence over time. By this, it is easier to ensure sufficient excitation and observability for parameter estimation. For example, it may prevent loss of observability when driving at constant slip for a long time. It also offers the possibility of convenient post-processing and confidence classification of data before delivered to the optimization algorithm. As a result, change detection and handling of outliers can be done intuitively. Additionally, the method reduces effects of measurement noise, which is particularly important for the slip. The storage-bin filtering should be regarded as a practical method and we have not yet supported it with thoroughly theoretical analysis.

Definition Storage-bins are used to estimate an approximation of a function $g : x \to y$ at discrete points along the ranges of x or y, from imperfect samples $\hat{x}$ and $\hat{y}$. The ranges of x and y are partitioned into disjoint intervals $\mathcal{X}_i$ and $\mathcal{Y}_i$ defined by points x_i and y_i such that:

$$\begin{aligned} \mathcal{X}_i &= \{x | x_{i-1} < x \leq x_i\} \\ \mathcal{Y}_i &= \{y | y_{i-1} < y \leq y_i\} \end{aligned} \tag{7.6}$$

A basic form of a data bin X_i is a tuple $X_i = (\mathcal{X}_i, x'_i, y'_i)$ where x'_i and y'_i gives the local estimation of g for $x \in \mathcal{X}_i$. Likewise, a data bin Y_i is a tuple $Y_i = (\mathcal{Y}_i, x''_i, y''_i)$ where x''_i and y''_i gives the local estimation of g for $y \in \mathcal{Y}_i$. Monotonicity of g is obviously required for unique mapping of y to the Y_i-bins. For non-monotonic functions still the $\mathcal{X}_i$ mapping is valid.

Estimation The data-bin estimation can be regarded as event based rather than time based, since the estimate in any particular bin is updated only when measurement values fall within the corresponding range. Basic estimation is done by computing (x'_i, y'_i) and (x''_i, y''_i) as the recursive average of samples $\hat{x}$ and $\hat{y}$. To quickly get an accurate bin value at an initialisation a sample-count limit N_i and a sample count $n_i \in [0, N_i]$ to the bin tuples are introduced, such that the bin-value is an average of all values up to N_i, by having the forgetting factor $\lambda_i = 1 - 1/n_i$. After that, the forgetting factor is kept constant such that the estimates mainly

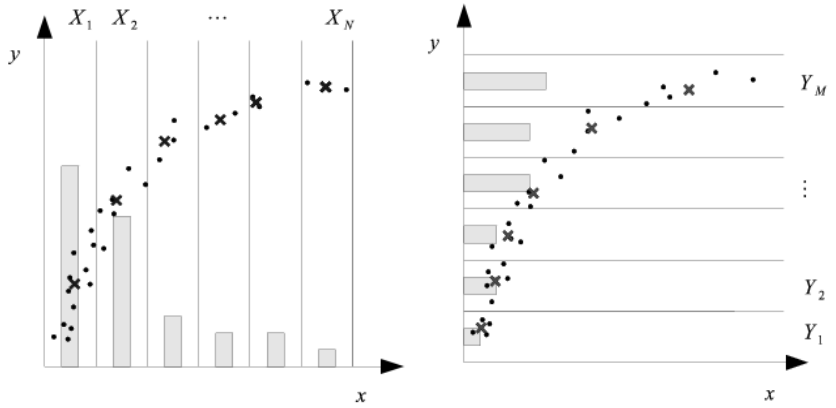

Figure 7.16 Illustration of data-bin concept. The dots represent samples that have been stored in the bins, and the crosses the resulting estimates. The staples indicate the present number of samples in the bin.

depend on the last N_i samples. Formally, the recursive-average estimates are given by:

$$x'_i(k) = \begin{cases} \lambda_i(k) x'_i(k-1) + (1 - \lambda_i(k))\, \hat{x}(k), & \text{when} \quad \hat{x}(k) \in \mathcal{X}_i \\ x'_i(k-1), & \text{otherwise} \end{cases} \tag{7.7}$$

and

$$y'_i(k) = \begin{cases} \lambda_i(k) y'_i(k-1) + (1 - \lambda_i(k))\, \hat{y}(k), & \text{when} \quad \hat{x}(k) \in \mathcal{X}_i \\ y'_i(k-1), & \text{otherwise} \end{cases} \tag{7.8}$$

The (x''_i, y''_i) are analogously formed by the $\hat{y}(k) \in \mathcal{Y}_i$ condition. Figure 7.16 illustrates some properties of the bin estimator for a function that relates slip and force in presence of measurement noise. Note how the Y_i (relating to the tire force) and X_i (relating to the slip), give better resolution in x at small and large x-values, respectively, because of the character of the brush-model function. This motivates the use of both sets of bin estimates (x'_i, y'_i) and (x''_i, y''_i) in the cost function (7.5), using $x = \sigma_x$ and $y = f_x$.

Statistical properties The averaging in the bin estimates computation reduces the effects of measurement noise. In theory, since the estimates (x'_i, y'_i), (x''_i, y''_i) are formed by sums of the samples, they will approach a normal distribution as stated by the Central Limit Theorem. That is,

the estimate x_i' will be aligned to the center of the bin X_i, and the estimate y_i' will go toward the mean value of function in the actual bin, i.e. $|X_i|^{-1}\int_{x\in X_i} g(x)\,dx$, under the assumption of equal and uniform distribution of the samples $\hat{x}$. Note that the local estimate only fulfills $y_i' = g(x_i')$ if the length on the interval $|X_i|$ is infinite. The error depends on the deviation from linearity of g in the bin range. The variance of the estimates decrease with the rate $1/n_i$. In practice, it is unlikely that the Central Limit Theorem convergence will have any significant visible effects, since the sample-count limit N_i will truncate the averaging sum.

Confidence assessment The data-bin tuple can also be extended with measures of the content quality. In particular, a recursive variance estimate of the samples can be introduced. Likewise, a freshness measure can be introduced to keep track of which data bins that contain the most recent information. Measures like this can be used to form weights w_i to be used in the cost function (7.5) for parameter estimation.

Optimization routine

The estimator is an optimization algorithm that from a set of data points, $\Omega = \{\Omega_i = [x_i, y_i],\ [\boldsymbol{x},\boldsymbol{y}] = [\boldsymbol{x}',\boldsymbol{y}'] \bigcup [\boldsymbol{x}'',\boldsymbol{y}'']\}$, calculates the parameters, $\boldsymbol{\theta}$, included in a function, g, such that the cost function

$$V(\Omega,\boldsymbol{\theta}) = \sum_{i=1}^{N} \frac{w_i e^2(\Omega_i,\boldsymbol{\theta})}{2} \tag{7.9}$$

is minimized. The number of coupled observations in Ω is N. The weighting of each data point for the estimation is specified in the vector $\boldsymbol{w} = \{w_i \in [0,1]\}$. The error is derived as

$$e_i = e(\Omega_i,\boldsymbol{\theta}) = y_i - g(x_i,\boldsymbol{\theta}) \tag{7.10}$$

Two different optimization algorithms are found suitable in the actual case. The *least-squares* method, a robust method, limited to linear parameter relations and therefore used to detect the slope curvature at low slips where the third order term, from Equation (7.3) is neglectable. The iterative and more computer demanding *Gauss-Newton* algorithm catches non-linear behavior and is used to reach a more accurate and reliable estimation when data points closer to the friction limit are available. The methods and their implementation using the brush model are described in the following.

The least-squares method The least-squares method is a linear-regression analysis method based on the model formulation

$$y_i = \boldsymbol{\phi}^T\boldsymbol{\theta} + e_i \tag{7.11}$$

where the output, y_i and the input, x_i are measured, calculated, or, in other way derived signals. The elements in the regressor vector $\boldsymbol{\phi}$ correspond to the parameters for estimation in the vector $\boldsymbol{\theta}$. The linearised approximation, $\boldsymbol{\phi}^T\boldsymbol{\theta}$ should not largely deviate from the real parameter relation for proper work of the least squares. The method in this form is a typical offline-method, which means that a batch of data, is necessary for the calculation of the parameters. For on-line use, the method is rewritten, as the *recursive least-squares*, see for example [Ljung and Söderström, 1983]. The result of the least-squares, derived for example, in [Gelb *et al.*, 1977], is the estimate that minimizes the sum of the square of the errors (7.9) and can be calculated as

$$\hat{\boldsymbol{\theta}} = (\boldsymbol{\Phi}^T\boldsymbol{W}\boldsymbol{\Phi})^{-1}\boldsymbol{\Phi}^T\boldsymbol{W}\boldsymbol{y} \tag{7.12}$$

The regressor matrix, $\boldsymbol{\Phi}$ contains the corresponding regressor vectors as $[\boldsymbol{\phi_1}\ \boldsymbol{\phi_2}\ ..\ \boldsymbol{\phi_N}]^T$ and the weight matrix is formed as $\boldsymbol{W} = \boldsymbol{I}\boldsymbol{w}$.

Using the least-squares method together with the brush model, the demand on linearity in the parameters, restricts the working range. For low slip, the tire stiffness can be calculated by choosing $\theta = C_{0x}$, with $\boldsymbol{\phi_i} = -x_i$. For estimation of the friction when a curvature of the force-slip relation is detected, the parameters are, $\boldsymbol{\theta} = [C_{0x} \quad \theta_2]^T$ and the regressors $\boldsymbol{\phi_i} = [-x_i \quad x_i|x_i|]^T$. The friction coefficient can be derived from the result as $\mu = C_{0x}^2/(3\theta_2)$. The neglection of the third-order factor of the slip from the brush model will give an error at higher slip and the method is not reliable if the data set includes slip values above σ_x°. The input and output signals, x, y are given by the σ_x and f_x values derived and stored using the storage-bin algorithm.

Gauss-Newton optimization In the area of convex optimization the Gauss-Newton method is used as a substitute to the least-squares method when non-linear problems have to be solved. The general problem is to minimize the sum of errors (7.9). A non-linear problem can in most cases not be solved directly and the solution has to be found by iteration. The amount of iterations depends, e.g. on the properties of the function, the initial values of the parameters and the required accuracy on the estimates. A common way is to update the parameters in the direction of steepest descent of the cost, $V(\Omega,\boldsymbol{\theta})$, hence $\boldsymbol{\theta}_{k+1} = \boldsymbol{\theta}_k - \nabla V(\Omega,\boldsymbol{\theta}_k)$. In Newton's method the quadratic term, corresponding to the change of the gradient,

is used to enhance the step length and direction of the search. The update becomes $\boldsymbol{\theta}_{k+1} = \boldsymbol{\theta}_k - \boldsymbol{H}^{-1}(\Omega, \boldsymbol{\theta}_k)\nabla V(\Omega, \boldsymbol{\theta}_k)$ where $\boldsymbol{H}$ is the *Hessian*, a quadratic matrix, whose entries are the second order derivatives of V with respect to $\boldsymbol{\theta}$, defined as

$$\boldsymbol{H}(\Omega, \boldsymbol{\theta}) = \frac{\partial^2 V}{\partial\theta_i \partial\theta_j}(\Omega, \boldsymbol{\theta}) \tag{7.13}$$

In most cases the calculation of the Hessian is not convenient and in the Gauss-Newton method it is approximated as $\boldsymbol{H}(\Omega, \boldsymbol{\theta}) \approx 2\boldsymbol{J}(\Omega, \boldsymbol{\theta})\boldsymbol{W}\boldsymbol{J}^T(\Omega, \boldsymbol{\theta})$. The Jacobian matrix of $\boldsymbol{e}$ is defined as, $\boldsymbol{J}(\Omega, \boldsymbol{\theta}) = (\partial e_i/\partial\theta_j)$ with $i = 1...N$ denoting the row number and j the column number. The update scheme becomes

$$\boldsymbol{\theta}_{k+1} = \boldsymbol{\theta}_k - (\boldsymbol{J}(\Omega, \boldsymbol{\theta}_k)^T\boldsymbol{W}\boldsymbol{J}(\Omega, \boldsymbol{\theta}_k))^{-1}\boldsymbol{J}(\Omega, \boldsymbol{\theta}_k)\boldsymbol{W}\boldsymbol{e})) \tag{7.14}$$

For the Gauss-Newton method to converge it is required that the initial parameters are sufficiently close to the optimal values and that the approximation of $\boldsymbol{H}$ is valid, which is the case if the residual errors $\boldsymbol{e}$ are small enough [Böiers, 2004].

To adapt the method to the brush model, $\boldsymbol{\theta}$ will denote the parameters $[C_{0x}\ \mu]$. The error vector, $\boldsymbol{e}$ is calculated from (7.10) with $g = \Psi$ as the brush model from (7.3). The model output, y, and the input, x, are replaced by the contents in the data bins, the tire force f_x and the tire slip σ_x respective. The Jacobian matrix becomes

$$\boldsymbol{J}(\Omega, \theta) = \begin{bmatrix} \frac{\partial e_1}{\partial C_{0x}} & \frac{\partial e_2}{\partial C_{0x}} & \cdots & \frac{\partial e_N}{\partial C_{0x}} \\ \frac{\partial e_1}{\partial \mu} & \frac{\partial e_2}{\partial \mu} & \cdots & \frac{\partial e_N}{\partial \mu} \end{bmatrix}^T \tag{7.15}$$

where respective partial derivative is given by

$$\frac{\partial e}{\partial C_{0x}} = \begin{cases} -\sigma_x + \frac{2}{3}\frac{C_{0x}\sigma_x|\sigma_x|}{\mu} - \frac{1}{9}\frac{C_{0x}^2\sigma_x^3}{(\mu)^2} & \text{if} \quad |\sigma_x| < \sigma_x^\circ \\ 0 & \text{otherwise} \end{cases} \tag{7.16}$$

and

$$\frac{\partial e}{\partial \mu} = \begin{cases} -\frac{1}{3}\frac{C_{0x}^2\sigma_x|\sigma_x|}{\mu^2} + \frac{2}{27}\frac{(C_{0x}\sigma_x)^3}{\mu^3} & \text{if} \quad |\sigma_x| < \sigma_x^\circ \\ -\text{sign}(\sigma_x) & \text{otherwise} \end{cases} \tag{7.17}$$

with $\sigma_x^\circ = 3\mu/C_{0x}$. The method works on a batch of data just as the method of least-squares. The benefit with Gauss-Newton is that it catches the nonlinearity in the brush model, which makes the result more accurate at slip values close to and above the limit slip. A drawback is that the method is more computer demanding, due to the many operations necessary to derive $\boldsymbol{J}$ and the risk of numerous iterations for an accurate result.

Properties and further functionalities of the estimator

Combining the storage-bin concept with one of the presented optimization algorithms gives a parameter estimator that copes with space-domain persistence in a consistent manner. The bin-filtering will have consequences on the signal properties, which may affect the reliability of the resulting estimates. This will be discussed in the following. The low-pass filtering of the data in the bin-storage will only partly cover the ability of the algorithm to adapt for changing parameters. Proposals on how to enhance such behavior and how to minimize the impact of outliers are also discussed below.

Effects on the optimization due to the storage-bin classification
Methods derived in the area of parameter optimization mainly aims at minimizing the measurement error of a model output, hence the plant is assumed to be on the form $y = G(\theta, x) + e$, where the input, x, is calculated by the controller before fed into the system and therefore known with good accuracy. In the present case, the system is given an excitation from where it is possible to obtain two signals from measurements on the vehicle. Due to the relation between these signals information can be extracted such that estimation of the friction coefficient is possible. Hence, there are measurement errors on both included signals. In the process of computation and estimation of the particular signals used for the parameter optimization further errors and uncertainties are encountered. Both the input and output are corrupted by noise.

There are estimation and optimization methods that cope with systems having noise on both the input and the output signals. One example is the total least-squares-method described in [de Groen, 1996], where the orthogonal distance between the data points and the adopted function is minimized. In [Carlson and Gerdes, 2003] this method is applied estimating the braking stiffness and rolling radius of a tire. Image-processing methods treat similar problems when locating obstacles in a picture. The most probable incline, shape or curvature of an edge are to be identified out of a number of points with the correct color. Methods for this have to deal with noise in both directions.

An obvious effect of the use of storage-bins is that the noise in the two signals are differently treated. The signal deciding which bin to activate,

further on called the leading signal, is filtered in a way that decreases the covariance if it stays in one bin, while it increases the covariance if the noise spreads over numerous bins, which it normally does. The uncorrelated noise on the other, further on called the trailing signal, is effectively filtered and the bin memory will provide a recursive average of that signal. Correlated noise or signal dependency with the leading signal are averaged within the bin, but are captured by the bin changes provoked by variations of the leading signal.

The main purposes with the storage-bin concept is to provide an appropriate way to remember recorded data and take control over the weighting of data such that a lot of measurement data in one region will not overshadow the behavior in another region where a lower amount of data is available. A secondary effect, which has to be treated correctly not to arise erroneous inferences on the optimization, is the influence of the data filtering.

To summarize, in the leading direction the noise properties will spread out to a uniform distribution over the affected bins and the variance of the signal-noise increases. In the trailing direction the value in the bin converges to the average of the including data points. Hence, the noise covariance in the trailing signal will be efficiently diminished when the bins fills up with data points. In the leading direction the noise properties will be corrupted and the covariance is enlarged and hard to predict, which will effect the optimization.

Example To further study the effect of the classification of the signals into disjoint intervals, two signals (x, y) corresponding to the slip and the normalized tire force are created with realistic assumptions on magnitude and noise variance. Since the effect of the bin-storage is dependent on the shape of the tire curve, two situations, that reflect the tire behavior at low respective high slips are analysed. In the low slip region the linear slope of the curve is to be estimated. The high slip region is in the interval around the peak force where the tire force is saturated and the level of a horizontal line will be estimated.

In the first case, shown in Figure 7.17, the y-signal is obtained as $y_m = kx + e_y$ and the x-signal as $x_m = x + e_x$. The deviations are set to $\sigma_{ex} = 0.25$ and $\sigma_{ey} = 0.0125$. The value of σ_{ex} depends on the wheel speed magnitude and quality and the choice of realistic variance of e_y depends on how y is derived. In this case the variance roughly corresponds to obtaining y from a filtered acceleration signal. If the engine torque is used, as described in Section 7.4 σ_{ey} decreases further. Using a force sensor similar to the equipment used by VTI, see Section 7.2 would give a larger noise level.

The x-values for generating the data are 300 points evenly distributed

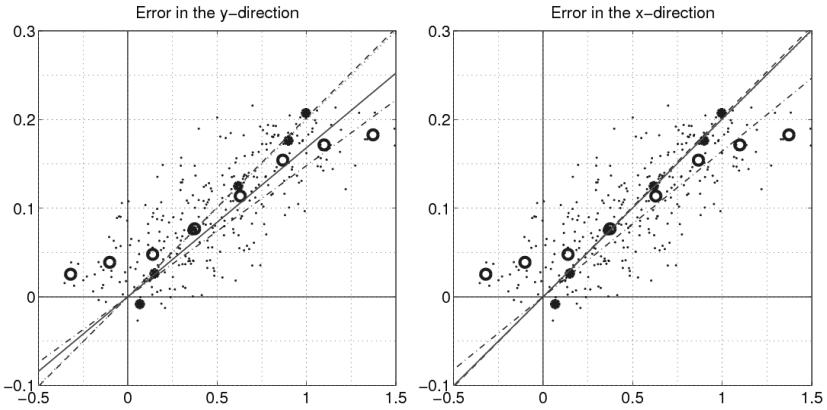

Figure 7.17 Illustration of the deviation in result using the different bins compared to the real data for least-squares optimization at low slip . The larger filled points are Y-bin values and the large circles are X-bin values. The dotted line denotes the real slope $k = 0.2$. The solid line shows the result for use of all data points. For the dashed and dashed-dotted lines the Y-bins and X-bins, respective, are used. The error in the left-most plot is minimized in the vertical direction and to the right in the horizontal direction.

in the interval $x = [0, 1]$. Performing a least-squares regression on all included data points assuming $y_m = \hat{k}x_m + e_y$ will give a result biased as $\hat{k} = k\sum x_i^2/(\sum x_i^2 + N\sigma_{ex}^2)$. It is also clear from the left-most plot in Figure 7.17 that the Y-bins consisting of the $[x_i'', y_i'']$-values, with y as leading signal, are averaged in the x-direction and gives a better estimate, but the X-bins ($[x_i', y_i']$), with x as leading signal, reinforces the mismatch and shows an even more biased result. Since $\sigma_{ex} > \sigma_{ey}$ a better estimate of the slope can be reached by using the relation $x_m = y_m/\hat{k} + e_x$ for the least-squares estimation, see right-most plot in Figure 7.17. The result is a less biased estimate, $\hat{k} = (k^2\sum x_i^2 + N\sigma_{ey}^2)/(k\sum x_i^2)$ using all data points. Minimizing the error in the x-direction for the bin-values do not largely change the result for the Y-bins, since they already are derived as an average in the x-direction. The estimation from X-bins are, however, enhanced but still not as good as using the Y-bins.

The estimation of the friction level at high slip is illustrated in Figure 7.18. Here, it is only possible to minimise the error in the y-direction. Since the brush-model is not strictly monotone in this area the Y-bins can not be placed such that they resemble the tire model. Therefore the X-bins have to be used in this region.

As a result of this discussion the weight in the cost-function in the real

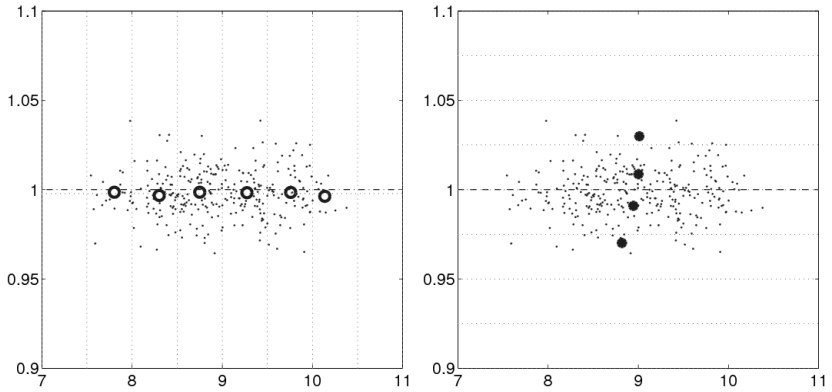

Figure 7.18 Illustration of the bin classification at high slip. The bin-values are here used to estimate the level of a straight horizontal line. The left plot shows the storage of $[x_i', y_i']$ and the right plot $[x_i'', y_i'']$.

implementation should be reduced on the X-bins (related to the slip) for low slip.

Time varying tire parameters It is assumed to this point that the estimated function Ψ is time invariant. The tire parameters are assumed to vary in two different manners. Either the variation is small and slow, signifying temperature variations during driving, tire wear etc. or they are changing abruptly as when the vehicle rolls in on a different surface.

If Ψ depends on time-varying parameters, $\boldsymbol{\theta}(t)$, it is, in general, difficult to maintain the storage-bin contents in a consistent state. But combining the low-pass filter in the storage-bins with freshness information it can be guaranteed that the latest updated bins are most significant in the optimization. Also old data not necessary for the persistence of the excitation can be disregarded.

If $\boldsymbol{\theta}(t)$ changes at a discrete event in time, the changes can be detected by using information on bin variance or from the parameter optimization. A sudden change of $\boldsymbol{\theta}(t)$ at time t_1 such that $\boldsymbol{\theta}(t) = \boldsymbol{\theta}_0$ for $t < t_1$ and $\boldsymbol{\theta}(t) = \boldsymbol{\theta}_1$ for $t \geq t_1$ will lead to a corresponding increase in the estimated variance v in the storage-bins at the present operating point. This may be used to trigger operations, e.g. a reset in the oldest updated storage-bins, to be performed at a change detection. Suddenly occurring inconsistencies in the bin contents may also lead to a corresponding increase of the cost function (7.5) in the parameter optimization, which may also be used as a trigger. Other sensors available on the vehicle can also be employed for this purpose. Starting the windscreen wipers may, for example, be one

event that signifies a change in surface condition. The a sudden change of the variance on the wheel speed may also denote a potential surface change.

Outliers To reduce the effects of noise on bin-values that contain a limited number of measurements, the weight of each bin will depend on the number of collected data points as

$$w_i(n) = \begin{cases} 0 & \text{if} \quad n < N_{\text{low}} \\ \dfrac{n - N_{\text{low}}}{N_{\text{high}} - N_{\text{low}}} & \text{if} \quad n < N_{\text{high}} \\ 1 & \text{otherwise} \end{cases} \tag{7.18}$$

The variance measure can be used to eliminate outliers, for example by allowing only new samples that lies within a variance-dependent range from the current estimate. The effect of outlying bin-values can also be reduced by two steps in the optimization. After a successful optimisation the residuals of all bin-values (7.10) are analysed and any bin having a residual larger than a factor times the standard deviation of all residuals will have its weight reduced. Care must be taken so that such mechanisms do not interfere with change detection.

7.4 Algorithm Implementation

The algorithm was implemented in a dSPACE AutoBox using code generated by Real-Time-Workshop from a Simulink model for use in a front-wheel driven Volvo S40. The data-bin storage and the parameter optimization were directly coded in C. The dSPACE-box contained a 1 GHz PowerPC with the possibilities of floating-number operations and the possibility of data acquisition at 1 kHz with an A/D-conversion of 16 bit resolution. The sampling time for the estimator code is 10 ms. This section shortly describes the implementation and the computations required to derive the signals used by the friction estimator. The algorithm in this implementation is only active during acceleration, since the required accuracy on the vehicle speed estimation was not reached by other means than using undriven or unbraked wheels. The implementation is only intended for straight driving without any cornering.

Implementation structure

The model structure is described in Figure 7.19. The input signals to the algorithm, the wheel speeds, the engine torque and rotation speed are

already available signals in the car. Hence, no extra sensors are needed. The operations required to derive the normalized tire force and the slip that are the inputs to the estimator are described in the following.

Input signal conditioning All signals are low-pass filtered.

Acceleration estimator The purpose of this block is to derive an acceleration signal for the calculation of the vertical load on each wheel. The vehicle acceleration is calculated by filtering and differentiation of the speed of the undriven rear wheels.

Vertical force estimator The vertical wheel load, F_z, on each wheel has to be determined to calculate the normalized tire force and the rolling wheel-radius. The tire load is calculated from the force and moment equilibrium of the car, concerning only longitudinal motion changes.

$$2(F_{zf} + F_{zr}) - mg = 0 \tag{7.19a}$$
$$2F_{zr}l - ma_x h - mgl_f = 0 \tag{7.19b}$$

where l is the length between the wheel axles and l_f is the horizontal distance from the front axle to the vehicle center of gravity. The height of the latter is denoted by h.

Gear estimator The different gear ratios of the gear-box are stored in a table. By comparing the relation between the wheel speed and the engine rotation the most appropriate ratio is chosen.

Driving force estimator The tire force is generated by multiplying the engine torque with the actual gear ratio and the approximate effective radius, given as a vehicle parameter. Energy losses in the power line are accounted for.

Normalized force estimator The force input to the friction estimator is derived by normalizing the tire force on the front wheels with the corresponding vertical tire load.

Wheel radius correction For good optimization result it is important that the rolling radius, R_e, of each wheel is accurately estimated. The rolling radius affects the slip calculation and a deviation from its nominal value causes a horizontal shift on the force-slip relation, such that it do not cross the origin. There are many factors that affect R_e and the deviation, δR, has to be continuously updated by comparing the wheel speeds of each tire with a reference speed when no forces are transmitted by the

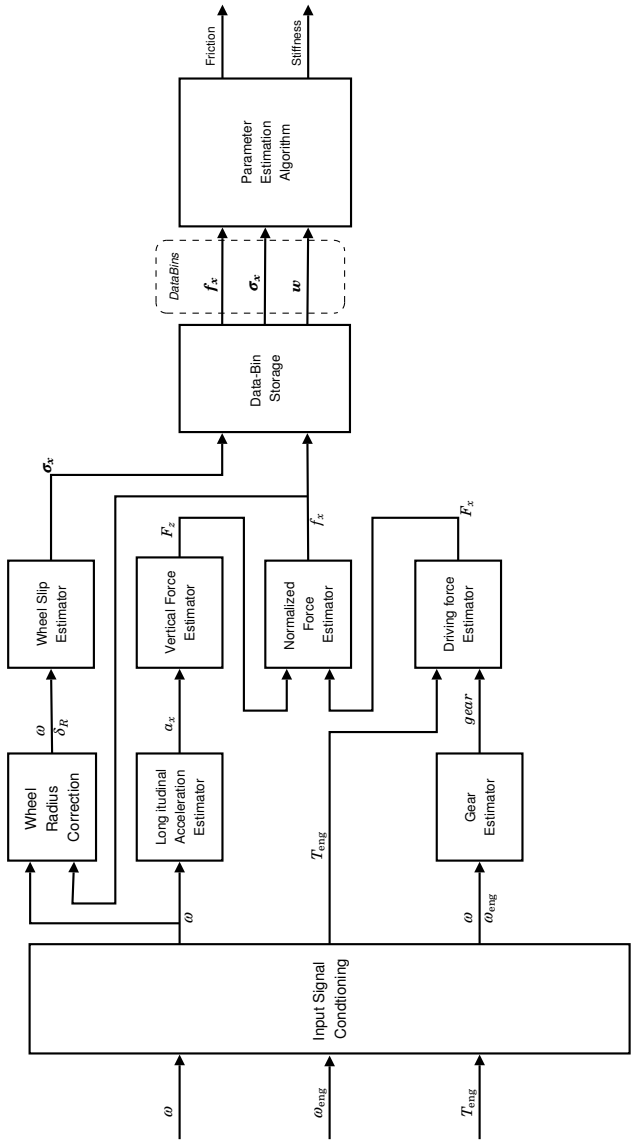

Figure 7.19 Schematic block diagram of the implementation of the road friction estimator.

tire. If the periods of free rolling are not sufficient the estimation can be complemented by adding one extra parameter, denoting the horizontal shift, in the optimization routines. The resulting Jacobian is derived in Appendix C.

Since the undriven rear wheels are used as reference for the vehicle speed, only the differences in-between the radii of each tire are necessary estimates for the slip computation. The deviations, δR, are derived by comparing rotational speed of each wheel, ω_i, with the rotational speed of the front-left wheel, ω_{fl} and computing correction factors for the wheels as

$$\delta R_i = \delta R_i + K(R_{efl}\omega_{fl} - (R_{ei})\omega_i) \tag{7.20}$$

where $R_{ei} = R_{\text{nom}}(1 + \delta R_i + \Delta R_i(\cdot))$ is the rolling radius for the wheel i. Known dependencies on other factors, such as the vertical load on the tire can be included in $\Delta R(\cdot)$. Correction is only performed when no horizontal forces are transmitted by the tire.

In many cases the dependency of the vertical load on the rolling radius is small and almost neglectable. Investigations performed in the project have shown that incorporating the assumed load effects on the radius, reduces the braking stiffness estimate on asphalt about 25%, during acceleration. Measurements performed within the project, see Figure 7.15, and tests in the Pirelli laboratory [Pirelli, 2005] show an approximate relation between the increment of rolling radius and the vertical load as

$$\Delta R = k_l(F_{\text{nomz}} - F_z)/R_{\text{nom}} \tag{7.21}$$

which should be included in (7.20). The relation and certainly the value of k_l is tire specific and dependent on many other factors, but at an average the optimization is enhanced, by using this correction and setting $k_l = 0.7 \cdot 10^{-6}$ m/N.

Wheel slip estimator The tire slip on each of the driven wheels is calculated according to the σ-definition, see also (2.5) as

$$\sigma_{xfl} = \frac{v_x - R_{efl}\omega_{fl}}{R_{efl}\omega_{fl}} \tag{7.22}$$

and corresponding for the right wheel. The reference velocity is formed as

$$v_x = \frac{R_{erl}\omega_{rl} + R_{err}\omega_{rr}}{2} \tag{7.23}$$

Implementation of the friction estimator

The bins in the storage algorithm are filled with slip and force values according to the description in Section 7.3. The $\hat{x}$-values are replaced by measurements of the slip σ_x and $\hat{y}$-values are replaced by the normalized tire force. Consequently the X- and Y-intervals are refereed to as S- and F-bins. The estimator implementation reported in this thesis contains no change-detection. The impact of outliers is reduced by (7.18). From the experiences derived in the discussion concerning the reliability of the S- and F-bin values, the weights corresponding to S-bins with $|\sigma_x| < K_s$ are set to zero to enhance the estimation of the tire stiffness at low slip.

The parameter estimation routine works as described in Section 7.3 with one iteration per sample. Some rules are set to ensure that the bins contain enough information for a valid estimate. Attempting to estimate the friction based on an insufficient amount of data may produce completely erroneous results and conclusions about the reliability. The rules for the estimation scheme are made clear in Algorithm 1. The condition on Line 1 states that there must be reliable values (at least N_{low} measurement points) in K_1 number of bins for estimation of the tire stiffness. Before trying to estimate the friction, there must be even more reliable bins ($K_2 > K_1$) together with a minimum demand on the magnitude of the lowest available slip and force value in the bins. Implicitly, this also is a check of the ability to invert the matrices $H^T H$ and $\Phi^T\Phi$, even if each determinant has to checked before any inversion procedure.

7.5 Results

This section presents the results of the implemented estimator for the winter tire on asphalt, snow and ice. The properties of the estimator are discussed together with an analysis of the possibility to affect the behavior by the tuning parameters. The results are further exemplifications on the behavior and function of the algorithm. To give a clear picture of the algorithm properties, the excitation procedure is an acceleration ramp, proceeded by a free rolling sequence used for calibration of the wheel radii. The estimator is reset and initialised before each test and the storage-bins contains no prior information.

The measurements were performed on a Volvo S40 at Colmis Proving Ground in Arjeplog. The presented results are derived from off-line computations of measured data. Though, the implementation was successfully running on-line and the execution of computational operations was verified to be well within the processing limits for the dSPACE AutoBox, it was decided to record the sampled signals to be able to elaborate the

Algorithm 1 Pseudo-code implementation of the rules of the friction estimator.

Require: $\Omega \in \{\Omega_i = [\sigma_{xi}, f_{xi}, w_i]\}$, $\hat{C}_{0x}^{\text{Old}}$, $\hat{\mu}^{\text{Old}}$
Produces: $\hat{C}_{0x}$, $\hat{\mu}$
1: **if** $\sum_\Omega (w_i > 0) \geq K_1$ **then**
2: Calculate C_{0x}^{L1} using the Least-Squares method as described in (7.12) with $\boldsymbol{\phi_i} = -\sigma_{xi}$
3: Compute the corresponding cost function, J_{cx} from (7.9)
4: **if** $(\sum_\Omega (w_i > 0) \geq K_2)$ & $(\max(|f_{xi}|) > K_f)$ & $(\max(|\sigma_{xi}|) > K_\sigma)$ **then**
5: Estimate $C_{0x}^{\text{L2}}, \mu^{\text{L2}}$ using the Least-Squares method as described in (7.12) with $\boldsymbol{\phi_i} = [-\sigma_{xi} \quad \sigma_{xi}|\sigma_{xi}|]^T$
6: Compute the corresponding cost function, $J_{cx\mu}$ from (7.9)
7: **if** $\mu^{\text{L2}} \in [0, K_\mu]$ **then**
8: **if** $J_{cx\mu} < K_j J_{cx}$ **then**
9: Estimate $C_{0x}^{\text{GN}}, \mu^{\text{GN}}$ by one iteration of the Gauss-Newton algorithm (7.14).
10: $\hat{C}_{0x}, \hat{\mu} \Leftarrow C_{0x}^{\text{GN}}, \mu^{\text{GN}}$
11: **else**
12: $\hat{C}_{0x}, \hat{\mu} \Leftarrow C_{0x}^{\text{L2}}, \ \hat{\mu}^{\text{L2}}$
13: **end if**
14: **else**
15: $\hat{C}_{0x}, \hat{\mu} \Leftarrow C_{0x}^{\text{L1}}, \ \hat{\mu}^{\text{Old}}$
16: **end if**
17: **else**
18: $\hat{C}_{0x}, \hat{\mu} \Leftarrow C_{0x}^{\text{L1}}, \ \hat{\mu}^{\text{Old}}$
19: **end if**
20: **else**
21: $\hat{C}_{0x}, \hat{\mu} \Leftarrow C_{0x}^{\text{Old}}, \ \hat{\mu}^{\text{Old}}$ (Algorithm inactive)
22: **end if**

calibration of the algorithm afterwards.

To be able to verify the functions and limits for the main friction estimator, i.e. line 9 in Algorithm 1, the tuning is set such that it is activated at a low amount of available force and slip values. Valid information in at least 6 bins is the demand for starting the Gauss-Newton algorithm.

Estimation results on asphalt

The measured and estimated signals on asphalt are shown in Figure 7.20. It can be seen that the friction estimate quickly reaches the maximum allowed value of 1.5. Without this limit the estimator would show an infinite friction, since the available friction utilization of the tire force is too low to be able to detect any curvature from the data. An exception is the time slot between 6.5 and 7.2 s, where low friction is predicted. This is a non-acceptable result, since the algorithm would not be able to distinguish

between asphalt and snow at that period. It should, however, be noted that the slip values in the bins are very low and the high sensitivity towards wheel speed noise at low slip is one factor for the discrepancy. By a more conservative tuning, for example using $K_\sigma > 0.005$ (see Algorithm 1) no estimation would be available at the actual time slot and the misjudgement is avoided. Also the disturbance on the braking stiffness estimation in this period, invoked by the start of the Gauss-Newton iteration would then be prevented. The plots of the bin-contents in Figure 7.21 explains the reason for the erroneous estimation at t=6.7 s. The group of bins surrounded by the dashed circle have a disturbance that gives an apparent curvature in the tire-force relation. It is also clear from the right-most plot that this group deviates from the others. The linearity of the bin-values in the right-most plot also shows the difficulty of estimating the friction at the low tire-force utilization. The remarkable difference of the tire stiffness compared to previously reported VTI-measurement will be discussed later.

Estimation results on snow

In the test on snow, see Figure 7.22, the estimator stabilizes at $t \approx$7.7 s. The maximal f_x-value in any bin at that time is below 0.2, approximately 50% of the available friction. The precision of the delivered friction estimate is $\pm$0.2 at that time, but improves with the increase of the available force measurements. The underestimation of the friction, explained by the error of the brush model on snow, also discussed in Section 7.2, is an accuracy problem, limiting the precision of the method. The mismatch between the model and the real tire behavior is clear from the plots in Figure 7.23. It is, however, obvious that the difference in tire behavior is clearly distinguished from asphalt at low tire force excitation.

Estimation results on ice

It is difficult to catch the friction coefficient on ice before reaching full utilization of the friction. Directly when starting the real estimation, at the condition of having data in 6 bins ($t \approx$5.8 s), see Figure 7.25, the friction is fully utilized, but a good estimate of both tire parameters is provided. The conclusion is comparable to the result presented in Table 7.2, describing friction estimation from the VTI-measurements, where it was not possible to catch a correct estimation before full sliding started. On the other hand, the algorithm certainly provides a good estimate directly when the sliding starts. This is a great benefit compared to conventional stabilization systems that waits for a certain wheel retardation before detecting a wheel-lock situation where the friction might be estimated directly from the corresponding actual tire force. The measurement sequence on ice is shown in Figure 7.24.

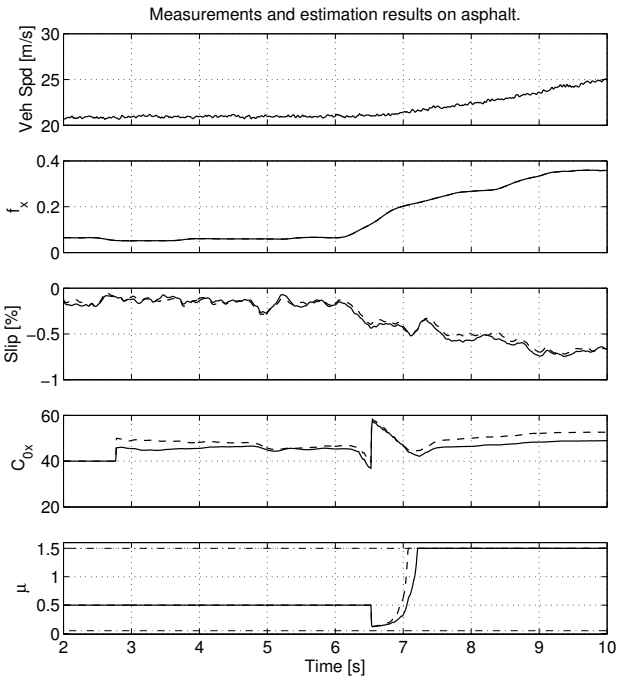

Figure 7.20 Plot of measured vehicle velocity, the calculated normalized tire force, and wheel slip and resulting estimations of the normalized braking stiffness and friction coefficient on asphalt. Solid line denotes left wheel and dashed line right wheel.

Discussions

As mentioned previously the algorithm is tuned to be fast and rather volatile in the presented results. The tuning parameters are set according to Table 7.5. In a real application it is important to tune it slower and more robust towards noise and disturbances, since it is favourable to prevent the deliverance of an erroneous estimate. The algorithm should, however, be fast enough not to unnecessarily delay any reliable prediction, even on ice. The parameters deciding when the storage-bins contain sufficient data for friction estimation are K_2, K_σ, and K_f. Where K_2 describes the lowest number of bins containing reliable force and slip values and K_σ and K_f determine the minimum requirement of the magnitude of the available slip and force values, respectively. These parameters denote fix limits on the bin-contents, independent on the road foundation. If the data contents are below these limits only the normalized braking stiffness is estimated.

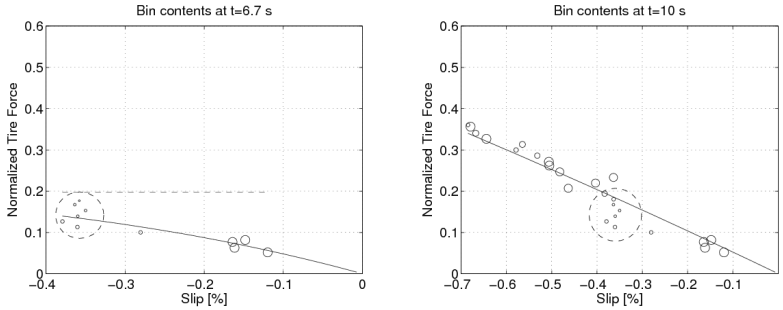

Figure 7.21 Illustration of the bin contents from the winter tire test on asphalt, shown together with the estimated tire characteristics for the right wheel during the time instants 6.7 s (left plot) and 10 s (right plot). The size of the marker is relative to the weight of the bin in the cost function. Only F-bins are present in the plots, since the weight of the S-bins are reduced for slip below $K_s = 0.02$. The group of points surrounded by the dashed circle contains a disturbance that enforces the bad estimation during the time period t =6.5–7.1 s.

The estimations performed by the least-squares method are independent of the prior estimations. The choice of initial value on the estimate, C_x^{init} and μ^{init}, at the algorithm initialization is therefore small. But before starting the Gauss-Newton solver it should be secured that the actual estimates are in a valid range, not to risk an unstable iteration. The choice of $K_j < 1$ guarantees that a curvature is discerned from the available bin-values, before starting Gauss-Newton iterations. The least-squares algorithm on Line 5 in Algorithm 1 should then have provided descent initial estimates. The parameter K_j determines how much the cost function should decrease when using a second order relation instead of a first order relation. If the curvature is small the estimation of two parameters in a linear relation, see (7.11) is sufficient. A difficulty with the least-squares estimation is that negative values on the friction can be obtained, if a negative curvature is detected. This is viewed as an temporal error and only the stiffness from the one-parameter linear estimation should be delivered in such case.

The quickness of the algorithm to adapt to a changing condition is determined by N_i, which should be set large enough such that temporal disturbances do not have a too large effect the estimation, but small enough such that smaller deviations in tire characteristics, i.e. due to temperature changes, can be correctly accounted for. Larger changes should be detected by a change-detection algorithm, enforcing a complete reinitialisation of the bin-memory. The estimation robustness is adventured if some bins contains measurements from new conditions and other from

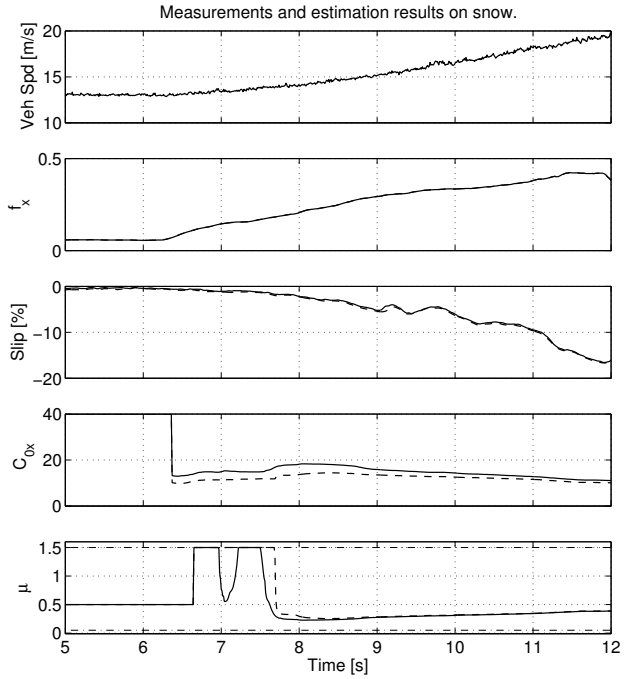

Figure 7.22 Measured signals and result of friction estimation of the winter tire on snow. Solid line denotes left wheel and dashed line right wheel.

older conditions.

The parameters N_{low} and N_{high} are limits for the reliability of the bin-value, stating that a certain number of data points are required for full weight of a bin. It is logically to set $N_{\text{high}} = N_i$, since N_{high} points out that the bin-value has full confidence.

There is a large difference in the normalized braking stiffness between the estimation on the car and the VTI measurements on asphalt. The difference is almost a factor two, 50 compared to 25. One reason for the stiffness deviation is the load dependency of the wheel radius. The test wheel on the VTI-truck is not exposed to any load transfer during the force ramp, which is inevitable for the personal car. Without adjustments for the load dependency, the stiffness would be about 70 and a further increase of the impact of load dependency, by raising k_i, can not be motivated. Another explanation might be an existing difference in the motion of the front and rear axle, e. g. due to longitudinal deflection of the suspension caused

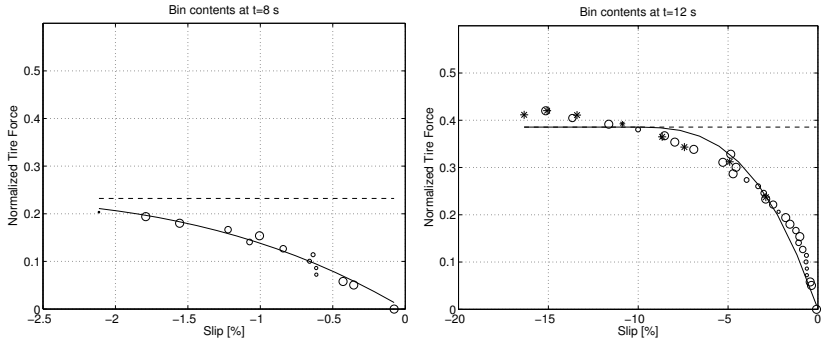

Figure 7.23 Bin contents from measurement of the winter tire on snow together with estimated tire characteristics for the right wheel during the time instants 8 s (left plot) and 12 s (right plot). The size of the marker denote the weight of the bin in the cost function. The F-bins are marked with 'o' and the s-bins with '*'.

by the applied acceleration torque. Simulations show, however, that this has a small and neglectable effect. The derivation of the normalized force introduces error sources, as efficiency losses, gear ratios, and uncertainties in torque measurements and load transfer etc that might affect the results. A distinct difference between the measurements are that the VTI measures while braking, when the estimator implemented in the personal car only uses driving data. The potential error sources will be further penetrated in the future work. Any physical reason for the tire to be stiffer on the car relative the test vehicle has not yet been found.

It is very important that the tire radius is accurately determined. For foundations such as e.g. asphalt that gives a high stiffness on the tire the accuracy on $\delta R/R_{nom}$ must be lower than one per thousand. It is not entirely verified that it is possible to obtain this high accuracy. As previously mentioned, the radius estimator can be combined with the estimation of the horizontal shift as a third parameter in the Gauss-Newton algorithm. The expression for the extended Jacobian is described in Appendix C.

In Figure 7.26 the resulting estimates are shown for the measurement case from Figure 7.20 when starting with incorrect wheel radius, but correcting its value by inclusion of the horizontal shift as an estimated parameter in the Gauss-Newton iteration. It is clear from the results that the estimates stabilize and that the stiffness value is identical to the result with correct and fixed wheel radius. This ensures that the horizontal shift is correctly estimated. The period of an uncertain friction estimation is, however, longer which indicates, not surprisingly, that the estimation of three parameters makes the algorithm more sensitive towards noise

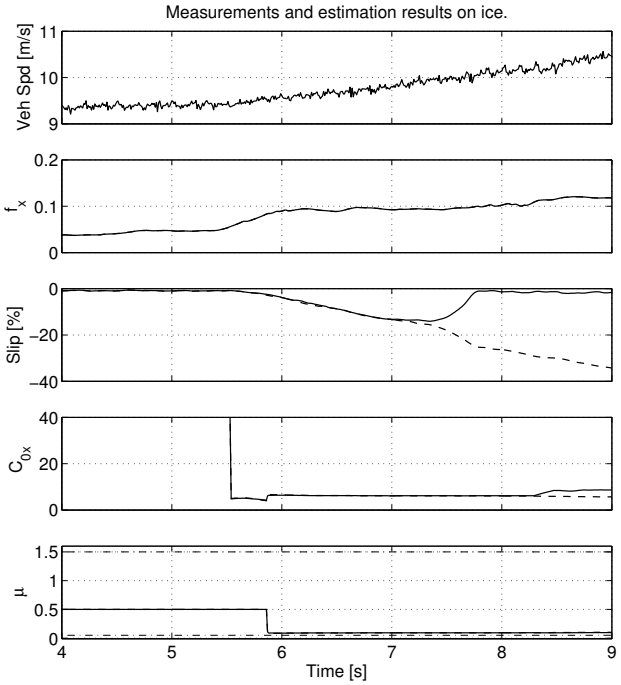

Figure 7.24 Measured signals and result of friction estimation of the winter tire on ice. Solid line denotes left wheel and dashed line right wheel.

and errors, but on the other hand gives a better estimate if the data excitation is sufficient and an accurate wheel radius is hard to obtain by other means.

7.6 Conclusions

This chapter has described a new type of friction estimator based on force and slip measurements. The tire behavior is assumed to follow the brush model prescribing the force and slip relation, depending on the braking stiffness of the tire and the road-tire friction. From the measurements these two parameters can be derived. A major invention of the proposed method is the way to collect the sampled measurements into bins, such that the available data used for optimization is evenly spread and weighted along the force and slip axis.

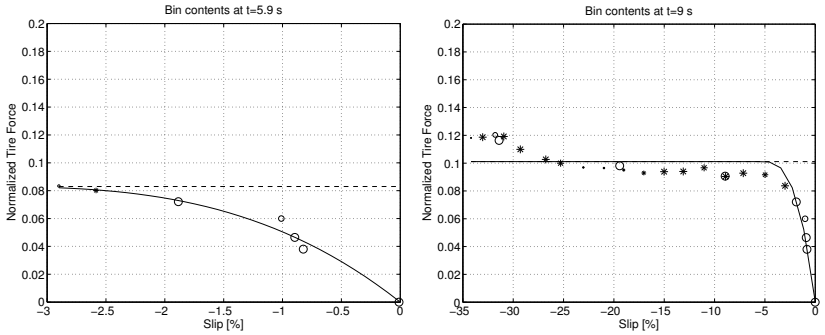

Figure 7.25 Bin contents from measurement of the winter tire on ice together with the estimated tire characteristics for the right wheel during the time instants 5.9 s (left plot) and 9 s (right plot). The size of the marker denote the weight of the bin in the cost function. The F-bins are marked with 'o' and the s-bins with '*'.

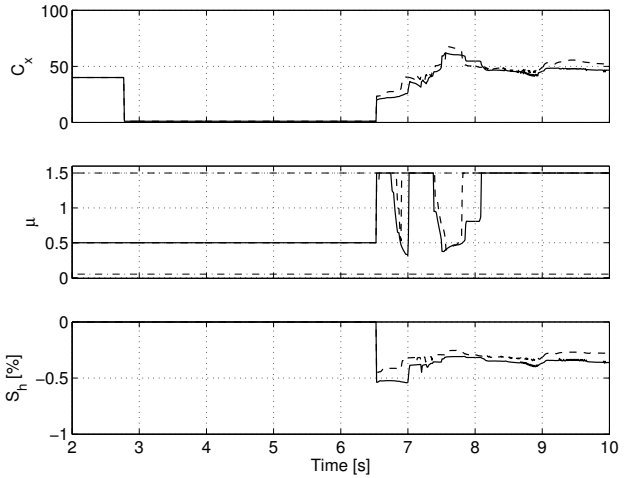

Figure 7.26 Plot of parameter estimation with the horizontal shift as as third estimated factor. The measurement sequence is the same as one shown in Figure 7.20.

The algorithm switches between different optimization methods depending on the contents in the bins. If only low slip and forces are available the braking stiffness is estimated as the sole parameter using the least-squares method. For slightly higher values of the signals both the friction and the stiffness are derived by the same method. When the curvature of the force-slip relation becomes evident the Gauss-Newton method

Table 7.5 List of tuning parameter for the actual implementation of road friction estimator

Parameter	Description	Nom. value
C_x^{init}	Initial value on C_x	40
μ^{init}	Initial value on μ	0.5
K_s	Slip limit for using S-bin	0.02
K_1	Required filled bins for C_{0x}-estimation	3
K_2	Required filled bins for C_{0x}, μ-estimation	6
K_j	Residual difference to enable Gauss-Newton algorithm	1
K_σ	Slip limit for enable μ-estimation	0
K_f	Limit on normalized force to enable μ-estimation	0
k_l	Load dependence on rolling radius	$0.7 \cdot 10^{-6}$
N_{low}	Threshold for measurement points in bin	2
N_{high}	Number of measurement points in bin to maximize weight	20
N_{s}	Number of slip bins	150
S_{max}	Maximum slip bin value	0.5
N_{f}	Number of force bins	150
F_{max}	Maximum force bin value	1.2
N_i	Number of points in bin memory	100

is used for better accuracy. The evaluation of the result has focused on the Gauss-Newton method.

The estimator works well in the presented situations. From no prior information it distinguishes between snow and asphalt for an available normalized tire force below 0.25. The estimate on snow available at that time is lower than expected, which depends on that the tire behavior on snow slightly differs from the model. The estimator detects and prescribes the low friction on ice when the tire force reaches its peak level

which is before the wheel starts its locking phase and before a high acceleration/retardation can be noticed. The accuracy on asphalt has not been further validated, since larger accelerations, than could be achieved during the measurement occasion, are needed to reach sufficient friction utilization. The output from the estimator, in that test, only indicates that there are much more friction available. One of the task for the future work is to optimize the signal quality and estimation performance to reduce the need of friction utilization for a sufficiently accurate friction determination. The estimator has been validated through force excitation as an acceleration ramp. Its structure has been constructed to effectively cope with weighting problems when the tire force is kept constant on a certain level for a long time or varying in a way such that the data is not well spread in the force-slip plane. The accuracy for estimation during this kind of unfavourable excitations needs further validation. The estimator implementation is so far restricted to acceleration with two-wheel driven vehicles. The major reason for this restriction is the insufficient accuracy of the estimate vehicle reference velocity if not measured by the undriven wheel-rotations. Further work incorporates enlargement of the usable area of the estimator to work for both braking and acceleration during simultaneous cornering.

8

Conclusions

The thesis has presented research performed mainly in the related areas of tire modeling and friction estimation. The theory behind the brush tire model developed by the pioneers in tire modeling has been a central theme throughout the work. The thesis contains an extensive review of the brush model including the effects of camber. It also presents a validation of the model towards measurements and an evaluation of the variation of the included parameters, due changes in conditional factors, such as load and road surface.

A new method to derive the tire forces for simultaneous braking, cornering and camber, by combining empirical models for pure braking, cornering and cambering has been presented. Based on brush-model mechanics, the combined-slip forces may be described by a scaling of corresponding empirical pure-slip forces. The way to derive the scale factors by dividing the expression for the combined slip force with the pure slip force in the appropriate direction is an unique approach. The generation of the camber force has been described and included in a simple, but physically motivated manner. The pure-slip tire model can be given as a empirical model or as raw tabular data, as long as the horizontal and vertical shift are zero, i.e. that there is no tire force for zero slip.

A major aim of the semi-empirical modeling has been to extract as much information from the available pure-slip curve as possible. The physical approach has made it possible to include velocity dependency and conversion between braking and driving data in the model. The proposed model is simple to use, since it does not introduce any new parameters and all necessary information is given by the chosen pure-slip model.

A dynamic extension of the steady-state combined-slip model is proposed, based on qualitatively realistic tire relaxation behaviour. The model includes cross-couplings between longitudinal and lateral dynamics, that are not commonly found in other models of similar complexity. The issue of stability is handled by including a physically motivated damping.

The tire model was successfully implemented in Matlab and Modelica code and tested together with the VehicleDynamics Library in the multi-body simulation environment, Dymola. The implementation was verified to be well-working and computationally sound on both platforms. Good results are obtained in validation with the available empirical data. Experimental validation indicates that the proposed model and previous models perform similarly. The efficiency in computational means compared to other models has not yet been evaluated. The presented model is advantageous in that it combines the data-fitting accuracy of empirical pure slip models with the stringency of physical modeling. This claims descent behavior, according to the physical constraints, in the defined working area without the need for calibration, at the cost of quite large expressions. The methodology to derive the scale-factors based on first principles makes it straight forward to include new functionality to the model.

The wheel speed signal is a most important signal in many system applications. Based on problems observed during measurements, a few ways to reduce noise from the signal are discussed in the thesis. One method to compensate the wheel-speed signal for disturbances caused by axle and suspension deflections during transients in brake applications is proposed. The disturbance is predicted by a first order feedforward filter of the brake torque signal. From the validation it can be seen that the signal error can, by this simple means be reduced by at least 50%. This is probably sufficient to significantly increase the performance of vehicle systems relying on the wheel-speed signal during brake-force transients.

The thesis also describes the development of a new type of friction estimator based on the assumption that the tire behavior follows the brush model. Since the brush model predicts the tire characteristic, as depending on the braking stiffness and friction coefficient, these parameters can be estimated from the force and slip measurements. Experimental data has been collected and evaluated to ensure the validity of the brush model during certain conditions. The shortcomings and limitations of the model accuracy are discussed. A major invention in the proposed method is the way of collecting the measurements into bins, such that the available data used for optimization is evenly weighted along the force and slip axis. The least-squares and the Gauss-Newton methods are used for finding the most accurate values of the stiffness and friction.

The estimator has been implemented and validated on a passenger car. For a sequence in the form of an acceleration ramp it has shown to work well in the tested situations.

As expected, the amount of friction utilization is strongly connected to the accuracy of the estimation and the usability of the method will strongly relate to the requirement regarding accuracy and possibilities for utilization.

The structure of the estimator is developed to effectively cope with weighting problems when the tire force is kept constant on a certain level for a long time or varying in a way such that the data is not well spread in the force-slip plane. The accuracy for estimation during this kind of unfavourable excitations needs further validation. It can be concluded that this way of approaching the problem of friction estimation is promising.

8.1 Ideas of Further Research

All of the presented methods and ideas can be further developed, analysed, and tested. The particular needs have been described in the respective sections, from where the most urgent and important issues are concluded in the following list:

- The wheel speed signal is essential for many vehicle systems and further work to improve the quality of that signal is important. The proposals mentioned in the thesis have to be further evaluated and developed by testing in real implementations.
- The proposed semi-empirical tire-model is, in its present state, useful for a number of applications, but the addition of effects of turn-slip and flexible carcass would further enhance the applicability. The physical foundation of the model is expected to make this possible with reasonable effort. Further validation of, particularly, the effects of camber are need.
- It has to be emphasised that the proposed friction estimator is developed in an ongoing project. The presented result should therefore be seen as the first glimpse of the possibilities to use this type of methodology for this purpose. A large amount of work is still required to achieve good response of the estimate when changing surface and to ensure the ability of catching slow variations of the parameters. Solutions for change detection and outlier management have to be implemented and calibrated, such that a maximum of robustness and accuracy is achieved. Improvement of signal quality and estimator performance to minimize the need of friction utilization are other needs. Further, a lot of tests and validations are necessary really evaluate the performance in action and to reveal not yet discovered weak points.
- A demand for developing a slip-based friction estimator for use during braking or for “All Wheel Drive” vehicles is to have a good estimate of the vehicle velocity or to succeed in removing this dependence from the estimator structure. The area of usability is also to be enlarged to enable friction estimation during cornering, when a lateral slip affects the longitudinal tire properties.

An important conclusion of a research project is often how the work should proceed in the development of an idea or a product. Since the possible fields of improvements in vehicle related issues have been expanded, by the newly available techniques and instrumentation possibilities, it is important to put the efforts where they have the best effect. Hopefully, this thesis may serve as a guide in this purpose for the related topics.

9

Bibliography

Analog Devices (2001): *Wheel speed sensor for ABS systems, AD22157*.

Åström, K. J. (1970): *Introduction to Stochastic Control Theory*. Academic Press.

Åström, K. J. and B. Wittenmark (1994): *Adaptiv Control*. Addison-Wesley Pub Co.

Bakker, E., L. Nyborg, and H. B. Pacejka (1987): "Tyre modelling for use in vehicle dynamics studies." SAE Technical Paper 870421.

Bakker, E., H. B. Pacejka, and L. Lidner (1989): "A new tire model with an application in vehicle dynamics studies." SAE Technical Paper 890087.

Bayle, P., J. F. Forissier, and S. Lafon (1993): "A new tire model for vehicle dynamics simulations." *Automotive Technology International*, pp. 193–198.

Bernard, J. E., P. S. Fancher, R. Gupta, H. Moncarz, and L. Segel (1975): "Vehicle-in-use limit performance and tire factors - the tire in use. appendix a, b. c." Technical Report UM-HSRI-PF-75-1-2. Highway Safety Research Institute, Ann Arbor, Michigan.

Böhm, F. and H.-P. Willumeit, Eds. (1996): *Tyre Models for Vehicle Dynamics Analysis*. Swets & Zeitlinger Publishers. Supplement to Vehicle System Dynamics Volume 27.

Böiers, L. C. (2004): *Lectures on Optimization*. Center for Mathematical Science, Lund University.

Brach, R. M. and R. M. Brach (2000): "Modeling combined braking and steering tire forces." SAE Technical Paper 2000-01-0357.

Carlson, C. and C. Gerdes (2003): "Nonlinear estimation of longitudinal tire slip under several driving conditions." In *Proceedings of the American Control Conference*, vol. 6, pp. 4975–4980.

Casselgren, J., M. Sjödahl, and M. S. Sara Woxneryd (2007): "Classification of road conditions – to improve safety." In *11th International Forum on Advanced Microsystems for Automotive Applications*. Berlin. To be published.

Clark, S. K., R. N. Dodge, and G. H. Nybakken (1971): "An evaluation of string theory for the prediction of dynamic tire properties using scale model aircraft tires." Technical Report. University of Michigan.

Colmis AB (2006): "Colmis proving ground, Arjeplog, Sweden." Internet. http://www.colmis.com.

Continental (2003): "History of the tire." Internet. http://www.conti-online.com/generator/www/us/en/continental/transport/themes/about_continental/tire_history/tire_history_en.html.

de Groen, P. (1996): "An introduction to total least squares." *Nieuw Archief voor Wiskunde*, pp. 237–253.

Do, M.-T. and Y. Delanne (2003): "Prediction of tire/wet road friction and its variation with speed from road macro- and microtexture, and tire-related properties." Technical Report. French Public Works Research Laboratory, France.

Dugoff, H., P. S. Fancher, and L. Segel (1969): "Tire performance characteristics affecting vehicle response to steering and braking control inputs. final report." Technical Report. Highway Safety Research Institute, Ann Arbor, Michigan.

Dynasim (2006): "Dymola, dynamic modeling laboratory." Internet. http://www.dynasim.se/.

Eichhorn, U. and J. Roth (1992): "Prediction and monitoring of tyre/road friction." In *XXIV FISITA Congress: Safety, the Vehicle, and the Road*, pp. 67–74. London.

Ellis, J. R. (1994): *Vehicle Handling Dynamics*. Mechanical Engineering Publications Limited, London.

Fancher, P. S., L. Segel, C. C. MacAdam, and H. Pacejka (1972): "Tire traction grading procedures as derived from the maneuvering characteristics of a tire-vehicle system. volume i and ii. final report." Technical Report HSRI-71-129. Highway Safety Research Institute, Ann Arbor, Michigan.

Gäfvert, M. (2003): *Topics in Modeling, Control, and Implementations in Automotive Systems*. PhD thesis ISRN LUTFD2/TFRT--LUTFD2/TFRT–1066–SE--SE, Lund University.

Gäfvert, M. and J. Svendenius (2003): "Construction of semi-empirical tire models for combined slip." Technical Report ISRN LUTFD2/TFRT--7606--SE. Department of Automatic Control, Lund University, Sweden.

Gäfvert, M. and J. Svendenius (2005): "A novel semi-empirical tire model for combined slip." *Vehicle System Dynamics*, **43:5**.

Gäfvert, M., J. Svendenius, and J. Andreasson (2006): "Implementation and application of a semi-empirical tire-model in multi-body simulation of vehicle handling." In *Proceedings of the 8th International Symposium on Advanced Vehicle Control*. Taipei, Taiwan.

Gelb, A., J. Kasper, R. Nash, C. Price, and A. Sutherland (1977): *Applied Optimal Estimation*. The MIT press.

Gim, G. and P. E. Nikravesh (1991): "An analytical model of pneumatic tires for vehicle dynamics simulations. Part 2: Comprehensive slips." *International Journal of Vehicle Design*, **12:1**, pp. 19–39.

Gipser, M. (2005): "FTire homepage." Internet. http://www.ftire.com.

Gothie, M., T. Parry, and P. Roe (2001): "The relative influence of the parameters affecting road surface friction." In *2nd International Colloquium on Vehicle Tyre Road Interaction*. Florence, Italy.

Goyal, S. (1989): *Planar Sliding of a Rigid Body with Dry Friction: Limit Surfaces and Dynamics of Motion*. PhD thesis, Cornell University, Department of Mechanical Engineering.

Guo, K., Y. Zhuang, S. Chen, and L. Willlam (2006): "Experimental research on friction of vehicle tire rubber." *Frontiers of Mechanical Engineering in China*, **1:1**, pp. 14–20. DOI 10.1007/s11465-005-0001-z.

Gustafsson, F. (1997): "Slip-based tire-road friction estimation." *Automatica*, **33:6**, pp. 1087–1099.

Gustafsson, F., J. Nilsson, and T. Gustavsson (2006a): "Method and system of determining the absolute velocity of a vehicle." Patent no. EP1642140.

Gustafsson, M., C.-M. Berglund, B. Forslund, and I. Forslund (2006b): "Effekter av vinterdäck – en kunskapsöversikt." Technical Report. VTI. Report 543.

Hägglund, T. and K. J. Åström (2000): "Supervision of adaptive control system." *Automatica*, **36**, pp. 1171–1180.

Haney, P. (2003): *Racing & High Performance Tire: Using Tires to Tune for Grip and Balance*. SAE.

Hirschberg, W., G. Rill, and H. Weinfurter (2002): "User-appropriate tyre-modelling for vehicle dynamics in standard and limit situations." *Vehicle System Dynamics*, **38:2**, pp. pp. 103–125.

Isermann, R., P. Scheerer, O. Nelles, and R. Schwarz (2000): "Method for compensating variations of a wheel speed sensor." Patent no. 6,446,018. Assignee: Continental Teves.

ISO 8855 (1991): "Road vehicles — Vehicle dynamics and road-holding ability — Vocabulary."

Johansson, R. (2002): *System Modeling and Identification*. Prentice Hall.

Kageyama, I. and S. Kuwahara (2002): "A study on tire modeling for camber thrust and camber torque." JSAE Review Paper No. 20024252.

Kiencke, U. and L. Nielsen (2000): *Automotive Control Systems: For Engine, Driveline, and Vehicle*. Springer-Verlag.

Kim, S. and A. Savkoor (1996): "The contact problem of in-plane rolling of tires on a flat road." In Böhm and Willumeit, Eds., *Tyre Models for Vehicle Dynamic Analysis*, pp. 189–206. Swets & Zeitlinger. Supplement to Vehicle System Dynamics Volume 27.

Levy, G. and N. Fangeat (2004): "Automatic stability control system for a vehicle using an invariant charaterizing any tire." Patent no US 2004/0032165 A1.

Ljung, L. and T. Söderström (1983): *Theory and Practice of Recursive Identification*. The MIT Press.

Lugner, P. and P. Mittermayr (1991): "A measurement based tyre characteristics approximation." In Pacejka, Ed., *Tyre Models for Vehicle Dynamics Analysis*, pp. 127–144. Swets & Zeitlinger. Supplement to Vehicle System Dynamics Volume 21.

Matschinsky, W. (1997): *Road Vehicle Suspension*. John Wiley & Sons, Inc. ISBN 1-86058-202-8.

Meschke, G., C. Liu, and H. Mang (1996): "Large strain finite-element analysis of snow." *Journal of Engineering Mechanics*, **122:7**, pp. 591–602.

Michelin (2004): "Annual report." Internet. www.michelin.com.

Mizuno, M., H. Sakai, and K. Oyama (2005): "Developement of a tyre force model incorporating the influence of the tyre surface." In Lugner and Plöchl, Eds., *Tyre Models for Vehicle Dynamic Analysis*, pp. 395–402. Taylor & Francis. Supplement to Vehicle System Dynamics Volume 43.

The Modelica Association (2005): *Modelica®— A Unified Object-Oriented Language for Physical Systems Modeling: Language Specification Version 2.2*.

Modelon (2006): "VehicleDynamics Library for Modelica." Internet. http://www.modelon.se/index.php?did=25&level=2.

Müller, S. and M. Uchanski (2001): "Slip-based tire-road friction estimation during braking." In *Proceedings of IMECE01*. ASME.

Müller, S., M. Uchanski, and K. Hedrick (2003): "Estimation of the maximum tire-road friction coefficient." *Journal of Systems, Measurements and Control*.

Nguyen, P. K. and E. R. Case (1975): "Tire friction models and their effect on simulated vehicle dynamics." In *Proceedings of a Symposium on Commercial Vehicle Braking and Handling*, number UM-HSRI-PF-75-6, pp. 245–312.

Nicholas, V. T. and T. Comstock (1972): "Predicting directional behavior of tractor semitrailers when wheel anti-skid brake systems are used." In *ASME Winter Annual Meeting*, number Paper No. 72–WA/Aut-16.

Nielsen, L. and L. Eriksson (1999): "Course material vehicular systems.". Linköping Institute of Technology, Vehicular Systems, ISY.

Nordström, O. (1983): *Antilåssystem för tunga fordon, VTI Rapport nr 257*. Klintland grafiska.

Nordström, O. and H. Åström (2001): "Upgrading of VTI friction test vehicle BV12 for combined braking and steering tests under aquaplaning and winter conditions." In *2nd International Colloquium on Vehicle Tyre Road Interaction*. Florence, Italy.

Oertel, C. and A. Fandre (1999): "Ride comfort simulations and step towards life time calculations: RMOD-K and ADAMS." In *International ADAMS Users' Conference, Berlin*.

Olsson, H. (1996): *Control Systems with Friction*. PhD thesis ISRN LUTFD2/TFRT--1045--SE, Department of Automatic Control, Lund University, Sweden.

Optical Sensors (2006): "Road eye – a laser sensor for monitoring road state." Internet. http://opticalsensors.se/roadeye.htm.

Pacejka, H. B. (1988): "Modelling of the pneumatic tyre and its impact on vehicle dynamic behavior." Technical Report i72B. Technische Universiteit, Delft.

Pacejka, H. B. (2002): *Tyre and Vehicle Dynamics*. Butterworth-Heinemann.

Pasterkamp, W. R. and H. B. Pacejka (1997): "The tyre as a sensor to estimate friction." *Journal of Vehicle System Dynamics*, **27**, pp. 409–422.

Pauwelussen, J. P., G. Anghelache, C. Theodorescu, and A. Schmeitz (1999): *European Tyre School*, chapter 10 — Truck tyre behavior in use and testing methods. Nokian Tyres plc. http://www.tut.fi/plastics/tyreschool.

Pavkovi, D., J. Deur, J. Asgari, and D. Hrovat (2006): "Experimental analysis of potentials for tire friction estimation in low-slip operating model." SAE Technical Paper 2006-01-05561.

Persson, N. (2002): "Event based sampling with application to spectral estimation." Technical Report. Department of Electrical Engineering, LiU, Sweden. Lic. Thesis No 981.

Persson, N. and F. Gustafsson (2001): "Event based sampling with application to vibration analysis in pneumatic tires." In *IEEE International Conference on Acoustics, Speech, and Signal Processing*, vol. 6, pp. 3885–3888. IEEE, Salt Lake City, UT, USA.

Persson, N., F. Gustafsson, and M. Drevö (2002): "Indirect tire pressure monitoring using sensor fusion." SAE Technical Paper 2002-01-1250.

Pirelli (2005): "Measurement of tire rolling radius." Confidential.

Pohl, A., R. Steindl, and L. Reindl (1999): "The "intelligent tire" utilizing passive saw sensors-measurement of tire friction." *IEEE Transactions on Instrumentation and Measurement*, **48:6**.

Pottinger, M. G., W. Pelz, and G. Falciola (1998): "Effectiveness of the slip circle: "COMBINATOR", model for combine tire cornering and braking forces when applied to a range of tires." SAE Techical Paper 982747.

ProAuto Limited (2006): "Tech talk - anti-lock braking systems – Part 3." *Motor Industry Magazine*, March, pp. 38–39.

Radt, H. (1995): "Tire data treatment." In Milliken and Milliken, Eds., *Race Car Vehicle Dynamics*. Society of Automotive Engineers, Warrendale, U.S.

Ray, L. (1997): "Nonlinear tire force estimation and road friction identification: Simulation and experiments." *Automatica*, **33:10**, pp. 1819–1833.

SAE Recommended Practice J670e (1976): "Vehicle dynamics terminology."

Saino, P. (2001): "Snow surface model for tyre performance simulation." In *2nd International Colloquium on Vehicle Tyre Road Interaction*. Florence, Italy.

Salaani, K., D. Guenther, and G. Heydinger (1999): "Vehicle dynamics modeling for the national advanced driving simulator of a 1997 Jeep Cherokee." SAE Paper No. 1999-01-0121.

Schmeitz, A., I. Besselink, J. de Hoogh, and H. Nijmeijer (2005): "Extending the magic formula and swift tyre model for inflationpressure changes." In Wies and Wallentowitz, Eds., *Reifen, Fahrwerk, Fahrbahn*, pp. 201–225. Hannover, Germany.

Schofield, B., T. Hägglund, and A. Rantzer (2006): "Vehicle dynamics control and controller allocation for rollover prevention." In *Proceedings of the IEEE International Conference on Control Applications*. Munich, Germany.

Schuring, D. J., W. Pelz, and M. G. Pottinger (1996): "A model for combined tire cornering and braking forces." In *Investigations and Analysis in Vehicle Dynamics and Simulation*, pp. 61–83. SAE International. SAE Technical Paper 960180.

Schwarz, R. (1999): *Rekonstruktion der Bremskraft bei Fahrzeugen mit Elektromechanisch Betätigten Radbremsen*. PhD thesis, Technische Universität Darmstadt.

Schwarz, R., O. Nelles, P. Scheerer, and R. Isermann (1997a): "Increasing signal accuracy of automotive wheel-speed sensors by on-line learning." In *Procedings of the American Control Conference*, pp. 1131–1135. New Mexico.

Schwarz, R., M. Willimowski, R. Isermann, and P. Willimowski (1997b): "Improved wheel speed and slip determination considering influences of wheel-suspension dynamics and tire dynamics." SAE-paper No. 971117.

Sharp, R. (2004): "Testing and improving a tyre shear force computation algorithm." *Journal of Vehicle System Dynamics*, **41:3**, pp. 223–247.

Sharp, R. and M. Bettella (2003): "Shear force and moment descriptions by normalisation of parameters and the "magic formula"." *Journal of Vehicle System Dynamics*, **39:1**, pp. 27–56.

Solyom, S., A. Rantzer, and J. Lüdemann (2004): "Synthesis of a model-based tire slip controller." *Vehicle System Dynamics*, **41:6**, pp. 477–511.

Sugai, M., K. Asano, and T. Umeno (2003): "Physical quantity estimating apparatus and tire state determining aparatus, and estimating method of same and determination of same." Patent no. US 2003/0192375 A1.

Svendenius, J. (2003): "Tire models for use in braking applications." Licentiate thesis ISRN LUTFD2/TFRT--3232--SE. Department of Automatic Control, Lund University, Sweden.

Svendenius, J. (2007a): "Validation of the brush model towards VTI-measurement data recorded at Hällered 2005." Technical Report ISRN LUTFD2/TFRT—7616–SE. Department of Automatic Control, Lund University, Sweden. RFE-project.

Svendenius, J. (2007b): "Validation of the brush model towards VTI-measurement data recorded in Arjeplog 2006." Technical Report ISRN LUTFD2/TFRT—7617–SE. Department of Automatic Control, Lund University, Sweden. RFE-project.

Svendenius, J. and M. Gäfvert (2004a): "A brush-model based semi-empirical tire-model for combined slips." SAE Technical Paper 2004-01-1064.

Svendenius, J. and M. Gäfvert (2004b): "A semi-empirical tire-model for transient combined-slip forces." In *AVEC '04*.

Svendenius, J. and M. Gäfvert (2005): "A semi-empirical tire model for combined slips including the effects of cambering." In Lugner and M.Plöchl, Eds., *Tyre Models For Vehicle Dynamics Analysis*, vol. 43, pp. 317–328. Taylor & Francis Group, Glasgow. Supplement to Vehicle System Dynamics Volume 43.

Svendenius, J. and M. Gäfvert (2006): "A semi-empirical dynamic tire model for combined-slip forces." *Vehicle System Dynamics*, **44:2**, pp. 189 – 208. Special Issue: AVEC '04: 7th International Symposium on Advanced VEhicle Control, 23-27 August 2004 HAN University, Arnhem, The Netherlands.

Svendenius, J. and B. Wittenmark (2003): "Brush tire model with increased flexibility." In *ECC*. European Union Control Association, Cambridge, UK.

Thomson, J. (2003): "What we should know about tires." Internet. http://www.jags.org/TechInfo/2001/05May/tires.

Thorvald, B. (1998): *On truck tyre modelling*. PhD thesis ISRN LUTFD2/TFRT--KTH/FKT/DA–98/29–SE--SE, KTH.

Tielking, J. T. and N. K. Mital (1974): "A comparative evaluation of five tire traction models." Technical Report UM-HSRI-PF-74-2. Highway Safety Research Institute, Ann Arbor, Mich.

TYDEX-Working group (1997): "Tydex-format, description and reference manual."

Umeno, T., E. Ono, and K. Asano (2002): "Estimation of tire-road friction by tire rotation vibration." SAE paper no. 2002-01-1183.

Vägverket (2006a): "EU-project: INTRO – Intelligent Roads." Internet. http://www.vti.se/templates/Page____5777.aspx.

Vägverket (2006b): "Homepage of IVSS." Internet. http://www.ivss.se/.

Vägverket (2006c): "IVSS-project: Slippery Road Information System." Internet. http://www.ivss.se/templates/ProjectPage.aspx?id=206.

Velenis, E., P. Tsiotras, and C. C. de Wit (2002): "Extension of the LuGre dynamic tire friction model to 2D motion." In *Mediterranean Conference on Control and Automation (MED2002)*, vol. 10th. Lisbon, Portugal.

Volvo AB (2006): "Volvo proving ground Hällered." Internet. Available from www.volvo.com/NR/rdonlyres/F7CB2A13-6BD6-495E-898E-D491 A2683BE9/0/hallered_proving_ground_rsp_83364_eng.pdf.

Wallman, C.-G. and H. Åström (2001): "Trafiksäkerhet, vägkonstruktion, drift och underhåll, vägunderhåll, vinterunderhåll." Technical Report. Statens väg-och transportforskningsinstitut. VTI meddelande 991 A.

Wong, J. Y. (2001): *Theory of Ground Vehicles*, 3rd edition. John Wiley & Sons, New York.

Yasui, Y., W. Tanaka, Y. Muragishi, E. Ono, M. Momiyama, H. Katoh, H. Aizawa, and Y. Imoto (2004): "Estimation of lateral grip margin based on self-aligning torque for vehicle dynamics enhancement." SAE Technical Paper 2004-01-1070.

A

Nomenclature

The tables below describe the nomenclature and the notations used in the thesis. If there is a different ISO-definition for an entity the corresponding ISO notation is prescribed in the second column. The description, together with a reference to the defining equation of the entity, is given in the third column.

Nomenclature	ISO	Description
Coordinates and Positions		
x	x	Longitudinal direction, in the front direction of the vehicle
y	$-y$	Lateral direction
z	$-z$	Vertical direction, positive downwards
x_r		Longitudinal coordinate for bristle position at the road contact
y_r		Lateral coordinate for bristle position at the road contact
Movements		
$\bar{v}$		Horizontal wheel hub velocity vector
v_x		Longitudinal wheel hub velocity
v_y		Lateral wheel hub velocity
v_{sx}		Longitudinal tire slip velocity (2.3)
v_{sy}		Lateral tire slip velocity (2.3)
v_c		Carcass velocity (2.2)
ω		Wheel rotational velocity
ω_0		Wheel rotational velocity (free rolling)

γ	ϵ_V	Camber angle
Forces and Torques		
$\bar{F}$		Force vector
F_x		Longitudinal tire force
F_y	$-F_y$	Lateral tire force
F_z	$-F_z$	Vertical tire force
$\bar{f}$	$\bar{\mu}_W$	Force vector normalized by vertical force
M_z		Self-aligning torque
M_z'		Self-aligning torque
M_z''		Second order torque addition, due to deformation
M_y		Rolling resistance
M_x		Overturning torque
$d\bar{F}$		Force vector on infinitesimal bristle
Deflections		
δ_x		Longitudinal deflection of tire, fig 4.15
δ_y		Lateral deflection of tire
δ_{xs}		Longitudinal tire deformation due to slip (4.3)
δ_{ys}		Lateral tire deformation due to slip
δ_{xb}		Longitudinal deflection of bristle
δ_{yb}		Lateral deflection of bristles
δ_{yc}		Lateral deflection of carcass relative leading edge of contact patch
δ_{yctot}		Total lateral deflection of carcass
$\delta_{y,cam}$		Lateral deflection of due to camber
Slip		
α	α	Slip angle (2.1)
λ	$-S_{Xw}$	Longitudinal slip (2.5– 2.6)

s_H	Horizontal shift (7.2)
σ_x	Longitudinal physical slip (2.5)
σ_y	Lateral physical slip (2.5)
β	Slip velocity angle (2.4)
β_f	Angle for calculation of friction force direction (4.28)
β'	Suggestion for β_f to achieve collinearity (4.20)
β^{SPM}	Suggestion for β_f, slip-projection (4.23)
β^{MDR}	Suggestion for β_f, MDR-principle (4.24)
ψ	Normalized slip (4.49)
Parameters	
R_0	Unloaded radius of tire
R	Tire radius (distance from hub to contact patch). Force lever arm
R_e	Rolling radius
σ_{ax}	Longitudinal relaxation length
σ_{ay}	Lateral relaxation length
C_x	Braking stiffness
C_y	Cornering stiffness
C_y'	Cornering stiffness, calculated under the assumption of a flexible carcass.
C_γ	Camber stiffness
C_γ'	Camber stiffness, derived from (4.53), (4.45) and (4.42)
C_{cx}	Longitudinal carcass stiffness
C_{cy}	Lateral carcass stiffness
C_c	Lateral carcass bending-stiffness
c_p	Rubber bristle stiffness
μ	Friction coefficient
J_w	Wheel inertia

Semi-Empirical

Scale Factors

G_{ax}	Longitudinal scale factor for adhesion force (5.9)
G_{ay}	Lateral scale factor for adhesion force (5.9)
G_{sx}	Longitudinal scale factor for sliding force (5.13)
G_{sy}	Lateral scale factor for sliding force (5.13)
G_{camy}	Lateral scale factor for camber force (5.11)
G_{mz}	Torque scale factor for pure-slip torque (5.20)
G_{fz}	Torque scale factor for lateral force (5.21)
G_{camz}	Torque scale factor for camber (5.22)

Misc.

Υ	Force expression (5.10)
Λ	Normalisation of the normalized slip (5.15)
Λ_z	Normalisation of the normalized slip (5.23)
$\Gamma_{x,y}$	Sliding force scale factor without friction ellipse limitation (5.14) and (5.16)

Wheel Speed Correction

θ	Nominal angle between teeth
$\delta\theta$	Angular deviation
N	Number teeth on tooth wheel
i	Tooth number
j	Revolution number
φ_a	Angular deflection of axle
M_B	Braking torque
J_a	Axle inertia
D_a	Damping in axle
K_a	Axle stiffness

Friction Estimation

θ	Parameters for estimation
V	Cost function (7.9)
w_i	Weight of bin i in cost function
$\mathcal{X}$	Bin intervals, S-bin (slip) (7.6)
$\mathcal{Y}$	Bin intervals, F-bin (force) (7.6)
$\boldsymbol{J}$	Jacobian matrix (7.15)
$\boldsymbol{H}$	Hessian matrix (7.13)
λ_i	Forgetting factor for bin i

Subscripts

Notation	Valid on	Description
$_a$	F, M, G, μ	Contribution from adhesive part of contact patch
$_s$	F, M, G	Contribution from sliding part of contact patch
$_s$	μ	Static friction
$_k$	μ	Kinetic friction
$_0$	F, M	Pure-slip entity
$_0$	C	Normalized entity, $C_{0x} = C_x/F_z$
$_x$	Vectors	Longitudinal direction
$_y$	Vectors	Lateral direction
$_z$	Vectors	Vertical direction, positive downwards
$_{cam}$	F, M, δ_y	Contribution from camber
$_v$	F, M, δ_y	Vehicle entity
$_{ij}$	$\bar{v}, \lambda, \alpha, \bar{F}, \bar{M}$	Wheel identifier, where $i = f, r$ (front or rear) or 1.. *number of axles* on the vehicle and $j = l, r$ (left or right).
$_m$	...	Measured quantity

Superscripts

Notation	Valid on	Description
$\hat{}$	$F, M, C, ...$	Measured or estimated quantity
$^\circ$	$\lambda, \alpha, \bar{\sigma}$	Slip where transition to full sliding occurs
*	$\lambda, \alpha, \bar{\sigma}, F, M$	Point for friction maximum. Corresponds to subscript $_{crit}$ and $_{max}$ in ISO 8855
$^-$	Vectors	Vector (x, y, z)
$'$	v, λ, α	Value, measured at the rim under the assumption of a flexible carcass
$'$	σ_x, f_x, x, y	S-bin value (the slip signal is leading)
$''$	σ_x, f_x, x, y	F-bin value (the force signal is leading)
reg	$\sigma_{0x,y}$	Region-based pure slips, Eq (5.18)
vel	$\sigma_{0x,y}$	Velocity-invariant pure slips, Eq (5.12)

B

Scale Factors and Slip Conversion

The derivation of the scale factors is only performed in the lateral direction, but the procedure for the longitudinal scale factors is similar.

Adhesive slip scale factors

$$\begin{aligned} G_{ay}(\sigma_x, \sigma_y, \gamma) &= \frac{F_{ay,slip}(\sigma_x, \sigma_y, \gamma)}{F_{0y}(\sigma_{0ya})} \\ &= \frac{-C_y\sigma_y(1-\psi(\sigma_x, \sigma_y, \gamma))^2}{-C_y\sigma_y(1-\psi(0, \sigma_y, 0))^2 - F_z\mu_y \sin(\beta)\psi^2(0, \sigma_y, 0)\,(3-2\psi(0, \sigma_y, 0))} \\ &= \frac{-C_y\sigma_y(1-\psi(\sigma_x, \sigma_y, \gamma))^2}{-C_y\sigma_y(1-\psi(0, \sigma_y, 0))^2 - F_z\mu_y\sigma_y^\circ\frac{\sigma_y}{\sigma_y^\circ}\psi(0, \sigma_y, 0)\,(3-2\psi(0, \sigma_y, 0))} \\ &= \frac{3\,(1-\psi(\sigma_x, \sigma_y, \gamma))^2}{\Upsilon(0, \sigma_y, 0)} \end{aligned} \tag{B.1}$$

when $\psi < 1$, otherwise $G_{ay}(\sigma_x, \sigma_y, \gamma) = 0$.

$$\Upsilon(x, y, z) \triangleq \psi^2(x, y, z) - 3\psi(x, y, z) + 3 \tag{B.2}$$

Camber scale factor

$$G_{camy}(\sigma_x, \sigma_y, \gamma)) = \frac{F_{camy}(\sigma_x, \sigma_y, \gamma)}{F_{0cam}(\gamma)} = 2\psi^3(\sigma_x, \sigma_y, \gamma) - 3\psi^2(\sigma_x, \sigma_y, \gamma) + 1 \tag{B.3}$$

Sliding scale factors

$$
\begin{aligned}
G_{sy}(\sigma_x,\sigma_y,\gamma) &= \frac{F_{sy}(\sigma_x,\sigma_y,\gamma)}{F_{0y}(\sigma_{0ys})} \\
&= \frac{-F_z\mu_y\sin(\beta')\psi^2(\sigma_x,\sigma_y,\gamma)\,(3-2\psi(\sigma_x,\sigma_y,\gamma))}{-C_y\sigma_{0y}^{\mathrm{vel}}(1-\psi(0,\sigma_{0y}^{\mathrm{vel}},0))^2 - F_z\mu_y\psi^2(0,\sigma_{0y}^{\mathrm{vel}},0)\left(3-2\psi(0,\sigma_{0y}^{\mathrm{vel}},0)\right)} \\
&= \sin(\beta')\frac{\sigma_y^\circ}{\sqrt{\sigma_x^2+\sigma_y^2}\,\mathrm{sgn}(\sigma_{0y}^{\mathrm{vel}})}\frac{\psi^2(\sigma_x,\sigma_y,\gamma)(3-2\psi(\sigma_x,\sigma_y,\gamma))}{\Upsilon(0,\sigma_{0y}^{\mathrm{vel}},0)} \\
&\qquad\cdot\sqrt{\left(\frac{v_0}{v}\right)^2\left((1+\sigma_x)^2+\sigma_y^2\right)-(\sigma_x^2+\sigma_y^2)}
\end{aligned}
\tag{B.4}
$$

remark that

$$
\begin{aligned}
\Lambda &= \frac{\psi(\sigma_x,\sigma_y,\gamma)}{\sqrt{\sigma_x^2+\sigma_y^2}} \\
&\frac{\gamma^{\circ 2}}{\gamma^{\circ 2}-\gamma^2}\left(\sin(\beta)\sigma_y^\circ\frac{\gamma}{\gamma^\circ}+\sqrt{\left(\frac{\cos(\beta)}{\sigma_x^\circ}\right)^2+\left(\frac{\sin(\beta)}{\sigma_y^\circ}\right)^2-\left(\frac{\cos(\beta)\gamma}{\sigma_x^\circ\gamma^\circ}\right)^2}\right)
\end{aligned}
\tag{B.5}
$$

using

$$
\sin(\beta)=\frac{\sigma_y}{\sqrt{\sigma_x^2+\sigma_y^2}};\qquad \cos(\beta)=\frac{\sigma_x}{\sqrt{\sigma_x^2+\sigma_y^2}} \tag{B.6}
$$

Scale factors for the self aligning torque

$$
\begin{aligned}
M_z(\sigma_x,\sigma_y,\gamma) &= (M_{0z}(\sigma_y^{\mathrm{reg}}) - t_{0a}(0,\sigma_y^{\mathrm{reg}},0)F_{ay,slip}(0,\sigma_y^{\mathrm{reg}},0))\sin(\beta') \\
&\quad + t_a(\sigma_x,\sigma_y,\gamma)F_{ay,slip}(\sigma_x,\sigma_y,\gamma) + M_{z,cam}(\sigma_x,\sigma_y,\gamma) \\
&= G_z(\sigma_x,\sigma_y,\gamma)M_{0z}(\sigma_y^{\mathrm{reg}}) + G_{fz}(\sigma_x,\sigma_y,\gamma)F_{0y}(\sigma_y^{\mathrm{reg}}) + G_{camz}\hat{F}_{0cam}(\gamma)
\end{aligned}
\tag{B.7}
$$

where

$$
G_{mz}=\sin(\beta') \tag{B.8}
$$

and

$$
\begin{aligned}
G_{fz} &= \frac{t_a(\sigma_x,\sigma_y,\gamma)F_{ay,slip}(\sigma_x,\sigma_y,\gamma)}{F_{0y}(0,\sigma_y^{\mathrm{reg}},0)} - \frac{t_{0a}(0,\sigma_y^{\mathrm{reg}},0)F_{ay,slip}(0,\sigma_y^{\mathrm{reg}},0)}{F_{0y}(0,\sigma_y^{\mathrm{reg}},0)}\sin(\beta') \\
&= \frac{t_{0a}(\sigma_x,\sigma_y,\gamma)}{F_{0y}(0,\sigma_y^{\mathrm{reg}},0)}(F_{ay,slip}(\sigma_x,\sigma_y,\gamma) - F_{ay,slip}(0,\sigma_y^{\mathrm{reg}},0)\sin(\beta')) \\
&= \frac{a}{3}\frac{(4\psi-1)(1-\psi)^2}{\Upsilon}\left(\frac{\sigma_y}{\sigma_y^\circ\psi}-\sin(\beta')\right) = \frac{a}{3}\frac{(4\psi-1)(1-\psi)^2}{\Upsilon}\left(\frac{\sin(\beta)}{\sigma_y^\circ\Lambda}-\sin(\beta')\right)
\end{aligned}
\tag{B.9}
$$

where t_a is the pneumatic trail for the adhesive region defined as

$$
t_a(\sigma_x,\sigma_y,\gamma)=\frac{M_{az}(\sigma_x,\sigma_y,\gamma)}{F_{ay,slip}(\sigma_x,\sigma_y,\gamma)} \tag{B.10}
$$

Finally

$$
G_{camz}=\frac{M_{z,cam}(\sigma_x,\sigma_y,\gamma)}{F_{cam}(0,\sigma_y^{\mathrm{reg}},0)} \tag{B.11}
$$

simply derived from Equation (4.56) and (4.52).

Computation of velocity invariant slips

The relative velocity v_s at the combined slip (σ_x,σ_y) and the wheel-travel velocity v is given by

$$
v_s=\sqrt{v_{sx}^2+v_{sy}^2}=\frac{v\sqrt{\sigma_x^2+\sigma_y^2}}{\sqrt{(1+\sigma_x)^2+\sigma_y^2}} \tag{B.12}
$$

For the pure longitudinal slip at the wheel-travel velocity $v_{0x}=v_0$ and the slip velocity $v_{0sx}=v_s\,\mathrm{sgn}(\sigma_x)$ the slip definition gives:

$$
\sigma_{0x}^{\mathrm{vel}}=\frac{v_{0sx}}{v_{0x}-v_{0sx}}=\frac{v_s\,\mathrm{sgn}(\sigma_x)}{v_0-v_s\,\mathrm{sgn}(\sigma_x)}=\frac{\sqrt{\sigma_x^2+\sigma_y^2}\,\mathrm{sgn}(\sigma_x)}{\frac{v_0}{v}\sqrt{(1+\sigma_x)^2+\sigma_y^2}-\sqrt{\sigma_x^2+\sigma_y^2}\,\mathrm{sgn}\,(\sigma_x)} \tag{B.13}
$$

and for the lateral case with $v_{0sy}=v_s\,\mathrm{sgn}(\sigma_y)$, $v_{0x}=\sqrt{v_0^2-v_{0sy}^2}$ and $v_{0sx}=0$,

$$
\sigma_{0y}^{\mathrm{vel}}=\frac{v_{0sy}}{v_{0x}-v_{0sx}}=\frac{v_s\,\mathrm{sgn}(\sigma_y)}{\sqrt{v_{0x}^2-v_{0sy}^2}}=\frac{\sqrt{\sigma_x^2+\sigma_y^2}\,\mathrm{sgn}(\sigma_y)}{\sqrt{\left(\frac{v_0}{v}\right)^2\left((1+\sigma_x)^2+\sigma_y^2\right)-(\sigma_x^2+\sigma_y^2)}} \tag{B.14}
$$

Use of slip expressed in λ and α

In many occasions the slip expressed in λ and α is more convenient to use. The pure-slip tire forces are also mostly expressed as functions of these slips. Here follows guidelines for necessary conversions if λ and α are preferred. Calculate $\psi(\sigma_x,\sigma_y,\gamma)$ by use of the following formulas

$$
\sigma_x=\frac{\lambda}{1-\lambda};\qquad \sigma_y=\frac{\tan(\alpha)}{1-\lambda} \tag{B.15}
$$

The limit slips are calculated as

$$
\lambda^\circ=\begin{cases}\dfrac{\sigma_x^\circ}{1+\sigma_x^\circ} & \text{if}\quad \lambda>0;\text{Braking}\\[2ex] \dfrac{\sigma_x^\circ}{1-\sigma_x^\circ} & \text{if}\quad \lambda<0;\text{Driving}\end{cases} \tag{B.16}
$$

$$\alpha^\circ = \operatorname{atan}(\sigma_y^\circ) \tag{B.17}$$

For the adhesive region the deformation-invariant pure-slips are calculated as

$$\lambda_{0a} = \lambda \tag{B.18}$$

$$\alpha_{0a} = \arctan\left(\frac{\tan(\alpha)}{1-\lambda}\right) \tag{B.19}$$

and for the sliding region the velocity-invariant pure-slips as

$$\lambda_{0s} = \frac{v}{v_0}\sqrt{(\lambda\cos(\alpha))^2 + \sin^2(\alpha)}\,\operatorname{sgn}(\lambda) \tag{B.20a}$$

$$\sin(\alpha_{0s}) = \frac{v}{v_0}\sqrt{(\lambda\cos(\alpha))^2 + \sin^2(\alpha)}\,\operatorname{sgn}(\alpha) \tag{B.20b}$$

The region-invariant slips as derived as

$$\lambda_{0z} = \frac{\lambda^\circ\psi(\sigma_x,\sigma_y,\gamma)}{1-\lambda^\circ+\lambda^\circ\psi(\sigma_x,\sigma_y,\gamma)}\operatorname{sgn}(\lambda) \tag{B.21a}$$

$$\alpha_{0z} = \arctan(\tan(\alpha^\circ)\psi(\sigma_x,\sigma_y,\gamma)\operatorname{sgn}(\alpha)) \tag{B.21b}$$

The slip-velocity angle is derived as

$$\tan(\beta) = \frac{\sin(\alpha)}{\lambda\cos(\alpha)} \tag{B.22}$$

C

Extension of Optimization Algorithm to Include Horizontal Shift

To include the horizontal shift in the parameter estimations the brush model definition has to slightly redefined

$$\Psi(\sigma_x, C_{0x}, \mu, s_h) = \begin{cases} -C_{0x}(\sigma_x+s_h) + \dfrac{1}{3}\dfrac{(C_{0x}^2(\sigma_x+s_h))|(\sigma_x+s_h)|)}{\mu} \\ -\dfrac{1}{27}\dfrac{(C_{0x}(\sigma_x+s_h))^3}{\mu^2} & \text{if} \quad |\sigma_x| < \sigma_x^\circ \\ -\mu\cdot\operatorname{sign}(\sigma_x) & \text{otherwise} \end{cases} \tag{C.1}$$

Using the least-squares method for low-slips the regressor vector can be set as $\phi_i = [1 \quad x_i]$ estimating the parameters $\boldsymbol{\theta} = [\theta_0 \quad C_{0x}]$ from where the horizontal shift is derived as $s_h = \theta_0/C_{0x}$. In fact, it is the vertical shift that is estimated, but in the linear region the relation between horizontal and vertical shift is proportional. The same relation do not hold when extending slip area to include detection of the curvature of the force-slip relation. Using the regressor $\phi_i = [1 \quad x_i \quad x_i|x_i|]^T$ with $\boldsymbol{\theta} = [\theta_0 \quad C_{0x} \quad \theta_2]$ and $s_h = \theta_0/C_{0x}$ and $\mu = C_{0x}^2/(3\theta_2)$ might provide erroneous result.

Using the Gauss-Newton algorithm, the Jacobian matrix has to be extended with the derivative of the shift factor as

$$\boldsymbol{J}(\Omega,\theta)=\begin{bmatrix}\frac{\partial e_1}{\partial C_{0x}} & \frac{\partial e_2}{\partial C_{0x}} & \cdots & \frac{\partial e_N}{\partial C_{0x}}\\ \frac{\partial e_1}{\partial \mu} & \frac{\partial e_2}{\partial \mu} & \cdots & \frac{\partial e_N}{\partial \mu}\\ \frac{\partial e_1}{\partial s_h} & \frac{\partial e_2}{\partial s_h} & \cdots & \frac{\partial e_N}{\partial s_h}\end{bmatrix}^T \tag{C.2}$$

with

$$\frac{\partial e}{\partial s_h}=\begin{cases}C_{0x}-\frac{2}{3}\frac{C_{0x}^2|\sigma_x+s_h|}{\mu}+\frac{1}{9}\frac{\left(C_{0x}(\sigma_x+s_h)\right)^2}{(\mu)^2} & \text{if} \quad |\sigma_x|<\sigma_x^\circ\\ 0 & \text{otherwise}\end{cases} \tag{C.3}$$